TRANSACTIONS
OF THE ASME
Series B

Journal of
ENGINEERING FOR INDUSTRY

May 1959

Divisions: AVIATION • MACHINE DESIGN • MANAGEMENT • PROCESS INDUSTRIES
MAINTENANCE AND PLANT ENGINEERING • RAILROAD • PRODUCTION ENGINEERING
MATERIALS HANDLING • RUBBER AND PLASTICS • PETROLEUM • SAFETY • TEXTILE
WOOD INDUSTRIES • Research Committees: METAL PROCESSING • FLOW OF
BULK MATERIALS • ELEVATORS • MECHANICAL SPRINGS

Published Quarterly by
THE AMERICAN SOCIETY OF MECHANICAL ENGINEERS

TRANSACTIONS OF THE ASME
Series B

Journal of
ENGINEERING FOR INDUSTRY

VOLUME 81 • SERIES B • NUMBER 2
May 1959

CONTENTS

95 **The Strength of Thick-Walled Cylinders**
B. Crossland, S. M. Jorgensen, and J. A. Bones

115 **Steady-State Creep Analysis of the Weight Loadings of Furnace Tubes on Multiple Supports**
J. L. Jacobowitz and C. K. Mader

126 **How to Replace Gears by Mechanisms (Linkages)**
Kurt Hain and Gerhard Marx

131 **The Effect of a Lead Additive on the Machinability of Alloy Steels**
Norman Zlatin and J. V. Gould

139 **Controlled Contact Cutting Tools**
B. T. Chao and K. J. Trigger

152 **A Study of the Effects of Tool Flank Wear on Tool Chip Interface Temperature**
D. R. Olberts

159 **Synthesis of Path-Generating Mechanisms by Means of a Programmed Digital Computer**
Ferdinand Freudenstein and G. N. Sandor

169 **Synthesis of the Four-Bar Linkage to Match Prescribed Velocity Ratios**
Philip Barkan and E. J. Tuohy

178 **High-Range Plasticity of Metals Beyond Normal Work-Hardening**
E. V. Crane and W. S. Wagner

183 **Self-Excited Vibrations in Metal Cutting**
N. H. Cook

EDITORIAL DEPARTMENT

Editor, J. J. JAKLITSCH, JR.
Editor Emeritus, GEORGE A. STETSON
Consulting Editor, LEO BLODGETT
Production, JEAN NORTH
Art Editor, HENRY BALFOUR

OFFICERS OF THE ASME

President, G. B. WARREN
Secretary, O. B. SCHIER, II
Treasurer, E. J. KATES
Assistant Treasurer, H. J. BAUER

PUBLICATIONS COMMITTEE

Chairman, JOHN de S. COUTINHO
B. G. A. SKROTZKI
HENDLEY N. BLACKMON
R. D. MINDLIN
MARTIN GOLAND

Junior Representatives
A. T. WUSKA
A. S. GOLDSTEIN

REGIONAL ADVISORY BOARD

Region I, ROY L. PARSELL
Region II, GLENN R. FRYLING
Region III, F. J. HEINZE
Region IV, FRANCIS C. SMITH
Region V, H. M. CATHER
Region VI, C. R. EARLE
Region VII, M. POPOVICH
Region VIII, LINN HELANDER

Published quarterly by The American Society of Mechanical Engineers. Publication office at 20th and Northampton Streets, Easton, Pa. The editorial department is located at the headquarters of the Society, 29 West Thirty-Ninth Street, New York 18, N.Y. Cable address, "Mechaneer," New York. Price $3.00 a copy, $10.00 annually; to members, $1.50 a copy, $5.00 annually. Add 50 cents for postage to all countries outside the United States, Canada, and Pan American Union. Changes of address must be received at Society headquarters seven weeks before they are to be effective on the mailing list. Please send old as well as new address. . . . By-Law: The Society shall not be responsible for statements or opinions advanced in papers or . . . printed in its publications (B13, Par. 4). . . . Application to mail at second-class postage rates is pending at the Post Office at Easton, Pa. . . . © Copyrighted, 1959, by The American Society of Mechanical Engineers. Reprints from this publication may be made on condition that full credit be given the Transactions of the ASME, Series B — Journal of Engineering for Industry, and the author, and that date of publication be stated.

TRANSACTIONS OF THE ASME
Is indexed by the Engineering Index, Inc.

TRANSACTIONS OF THE ASME Series D

Journal of
BASIC ENGINEERING
Vol. 81 • Series D • No. 1

CONTENTS FOR MARCH, 1959

1 Ball Motion and Sliding Friction in Ball Bearings, by A. B. Jones. (58—AV-14)
13 A Variational Approach to Lubrication Problems and the Solution of the Finite Journal Bearing, by D. F. Hays. (58—SA-54)
24 On the Necessity of Unsteady Flow in Fluid Machines, by R. C. Dean, Jr.
29 Prediction of Choking Flow in Centrifugal Impellers, by Harold Lown and F. J. Wiesner, Jr. (58—SA-15)
37 Concerning Subharmonic Oscillations Which May Exist in Nonlinear Systems Having Odd Restoring Forces, by C. A. Ludeke and William Pong.
41 An Analytic Frequency-Response Solution for a Higher Order Servomechanism With a Nonlinear Control Element, by A. M. Hopkin and K. Ogata. (58—SA-35)
46 Antifriction Instrument-Bearing Torque Testing and the Resistance to Motion of Such Bearings, by A. B. Asch. (58—SA-34)
49 Analysis and Characteristics of the Three-Lobe Bearing, by O. Pinkus. (58—LUB-2)
56 An Investigation of Dry Adhesive Wear, by R. P. Steijn. (58—LUB-8)
67 Sliding Wear and Metal Transfer Under Unlubricated Conditions, by R. P. Steijn. (58—LUB-9)
79 On the Mechanism of Gear Lubrication, by V. N. Borsoff. (58—LUB-4)
94 The Influence of the Molecular Mean Free Path on the Performance of Hydrodynamic Gas Lubricated Bearings, by Albert Burgdorfer. (58—LUB-7)

TRANSACTIONS OF THE ASME Series E

Journal of
APPLIED MECHANICS
Volume 81 • Series E • Number 1

CONTENTS FOR MARCH, 1959

TECHNICAL PAPERS

3 Experimental Surface-Wave Method for Recording Force-Time Curves, J. N. Goodier, W. E. Jahsman, and E. A. Ripperger. (58—A-51)
8 Forced Torsional Vibration of Systems With Distributed Mass and Damping, K. E. Bisshopp. (58—A-8)
13 Frequencies of a Flexible Circular Plate and Light Elastic Half-Space, G. N. Bycroft. (58—A-37)
18 Analytical Design of Disk Cams by Independent Position Equations, F. H. Raven. (58—A-17)
25 Stress Distribution and Plastic Deformation in Rotating Cylinders, E. A. Davis and F. M. Connelly. (58—A-10)
31 Transient and Residual Stresses in Heat-Treated Cylinders, J. H. Weiner and J. V. Huddleston. (58—A-21)
40 The Nonlinear Bending of Thin Rods, T. P. Mitchell. (58—A-50)
44 Stresses and Deflections in Circular Plate Loaded Over a Segment, W. A. Bassali and M. Nassif. (58—A-27)
55 Transverse Flexure of a Thin Plate Containing Two Circular Holes, O. Tamate. (58—A-35)
61 Limit Analysis of Symmetrically Loaded Thin Shells of Revolution, D. C. Drucker and R. T. Shield. (58—A-26)
69 On Influence Coefficients and Nonlinearity for Thin Shells of Revolution, Eric Reissner. (58—A-33)
73 A Theorem of Maximum Strain Energy, E. H. Brown. (58—A-40)
77 Plastic Stress-Strain Relationships—Effect of Loading Path and History, S. S. Gill and J. Parker. (58—A-11)
88 A Stress-Strain Relation for Hexagonal Close-Packed Array of Spheres, J. Duffy. (58—A-53)
95 A Mathematical Model of the Stress-Strain Diagram and Hysteresis Loop, I. R. Whiteman. (58—A-68)
101 A Definition of Stable Inelastic Material, D. C. Drucker. (58—A-31)
107 Retarded Flow of Bingham Materials, Alfred Slibar and P. R. Paslay. (58—A-34)
114 An Experiment on Compressible-Flow Perturbations, T. A. D'Ews Thomson and R. E. Meyer. (58—A-52)
120 Transient Film Condensation, E. M. Sparrow and Robert Siegel. (58—A-13)
122 Effect of Turbulence on Slider-Bearing Lubrication, Y. T. Chou and Edward Saibel. (58—A-30)
127 Theory of Flight of the Sounding Rocket, V. C. Liu. (58—A-32)

DESIGN DATA AND METHODS

130 Stress-Concentration Factors for T-Heads, M. Hetényi.

BRIEF NOTES

133 Buoyancy Effects in Forced-Convection Flow, E. M. Sparrow and J. L. Gregg. 134 Thermally Induced Twists in Thin Plates, L. S. Han and K. L. Bergman. 136 Deflections and Vibrations of Clamped Sectorial Plates, M. Ben-Amoz. 137 Thermal Distributions Without Thermal Stresses, H. H. Hilton. 138 Thin-Walled Cylinders Under Torsion and Pressure, H. S. Suer and L. A. Harris. 140 Transient Heat Transfer for Flow in Ducts, Robert Siegel. 142 Upper and Lower Bounds for Stiffness of Plates, Eric Reissner. 143 Cross-Section Distortion and the Timoshenko Beam Equation, A. D. S. Barr. 144 Analysis of Paraboloidal Shells, Robert Schmidt. 145 Natural Frequencies of Two Nonlinear Systems, E. W. Gaylord. 146 Response of a Slab to Impact, J. N. Goodier and E. A. Ripperger. 147 Thermal Stresses in Long Cylindrical Shells, C. H. Tsao. 148 Dynamic Characteristics of Undamped Vibration Systems, M. E. Gurtin.

DISCUSSION

150 Discussion of previously published papers by A. J. Durelli and A. S. Kobayashi; J. W. Dally, A. J. Durelli, and W. F. Riley; R. Plunkett; J. W. Miles; T. H. Lin.

154 BOOK REVIEWS

TRANSACTIONS OF THE ASME Series A

Journal of
ENGINEERING FOR POWER

Volume 81 • Series A • Number 2

CONTENTS FOR APRIL, 1959

111 The Control System of a 225,000-Kw Double-Automatic Extraction Steam Turbine and Related Reducing Stations, by M. A. Eggenberger and P. G. Ipsen. (58—SA-36)

123 Design of 321-Mw Cross-Compound Steam Turbine—River Rouge Unit No. 3, by C. D. Wilson. (58—SA-22)

133 Five Years' Experience on the Consolidated Edison System With Protection of Turbine Generators and Boilers by Automatic Tripping, by W. C. Beattie, H. A. Bauman, J. M. Driscoll, P. T. Onderdonk, and R. L. Webb. (58—Pwr-8)

142 A Simplified Regenerator Theory, by W. F. Schalkwijk. (58—A-135)

151 Development of a Smooth Running, Double-Spool, Gas-Turbine Rotor System, by J. R. Schnittger. (58—A-197)

161 M-252 Alloy for Heavy-Duty Gas-Turbine Buckets, by G. R. Fusner and D. L. Newhouse. (58—A-191)

177 The Calibration of Thermocouples by Freezing-Point Baths and Empirical Equations, by R. P. Benedict. (58—A-175)

189 Theoretical Stresses Near a Circular Opening in a Flat Plate, Reinforced With a Cylindrical Outlet, by E. O. Waters. (58—A-171)

201 Effect of Steam-Turbine Reheat on Speed-Governor Performance, by Charles Concordia. (58—A-36)

208 Load Capacity Tests on Tapered-Land and Pivoted-Shoe Thrust Bearings for Large Steam-Turbine Application, by R. E. Brandon and H. C. Bahr. (58—A-172)

TRANSACTIONS OF THE ASME Series C

Journal of
HEAT TRANSFER

Vol. 81 • Series C • No. 2

CONTENTS FOR MAY, 1959

95 Heat and Mass Transfer From a Rotating Disk, by F. Kreith, J. H. Taylor, and J. P. Chong.

106 Numerical and Machine Solutions of Transient Heat-Conduction Problems Involving Melting or Freezing, Part I, by W. D. Murray and Fred Landis. (58—HT-16)

113 A Theory of Rotating Condensation, by E. M. Sparrow and J. L. Gregg. (58—A-70)

121 Laminar Heat Transfer in Rectangular Channels, by L. S. Han. (58—A-124)

129 Heat Transfer to Water in Thin Rectangular Channels, by S. Levy, R. A. Fuller, and R. O. Niemi. (58—A-127)

144 Combined Geometric and Network Analog Computer for Transient Heat Flow, by Victor Paschkis (58—A-69)

151 Heat Transfer From an Annular Fin of Constant Thickness, by H. H. Keller and E. V. Somers. (58—A-116)

157 A Variational Method for Fully Developed Laminar Heat Transfer in Ducts, by E. M. Sparrow and R. Siegel. (58—A-92)

168 The Effect of Surface Roughness on the Convection Heat-Transfer Coefficient for Fully Developed. Turbulent Flow in Ducts With Uniform Heat Flux, by R. T. Lancet. (58—A-122)

B. CROSSLAND

Senior Lecturer in Mechanical Engineering, University of Bristol, Bristol, England

S. M. JORGENSEN

Mechanical Engineer, Foster Wheeler Corporation, New York, N. Y.

J. A. BONES

Lecturer in Mechanical Engineering, University of Bristol, Bristol, England

The Strength of Thick-Walled Cylinders

Comprehensive pressure tests have been carried out on thick-walled, closed-ended cylinders made from a mild steel and a hardened and tempered steel, the maximum pressure reached being 94,000 lb/in.[2] *The complete theoretical behavior of the cylinders is computed from shear stress-strain data obtained from torsion tests and is shown to be in very close agreement with the experimental results. In addition, a method is given for deriving the large strain behavior of the cylinders from tension test data. When compared with the experimental results this approach gives larger errors, the theoretical values of pressure being consistently high. Finally, ultimate pressures have been calculated from two empirical expressions.*

Introduction

When a thick-walled cylinder is subjected to a slowly increasing internal pressure it will initially be wholly elastic with the bore most highly stressed. At the initial yield pressure yield occurs at the bore and the cylinder becomes partially plastic with a plastic core and elastic outer shell. With increasing pressure the plastic-elastic boundary moves outward until it reaches the outer surface of the cylinder. Further expansion of the now fully-plastic cylinder may occur at a constant or "collapse" pressure until strain-hardening starts to occur at the bore. The cylinder will then withstand increasing pressure so long as the strengthening effect of strain-hardening is greater than the weakening effect of reduced wall thickness caused by expansion. At the ultimate or maximum pressure these effects become equal and further straining and finally failure of the cylinder occur at lower pressures.

A comprehensive survey of previous work on this subject, both theoretical and experimental, is given in Crossland and Bones [1][1] and will not be repeated here. Briefly three forms of solution have been proposed theoretically:

(*a*) Near-exact mathematical solutions so cumbersome as to be of little practical use to engineers.

(*b*) Empirical equations which give the ultimate pressure in terms of a single point on the stress-strain curve, usually the ultimate tensile stress.

(*c*) Solutions based on certain simplifying assumptions giving a numerical form which is reasonably simple to use and which fits the experimental results extraordinarily closely.

Theoretical details of one of the third form of solution are briefly set out in the Appendix. Fundamentally the assumptions made, which are well justified by experiment, enable the triaxial stress system in a closed-ended, thick-walled cylinder under internal pressure to be reduced to that of a simple shear plus a superimposed hydrostatic tension. This is known to be true in the elastic region and it is shown to be acceptably correct in the partially plastic and fully plastic regions. This established, and knowing that the hydrostatic stress has no significant effect on the behavior under shear stress of most engineering materials (Crossland [2]), the behavior of the cylinder may then be readily derived from shear stress-strain data for the material. In particular, the pressure-expansion curve at large strains and the ultimate pressure may be obtained using a method due to Manning [3].

The shear stress-strain data required are most readily obtained from a torsion test but the authors, realizing that the results of a tension test are more commonly available, have also given a solution based on tension test results which does, however, involve further assumptions.

In this paper the results of experiments involving pressure, tor-

[1] Numbers in brackets designate References at end of paper.

Contributed by the Petroleum Division and presented at the Petroleum-Mechanical Engineering Conference, Denver, Colo., September 21–24, 1958, of The American Society of Mechanical Engineers.

Note: Statements and opinions advanced in papers are to be understood as individual expressions of their authors and not those of the Society. Manuscript received at ASME Headquarters, June 27, 1958. Paper No. 58—Pet-20.

Nomenclature

σ_r, σ_t, σ_z = radial, hoop, and axial stresses (tension positive)
ϵ_r, ϵ_t, ϵ_z = corresponding strains
a = initial inner radius of thick-walled cylinder
b = initial outer radius
r = any initial intermediate radius
$K = \frac{b}{a}$ = diameter ratio
na = radius of plastic boundary
u = radial displacement of cylindrical surface radius r
u_a = radial displacement at bore
u_b = radial displacement at outer surface
P = internal pressure
P_{iy} = initial yield pressure
P' = internal pressure for partially-plastic state
P_c = collapse pressure
P_u = ultimate pressure
P_n = pressure at plastic-elastic boundary
P_τ = pressure summation based on torsion test data
P_σ = pressure summation based on tension test data
τ = shear stress
τ_{iy} = upper yield shear stress
τ_y = lower or plastic yield stress
γ = shear strain
γ_e = equivalent shear strain
d = diameter of torsion specimen
σ = tensile stress
σ_e = equivalent tensile stress
σ_u = ultimate tensile stress
l = initial length of element of tension specimen
v = extension of element
$\epsilon_e = \frac{v}{l}$ = equivalent engineer's tensile strain
E = Young's modulus
μ = Poisson's ratio

sion, and tension tests on two steels, a mild steel and a hardened and tempered alloy steel, called Vibrac, are reported. Some of these results have been reported by Crossland and Bones [1]. Seventeen mild steel cylinders, having diameter ratios of up to 8, and five Vibrac steel cylinders, having diameter ratios of up to 2, were pressure tested, the maximum pressure reached being 94,000 lb/in.^{2} The theoretical behavior of the thick-walled cylinders is derived from both the torsion and tension test data. The theoretical results based on torsion data are shown to be in very close agreement with the experimental results. Those based on tension data are less accurate and give consistently high values for pressure. Moreover, it is shown that the standard tension test, discontinued on reaching the ultimate stress, does not give sufficient large strain information about the material to enable more than a limited range of theoretical results to be computed. This limitation is overcome if Jorgensen's [4] postulate, that ultimate pressure is reached when the stress at the bore equals the ultimate tensile stress, is accepted. Theoretical ultimate pressures calculated on this basis fit the experimental results closely. Finally, the simple mean diameter formula which gives ultimate pressure explicitly in terms of ultimate tensile stress and diameter ratio:

$$P_u = 2\sigma_u \frac{(K-1)}{(K+1)}$$

is shown to give reasonable and safe values.

Apparatus

Torsion Tests. Torsion specimens were made to the form shown in Fig. 1 and were tested in the machine described by Morrison [5]. Changes of 45 lb/in.^{2} in shear stress and 10^{-6} (at small strains) in strain could be detected and the accuracy of calibration in each case was within 0.5 per cent.

Tension Tests. Two sizes of specimen, shown in Fig. 2, were tested in a machine designed by Robertson [6] in which the load is measured by a stiff load bar in tandem with the specimen, an arrangement which allows readings beyond the ultimate to be obtained. Axial strains were measured using one Martens-type extensometer on the small specimens and three equally spaced extensometers on the large specimens. Changes of 45 lb/in. stress and 5×10^{-6} strain could be detected and the accuracy of calibration in each case was within 1 per cent.

Pressure Tests. The high-pressure apparatus has been described

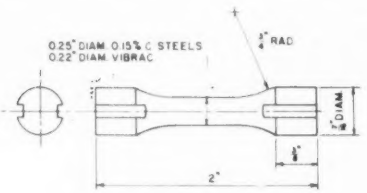

Fig. 1 Torsion specimen

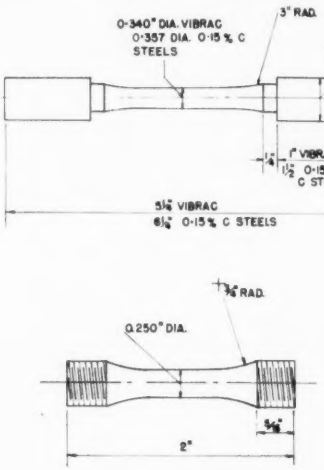

Fig. 2 Tension specimens

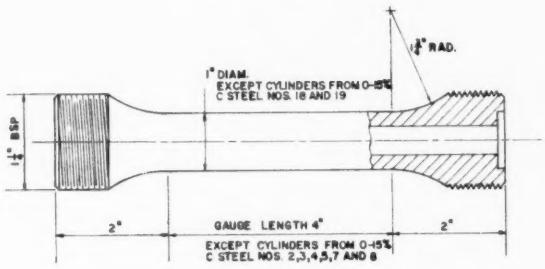

Fig. 3 Test cylinder

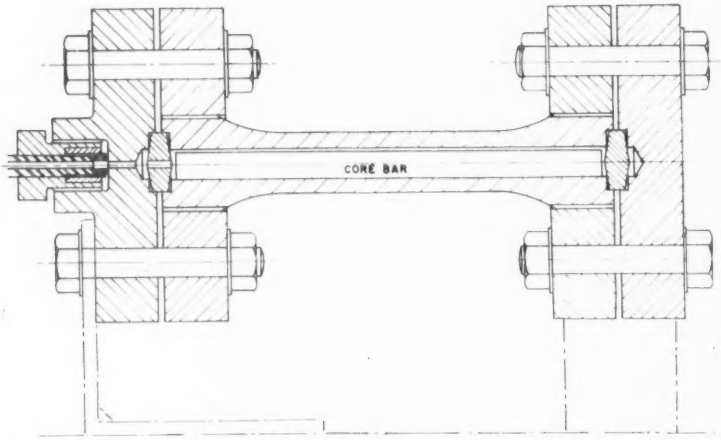

Fig. 4 Cylinder test assembly

in detail by Crossland and Bones [7] and a mixture of castor oil and brake fluid was used as the high-pressure liquid. This mixture does not freeze readily and has reasonable lubricating properties. The free-piston gage which is used to measure pressure has a sensitivity of 100 lb/in.^{2} at 100,000 lb/in.^{2} and is accurate to within 1 per cent over the complete pressure range of 5000 to 100,000 lb/in.^{2} Under pressure there is always some leakage past the piston of the pressure gage and at 100,000 lb/in.^{2} this was found to give a rate of decrease in pressure of not greater than 45 lb/in.^{2}/min.

Fig. 3 shows the form to which the thick-walled cylinders were machined and Fig. 4 is a cross-sectional drawing of a cylinder connected to the high-pressure system.

Measurements of diametral and axial strains at the external surface were made throughout the tests on most of the thick-walled cylinders. To measure axial strain two Martens-type extensometers of 2-in. gage length were fitted diametrally opposite one another and the diametral strains on two diameters at right angles in the central cross section were measured with optical extensometers similar to those of Cook [8]. A photograph of a cylinder set up with extensometers is shown in Fig. 5.

Changes of 5×10^{-6} in axial strain and 2×10^{-6} in diametral strain could be detected and the accuracy of calibration was within 0.5 and 1 per cent, respectively. Diametral strains of greater than 0.007 were measured with a micrometer sensitive to 0.0001 strain.

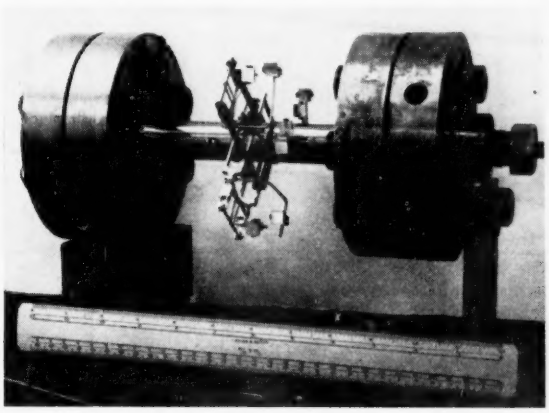

Fig. 5 Thick-walled cylinder set up for testing

Materials Tested and Position of Specimens

Table 1 gives the percentage compositions and other details of the two steels tested.

Table 1

	C	Si	S	P	Mn	Ni	Cr	Mo
0.15% carbon steel	0.15	0.047	0.048	0.020	0.66	...	...	...
Vibrac steel	0.3	0.24	0.012	0.013	0.66	2.57	0.58	0.60

	Form and condition	Supplier
0.15% carbon steel	2-in. diameter hot-rolled bar	Park Gate Iron & Steel Co.
Vibrac steel	13½-in. lengths of 2½-in. diameter hot-rolled bar individually oil quenched from 830 C and tempered at 660 C	English Steel Corporation

Fig. 6 shows the positioning of the specimens in the bars. It will be seen that the torsion and tension specimens were arranged to coincide in cross-sectional position with the cylinder walls and that they were distributed longitudinally between the thick-walled cylinders so as to give complete information about the properties of the bar.

A high-vacuum furnace was used to heat-treat all finished specimens. Those from 0.15 per cent carbon steel were normalized by heating at 900 C for one hour and cooling in the vacuum tube and those from Vibrac steel were stress-relieved at 600 C for one hour.

Technique of Testing

Torsion Tests. After the elastic behavior and yield point had been determined increments of strain were applied and the torque and twist measured after a delay of three minutes. The tests were continued to failure.

Tension Tests. Similarly, after yield, readings of load and extension were noted three minutes after the application of a strain increment. It was verified that for large axial strains the volume of

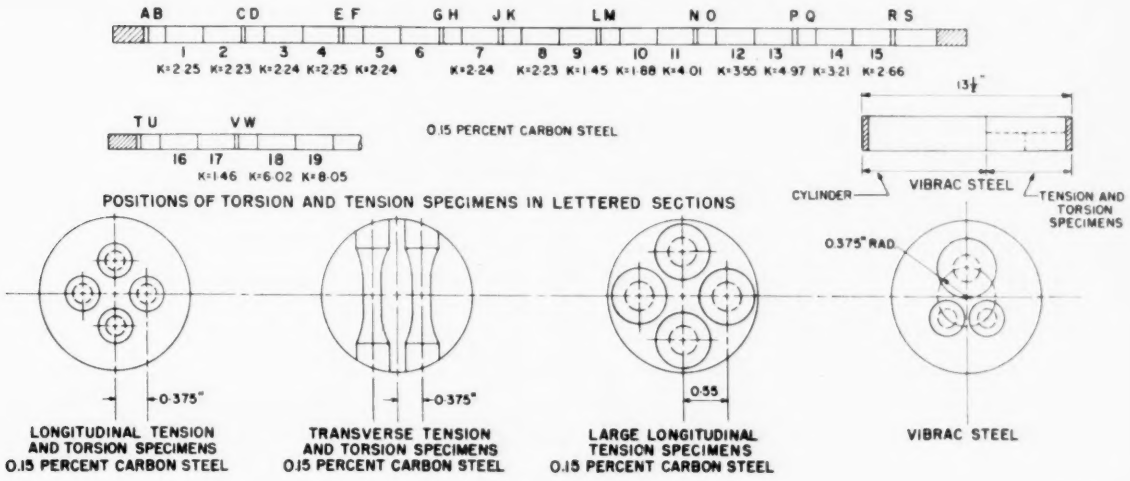
AB CD EF GH JK LM NO PQ RS
1 2 3 4 5 6 7 8 9 10 11 12 13 14 15
K=2·25 K=2·23 K=2·24 K=2·25 K=2·24 K=2·24 K=2·23 K=1·45 K=1·88 K=4·01 K=3·55 K=4·97 K=3·21 K=2·66
TU VW
16 17 18 19
K=1·46 K=6·02 K=8·05
0·15 PERCENT CARBON STEEL
POSITIONS OF TORSION AND TENSION SPECIMENS IN LETTERED SECTIONS
13½"
CYLINDER
VIBRAC STEEL
TENSION AND TORSION SPECIMENS
0·375" RAD
0·375"
0·375"
0·55
LONGITUDINAL TENSION AND TORSION SPECIMENS 0·15 PERCENT CARBON STEEL
TRANSVERSE TENSION AND TORSION SPECIMENS 0·15 PERCENT CARBON STEEL
LARGE LONGITUDINAL TENSION SPECIMENS 0·15 PERCENT CARBON STEEL
VIBRAC STEEL

Fig. 6 Distribution of specimens

the specimen remained sensibly constant so axial strains greater than 0.02 were calculated from the diameter of the specimen, measured with a micrometer. After the ultimate tensile stress was reached and necking of the specimen became apparent the diameter of the minimum cross section and the radius of curvature of the neck profile at this cross section were measured from an image projected on to a screen with a magnification of about 30 times. The tests were thus continued at decreasing load to failure.

Pressure Tests. In the elastic region small increments of pressure were applied and strain and pressure readings were noted after a three-minute delay to allow the slight temperature increase caused by the compression of the oil to be dissipated. In the early post-yield and plastic regions pressure was maintained constant for a short period and then the intensifier was switched off and the readings taken after a further three minutes. The tests were continued until the ultimate pressure was passed and the specimens were then burst without further measurements.

Compatibility of Testing Techniques. In each of the three forms of test, measurements were made three minutes after applying an increment of strain. During this period an increase of strain in the specimen brings about a decrease in load; the relationship between them being a function of the stiffness of the machine and load bar relative to that of the specimen for the torsion and tension tests, and of the stiffness of the high-pressure system relative to that of the specimen for the pressure tests. Tests in torsion and tension in which readings were observed at various times after applying a strain increment showed that the rate of change in the reading after three minutes was negligible. Tests carried out on thick-walled cylinders in which readings were noted at various times after each increase in strain, and tests in which the pressure was maintained constant while strain readings were noted at various times demonstrated that such differences in technique have very little influence on the pressure/expansion curve obtained. It is considered that the techniques adopted do not introduce any discrepancies which invalidate comparison between the three forms of test.

Results

Torsion Tests. The results of the torsion tests are shown in Figs. 7 and 8. Only a few of the experimental points obtained for each

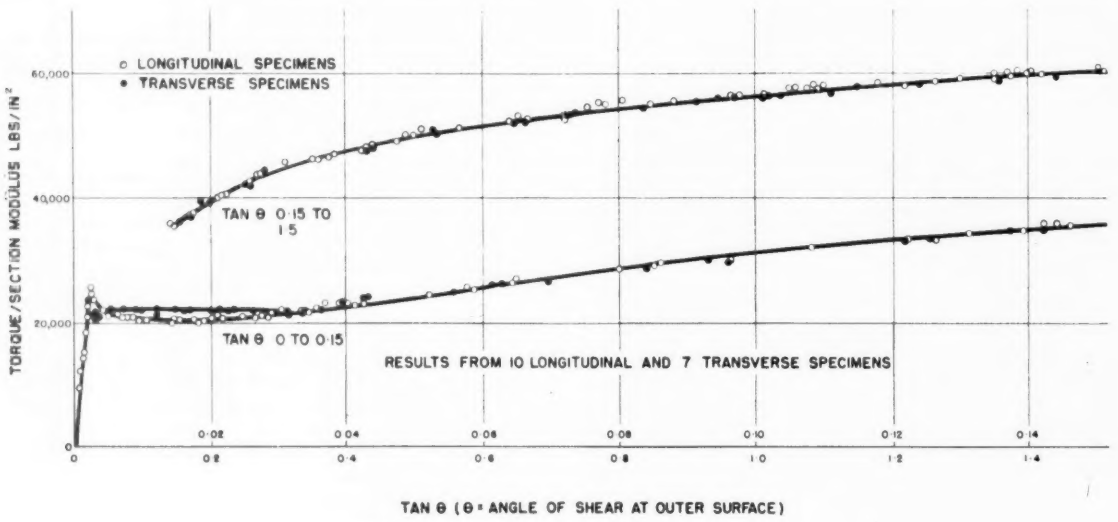

Fig. 7 0.15 per cent carbon steel torsion tests

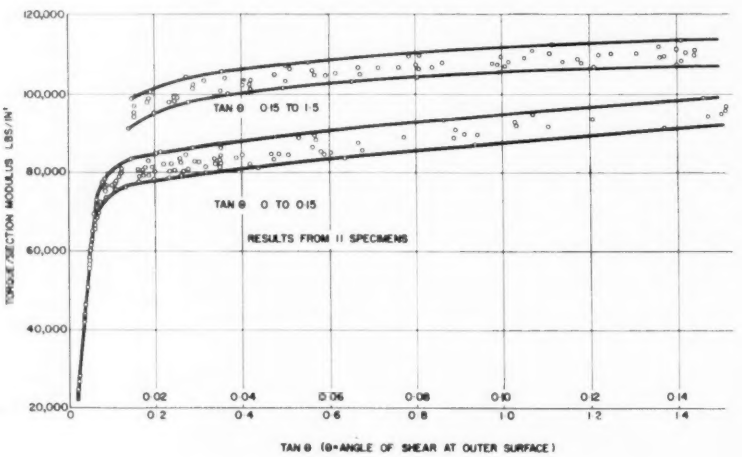

Fig. 8 Vibrac steel torsion tests

specimen are plotted and it should be noted that for any single specimen the experimental points lie on a smooth curve. Shear stress/strain curves (Figs. 9 and 10) have been derived from these results using the method given by Nadai [9]. The average properties of the two steels in torsion are given in Table 2.

Table 2

Direction of specimen	0.15% C — Transverse	0.15% C — Longitudinal	Vibrac Longitudinal
Upper yield stress, lb/in.^{2}	25,600	25,800	None
Plastic yield stress, lb/in.^{2}	16,600	15,200	60,000
Shear modulus, lb/in.^{2}	11.3×10^6	11.6×10^6	11.8×10^6

Tension Tests. The results of the tension tests as far as the ultimate are shown in Figs. 11 and 12 in terms of nominal stress and engineer's strain. Again it should be noted that each specimen gave a smooth curve. Accurate information about the elastic behavior and the upper yield stress could be obtained only from the large tensile specimens (see Fig. 2) where the eccentricity of loading was small and precisely known. At large strains the true stress at the neck has been determined using the analysis due to Bridgman [10] and the results are shown in Fig. 13. The average properties are given in Table 3.

Table 3

Direction of specimen	0.15% C — Transverse	0.15% C — Longitudinal	Vibrac Longitudinal
Upper yield tensile stress, lb/in.^{2}	Not measured	47,500	None
Plastic yield tensile stress, lb/in.^{2}	32,500	32,700	108,000
Ultimate tensile stress, lb/in.^{2}	54,600	57,100	122,000
Young's modulus lb/in.^{2}	Not measured	29.5×10^6	29.5×10^6

Pressure Tests. Preliminary tests were carried out to determine the effect of the gage length on the behavior of the thick-walled cylinders, using specimens from 0.15 per cent carbon steel having

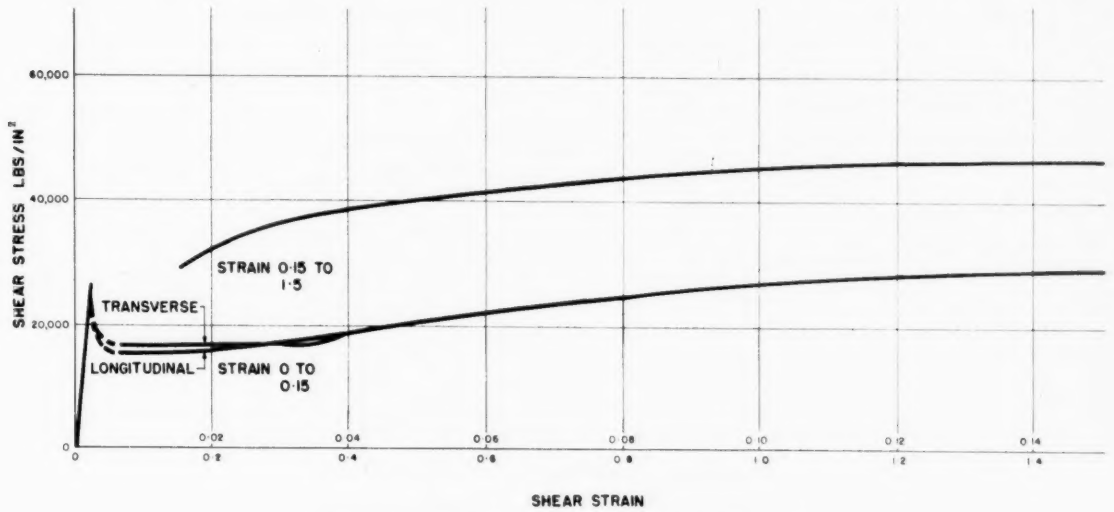

Fig. 9 0.15 per cent carbon steel derived shear-strain curves

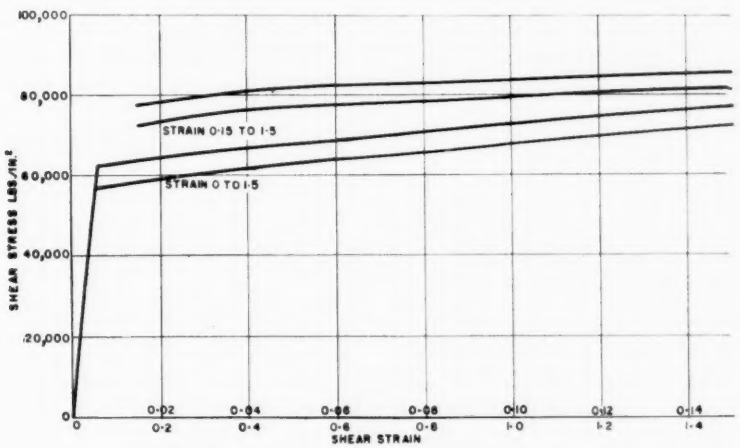

Fig. 10 Vibrac steel derived shear stress-strain curves

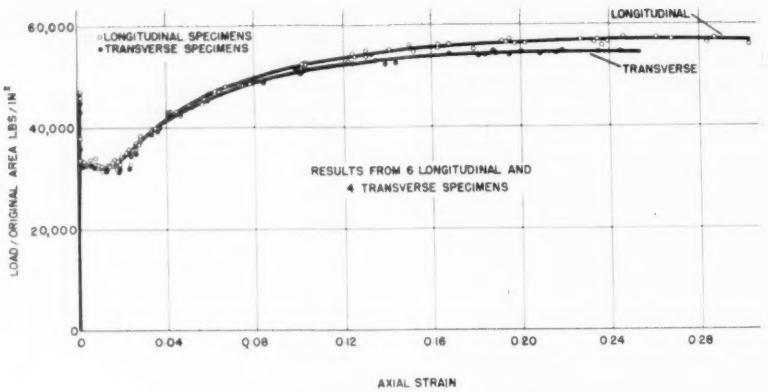

Fig. 11 0.15 per cent carbon steel tension tests

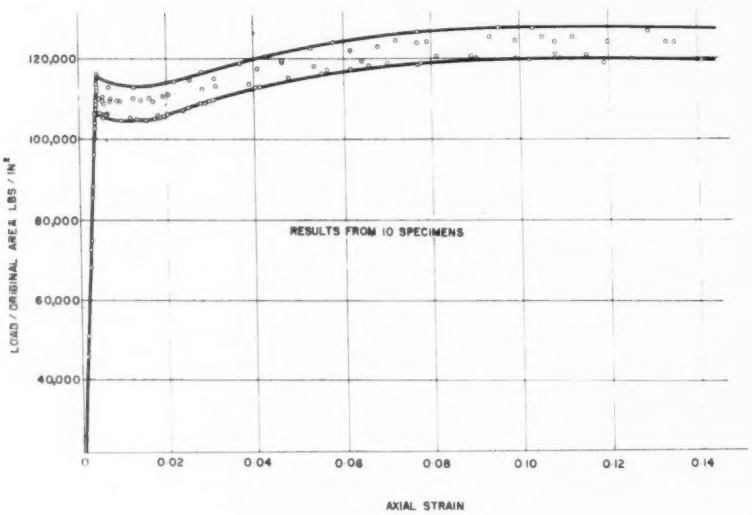

Fig. 12 Vibrac steel tension tests

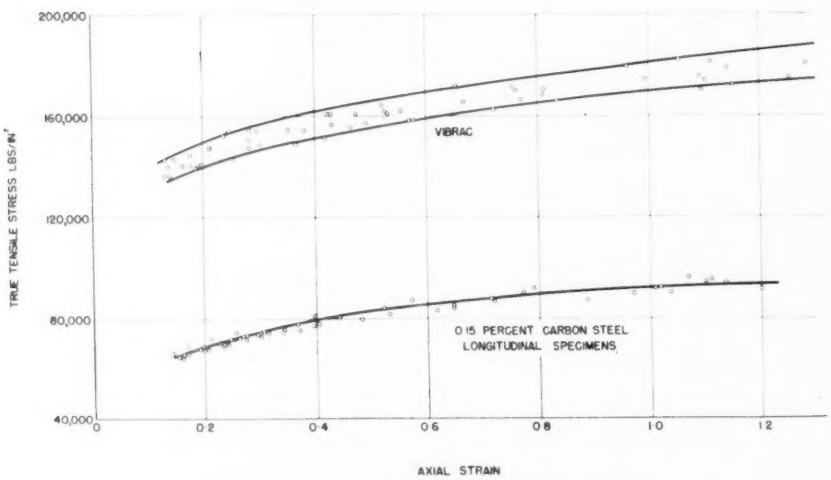

Fig. 13 Tension tests stress-strain curves at large strains

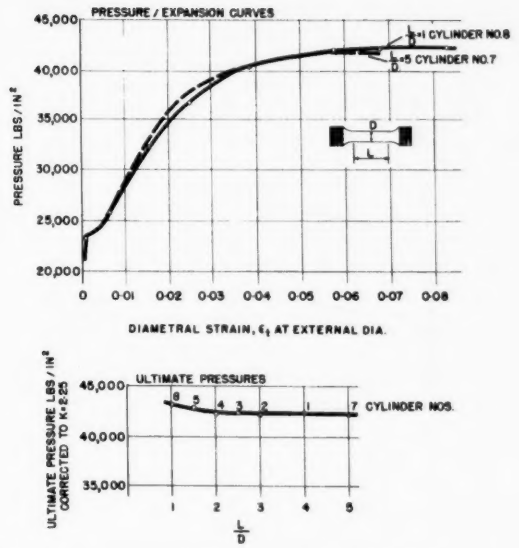

Fig. 14 0.15 per cent carbon steel pressure tests; effect of gage length

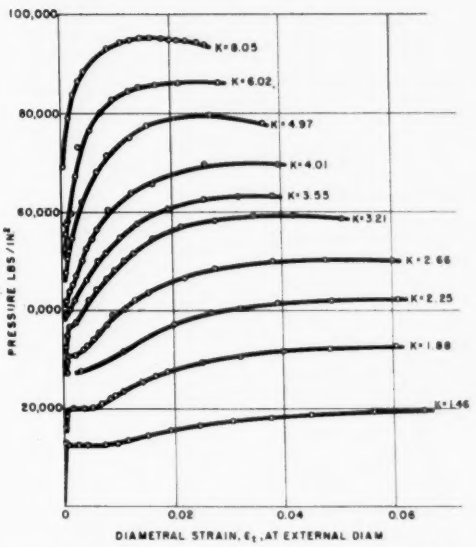

Fig. 16 0.15 per cent carbon steel pressure tests; pressure/expansion curves at large strains

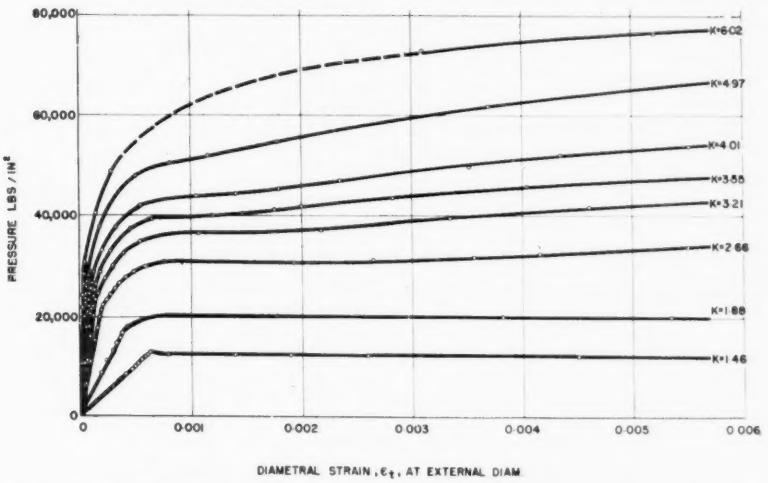

Fig. 15 0.15 per cent carbon steel pressure tests; pressure/expansion curves at small strains

a diameter ratio of 2.25. The results of these tests are shown in Fig. 14. The pressure/expansion curves for the cylinders having the extreme gage lengths are given and it is seen that the ends have a small strengthening effect at large strains for the very short cylinder. No differences were found in the pressure/expansion curves and hence in the ultimate pressures obtained for cylinders having a ratio of gage length to external diameter greater than 2. It follows that end effects in the standard thick-walled cylinder, for which this ratio is 4, are negligible.

The experimental pressure/expansion curves are shown in Figs. 15, 16, 17, and 18. No small strain readings for the cylinder having diameter ratio 8.05 could be obtained with the available size of double-diametral extensometer and for the cylinder having diameter ratio 6.02 the curve is shown by a broken line between 50,000 and 70,000 lb/in.^{2} since leakage in the high-pressure system invalidated the readings taken. In all of the 0.15 per cent carbon steel cylinders unsymmetrical yielding, manifesting itself as markedly different readings on the two diametral extensometers, was observed in the partially-plastic region; mean curves have been plotted in this region. No maximum in the pressure/expansion curve was obtained for the two cylinders having the smallest diameter ratios indicating that failure occurred before ultimate pressure was quite reached.

The average axial strains are shown in Figs. 19 and 20.

From the diametral and axial strains the shear yield stresses and elastic constants for the material may be calculated and mean values of these quantities are given in Table 4.

Table 4

	0.15% C	Vibrac
Upper yield shear stress, lb/in.^{2}	23,700 to 26,900	None
Plastic yield shear stress, lb/in.^{2}	15,700	60,000
Young's modulus, lb/in.^{2}	29.9×10^6	29.8×10^6
Poisson's ratio	0.282	0.283
Shear modulus, lb/in.^{2}	11.7×10^6	11.6×10^6

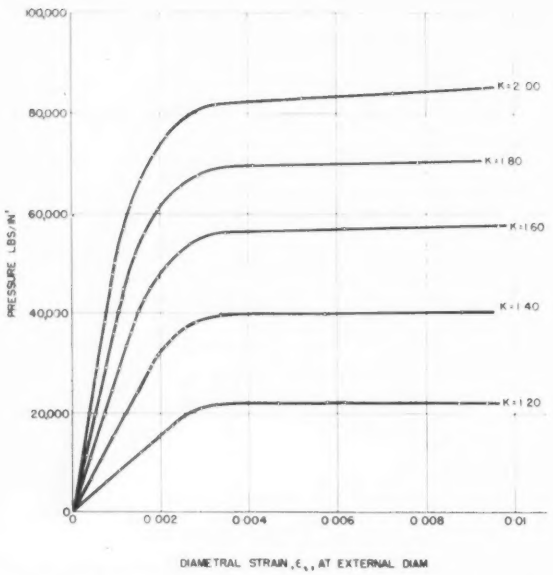

Fig. 17 Vibrac pressure tests; pressure/expansion curves at small strains

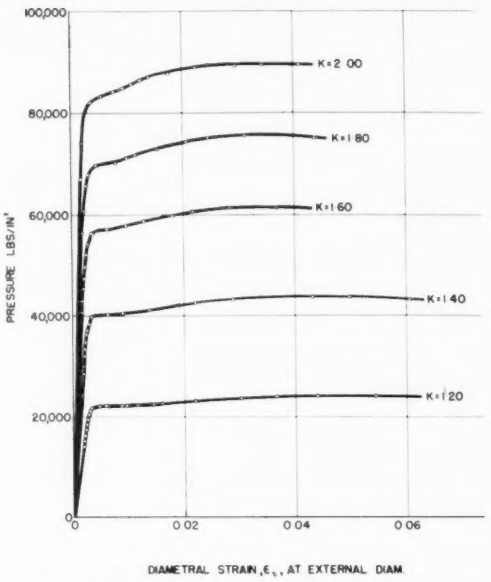

Fig. 18 Vibrac pressure tests; pressure/expansion curves at large strain

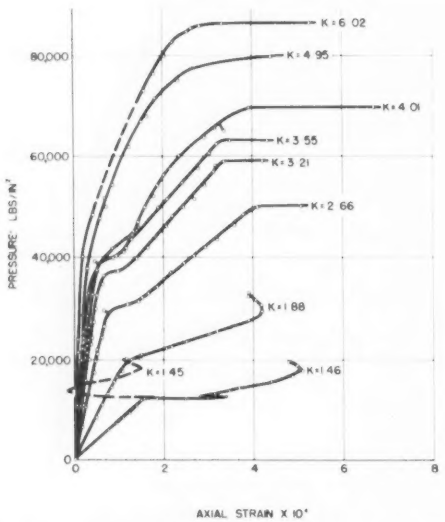

Fig. 19 0.15 per cent carbon steel pressure tests; axial strain

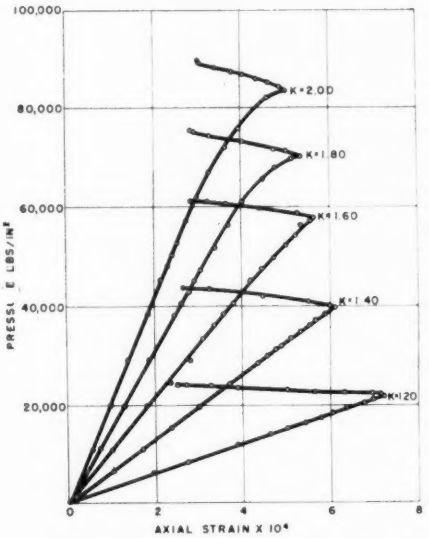

Fig. 20 Vibrac pressure tests; axial strain

Discussion of Results and Conclusions

Torsion Tests. Apart from small differences between the transverse and longitudinal results in the early post-yield region there are no significant variations in the torsion results for the 0.15 per cent carbon steel. The scatter of results for Vibrac steel is greater and does not appear to be completely attributable to variations from bar to bar since the differences between specimens from the same bar were found to be as much as one half the maximum difference shown. It must be remembered that Vibrac is a hardened and tempered steel which cannot be normalized as the 0.15 per cent carbon steel was; Less uniform and consistent properties would therefore be expected.

Tension Tests. The 0.15 per cent carbon steel results show little scatter, the longitudinal specimens giving a higher curve in the region of large strains and hence a higher ultimate tensile stress. The Vibrac results give similar scatter to that found in torsion.

Pressure Tests. *Initial Yield and Collapse Pressures.* In Fig. 21 the experimental values of the initial yield and collapse pressures for the 0.15 per cent C steel are shown plotted against diameter ratio. A theoretical curve for the initial yield pressure determined from equation (8) in the Appendix using values of the upper yield shear stress corrected for shear stress gradient is also shown. Morrison [5] has shown that the upper yield occurs at a critical value of the maximum shear stress which is a linear function of shear stress gradient. It follows that this function can be found if values of the upper yield shear stress at two different shear stress gradients are known. Now in a torsion test on a solid specimen the shear stress gradient is proportional to $2/d$ and in a tension

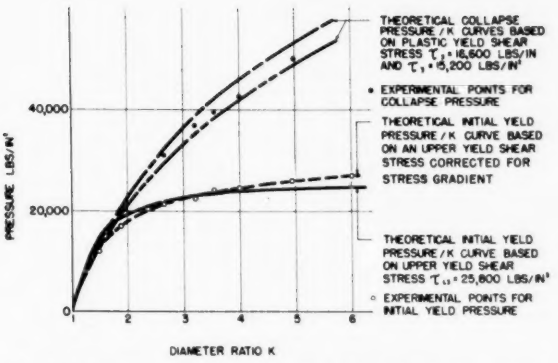
THEORETICAL COLLAPSE PRESSURE / K CURVES BASED ON PLASTIC YIELD SHEAR STRESS τ_y = 16,600 LBS/IN AND τ_y = 15,200 LBS/IN²
EXPERIMENTAL POINTS FOR COLLAPSE PRESSURE
THEORETICAL INITIAL YIELD PRESSURE / K CURVE BASED ON AN UPPER YIELD SHEAR STRESS CORRECTED FOR STRESS GRADIENT
THEORETICAL INITIAL YIELD PRESSURE / K CURVE BASED ON UPPER YIELD SHEAR STRESS τ_{y1} = 25,800 LBS/IN²
EXPERIMENTAL POINTS FOR INITIAL YIELD PRESSURE
PRESSURE LBS/IN²
40,000
20,000
0
1
2
3
4
5
6
DIAMETER RATIO K

Fig. 21 0.15 per cent carbon steel; initial yield and collapse pressures

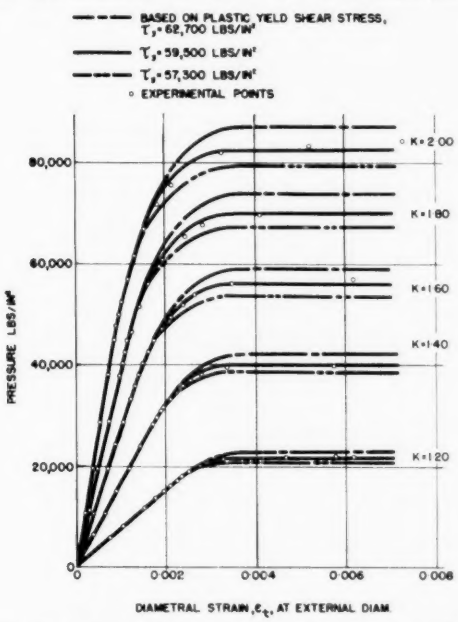

Fig. 22 Vibrac theoretical pressure/expansion curves at small strains

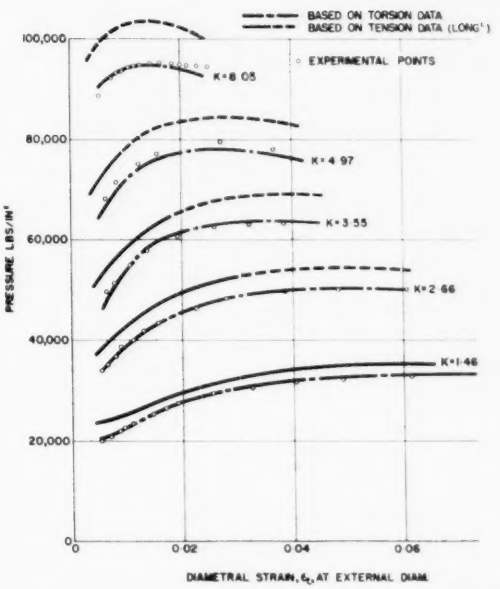

Fig. 23 0.15 per cent carbon steel theoretical pressure/expansion curves at large strains

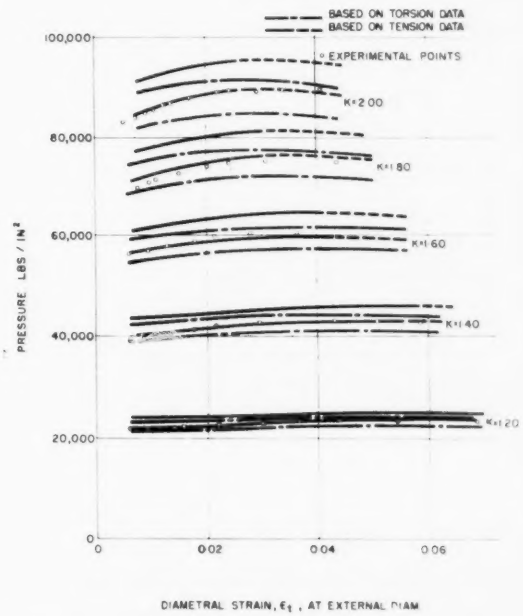

Fig. 24 Vibrac theoretical pressure/expansion curves at large strains

test the shear stress gradient is zero and the upper yield shear stress is 0.5 times the upper yield tensile stress. For the 0.15 per cent carbon steel the upper yield shear stress in torsion was 25,800 lb/in.² for specimens having $d = 0.25$ in. and in tension it was 23,700 lb/in.² The shear stress gradient at the bore of a thick-walled cylinder taken along the 45 deg spiral locus of maximum shear stress is proportional to $\sqrt{2}/a$, so that for a given cylinder the shear stress gradient may be evaluated and the corresponding value of the corrected upper yield shear stress found. The results show that, when this correction for shear stress gradient is made, the initial yield pressure can be calculated accurately from equation (8).

Theoretical curves for the collapse pressure determined from equation (14) using the extreme values of the plastic yield shear stress of 16,600 and 15,200 lb/in.² found in the torsion tests are also shown in Fig. 21. The experimental points are seen to lie between these curves. The collapse pressures for cylinders with diameter ratios greater than 5 were not measured. It is probable that for a cylinder of such large diameter ratio the bore material would begin to strain-harden before yield had spread to the outer surface preventing true collapse and the associated large increase in diametral strain. All the cylinders from 0.15 per cent carbon steel strained unsymmetrically in the partially-plastic region showing that yield does not spread concentrically in a material having a drop of stress at yield. Symmetry was, however, restored when the cylinders became completely plastic and it is evident from the results that collapse pressures may be calculated from equation (14) with acceptable accuracy.

The results for Vibrac steel are less decisive owing to the scatter in the torsion results. Two theoretical pressure/expansion

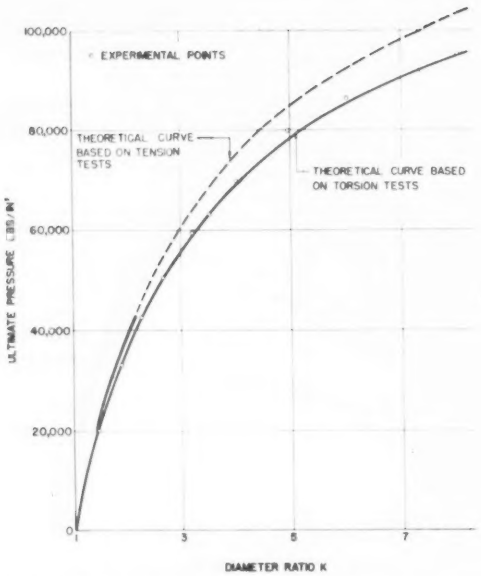

Fig. 25 0.15 per cent carbon steel pressure tests; ultimate pressure

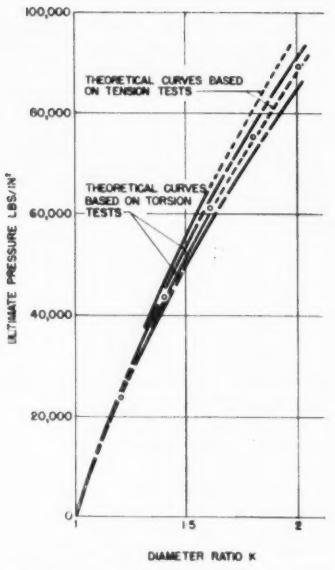

Fig. 26 Vibrac pressure tests; ultimate pressure

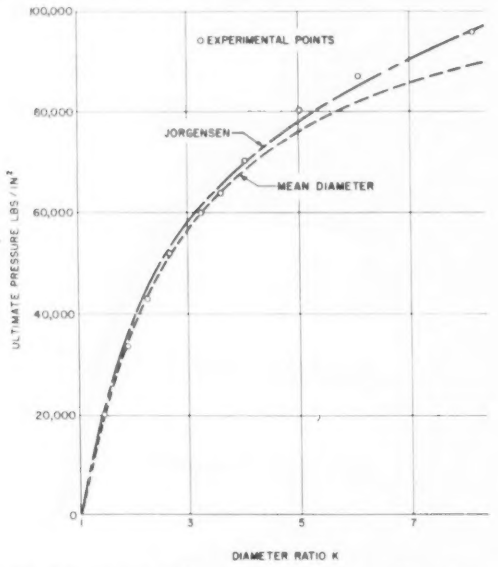

Fig. 27 0.15 per cent carbon steel pressure tests; ultimate pressure

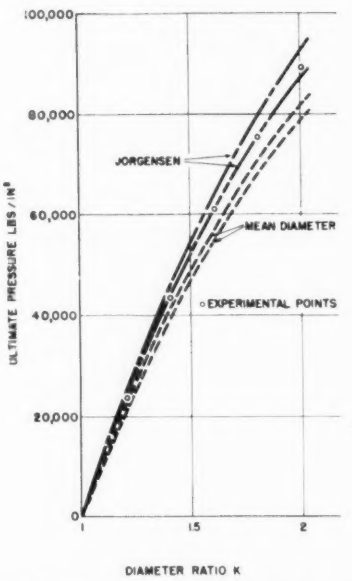

Fig. 28 Vibrac pressure tests; ultimate pressure

curves computed from equations (13) and (22) in the Appendix and based on the extreme values of the plastic yield shear stress obtained in torsion are compared with the experimental results in Fig. 22. These theoretical curves enclose the experimental points, the errors being not greater than 5 per cent. Theoretical curves based on a plastic yield shear stress of 59,500 lb/in.² are also shown in Fig. 22, and it is seen that these fit the experimental points for all the cylinders very closely. This batch of Vibrac does not give a constant plastic yield stress so that the pressure/expansion curves would be expected to continue to rise slightly immediately after yield has reached the outer surface and this was observed.

Pressure/Expansion Curves at Large Strains. The theoretical pressure/expansion curves for the 0.15 per cent carbon and Vibrac steels at large strains calculated from torsion test data by the method outlined in the Appendix are shown in Figs. 23 and 24. There is excellent agreement with the experimental points up to ultimate pressure. The theory of the Appendix is not applicable beyond the ultimate pressure as it takes no account of the localized bulging that then occurs. For Vibrac the experimental points lie between the theoretical curves based on the extreme shear stress/strain results.

The theoretical and experimental ultimate pressures are plotted in Figs. 25 and 26 and the agreement between them is very good even up to a diameter ratio of 8 for the 0.15 carbon steel.

Theoretical results computed from tension test data by the method given in the Appendix are also shown in Figs. 23, 24, 25,

and 26, and are seen to be consistently rather high. The full lines represent the limited range of results obtainable on the basis of a standard tension test giving no information about the behavior of the material beyond the ultimate tensile stress. If Jorgensen's [4] postulate, that ultimate pressure is reached when the bore stress equals the ultimate tensile stress, is accepted, then the limit of the full line in the pressure/expansion curve is the ultimate pressure. Ultimate pressures obtained in this way are shown in Figs. 27 and 28 and agree closely with the experimental results.

Also in Figs. 27 and 28 are shown theoretical ultimate pressure curves calculated from the mean diameter formula and it can be concluded that this purely empirical formula is a simple and reliable means of estimating ultimate pressure.

Axial Strains. In the theory of the Appendix it is assumed that the axial strain is negligible and that the volume remains unchanged, these assumptions implying that the cross-sectional area is constant. Examination of the results shows that the axial strain was at no time more than 3 per cent of the diametral strain at the outer surface and it would obviously be a much smaller proportion of the bore strain so that the assumption of negligible axial strain is justified. Further, the 0.15 per cent carbon steel cylinder having a diameter ratio of 8.05, though strained beyond the ultimate pressure, was not burst, so that assumption of constant cross-sectional area could be checked. From the dimensions before and after the pressure test the area was found to have remained constant to within 0.5 per cent. The bore diameter had increased from 0.1737 to 0.3802 in., representing a bore shear strain of 1.57 per cent, and the diameter ratio had decreased from 8.05 to 3.80. Fig. 29 is a photograph of a longitudinal cross section of this cylinder.

Fig. 29 0.15 per cent carbon steel; $K = 8.05$; longitudinal cross section

Failure of Thick-Walled Cylinders. The cylinders from 0.15 per cent carbon steel exhibited a wide variety of forms of failure and photographs of some of them are given in Figs. 30 and 31. This material contained many longitudinal inclusions which it is seen often caused the formation of subsidiary cracks at the outer surface and the bore.

All of the Vibrac cylinders showed shear failures along a spiral path through the cylinder wall and a typical example is shown in Fig. 32.

No firm conclusions have been drawn about the mechanism of failure.

APPENDIX

Theoretical Behavior of Thick-Walled Cylinders Under Internal Pressure

The complete derivation of some of the following relations will be found in Timoshenko [11].

(a) Elastic Deformation

From consideration of the equilibrium of an element of the cylinder wall it can be shown that

$$\sigma_t - \sigma_r = r \frac{d\sigma_r}{dr} \tag{1}$$

For an internal pressure P solution of equation (1) leads to the following equations for the radial and hoop stresses

$$\sigma_r = \frac{P}{K^2 - 1}\left(1 - \frac{b^2}{r^2}\right) \tag{2}$$

$$\sigma_t = \frac{P}{K^2 - 1}\left(1 + \frac{b^2}{r^2}\right) \tag{3}$$

For a closed-ended cylinder, assuming plane sections remain plane, it can be shown that the axial stress is uniform and is given by

$$\sigma_z = \frac{P}{K^2 - 1} \tag{4}$$

This stress system is equivalent to a simple shear stress

$$\tau = \frac{\sigma_t - \sigma_r}{2} = \frac{P}{K^2 - 1} \cdot \frac{b^2}{r^2} \tag{5}$$

with a uniform triaxial or volumetric stress

$$\frac{P}{K^2 - 1} \tag{6}$$

The shear stress is a maximum at the cylinder bore where

$$\tau_{\max} = P \cdot \frac{K^2}{K^2 - 1} \tag{7}$$

(b) Partially-Plastic Deformation

It has been demonstrated by Crossland [2] that the yield in shear is unaffected by the volumetric stress, consequently in a thick-walled cylinder yield occurs when the maximum shear stress reaches the shear yield stress τ_y, or τ_{iy} for materials with an upper yield point.

For a material with an upper yield point the internal pressure to cause yielding at the bore from equation (7) is

$$P_{iy} = \tau_{iy} \frac{K^2 - 1}{K^2} \tag{8}$$

It is assumed that the surface separating the elastic and plastic regions is cylindrical and concentric with the bore. In the plastic region the shear stress will be equal to the plastic shear yield stress τ_y and at the plastic-elastic boundary it will be τ_{iy} if the material has a drop of stress at yield. It can be considered that at the interface, which is at radius $r = na$, there is radial pressure

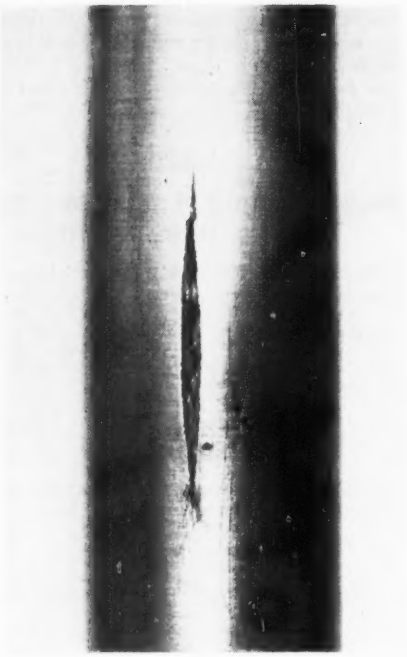

(a) External view; $K = 1.46$

(c) External view; $K = 2.25$

(b) Cross section; $K = 1.46$

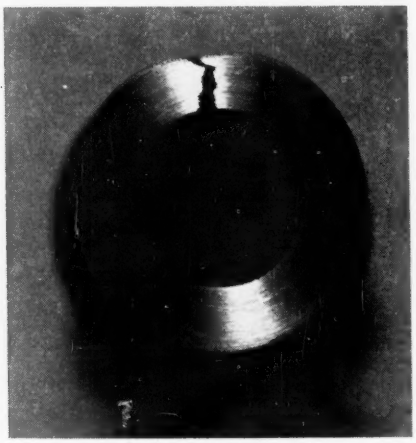

(d) Cross section; $K = 2.25$

Fig. 30 Failures in 0.15 per cent carbon steel cylinders

P_n and that the pressure at the bore is P'. Considering the elastic outer shell and using equation (8)

$$P_n = \tau_{iy} \frac{\left(\frac{Ka}{na}\right)^2 - 1}{\left(\frac{Ka}{na}\right)^2} = \tau_{iy} \frac{K^2 - n^2}{K^2} \tag{9}$$

In the plastic region if it is assumed that σ_z is the mean of σ_t and σ_r as in the elastic region then from equation (5)

$$\tau_y = \frac{\sigma_t - \sigma_r}{2} \tag{10}$$

Combining equations (10) and (1) gives

$$r \frac{d\sigma_r}{dr} = 2\tau_y$$

or

$$d\sigma_r = 2\tau_y \frac{dr}{r} \tag{11}$$

Integrating equation (11) between $r = na$ where $\sigma_r = -P_n$ and $r = a$ where $\sigma_r = -P'$ gives

$$-P_n + P' = 2\tau_y \log_e \frac{na}{a}$$

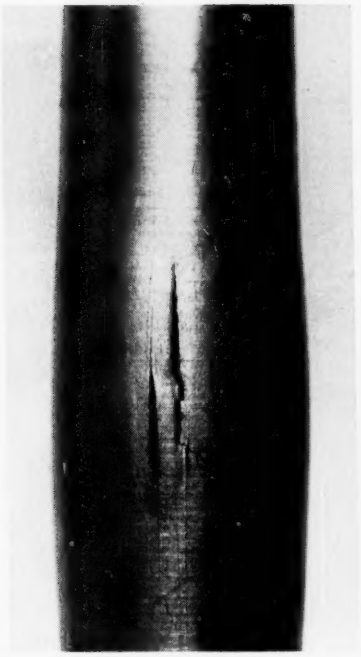

(a) External view; $K = 3.55$

(c) External view; $K = 4.97$

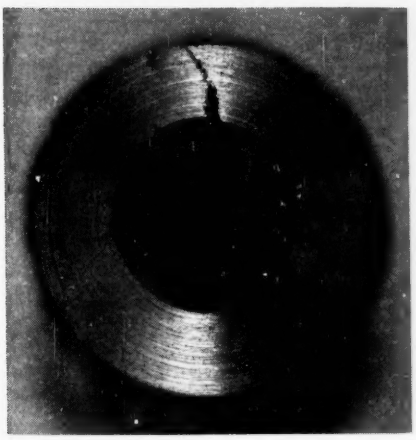

(b) Cross section; $K = 3.55$

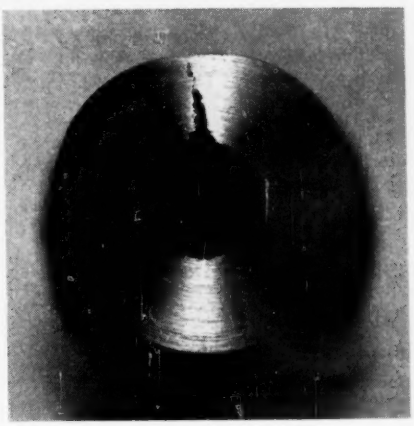

(d) Cross section; $K = 4.97$

Fig. 31 Failures of 0.15 per cent carbon steel cylinders

$$= \tau_y \log_e n^2 \tag{12}$$

Substituting in equation (12) for P_n from equation (9) gives

$$P' = \tau_{iy} \frac{(K^2 - n^2)}{K^2} + \tau_y \log_e n^2 \tag{13}$$

The collapse pressure, P_c, is given by equation (12) or (13) when $n = K$,

$$P_c = \tau_y \log_e K^2 \tag{14}$$

(c) Strains at Outer Surface

When the cylinder is wholly elastic

$$\epsilon_t = \frac{1}{E} [\sigma_t - \mu(\sigma_r + \sigma_z)] \tag{15}$$

At the outer surface, however, $\sigma_r = 0$ and for a closed-ended cylinder

$$\sigma_z = \frac{\sigma_t + \sigma_r}{2} = \frac{\sigma_t}{2}$$

so that equation (15) becomes

$$(\epsilon_t)_{r=b} = (\sigma_t)_{r=b} \frac{(2 - \mu)}{2E} \tag{16}$$

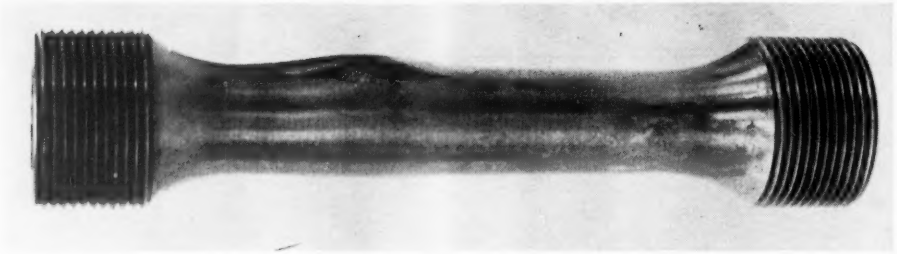

(a) External view; $K = 1.8$

and from equation (3)

$$(\sigma_t)_{r=b} = \frac{2P}{K^2 - 1} \tag{17}$$

so that

$$(\epsilon_t)_{r=b} = \frac{P}{E(K^2 - 1)}(2 - \mu) \tag{18}$$

The axial strain, which is uniform across the cylinder, can be similarly deduced, its value being given by

$$(\epsilon_z)_{r=b} = \frac{P}{E(K^2 - 1)}(1 - 2\mu) \tag{19}$$

When the inner portion of the cylinder wall is plastic up to $r = na$ and the outer portion is elastic the value of σ_t at the outer surface is

$$(\sigma_t)_{r=b} = 2P_n \frac{n^2}{K^2 - n^2} \tag{20}$$

and substituting for P_n from equation (9)

$$(\sigma_t)_{r=b} = 2\tau_{iy} \frac{n^2}{K^2} \tag{21}$$

then from equations (21) and (16)

$$(\epsilon_t)_{r=b} = \tau_{iy} \frac{(2 - \mu)}{E} \frac{n^2}{K^2} \tag{22}$$

Sometimes it is convenient to express equation (22) in terms of the strain at the outer surface at the initial yield pressure

$$\frac{(\epsilon_t)_{r=b} \text{ for } 1 < n < K}{(\epsilon_t)_{r=b} \text{ for } n = 1} = \frac{\tau_{iy} \dfrac{(2 - \mu)}{E} \dfrac{n^2}{K^2}}{\tau_{iy} \dfrac{(2 - \mu)}{E} \dfrac{1}{K^2}} = n^2 \tag{23}$$

(d) Large Plastic Deformation

In the analysis so far considered the dimensional changes have been neglected, but in the region of the ultimate pressure the strains are considerable and dimensional changes cannot be neglected.

It is assumed in the following that the axial plastic strain is negligible, a fact verified by the results reported here. This, coupled with the further assumption that there is no change of volume, leads to the conclusion that the area between any two radii remains constant during the expansion. Considering radii a and r this leads to the expression

$$r + u = (r^2 + 2u_a a + u_a^2)^{1/2} \tag{24}$$

If therefore a strained dimension is known or assumed for one radius, for instance $a + u_a$, then the expansion at any radius can be computed from equation (24).

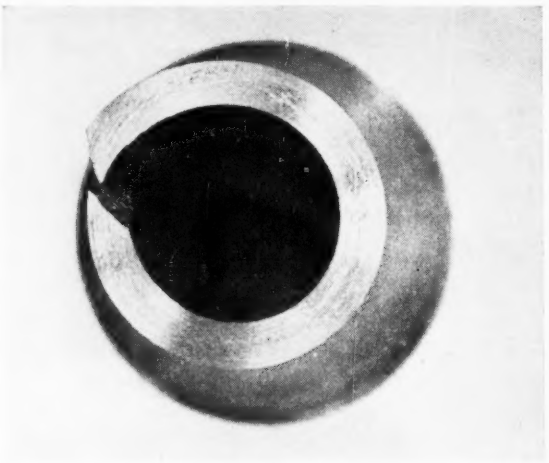

(b) Cross section; $K = 1.8$

Fig. 32 Failure of Vibrac cylinder

It is assumed that there is a unique relationship between the Mises-Hencky functions of stresses and strains or the octahedral shear stresses and strains as they are alternatively called.

In a thick-walled cylinder a radius r ultimately becomes $r + u$. Now consider an intermediate state when the radius is x and consider a displacement δx, then

$$\epsilon_t = \frac{\delta x}{x} \quad \text{and} \quad \epsilon_r = -\frac{\delta x}{x} \tag{25}$$

since the cross-sectional area is constant. The corresponding increment in the Mises-Hencky function of strains will be

$$\left[\left(\frac{\delta x}{x} + \frac{\delta x}{x}\right)^2 + \left(\frac{\delta x}{x}\right)^2 + \left(\frac{\delta x}{x}\right)^2\right]^{1/2} = \sqrt{6}\,\frac{\delta x}{x} \tag{26}$$

In a torsion test for an increment of shear strain $\delta\gamma$ the increment in the Mises-Hencky function will be

$$\sqrt{\frac{3}{2}}\,\delta\gamma \tag{27}$$

Now, in a tension test, an element originally of length l and finally length $l + v$, in an intermediate state has length y, say. Consider an increment in y of δy then the three principal strains are

$$\frac{\delta y}{y}, \quad -\frac{\delta y}{2y}, \quad \text{and} \quad -\frac{\delta y}{2y} \tag{28}$$

which gives an increment in the Mises-Hencky function of strains of

Table 5

1 r	2 r+u	3 Δ(r+u)	4 u	5 $\epsilon_1 \frac{u}{r}$	6 $2 \log_e \frac{r+u}{r}$ $-\gamma_0$	7 $\frac{2}{\sqrt{3}} \log_e \frac{r+u}{r}$	8 ϵ_e
1.0	2.0000		1.0000	1.0000	1.3863	.8004	1.2264
		.0518					
1.1	2.0518		.9518	.8653	1.2469	.7199	1.0542
		.0553					
1.2	2.1071		.9071	.7559	1.1240	.6512	.9179
		.0585					
1.3	2.1656		.8656	.6659	1.0207	.5893	.8027
		.0615					
1.4	2.2271		.8271	.5908	.9285	.5361	.7093
		.0642					
1.5	2.2913		.7913	.5275	.8471	.4891	.6309
		.0667					
1.6	2.3580		.7580	.4738	.7753	.4557	.5773
		.0689					
1.7	2.4269		.7269	.4276	.7113	.4109	.5082
		.0721					
1.8	2.4990		.6990	.3888	.6557	.3786	.4602
		.0730					
1.9	2.5710		.6710	.3532	.6049	.3492	.4177
		.0748					
2.0	2.6458		.6458	.3229	.5596	.3231	.3814
		.1524					
2.2	2.7982		.5982	.2719	.4847	.2797	.3214
		.1615					
2.4	2.9597		.5597	.2332	.4191	.2420	.2736
		.1644					
2.6	3.1241		.5241	.2016	.3618	.2129	.2374
		.1684					
2.8	3.2925		.4925	.1759	.3212	.1892	.2061
		.1716					
3.0	3.4641		.4641	.1547	.2907	.1661	.1807
		.3517					
3.4	3.8158		.4158	.1223	.2307	.1332	..1425
		.3603					
3.8	4.1761		.3761	.0990	.1895	.1094	.1159
		.3710					
4.2	4.5471		.3431	.0817	.1577	.0910	.0951
		.3783					
4.6	4.9254		.3254	.0685	.1330	.0768	.0796
		.3761					
5.0	5.3015		.3015	.0603	.1136	.0656	.0667
		.3795					
5.4	5.6810		.2810	.0502	.0971	.0566	.0582
		.3821					
5.8	6.0631		.2631	.0433	.0855	.0494	..0506
		.5771					
6.4	6.6302		.2302	.0360	.0707	.0409	.0417
		.5809					
7.0	7.2111		.2111	.0302	.0595	.0344	.0351
		.7743					
8.0	8.1854		.1854	.0232	.0453	.0264	.0270
		.9798					
9.0	9.1652		.1652	.0184	.0364	.0210	.0213
10.0	10.149		.149	.0149	.0296	.0171	.0174
		.987					
11.0	11.136		.136	.0124	.0243	.0141	.0142
		.988					
12.0	12.124	1.983	.124	.0103	.0200	.0119	.0120
14.0	14.107	1.986	.107	.0076	.0152	.0088	.0088
16.0	16.093	1.990	.093	.0058	.0116	.0067	.0067
18.0	18.083	1.991	.083	.0046	.0090	.0052	.0052
20.0	20.074	1.988	.074	.0037	.0074	.0043	.0043
24.0	24.062	1.991	.062	.0026	.0050	.0029	.0029
28.0	28.053		.053	.0019	.0038	.0022	.0022

Table 6 0.15 per cent carbon steel

1	2	3	4	5	6	7
	TORSION		TENSION			
			THROUGH-THICKNESS		LONGITUDINAL	
r	τ lbs/in^2	$\bar{\tau}$ lbs/in^2	σ_θ lbs/in^2	$\bar{\sigma}_\theta$ lbs/in^2	σ_z lbs/in^2	$\bar{\sigma}_z$ lbs/in^2
1.0	46,800	134,000	Information in this		84,800	119,000
1.1	46,800	131,800	strain region not		92,500	116,200
1.2	46,600	129,300	available since		91,500	113,500
1.3	45,900	127,000	transverse tension		88,000	110,600
1.4	45,300	124,000	specimens failed		87,800	107,700
1.5	44,400	121,700	shortly after		87,000	105,000
1.6	43,700	117,100	reaching ultimate		85,400	102,100
1.7	42,800	116,800	tensile stress.		83,400	128,800
1.8	42,400	114,000			81,600	126,000
1.9	41,900	111,900			80,300	122,500
2.0	41,200	109,300			78,400	120,900
2.2	40,100	105,000			76,000	115,300
2.4	39,200	100,400			72,800	110,900
2.6	38,100	96,100	67,400	103,000	70,600	106,300
2.8	37,000	92,200	65,700	101,000	68,500	102,300
3.0	36,100	88,500	64,300	97,200	66,800	98,400
3.4	34,100	81,700	61,100	90,200	62,700	91,000
3.8	32,300	75,800	58,000	84,000	59,300	84,600
4.2	30,700	70,500	55,100	78,300	56,500	79,000
4.6	29,900	66,000	52,500	73,500	53,500	73,900
5.0	28,200	61,700	50,200	69,100	51,100	69,400
5.4	26,900	57,900	47,700	65,200	48,400	65,400
5.8	25,100	54,500	45,900	61,600	46,800	61,800
6.4	23,300	50,000	43,200	57,000	43,900	57,000
7.0	21,900	46,300	41,000	52,900	41,000	52,900
8.0	20,200	41,000	37,200	47,100	37,200	47,700
9.0	18,100	36,700	35,200	42,600	35,200	42,600
10.0	17,000	33,100	33,800	38,300	33,800	38,300
11.0	16,600	30,000	32,900	34,700	32,900	34,700
12.0	16,300	27,200	32,700	31,500	32,700	31,700
14.0	16,100	22,300	32,700	25,800	32,700	25,800
16.0	16,100	18,000	32,700	20,900	32,700	20,900
18.0	16,100	14,200	32,700	16,500	32,700	16,500
20.0	16,100	10,800	32,700	12,600	32,700	12,600
24.0	16,100	5,000	32,700	5,800	32,700	5,800
28.0	16,100	0	32,700	0	32,700	0

$$\left[\left(\frac{\delta y}{y} + \frac{\delta y}{2y}\right)^2 + \left(-\frac{\delta y}{2y} + \frac{\delta y}{2y}\right)^2 + \left(-\frac{\delta y}{2y} - \frac{\delta y}{y}\right)^2\right]^{1/2} = \sqrt{\frac{9}{2}}\,\frac{\delta y}{y} \quad (29)$$

It is now possible to find the shear strain which is equivalent to the strain in a cylinder from (26) and (27)

$$\delta\gamma_e = \sqrt{\frac{2}{3}}\,\sqrt{6}\,\frac{\delta x}{x} = 2\,\frac{\delta x}{x} \quad (30)$$

and the shear strain equivalent to a displacement of u at radius r is

$$\gamma_e = \int_r^{r+u} 2\,\frac{dx}{x} = 2 \log_e \frac{r+u}{r} \quad (31)$$

Similarly, the corresponding equivalent tensile strain, from equations (26) and (29), is

$$\int_l^{l+v} \frac{dy}{y} = \log_e \frac{l+v}{l} = \int_r^{r+u} \frac{2}{\sqrt{3}}\,\frac{dx}{x} = \frac{2}{\sqrt{3}} \log_e \frac{r+u}{r} \quad (32)$$

(*i*) *Solution for Internal Pressure Based on Torsion Data.* By assuming a radial displacement at the bore, the displacement at any other radius may be calculated from equation (24), and the equivalent shear strain from equation (31). From a torsion test on a solid specimen a shear stress-strain curve may be derived using the method described by Nadai [9] and the values of the shear stress corresponding to a given equivalent shear strain can be found. The internal pressure can then be computed by integrating equation (1) and allowing for dimensional changes, this gives

$$P_r = 2 \int_{a+u_a}^{b+u_b} \frac{\tau}{r+u}\,d(r+u) \quad (33)$$

This integration is normally carried out arithmetically

Table 7 Vibrac steel

r	TORSION LOWER LIMIT τ_t lbs/in²	TORSION LOWER LIMIT P_τ lbs/in²	TORSION LOWER LIMIT τ_t lbs/in²	TORSION LOWER LIMIT P_τ lbs/in²	TENSION LOWER LIMIT σ_θ lbs/in²	TENSION LOWER LIMIT P_σ lbs/in²	TENSION LOWER LIMIT σ_θ lbs/in²	TENSION LOWER LIMIT P_σ lbs/in²
2.0	77,800	267,000	82,500	278,000	153,200	281,000	161,000	302,000
2.2	77,300	258,000	82,200	279,000	148,300	271,500	158,400	292,500
2.4	76,800	249,000	81,500	270,000	145,700	262,000	155,500	281,000
2.6	76,500	241,000	81,100	260,500	143,100	253,000	153,300	272,000
2.8	76,000	233,000	80,700	252,000	141,200	242,000	150,800	262,500
3.0	75,500	225,500	80,000	244,000	139,200	236,000	147,800	254,000
3.4	74,400	211,000	79,300	228,500	136,500	220,500	145,500	237,000
3.8	73,100	197,800	78,500	214,000	133,700	206,500	142,500	222,000
4.2	72,000	185,800	77,800	201,000	131,300	193,200	140,000	208,000
4.6	70,600	174,400	76,000	188,800	128,700	181,800	136,700	195,500
5.0	69,200	164,000	74,200	177,800	126,000	170,600	134,500	184,000
5.4	67,900	154,500	72,600	167,500	123,200	160,800	131,200	173,000
5.8	66,500	144,000	71,500	158,100	121,200	151,700	129,000	163,500
6.4	65,000	133,800	70,200	145,100	118,500	139,000	125,700	150,000
7.0	63,800	122,000	69,000	133,700	115,300	127,500	123,000	138,000
8.0	62,300	107,000	67,700	116,100	112,000	111,000	119,000	120,100
9.0	61,200	92,200	66,800	103,200	109,200	96,500	117,000	104,700
10.0	60,500	80,700	65,900	87,500	107,300	83,800	115,600	90,600
11.0	60,300	69,300	65,500	75,500	106,500	72,400	115,000	78,700
12.0	59,800	59,000	64,800	64,300	106,200	62,000	114,900	67,100
14.0	59,900	41,100	64,100	44,700	105,800	43,300	114,800	47,200
16.0	59,500	25,700	63,200	27,900	105,500	27,200	115,400	29,700
18.0	59,300	12,100	63,000	13,200	104,500	12,900	115,600	14,000
20.0	57,400	0	62,800	0	107,000	0	114,500	0

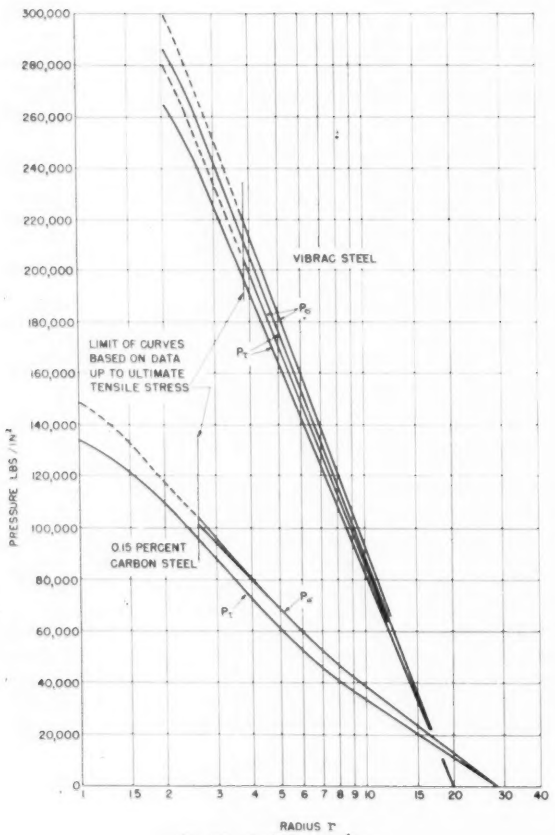

Fig. 33 Radial stress/log r

$$P = 2 \sum_{r=a}^{r=b} \frac{\tau}{r+u} \Delta(r+u) \tag{34}$$

(*ii*) *Solution for Internal Pressure Based on Tension Data.* With tension it is necessary to also establish the relationship between the tensile stress and the stresses in the thick-walled cylinder. To obtain the equivalent tensile stress consider the Mises-Hencky function of stresses. For a cylinder this function is

$$[(\sigma_t - \sigma_r)^2 + (\sigma_r - \sigma_z)^2 + (\sigma_z - \sigma_t)^2]^{1/2}$$

which can be simplified as the assumption of zero axial strain in the cylinder implies that σ_z is the mean of σ_r and σ_t, so the function becomes

$$\left[\frac{3}{2}(\sigma_t - \sigma_r)^2\right]^{1/2} \tag{35}$$

In tension the Mises-Hencky function of stresses is

$$\sqrt{2\sigma^2} \tag{36}$$

The equivalent tensile stress is then given by equating (36) and (35)

$$\sigma_e = \frac{\sqrt{3}}{2}(\sigma_t - \sigma_r) \tag{37}$$

Assuming a radial displacement at the bore it is possible from equation (24) to calculate the displacement at any radius and from equation (32) to find the equivalent engineer's tensile strain, $\epsilon_e = v/l$. The tensile stress (based on original area of specimen) corresponding to this strain can be found from tension test data, and the true equivalent tensile stress σ_e can then be obtained by multiplying this stress by $(1 + \epsilon_e)$. Beyond ultimate σ_e may be found by using the method due to Bridgman [10].

The internal pressure is then given by integrating equation (1) as before

$$P_a = \int_{a+u_a}^{b+u_b} \frac{\sigma_t - \sigma_r}{(r+u)}\, d(r+u)$$

$$= \int_{a+u_a}^{b+u_b} \frac{2}{\sqrt{3}} \frac{\sigma_e}{(r+u)}\, d(r+u) \qquad (38)$$

Again this is normally solved arithmetically

$$P = 2 \sum_{r=a}^{r=b} \frac{1}{\sqrt{3}} \frac{\sigma_e}{(r+u)} \Delta(r+u) \qquad (39)$$

(e) Computation of Pressure-Expansion Curve at Large Strains

The method for deriving the pressure-expansion curve and hence finding the ultimate pressure for a given cylinder is due to Manning [3].

A thick-walled cylinder with a large diameter ratio is assumed to have a convenient and sufficiently large bore strain and the equivalent strains throughout the cylinder are computed from equations (24), (31), and (32). In Table 5 a cylinder of diameter ratio equal to 28 and having a bore strain of 1 has been assumed and the equivalent shear and engineer's tensile strains are given in columns 6 and 8, respectively. Corresponding values of the shear stress are obtained from torsion data and the summation equation (34) evaluated at each interval as in Tables 6 and 7. This summation represents the distribution of radial stress throughout the wall of the assumed thick-walled cylinder and may be plotted against log r as in Fig. 33.

The pressure-expansion curve for a cylinder of given diameter ratio is obtained by considering a pair of ordinates a distance equivalent to log K apart and moving along the r-axis from right to left. At any position the strain at the outer surface will be that for the value of r corresponding to the right-hand ordinate (and equal to u/r from Table 5) and the corresponding internal pressure is given by the vertical distance between the intersections of the ordinates and the radial stress-log r curve.

Alternatively values of the equivalent tensile stress from a tension test may be used and the summation equation (39) evaluated as in Tables 6 and 7. This gives another radial stress-log r curve also shown in Fig. 33 from which the pressure-expansion curve for any given cylinder may be obtained as before.

References

1 B. Crossland and J. A. Bones, "Behavior of Thick-Walled Cylinders Subjected to Internal Pressure," *Proceedings, The Institution of Mechanical Engineers*, vol. 172, 1958.

2 B. Crossland, "Effect of Fluid Pressure on Shear Properties of Metals," *Proceedings, The Institution of Mechanical Engineers*, vol. 168, 1954, pp. 935–944.

3 W. R. D. Manning, "Overstrain of Tubes by Internal Pressure," *Engineering*, vol. 159, 1945, pp. 101 and 183.

4 S. M. Jorgensen, "Overstrain and Bursting Strength of Thick-Walled Cylinders," TRANS. ASME, vol. 80, 1958, pp. 561–570.

5 J. L. M. Morrison, "Yield of Mild Steel With Particular Reference to Effect of Size of Specimen," *Proceedings, The Institution of Mechanical Engineers*, vol. 142, 1940, pp. 193–223.

6 A. Robertson and A. J. Newport, Aeronautical Research Committee, R. & M. No. 1161, 1927.

7 B. Crossland and J. A. Bones, "Ultimate Strength of Thick-Walled Cylinders Subjected to Internal Pressure," *Engineering*, vol. 179, 1955, pp. 80 and 114.

8 G. Cook, "Stresses in Thick-Walled Cylinders of Mild Steel Overstrained by Internal Pressure," *Proceedings, The Institution of Mechanical Engineers*, vol. 126, 1934, pp. 407–455.

9 A. L. Nadai, "Theory of Flow and Fracture of Solids," vol. 1, 1950, McGraw-Hill Publishing Company, New York, N. Y.

10 P. W. Bridgman, "Studies in Large Plastic Flow and Fracture With Special Emphasis on the Effect of Hydrostatic Pressure," 1952, McGraw-Hill Publishing Company, New York, N. Y.

11 S. Timoshenko, "Strength of Materials," D. Van Nostrand Company, New York, N. Y.

DISCUSSION

W. R. D. Manning[2]

This is a study of the correlation between stress/strain relations under three different types of loading, namely, cylinders under internal pressure, tensile tests, and torsion tests, all under conditions of gross deformation. The experimental work (which incidentally has also been published by The Institution of Mechanical Engineers in Britain) has been carried out with refined apparatus, and great care was taken both in the selection of the specimens and in the measurement of the loads, pressures, and deformations. Two different types of steel were studied, a low carbon steel and a nickel-chrome-molybdenum steel, the latter being supplied by the English Steel Corp. of Sheffield, England, under the name of "Vibrac." The bars used in both cases had been specially selected and could, therefore, be regarded as representative of the best quality materials in their respective classes.

Basic shear stress/strain characteristics were derived from both torsion and tensile tests and from these data a theoretical investigation was made of the progressive deformation of the cylinders, which was then compared with the actual test results. It is shown that the use of torsion data gives curves for the dilatation of the Vibrac cylinders up to their bursting pressures which agree very well with experiment. The low carbon steel, however, was shown to have a marked drop between its upper and lower yield stress, both in the torsion and the tensile tests, but the results are also satisfactory in respect of cylinder bursting, although they could hardly have much real bearing on the earlier stages of plastic flow, since the theory is based on the assumption that the boundary between elastic and plastic material in a cylinder remains a concentric circle gradually spreading outward; in fact, it is known that in such cases overstrain produces wedges of plastic material which penetrate through the section on a relatively narrow front and cause distortion from the circular as they do so. This distortion was duly observed as is noted in the paper.

The correlation of shear stress/strain relations between tensile tests and the cylinders is discussed at considerable length in an appendix, where the basis used is the Mises-Hencky function of stress and a mathematically similar function of strain. The latter would seem to be an unnecessary complication, since it is also assumed that the material does not change its density and, therefore, any symmetrical function of the greatest and least strains will presumably be unique and equally valid for a correlation of the kind carried out by these authors. They point out that the resulting theoretical curves for diametral expansion of the cylinders with rising pressure lie above those computed from a torsion test, and they go on to explain that this is to be expected in view of the much more uniform distribution of stress in a tensile test and the considerable stress gradient in the cylinder. A point they have not mentioned, however, is that the material in the neck of the tensile specimen immediately before breaking may very easily contain actual cavities as the result of the triple tension caused by the neck, and the stresses and strains cannot, therefore, be reliably computed from the normal test records, even when these include (as in this case) measurements of the actual profile of the neck.

Finally, it is difficult to see that useful purpose is served by discussing purely empirical equations for the limiting pressures of cylinders. The so-called "Jorgensen postulate" may well be a useful rule for designers when dealing with material for which it has already been shown to apply by experiment, or by more fundamental analysis such as the authors describe. Since,

[2] Imperial Chemical Industries, Ltd., Welwyn Garden City, England.

however, such formulas have no true connection with the mechanism of these processes, this writer feels that a designer would be foolhardy indeed if he used any of them when dealing with new materials. Moreover, it is neither difficult nor expensive to obtain a torsion test record and thence to derive the limiting cylinder pressures by the methods shown here.

F. Rimrott[3] and J. Marin[4]

The authors have made a valuable contribution by obtaining experimental results on a subject on which adequate results are few. The authors were successful in testing thick-walled cylinders with diameter ratios up to 8.05. The results on these very thick-walled cylinders are significant since they make possible a more complete verification of the theoretical strength. The authors use the torsion test instead of the usually employed tension test as a basis for predicting the strength of thick-walled pressure vessels. They find that theoretical strength predictions based upon the torsion test are in better agreement with their test results than theoretical strength values based upon the tension test. However, further experiments will be needed to prove conclusively that the torsion test is preferable for strength prediction. It should also be noted that the tension test would be a preferable basis for strength predictions since theories of plasticity attempt to predict the behavior of a member from the uniaxial tension-test results.

In attempting to use the tension test for interpretation of the test results for thick-walled cylinders, the authors assume that the ultimate pressure is reached when the stress at the bore equals the ultimate tensile stress. The authors have recently shown [1] that the foregoing assumption is not always correct but that the stress at the bore at maximum pressure varies with the diameter ratio. As shown in Fig. 34, the significant stress at the bore at maximum pressure does equal the ultimate tensile strength for a diameter ratio of about 2.

The authors have compared their test results with Manning's method and the mean diameter formula. However, Manning's method is cumbersome and the mean diameter formula is based upon incorrect assumptions. It is suggested that a new formula (1), recently proposed by the authors, be considered for defining in a simple way strength of thick-walled cylinders. By this formula, the maximum pressure is defined by

$$p_u = \frac{2}{\sqrt{3}} \frac{\sigma_u}{1 + \epsilon_u} \log_e K$$

where

K = the ratio of the outer to the inner radius
σ_u = the nominal ultimate tensile stress

[3] Assistant Professor, Department of Engineering Mechanics, The Pennsylvania State University, University Park, Pa. Assoc. Mem. ASME.

[4] Head, Department of Engineering Mechanics, The Pennsylvania State University, University Park, Pa. Mem. ASME.

Table 8

0.15 per cent carbon steel: σ_u = 54,600 psi, ϵ_u = 0.25			
	Maximum pressure		
K	Theoretical value* (P_u)	Exper. value (P_u)	Dev.
8.05	n.a.	95,000	...
6.02	n.a.	86,000	...
4.97	80,872	80,000	+1%
4.01	70,046	70,000	+0%
3.55	63,185	63,000	+0%
3.21	58,823	59,000	−0%
2.66	49,344	50,000	−1%
2.25	40,900	42,000	−3%
1.88	31,839	32,000	−0%
1.46	19,087	19,500	−2%

Vibrac steel: σ_u = 121,000 psi, ϵ_u = 0.10			
	Maximum pressure		
K	Theoretical value* (P_u)	Exper. value (P_u)	Dev.
2	88,041	89,500	−2%
1.8	74,659	76,000	−2%
1.6	59,698	61,500	−3%
1.4	42,737	43,500	−2%
1.2	23,157	24,000	−4%

* $P_u = \frac{2}{\sqrt{3}} \frac{\sigma_u}{1 + \epsilon_u} \log_e K$

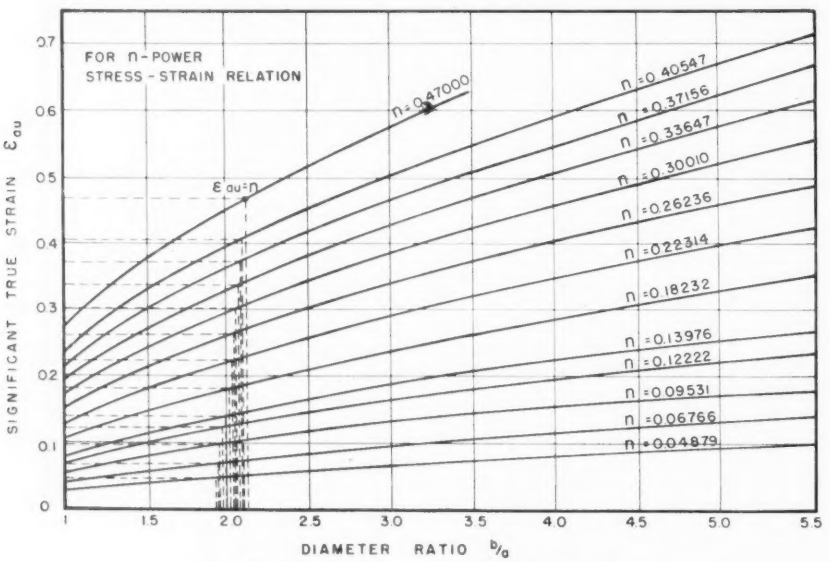

Fig. 34 Significant true strain at $r = a$ and instability

ϵ_u = the nominal tensile strain at the nominal ultimate tensile stress

The formula is proposed for values of K less than 5. Table 8 shows the excellent agreement obtained between the predicted values using the foregoing formula and the actual pressure values.

It should also be noted that a need exists for further studies regarding the failure of thick-walled cylinders as they relate to types and mechanisms of fracture. Theories for the maximum pressure have been proposed based upon the assumed existence of a point of instability. For some less ductile materials and for very thick-walled vessels, failure by fracture prior to instability may occur. In such cases, predictions based upon assumed points of instability are inadequate.

G. D. Galletly[5]

The correlation between experimental and theoretical ultimate pressures given by the authors is certainly most impressive. However, aside from the use of Jorgensen's postulate, there appears to be little in this long paper that was not given previously in the authors' reference [1].

Since Crossland and Bones also presented an ultimate pressure-diameter ratio curve for the 0.3 per cent carbon steel in reference [1] and compared it with the results of torsion tests and the mean-diameter formula, the writer would be interested in knowing why it was not mentioned (if only briefly) in the present work.

The writer also notes that the authors do not reference the work of Svensson[6] or Marin and Rimrott[7] on this subject. Presumably these papers were not available to them. However, the writer believes that it would be helpful to readers of the journal if the present authors discussed the theories proposed in references (6) and (7) in comparison with their own.

Authors' Closures

By S. M. Jorgensen

I am very pleased that Mr. Manning could contribute to this meeting, because it was through his work that I became interested in this subject. It was Mr. Manning who first pointed out, in 1945, the similarity in stress distribution in heavy-walled cylinders and torsion test specimens, and showed how this could be used to evaluate bursting pressures.

I agree with Mr. Manning that stresses and strains in the range where necking takes place cannot be reliably evaluated. I believe this is one of the reasons for the larger test deviations for the very heavy cylinders, which will have comparatively heavy inner layers with strains corresponding to necking range.

With regard to the empirical equations and Mr. Manning's opinion in such equations, I agree that such formulas should be used only as a last resort. A number of empirical heavy-wall formulas have been proposed, and quite a number of them on a very shaky basis.

The mean diameter formula is in this category. It is included here because its fairly close accuracy in predicting bursting pressure is quite amazing. It is a very handy tool when a quick, approximate estimate is needed.

The empirical formula that I have suggested contains comparatively little empiricism because it is an equation for the actual pressure-summation curve.

I certainly agree that a torsion test record is neither difficult nor expensive, but try and get one out of a steel company. It is difficult enough to get a simple tensile stress-strain record.

I share Professor Marin's opinion that a tensile test may eventually prove equal to a torsion test as a basis for strength predictions.

I want to point out again that the assumption of the bore stress being equal to the ultimate tensile stress has been used only in case of what we called an empirical formula. For the two steels that were tested, this assumption held, up to a K ratio of 4 for the 0.15 per cent carbon steel, and up to $K=2$ for the high tensile steel. The high tensile steel could not be tested to any higher ratio.

Messrs. Rimrott and Marin have proposed an empirical formula which they have checked against our experimental data and which shows excellent agreement.

The empirical formula, which was published by the author in reference [4], contained a ductility factor as measured by the nominal strain corresponding to the ultimate stress. A similar factor is included in the Rimrott-Marin formula. The necessity for this factor is quite obvious when it is realized that the bursting pressure is a function of the area under the stress-strain curve.

It is true that there is a need for further studies on this subject, and it is my sincere hope that the discussion here will have underlined this need, and that the industries which use this type of equipment will undertake such studies or will support such studies through the Pressure Vessel Research Committee.

By B. Crossland and J. A. Bones

We wish to thank Mr. Manning, Professor Marin, and Dr. Rimrott for their interesting contributions to the discussion. In reply to Mr. Manning, though the 0.15 per cent carbon steel cylinders did not strain symmetrically in the partially plastic region, it was interesting to note that symmetry was restored when the cylinder became completely plastic, and the collapse pressure agreed very well with that predicted on the assumption of symmetrical yielding.

Though it was true that a cavity frequently formed at the neck of a tension specimen, the authors thought that as soon as it formed, failure would occur immediately, unless the energy stored in the testing machine was extremely small. They would also have thought there would be a noticeable change in the slope of the strain hardening curve (Fig. 13) as soon as a cavity was formed. One of the authors had several times sectioned specimens which had been pulled nearly to failure, but he had unfortunately never managed to find a cavity.

In general, the authors agreed that it was desirable to carry out the fundamental analysis based on torsion results which they had suggested. But if, as was frequently the case, the only data available were either the ultimate tensile strength or an autographic record from a tension test, then it was necessary to resort to one of the empirical equations suggested, and it was not at all a bad thing to see how they agreed with experiment for the two materials investigated.

Though, as Professor Marin and Dr. Rimrott stated, the authors mainly used torsion test data, they had also provided very comprehensive tension test data, and had worked out the theoretical ultimate pressures from both. Fundamentally, what was required for computation on thick-walled cylinders was shear stress-strain data over the complete range of strains to failure. These data could nominally be obtained from any other simple test on the same material, but could be most easily and accurately obtained, especially in the region of large strains, from a torsion test. Tension data were more commonly available in industry and it is to be regretted that torsion data are very rarely equally accessible.

In Fig. 23, the end of the full line for the theoretical curves based on tension data indicates the point at which the equivalent

[5] Shell Development Company, Emeryville, Calif. Assoc. Mem. ASME.

[6] N. L. Svensson, "The Bursting Pressure of Cylindrical and Spherical Vessels," ASME Paper No. 57—A-15.

[7] J. Marin and F. P. J. Rimrott, "Design of Thick-Walled Pressure Vessels Based Upon the Plastic Range," Welding Research Council Bulletin No. 41, July, 1958, New York, N. Y.

tensile stress at the bore of the cylinder reaches the ultimate tensile stress. So Professor Marin and Dr. Rimrott will no doubt realize that the authors appreciated that the assumption, that the ultimate pressure was reached when the stress at the bore equals the ultimate tensile stress, was purely empirical, but it happens to give values of the ultimate pressure which were in good agreement with experiment.

It has been frequently stated that Manning's method is cumbersome, but those who have used the method would not agree that this is true. It must be realized that Table 5 had only to be worked out once, and the rest of the computation certainly did not take more than two or three hours.

The equation proposed by Professor Marin and Dr. Rimrott involves many more assumptions than the complete analysis given in the paper, and is limited in its range of application. Completing their Table 1, the theoretical values for the 0.15 per cent carbon steel cylinders of $K = 6.02$ and 8.05 are 90,700 lb/sq in. and 105,200 lb/sq in., and the deviation $+ 5^1/_2$ and $+ 11$ per cent, respectively. So the accuracy, over the full range of results, was little better than that given by the mean diameter formula.

The authors agreed that for less ductile materials failure by fracture prior to instability would occur: If the shear strain at fracture was constant, then it would be very simple, by using the methods advocated in this paper, to determine the pressure at which this critical shear strain was reached. Unfortunately, as has been shown by Crossland [2], the shear strain at failure was some function of the volumetric stress acting; as a result the shear strain at failure in a cylinder would be less than in a torsion test as there was a volumetric tensile stress in the cylinder which would reduce the ductility.

Mr. Galletly is hardly correct in saying there is little in our paper that has not already been reported in reference [1]. In fact, the theoretical treatment has been extended to cover the derivation of the pressure-expansion curve from tension results, and this made it necessary to make measurements of the diameter of the neck and the radius of curvature of the neck in the transverse plane during the tension tests in order that the true stress could be computed from Bridgman's analysis.

The reason for not including the results of the tests on 0.3 per cent carbon steel was that these tests were carried out much earlier and published separately. Subsequently as the result of correspondence with Mr. Jorgensen it was decided to include comprehensive tension tests in future test programs, but unfortunately none of the 0.3 per cent carbon steel was left and consequently no comprehensive tension data could be obtained for this batch of material.

The authors have now seen the papers by Svensson and Marin and Rimrott, which were not available when they wrote their paper. Though this work was extremely interesting they could not see any real advantage in using some hypothetical equation for the stress-strain curve, unless this represented a considerable saving in time. This appeared unlikely as it was possible to carry out the arithmetical integration they had suggested and abstract perhaps six pressure expansion curves in three to four hours, and their method had the added advantage of using the actual stress-strain curve.

Marin and Rimrott had suggested yet another near empirical equation which was little, if at all, better than the mean diameter formula, which they had found fitted their results remarkably well. However, we would prefer to work from torsion data, and we thought the paper presented had shown the advantages of this beyond any reasonable doubt. All that remained was for the steel companies to provide comprehensive torsion data as a matter of course.

Steady-State Creep Analysis of the Weight Loadings of Furnace Tubes on Multiple Supports

J. L. JACOBOWITZ

Section Engineer, Furnace-Exchanger Production Section, The M. W. Kellogg Company, New York, N. Y.

C. K. MADER

Manager, Furnace-Exchanger Division, The M. W. Kellogg Company, New York, N. Y.

Analysis of creep stress-strain relationships is made for horizontally supported furnace tubes including the effect of tube weight and internal pressure. Steady-state creep effects through the tube wall due to axially symmetrical heat input are also analyzed for these conditions. The original Bailey approach to the pressure problem only is extended to the larger scope undertaken. Maximum permissible tube spans are derived based on accepted criteria for creep stress and deflections.

The results of this work indicate that maximum allowable tube spans may often be theoretically increased beyond present usual design limits except for a few specific materials and instances where short spans are required at very high temperatures. In actual tube design, consideration should be given to experience in operation of any particular type of furnace so that secondary effects may be minimized. Increased economies in costs and flexibility in furnace layout as well as rational span determination are expected from use of these results.

Introduction

THE specifications of many companies often contain rules limiting the extent of furnace tube spans regardless of varying conditions of temperature, material, or type of service. A typical rule is to keep the span within a minimum of 25 diameters and a maximum of 35 diameters. The origin of these rules is obscure. In practice, the lower limit (and sometimes even shorter spans) have been arbitrarily selected for large tube diameters in extremely high temperature service. On the other hand, the 35-diameter limit has usually been rigidly maintained even for small, thick tubes operating below the creep range. The technical literature, in general, has apparently ignored this problem.

In addition to finding a rational method for setting tube spans, another objective of this investigation has been to achieve economies by reducing the number of alloy support castings and main structural frames required in a furnace, these savings being reflected in lower furnace material and erection costs. An additional aim has been to eliminate clumsy layout problems often arising because of tube support spacing restrictions in furnaces with multiple stacks or multiple tube diameters. Similarly, rational spacing for very high temperature work was urgently required.

The maximum shear theory and Bailey's original method of utilizing secondary creep data [1][1] have been adopted as a basis for the theoretical work. More recent investigators, as Marin and Pao [2, 3, 4] and Soderberg [5] have used some form of the distortion energy principle or Bailey's later method of obtaining secondary creep rates [6] in their work on pressure cylinders. However, a very good case, based on experimental work on chromium steel tubes, was made by Coffin, Shepler, and Cherniak [7] in favor of the maximum shear theory. It is believed that the nature of the results given herein would not differ to any appreciable extent, regardless of the type of strength theory employed

Contributed by the Petroleum Division and presented at the Petroleum-Mechanical Engineering Conference, Denver, Colo., September 21–24, 1958, of THE AMERICAN SOCIETY OF MECHANICAL ENGINEERS.

NOTE: Statements and opinions advanced in papers are to be understood as individual expressions of their authors and not those of the Society. Manuscript received at ASME Headquarters, July 9, 1958. Paper No. 58—Pet-14.

[1] Numbers in brackets designate References at end of paper.

Nomenclature

τ, τ_a = calculated and allowable values, respectively of shearing stress, psi

σ_θ, σ_r, σ_z = circumferential, radial, and axial pressure stresses, respectively, psi

σ'_z, σ'_{za} = axial weight stress and permissible axial weight stress, respectively, psi

M = bending moment, in-lb

dA = elementary area of tube cross section

x, y, z = horizontal, vertical, and axial co-ordinates of tube cross section

R, θ = radius and angle to any point, S

R_i, R_o = inner and outer tube radii, respectively, in.

r_c = radius of curvature of beam

$\dot{\epsilon}$ = axial weight creep rate at any point S, in/in/hr

ϵ = unit deformation

i, o = subscripts denoting inner and outer wall of tube

1, 2 = subscripts denoting points P and F, and N and U, respectively (Fig. 3)

B, n; $b(=1/n)$, a = material constants from creep data

B', n'; $b'_w(=1/n')$, a' = equivalent material constants including heat flow effects

v = function of term n

(Continued on next page)

in the investigation. For this reason, the maximum shear theory has been adopted, principally, so that derived results of this investigation could fit conveniently into a relatively concise tube calculation method.

It is recognized that due consideration should be given for any furnace to the many complex effects attendant upon actual operation. Some of these pertain to the complicated variation of temperature in adjacent tubes, fouling conditions, circumferential temperature variations, and reactions from external piping systems. These factors should be studied in conjunction with a rational and analytical theory prior to instituting changes in design based on long experience.

Permissible Stress Limits

According to the maximum shear theory, the condition governing design is that the calculated maximum shearing stress at any point shall not exceed the permissible shearing stress for the material. It may be shown [1] that for a thick-walled cylinder, subjected to internal pressure and operating in the creep range, this maximum shear stress occurs at the inside surface of the cylinder. This may be expressed in terms of principal stresses as follows:

$$\tau = 1/2(\sigma_\theta - \sigma_r) = \tau_a \tag{1}$$

where τ is the calculated shearing stress, σ_θ is the circumferential stress and σ_r is the radial stress occurring at the inside surface, and τ_a is the permissible shearing stress. Bailey [1] has developed formulas for τ based on pressure, radius, thickness, and material constants.

When a tube is supported horizontally, the bending moment due to tube weight (including contents and fins) adds axial compressive and tensile stresses to the upper and lower parts of the tube, depending on the point at which the moment is taken. In order that no additional strength beyond that called for by τ be required, the algebraic sum of the axial pressure and weight stresses may not exceed either of the principal stresses σ_θ or σ_r. The limiting conditions for the inside surfaces (which will be shown further to be critical locations) are, at the compressive side:

$$\sigma_z + (-\sigma'_{z1}) = \sigma_r \tag{2}$$

and at the tension side:

$$\sigma_z + \sigma'_{z1} = \sigma_\theta \tag{3}$$

where σ_z is the axial pressure stress and σ'_{z1} is the axial weight stress at points P and F (Fig. 2).

Substituting in Equation (1):

$$\tau_a = 1/2(\sigma_\theta - \sigma_z + \sigma'_{z1}) \quad \text{at the compression side} \tag{4}$$

and

$$\tau_a = 1/2(\sigma_z + \sigma'_{z1} - \sigma_r) \quad \text{at the tension side} \tag{5}$$

It may be demonstrated, from the concept of volume constancy, that the condition of zero axial creep in a thin wall tube under pressure alone corresponds to setting $\sigma_\theta = 2\sigma_z$. As it is also reasonable to stipulate zero axial creep in a thick-walled tube under internal pressure, an infinitesimally thin layer at the inner surface of the tube can be assumed to be under creep conditions similar to that of a thin-walled tube. Also, triaxial hydrostatic stresses induce no change in creep characteristics, so that σ_r may be subtracted from the stress system of the thin element (see Fig. 1).

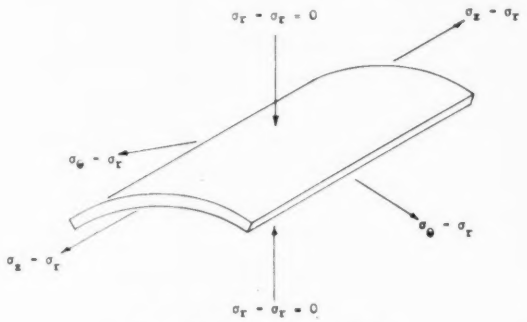

Fig. 1 Equivalent pressure stresses

The postulate of zero axial creep then requires (from volume constancy) that the circumferential stress be twice the axial:

$$\sigma_\theta - \sigma_r = 2(\sigma_z - \sigma_r) \tag{6}$$

or

$$\sigma_\theta = 2\sigma_z - \sigma_r \tag{7}$$

Including now the effect of the axial weight stress, Equation (7) may be substituted in Equation (4), giving the same result as Equation (5). This indicates that the critical value of shearing stress when the bending moment is applied occurs simultaneously at top and bottom of the inner face of the tube. Solving Equations (1), (4), and (5),

$$\tau_a = \frac{\tau}{2} + \frac{\sigma'_{z1}}{2} \tag{8}$$

Expressed this way, $\sigma'_{z1} = \sigma'_{za}$, the maximum allowable axial bending stress which may be added to the tube under pressure without adding additional strength. Simplifying Equation (8):

$$\sigma'_{za} = 2\tau_a - \tau \tag{9}$$

For the special case when the pressure thickness is fully utilized in design (i.e., $\tau = \tau_a$), Equation (9) reduces to:

$$\sigma'_{za} = \tau_a \tag{10}$$

Nomenclature

K_1 = function of term n
c_1, c_2 = constants of integration
c = moment coefficient
w = tube (plus contents) weight, lb/ft
L = tube length, ft
$L_{z\,max}$ = permissible tube length on basis of stress criteria, ft
$L_{\Delta\,max}$ = permissible tube length on basis of deflection criteria, ft
d_o, d_i, d_m = outside, inside, and average tube diameters, respectively, in.
h = average tube wall thickness, in.
t = time, hr
D = constant term for particular material and tube cross section (defined in text)
E = modulus of elasticity, psi
I = moment of inertia, in.^{4}
p = internal pressure, psi
Q = heat-transfer rate, Btu/hr/sq ft
T = temperature, deg F
C = metal conductivity, Btu/hr/sq ft/in/deg F
f, g, j = intercepts on log $\dot{\epsilon}$ scale
m, s = intercepts on log σ'_z scale
Δ_s = static deflection, in.
F, N, P, S, U = points on tube cross section (Fig. 3)

Creep Conditions in Furnace Tubes Without Heat Transfer Case of Low Pressure Stress

Creep Stress. If the tube is at creep temperature, its rate of axial creep $\dot{\epsilon}$ (expressed in inches per inch per hour) due to an applied external load alone (no pressure) has been found by many investigators [1, 4, 6] to obey the following physical relationship in the steady state:

$$\dot{\epsilon} = B(\sigma'_s)^n \tag{11}$$

where B and n are material constants for a given temperature.

The analysis in this section is based, accordingly, on the case of zero pressure stress. It may be reasonably used, nevertheless, when actual tube thickness is much larger than indicated by accurate stress analysis. See discussion of equations (31) and (32). This often occurs in practice due to minimum thickness requirements, safety factors, and corrosion allowances.

Assuming that a plane cross section before bending remains plane [8], the axial strain rate will be proportional to the distance of a fiber from the neutral axis (see Fig. 3):

$$\frac{\dot{\epsilon}}{\dot{\epsilon}_1} = \frac{R \sin \theta}{R_i} \tag{12}$$

where subscript 1 refers to points P and F of the tube.

As shown in Appendix 1, acceptance of these criteria leads to a relationship between σ'_{s1} and bending moment M given by:

$$\sigma'_{s1} = \frac{3n+1}{4n} \cdot \frac{M(R_i)^{1/n}}{(R_o)^{\frac{3n+1}{n}} - (R_i)^{\frac{3n+1}{n}}} \tag{13}$$

The value of the bending moment corresponds to a uniformly loaded continuous beam over multiple supports with small overhangs at the ends, represented by return headers. It may be expressed as cwL^2, where w is weight in lb/ft, L is span length in feet, and M is expressed in ft-lb. The value of c depends on the number of supports, the point at which the moment is taken and details of the overhang. For these conditions the maximum value of c is usually about 1/10, although it occasionally reaches 1/8. For this reason, and also to allow for the effect of unequal resting of the tube on the supports, the higher value is used here. Substituting for M in Equation (13) and converting it into in-lb with R in inches and σ in psi, the following results:

$$\sigma'_{s1} = \frac{1.5wL^2R_i^{1/n}}{(R_o)^{\frac{3n+1}{n}} - (R_i)^{\frac{3n+1}{n}}} \cdot \frac{3n+1}{4n}$$

Solving for $L_{s\,max}$, the maximum permissible span length, in feet, on the basis of stress criteria, and substituting σ'_{sa} for σ'_{s1}:

$$L_{s\,max} = \left[\left(\frac{2\sigma'_{sa}}{3w} \right) \left(\frac{4n}{3n+1} \right) \left(\frac{(R_o)^{\frac{3n+1}{n}} - (R_i)^{\frac{3n+1}{n}}}{(R_i)^{1/n}} \right) \right]^{1/2} \tag{14}$$

It is seen that for relatively high values of n and particularly for ratios of R_o/R_i approaching unity (as in thin-walled tubes) this becomes:

$$L_{s\,max} = \left[\left(\frac{2\sigma'_{sa}}{3w} \right) \left(\frac{4}{3} \right) (R_o^3 - R_i^3) \right]^{1/2}$$

This, in turn, factors and simplifies to an expression which may be used for the case of no heat transfer:

$$L_{s\,max} = 0.82\, d_m \left(\frac{\sigma'_{sa} h}{w} \right)^{1/2} \tag{15}$$

where d_m is the average tube diameter, in inches, and h is the average wall thickness, in inches.

Deflection Under Creep Conditions. Considering steady-state creep data only, Equation (11) may be expressed in terms of unit deformation $d\epsilon$ and unit time dt as follows:

$$\frac{d\epsilon}{dt} = B(\sigma'_s)^n \tag{16}$$

Integrating and applying Equation (46) of Appendix 1:

$$\epsilon_1 = B(\sigma'_{s1})^n t \tag{17}$$

For a beam subject to bending, the following elementary relationships may be applied to a cylindrical cross section:

$$\epsilon_1 = \frac{R_i}{r_c} \tag{18}$$

$$\frac{d^2y}{dz^2} = \frac{1}{r_c} \tag{19}$$

where r_c is the radius of curvature of the elementary beam section and y and z are vertical and axial co-ordinates of the cylindrical beam.

An equation for M in terms of z is also required. Selection of the end moments at the supports is dependent on number of supports and details of the overhang, as noted previously. As a conservative approach, with particular reference to the end spans, the end moments have been chosen (in in-lb) as $1/40\, wL^2 \cdot 12$ in deflection calculations for the purpose of this investigation. This gives a moment of $1/10\, wL^2 \cdot 12$ at the center.

Under creep conditions obeying the stipulations just made, it can be shown that the maximum deflection may be expressed as:

$$y_{max} = \frac{2vw^n(L)^{2n+2}t(12)^{n+2}}{(10)^{n+7}(d_m)^{2n+1}(2\tau_a h)^n} \tag{20}$$

where τ_a, in keeping with usual design practice, is the stress corresponding to a uniaxial tensile creep rate of one per cent in 10,000 hours, and v may be obtained from Fig. 2. The detailed derivation of this result is shown in Appendix 2.

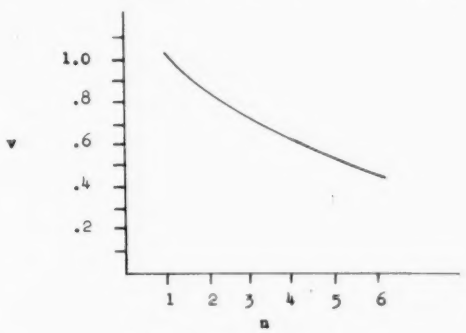

Fig. 2 Expression v versus n

It becomes necessary at this junction to establish criteria for y_{max} with relation to t. For this purpose, recourse has been had in these derivations to a rule of thumb used by many refinery operators, whereby tubes are retired when they can no longer be seen through due to creep. The refinery life, t, is taken here as 75,000 hours which is undoubtedly a severe condition for the tube. This corresponds to a 10-year plant life with an 85 per cent on-stream efficiency, although the total tube life is, to a great extent, determined by the design creep stress. Other ratios of y_{max}/t may be selected depending on design considerations, yielding slightly different results, as may be seen below. Also, d_m has been sub-

stituted for y_{max} as a close approximation for thin-walled tubes. Making these substitutions and writing $L_{\Delta max}$ for L, the maximum permissible span (in feet), as conditioned by the limiting creep deflection, becomes:

$$L_{\Delta\,max} = d_m \cdot \left[\left(\frac{0.46}{v} \right) (1.67)^n \left(\frac{\tau_a h}{w} \right)^n \right]^{\frac{1}{2n+2}} \tag{21}$$

or

$$L_{\Delta\,max} = d_m \cdot \left(\frac{0.46}{v} \right)^{\frac{1}{2n+2}} \cdot (1.67)^{\frac{n}{2n+2}} \cdot \left(\frac{\tau_a h}{w} \right)^{\frac{n}{2n+2}} \tag{22}$$

The middle two expressions of these four terms in Equation (22) are functions of n only. Their product for $n = 3$ is 1.14, for $n = 4$ is 1.17, and for $n = 6$ is 1.24. For simplicity of engineering design, a conservative product value of 1.15 will be adopted in this study. It may also be seen from inspection of these equations that certain factors have only a slight effect on $L_{\Delta\,max}$. This justifies, for engineering usage, many of the approximations made in the derivations. These include selection of the particular ratio for y_{max}/t, and the substitution of d_m instead of inside diameter for y_{max}. Each of these factors affects $L_{\Delta\,max}$ only to the $1/(2n + 2)$ power, or for practical purposes, from the 0.07 to the 0.12 power. Actual end moment conditions, however, will often considerably increase $L_{\Delta\,max}$.

With substitution of $b = 1/n$, Equation (22) may then be written in the form:

$$L_{\Delta\,max} = 1.15 d_m \left(\frac{\tau_a h}{w} \right)^{\frac{1}{2+2b}} \tag{23}$$

which is similar to the form of Equation (15), particularly, since $\sigma'_{sp} = \tau_a$ when the pressure thickness is fully utilized.

Creep Conditions in Furnace Tubes With Heat Transfer Case of Low Pressure Stress

The preceding derivations were based on the simplifying assumption that there was no heat flow into or out of the tube. In actual practice, a refinery furnace tube will receive heat from outside, resulting in a radial temperature gradient through the metal wall. In other services, a tube may be surrounded by a cooling medium, in which case there will be a reverse temperature gradient.

It will be recalled that the values of B and n were defined as material constants for a given temperature. As the temperature varies through the wall, B and n will likewise vary. It becomes necessary to find the effect of this variation on creep stress and deflection.

For the condition of axially symmetrical heat input under steady-state creep conditions, it is shown (in Appendix 3) that a new general creep stress-strain rate relationship may be expressed by the following:

$$\dot{\epsilon} = B'(\sigma'_s)^{n'} \tag{24}$$

B' and n' are here terms expressing both material constants and heat-transfer effects for the tube under weight stresses. The important term n' may be evaluated from:

$$\frac{1}{n'} = b'_w = b - \frac{Qad_o}{2C} \tag{25}$$

where Q is heat-transfer rate, in Btu/hr/sq ft, a is the average increase in stress interval between constant temperature lines of log σ'_s versus log $\dot{\epsilon}$ per decrease in temperature, d_o is outside diameter, in inches, and C is metal thermal conductivity, in Btu/hr/sq ft/in/deg F.

Derivation of the complete stress relationship including the effect of heat transfer (Appendix 4) is now possible. Equation (13) is then modified to:

$$\sigma'_{s1} = \frac{3n' + 1}{4n'} \cdot \frac{M(R_i)^{1/n'}}{(R_o)^{\frac{3n'+1}{n'}} - (R_i)^{\frac{3n'+1}{n'}}} \tag{26}$$

It may similarly be shown that the stress σ'_{s2}, at the extreme outer fibers (points N and U in Fig. 3) may be expressed as:

$$\sigma'_{s2} = \frac{3n' + 1}{4n'} \cdot \frac{M(R_o)^{1/n'}}{(R_o)^{\frac{3n'+1}{n'}} - (R_i)^{\frac{3n'+1}{n'}}} \tag{27}$$

Evaluation of Equation (25) for typical values of heat-transfer rate and substitution in Equations (26) and (27) gives the information in Table 1.

Adjunct to Table 1, the following is the effect of heat transfer giving the order of magnitude of n' for refinery furnaces:

For no or low heat-transfer rate	n' is ~ 3 to ∞
For moderate heat-transfer rate	n' is $\sim -\infty$ to -2
For very high heat-transfer rate and large diameter	n' is -1 to -0.25

Study of Table 1 shows that the effect of increasing heat transfer is to decrease outer fiber stress and to increase inner fiber stress. When n' is ∞, both stresses are equal. For high heat transfer, the inner fiber stress is larger. It is only for the case of heat transfer being close to zero ($n' = 3$ to 6) that outer fiber stress becomes larger (not shown in table). For all practical values of heat transfer, accordingly, adoption of σ'_{s1} based on $n' = -0.5$ should prove quite acceptable. Substituting and simplifying in a manner similar to development of Equation (15), the following equation results:

$$L_{s\,max} = 0.82 d_i \left(\frac{\sigma'_{sa} h}{w} \right)^{1/3} \tag{28}$$

where d_i is inside diameter and σ'_{sa} is the allowable stress, from Equation (9), at the inner wall temperature. For exceptionally high heat-transfer rate (by present refinery furnace standards) and large tube diameters, $L_{s\,max}$ will be proportional to an

Table 1 Inner and outer wall stresses for various values of b'_w. Case of low pressure stress.

	b'_w	n'	$\frac{3n'+1}{4n'}$	$R^{1/n'}$	$R_o^{\frac{3n'+1}{n'}} - R_i^{\frac{3n'+1}{n'}}$	σ'_{s1} approx.	σ'_{s2} approx.
Very low heat transfer	0	∞	0.75	1	$R_o^3 - R_i^3$	$\frac{M}{(d_m)^2 h}$	$\frac{M}{(d_m)^2 h}$
	−1	−1	0.5	R^{-1}	$R_o^2 - R_i^2$	$\frac{M}{d_i d_m h}$	$\frac{M}{d_o d_m h}$
	−2	−0.5	0.25	R^{-2}	$R_o - R_i$	$\frac{M}{(d_i)^2 h}$	$\frac{M}{(d_o)^2 h}$
Very high heat transfer	−4	−0.25	−0.25	R^{-4}	$R_o^{-1} - R_i^{-1}$	$\frac{d_o M}{(d_i)^3 h}$	$\frac{d_i M}{(d_o)^3 h}$

equivalent diameter somewhat less than d_i. However, this is undoubtedly too extreme for setting standard design.

It is also shown (in Appendix 4) that the maximum deflection for the condition of radial heat transfer will also be modified. The effect of heat transfer is to transform Equation (20) into:

$$y_{\max} = \frac{2B_i v(w)^n (L)^{2n+2} t (12)^{n+2}}{(10)^{n+1}(d_i)^{2n+1}(h)^n} \tag{29}$$

where B_i is the value of material constant B at the inner wall temperature.

From the assumption that a plane section before bending remains plane, the same equation may also be derived using σ'_{z2}, B_o, and d_o as a basis, where B_o is the value of B at the outer wall temperature.

Using the same limits as defined previously for no heat flow regarding deflection, time, and creep stress, $L_{\Delta\max}$ becomes:

$$L_{\Delta\max} = 1.15 d_i \left(\frac{\tau_a h}{w}\right)^{\frac{1}{2+2b}} \tag{30}$$

where τ_a is the allowable shearing stress at the inner wall temperature.

Creep Conditions in Furnace Tubes Case of High Pressure Stress

Creep Stress. When the tube thickness actually used is not substantially greater than that required for pressure, the addition of axial weight stresses induces significant changes in creep rates for the triaxial stress condition. Utilizing the maximum shear theory, it may be shown (7) that the axial creep rate may be given as

$$\dot{\epsilon} = B(\sigma'_z)(\sigma_\theta - \sigma_r)^{n-1} \tag{31}$$

when σ_θ is larger than $\sigma_z + \sigma'_z$. When σ_θ is smaller than $\sigma_z + \sigma'_z$, as may be the case when thickness is not fully utilized for pressure, the axial creep rate may be given as

$$\dot{\epsilon} = B(\sigma'_z)(\sigma'_z + \sigma_z - \sigma_r)^{n-1} \tag{32}$$

which is seen to reduce to Equation (11) for the case of zero pressure stress.

The following derivations are based on the creep law given by Equation (31). To a great extent the manner of solution as well as the discussion given in previous sections are pertinent here as well.

As shown in Appendix 5, adoption of accepted relationships for pressure stress, as well as Equation (31), leads to the following

$$\sigma'_{z1} = \frac{6n-2}{\pi n} \cdot \frac{M(R_i)^{\frac{3n-2}{n}}}{(R_o)^{\frac{6n-2}{n}} - (R_i)^{\frac{6n-2}{n}}} \tag{33}$$

With the same coefficients for bending moment as previously used, this gives

$$L_{z\max} = \left[\left(\frac{2\sigma'_{za}}{3w}\right)\left(\frac{\pi n}{6n-2}\right)\left(\frac{(R_o)^{\frac{6n-2}{n}} - (R_i)^{\frac{6n-2}{n}}}{(R_i)^{\frac{3n-2}{n}}}\right)\right]^{1/2} \tag{34}$$

Deflection Under Creep Conditions. Integrating Equation (31) for steady-state creep, we get

$$\epsilon_1 = B(\sigma'_{z1})(\sigma_{\theta 1} - \sigma_{r1})^{n-1} t \tag{35}$$

As shown in Appendix 5, use of this equation for deformation and similar assumptions for bending moment as made in the case of low pressure stress, leads to the following equation for maximum deflection:

$$y_{\max} = \frac{0.99 w L^4 t (12)^3 (\sigma_{\theta 1} - \sigma_{r1})^{n-1}}{10^3 (2\tau_a)^n} \cdot \frac{6n-2}{\pi n} \cdot \frac{(R_i)^{\frac{2n-2}{n}}}{(R_o)^{\frac{6n-2}{n}} - (R_i)^{\frac{6n-2}{n}}} \tag{36}$$

As before, setting arbitrary criteria of $y_{\max} = 2R_i$ and $t = 75{,}000$ hours, we may solve for maximum permissible length on the basis of deflection criteria, giving

$$L_{\Delta\max} = 1.5\left[\frac{(2\tau_a)^n}{(\sigma_{\theta 1} - \sigma_{r1})^{n-1}} \cdot \frac{n}{6n-2} \cdot \frac{(R_o)^{\frac{6n-2}{n}} - (R_i)^{\frac{6n-2}{n}}}{w(R_i)^{\frac{n-2}{n}}}\right]^{1/4} \tag{37}$$

For the case of pressure thickness fully utilized, this simplifies to

$$L_{\Delta\max} = 1.8\left[\frac{\tau_a\left((R_o)^{\frac{6n-2}{n}} - (R_i)^{\frac{6n-2}{n}}\right)}{w(6n-2)(R_i)^{\frac{n-2}{n}}}\right]^{1/4} \tag{38}$$

Heat-Transfer Effects. For the case of axially symmetrically input, the new creep stress-strain rate relationship may be expressed as in Equation (24). The important term n' may be evaluated (as shown in Appendix 5) from the following

$$\frac{1}{n'} = b'_w = 3 - 2b - \frac{Qad_\theta}{2Cb} \tag{39}$$

The new maximum stresses (σ_{z1}' and σ_{z2}') at inside and outside extreme fibers, respectively, then become

$$\sigma'_{z1} = \frac{3n'+1}{\pi n'} \cdot \frac{M(R_i)^{1/n'}}{(R_o)^{\frac{3n'+1}{n'}} - (R_i)^{\frac{3n'+1}{n'}}} \tag{40}$$

$$\sigma'_{z2} = \frac{3n'+1}{\pi n'} \cdot \frac{M(R_o)^{1/n'}}{(R_o)^{\frac{3n'+1}{n'}} - (R_i)^{\frac{3n'+1}{n'}}} \tag{41}$$

It is of interest to note that, when the value of n' obtained from Equation (39) for the condition of heat transfer rate $Q = 0$ is substituted into Equation (40), the latter becomes equivalent to stress expression (33). The value of n' in Equation (39) expresses the variation of log axial creep rate with respect to log axial creep stress through the tube wall for any angle θ. It includes not only the effect on creep rate of varying temperature but also of varying pressure stress through the tube wall. Evaluation of Equations (40) and (41) for typical values of n' is given in Table 2.

Adjunct to Table 2, n' takes on the following values for most refinery furnaces

For no or low heat-transfer rate	n' is ~ 0.4 to 1
For moderate heat-transfer rate	n' is ~ 1 to ∞, $-\infty$ to -0.5
For very high heat-transfer rate and large diameter	n' is ~ -0.25 to -0.1

Study of Table 2 shows a relationship between inner and outer wall stresses very similar to that given in Table 1, except that the designations from low to high heat-transfer rate correspond to somewhat different values of Q. An $n' = -0.25$ is here adopted,

Table 2 Inner and outer wall stresses for various values of b'_w. Case of high pressure stress.

	b_w'	n'	$\frac{3n'+1}{\pi n'}$	$R^{1/n'}$	$R_o^{\frac{3n'+1}{n'}} - R_i^{\frac{3n'+1}{n'}}$	σ'_{s1} approx.	σ'_{s2} approx.
Very low heat transfer	1	1	$\frac{4}{\pi}$	R	$R_o^4 - R_i^4$	$\frac{4d_iM}{\pi(d_m)^3h}$	$\frac{4d_oM}{\pi(d_m)^3h}$
	0	∞	$\frac{3}{\pi}$	1	$R_o^3 - R_i^3$	$\frac{4M}{\pi(d_m)^2h}$	$\frac{4M}{\pi(d_m)^2h}$
	−2	−0.5	$\frac{1}{\pi}$	R^{-2}	$R_o - R_i$	$\frac{4M}{\pi(d_i)^2h}$	$\frac{4M}{\pi(d_i)^2h}$
	−4	−0.25	$-\frac{1}{\pi}$	R^{-4}	$R_o^{-1} - R_i^{-1}$	$\frac{4d_oM}{\pi(d_i)^3h}$	$\frac{4d_iM}{\pi(d_o)^3h}$
Very high heat transfer	−5	−0.20	$-\frac{2}{\pi}$	R^{-5}	$R_o^{-2} - R_i^{-2}$	$\frac{4(d_o)^2M}{\pi(d_i)^3d_mh}$	$\frac{4(d_i)^2M}{\pi(d_o)^2d_mh}$

corresponding to a reasonable maximum heat input. Substitution in Equation (40) and simplifying, gives

$$L_{s\max} = 0.72d_i\left(\frac{d_i}{d_o}\cdot\frac{\sigma'_{s\theta}h}{w}\right)^{1/2} \tag{42}$$

It is also shown (in Appendix 5) that the maximum deflection for this condition of radial heat input under high pressure stress will be modified as follows:

$$y_{\max} = \frac{0.99wL^4(12)^3\times 8B_i}{10^3\pi d_i^3h}\cdot\frac{d_o}{d_i}\cdot(\sigma_{\theta 1} - \sigma_{r1})^{n-1} \tag{43}$$

Using the same limitations as defined previously for deflection, time, and creep stress, $L_{\Delta\max}$ becomes

$$L_{\Delta\max} = 0.89d_i\left(\frac{d_i}{d_o}\cdot\frac{\tau_c h}{w}\right)^{1/4} \tag{44}$$

Added Factors Bearing Upon Design Considerations

Several other effects apart from those just detailed were considered briefly before setting the recommended design formulas indicated. They are summarized herewith.

Static Deflection. The original elastic deflection has not been considered as a prime criterion in setting maximum length limitations. For practical considerations of bay span and panel dimensions as well as for psychological reasons, the designer may wish to limit very long calculated spans somewhat. As a comparison, it should be noted that usual practice limits refinery piping deflection to 1/2–1 in., presumably to facilitate drainage and avoid pockets as well as to keep natural frequency to a value such that pipes would not be resonant with random refinery vibrations. Pertaining to heat exchangers, the TEMA Code permits a tube span of 60 diameters for tubes greater than 1 in. in diameter.

As permissible length varies as only a low power of the creep deflection, static deflection has usually a very small effect on L_Δ. In the low pressure stress case, a permissible creep deflection of as little as $0.01\,d_i$ gives approximately $^2/_3 L_{\Delta\max}$ and a permissible creep deflection of $0.1\,d_i$ gives about $0.8L_{\Delta\max}$. For extremely large spans, when Δ_s, the initial static deflection, is large, and it is desired to limit *total* deflection to d_i, $L_{\Delta\max}$ may be modified as follows: Subtract Δ_s from d_i, and multiply the calculated $L_{\Delta\max}$ by the ratio, to the appropriate power, of this difference to d_i, giving the modified $L_{\Delta\max}$. In the low pressure case, the appropriate power is $1/(2n+2)$. For the high pressure case, it is 1/4.

Formula Evaluation. Corollary to the preceding paragraph, it should be noted that a small change in span length produces large change in creep deflection. Evaluation of $L_{\Delta\max}$ should, therefore, be accurately carried out and the result strictly maintained as a maximum.

Values for h and w to be used should be those corresponding to the tube conditions after corrosion, as the ratio of h to w is minimum at that time, giving lowest results for L. The value of $L_{s\max}$ for very low temperature may be computed on the basis of elastic conditions. For derivation of the necessary equation, $n = 1$ may be substituted in Equation (48) of Appendix 1, permitting exact integration and giving $0.72\,d_m$ instead of $0.82\,d_m$ in Equation (15).

Summary and Conclusions

The need for a rational determination of maximum furnace tube spans has existed for some time. This paper is devoted, in the main, to presentation of a mathematical analysis of the problem and to simplification of the results for engineering usage. It is thus concerned, primarily, with stress and deflection characteristics of tubes operating in the temperature range where steady-state metal creep occurs, subjected to internal pressure, tube weight, and axially symmetrical heat input.

The approach used herein generally follows R. W. Bailey's original treatment for the pressure condition only, but extends the scope to the more complicated conditions encountered in actual service. The analysis was developed along lines readily permitting the inclusion of results obtained in the M. W. Kellogg Company tube calculation method, but the principles used in the derivations may be used for adapting the results to similar methods.

For practical purposes of design, Equations (28) and (30) represent the criteria for selection of maximum permissible tube spans for the low pressure stress condition. For the high pressure stress condition, the corresponding criteria are determined by Equations (42) and (44). These results are based on the following conditions, employed within certain limits by a number of refinery furnace designers and operators:

(*a*) Permissible stresses inducing one per cent creep in 10,000 hours.
(*b*) Total furnace life of 75,000 hours.
(*c*) Creep deflections corresponding to one inside tube diameter.
(*d*) Relatively high heat-transfer rate (see text).
(*e*) Modified semifixed end supports (see text).

These equations are, for the low pressure stress condition:

$$L_{s\max} = 0.82\,d_i\left(\frac{\sigma'_{s\theta}h}{w}\right)^{1/3} \tag{28}$$

$$L_{\Delta\max} = 1.15 d_i \left(\frac{\tau_a h}{w}\right)^{\frac{1}{2+2b}} \tag{30}$$

and for the high pressure stress condition:

$$L_{s\max} = 0.72 d_i \left(\frac{d_i}{d_o} \cdot \frac{\sigma'_{sa} h}{w}\right)^{1/3} \tag{42}$$

$$L_{\Delta\max} = 0.89 d_i \left(\frac{d_i}{d_o} \cdot \frac{\tau_a h}{w}\right)^{1/4} \tag{44}$$

Stress σ'_{sa} is equal to τ_a when pressure thickness is fully utilized, but is generally higher, and may be given by the following expression:

$$\sigma'_{sa} = 2\tau_a - \tau \tag{9}$$

where τ is the calculated shearing stress from the Bailey or similar equations for the thickness actually used. These stresses correspond to the temperature and other conditions at the inner wall of the tube.

It is recognized that conditions (*a*) and (*b*) are to some extent mutually dependent according to stress-rupture data that the ratio of (*c*) to (*b*) is arbitrary and very conservative, and that conditions (*d*) and (*e*) may vary. Nevertheless, it is found that other design criteria, within reasonable limitations, will not necessarily affect these equations to a great degree. Actual end moment conditions, in many cases, will permit a much larger $L_{\Delta\max}$. When any of the design conditions are other than (*a*) to (*e*) Equations (25) and (26) of the text and (81) of Appendix 4 or Equations (39), (40), and (43) of Appendix 5 may be used for greater accuracy.

Application of these equations to actual furnace design indicates that, within the range of tube and service conditions most common in practice, the maximum critical length may often exceed 35 tube diameters, which has been the empirical maximum in many specifications. This is particularly true when deflection criteria, inserted principally for psychological reasons, are relaxed somewhat. It also indicates that even intermediate lengths commonly used may sometimes be unsafe for very high temperature, large diameter finned tubes. The analysis in the text also indicates the approach for restricting maximum spans based on considerations of static deflection, if so desired.

When application of these equations to particular cases indicates that spans may be somewhat increased, it will be found that this increase will prove advantageous in a variety of ways. Furnace designers will readily appreciate the resulting economies in material costs as well as greater flexibility in furnace layout.

It is recognized that due consideration should be given for any furnace to the many complex effects attendant upon actual operation. Some of these pertain to the complicated variation of temperature in adjacent tubes, fouling conditions, circumferential temperature variations, and reactions from external piping systems. Another important consideration involves evaluation of the necessity for particular deflection limitations. These factors should be studied in conjunction with a rational and analytical theory prior to instituting changes in design based on long experience.

Because it has been recognized that present restrictions are empirical, the 35 diameter or other maximum limitation was not always utilized to full advantage. In particular services, although not necessarily the most critical, spans were often arbitrarily limited to much shorter lengths. With adoption of standards based on rational and realistic criteria, there should be greater confidence and safety in setting tube spans.

References

1 R. W. Bailey, "Thick-Walled Tubes and Cylinders Under High Pressure and Temperature," *Engineering*, June 13, June 20, and June 27, 1950, pp. 712, 785, and 818.

2 J. Marin, "Design of Members Subjected to Creep at High Temperatures," *Journal of Applied Mechanics*, vol. 4, TRANS. ASME, vol. 59, 1937, p. A-21.

3 Y. Pao and J. Marin, "An Analytical Theory of the Creep Deformation of Materials," *Journal of Applied Mechanics*, vol. 20, TRANS. ASME, vol. 75, 1953, p. 245.

4 Y. Pao and J. Marin, "Deflection and Stresses in Beams Subjected to Bending and Creep," *Journal of Applied Mechanics*, vol. 19, TRANS. ASME, vol. 74, 1952, p. 478.

5 C. R. Soderberg, "The Interpretation of Creep Tests for Machine Design," TRANS. ASME, vol. 58, 1936, p. 733.

6 R. W. Bailey, "The Utilization of Creep Test Data in Engineering Design," *Proceedings, The Institution of Mechanical Engineers*, vol. 131, 1935, p. 131.

7 L. F. Coffin, Jr., P. R. Shepler, and G. S. Cherniak, "Primary Creep in the Design of Internal-Pressure Vessels," *Journal of Applied Mechanics*, vol. 16, TRANS. ASME, vol. 71, 1949, p. 229.

8 W. N. Findley and J. J. Poczatek, "Prediction of Creep-Deflection and Stress Distribution in Beams From Creep in Tension," *Journal of Applied Mechanics*, vol. 20, TRANS. ASME, vol. 77, 1955, p. 165.

APPENDIX 1

Creep Stress-Strain Rate Relationships Case of Low Pressure Stress

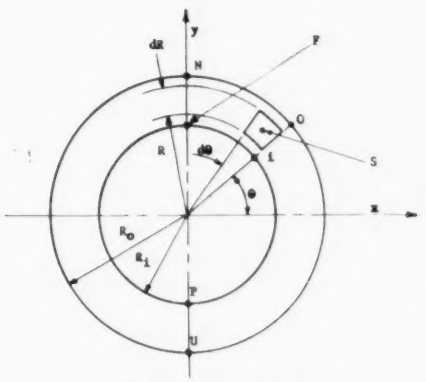

Fig. 3 Tube cross section

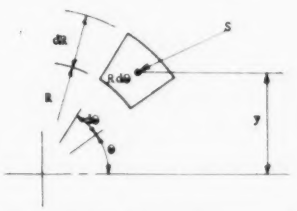

Fig. 4 Elementary area in tube cross section

Consider an infinitesimal element of the tube cross section about point *S*, as shown in Fig. 3 and enlarged in Fig. 4. The tube is subjected to the action of an axial bending moment only. Substituting in the fundamental equation for moment

$$M = \int \sigma'_s dA \cdot y$$

we get:

$$M = \int_{R_i}^{R_o} \int_0^{2\pi} \sigma'_s R \, d\theta \, dR \, R \sin\theta \tag{45}$$

From Equation (11) we may write the following relationship:

$$\frac{\dot{\epsilon}}{\dot{\epsilon}_1} = \left(\frac{\sigma'_s}{\sigma'_{s1}}\right)^n \tag{46}$$

Substituting Equation (12) in Equation (46) and solving for σ'_s we get:

$$\sigma'_s = \sigma'_{zi}\left(\frac{R \sin \theta}{R_i}\right)^{1/n} \tag{47}$$

Now, substituting Equation (47) into the moment equation (45), gives:

$$M = \int_{R_i}^{R_o}\int_0^{2\pi} \sigma'_{zi}\left(\frac{R \sin \theta}{R_i}\right)^{1/n} R\, d\theta\, dR\, (R \sin \theta)$$

$$M = \frac{4\sigma'_{zi}}{(R_i)^{1/n}}\int_{R_i}^{R_o}\int_0^{\pi/2} (R)^{\frac{2n+1}{n}} (\sin \theta)^{\frac{n+1}{n}}\, d\theta\, dR \tag{48}$$

The expression $(\sin \theta)^{\frac{n+1}{n}}$ cannot be integrated in closed form for an arbitrary value of n. However, as the usual range of values of n lies between 4 and 6, with even much higher values sometimes reported for certain conditions, the error inherent in assuming that $(n + 1)/n = 1$ is not very large. A better idea of the magnitude of this error will be shown. Making this substitution, integration of Equation (34) yields, after substitution of the appropriate limits:

$$M = \frac{4n}{3n + 1} \cdot \frac{\sigma'_{zi}}{(R_i)^{1/n}}\left(R_o^{\frac{3n+1}{n}} - R_i^{\frac{3n+1}{n}}\right)$$

$$\sigma'_{zi} = \frac{3n + 1}{4n} \cdot \frac{M(R_i)^{1/n}}{(R_o)^{\frac{3n+1}{n}} - (R_i)^{\frac{3n+1}{n}}} \tag{13}$$

Evaluation of the sin θ function integral of Equation (48) for values of n from 3 to 6 according to Simpson's rule have been carried out, as have exact solutions of Equation (14). They indicate that the values of $L_{s\,max}$ obtained from Equation (15) may be on the high side in an average case by about 2 to 4 per cent, with a possible maximum error of about 6 per cent. On the other hand, a relatively high value was adopted for moment coefficient c and the effect of the pressure stress in decreasing the bending moment was neglected. The latter effect is similar to that induced in a laterally deflected tie-rod by an axial pull. Analysis of this reduction in stress for a typical case showed it to be of the order of magnitude but of the opposite sign from the error involved in the approximate integration of the sin θ function.

APPENDIX 2

Derivation of Creep Deflection Relationships Case of Low Pressure Stress

When Equations (17) and (18) are substituted into Equation (19), we get:

$$\frac{d^2y}{dz^2} = \frac{B(\sigma'_{zi})^n t}{R_i} \tag{49}$$

This may be rewritten as:

$$\frac{d^2y}{dz^2} = \frac{M^n t}{D} \tag{50}$$

where, referring to Equation (13), D is a constant term for a particular tube cross section and material, defined as:

$$D = \frac{1}{B}\left[\left(\frac{4n}{3n + 1}\right)\left(R_o^{\frac{3n+1}{n}} - R_i^{\frac{3n+1}{n}}\right)\right]^n \tag{51}$$

The moment at any point at a distance z from a support may be written as:

$$M = \left(-\frac{1}{40} wL^2 + \frac{1}{2} wLz - \frac{1}{2} wz^2\right) 12 \tag{52}$$

making the end moment assumption described in the text under Equation (19). Equation (50) now becomes:

$$\frac{d^2y}{dz^2} = \left(-\frac{1}{40} wL^2 + \frac{1}{2} wLz - \frac{1}{2} wz^2\right)^n \frac{12^n t}{D} \tag{53}$$

Solutions for y of Equation (53) with various values of n have been carried out. The constants of integration may be determined from the conditions that $dy/dz = 0$ when $z = L/2$, and that $y = 0$ when $z = 0$. The general equation for y_{max}, which occurs at $z = L/2$, then becomes:

$$y_{max} = \frac{vw^n L^{2n+2} t (12)^{n+2}}{10^{n+1} D} \tag{54}$$

where v is a function of n illustrated in Fig. 2. When $n = 1$, this reduces to the elastic case when EI is substituted for D/t:

$$y_{max} = \frac{0.99 wL^4 t (12)^3}{10^2 D} \qquad \text{for } n = 1 \tag{55}$$

The rationale of Equation (54) is more clearly seen by rewriting it in a form similar to elastic deflections:

$$y_{max} = \frac{K_1 t}{D}\left(\frac{wL^2}{10}\right)^n L^2 \tag{56}$$

In order to simplify Equation (54) or (56), it is desired to eliminate D in favor of terms more easily found and applied. Referring to the definition of D in Equation (51) and reducing, just as in the development of Equation (15) from Equation (14), the following close approximation is obtained:

$$D = \frac{d_m}{2B}\,[(d^2{}_m)^2 h] \tag{57}$$

B may be expressed in terms of permissible stress and value n by substituting in Equation (11). In keeping with design practices prevalent in a good part of the industry, the maximum permissible shearing stress τ_a is defined as the stress corresponding to a uniaxial tensile creep rate of 1 per cent in 10,000 hours. Since Equation (11) is expressed in terms of a tensile stress which is twice τ_a, the following may be written:

$$10^{-6} = B(2\tau_a)^n$$

or

$$B = \frac{1}{10^6(2\tau_a)^n} \tag{58}$$

The expression for D now becomes:

$$D = \frac{d_m[2\tau_a(d_m)^2 h]^n 10^6}{2} \tag{59}$$

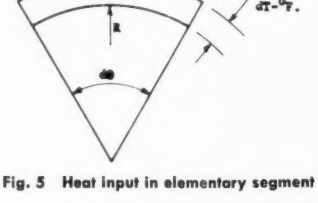

Fig. 5 Heat input in elementary segment

which may be substituted into Equation (40) to give:

$$y_{max} = \frac{2vw^n(L)^{2n+2}l(12)^{n+2}}{(10)^{n+7}(d_m)^{2n+1}(2\tau_o h)^n} \tag{20}$$

APPENDIX 3

General Effect of Heat Transfer Case of Low Pressure Stress

Fig. 5 represents an element of the tube wall at radius R and of unit length, subjected to heat flow radially inward. Let the heat density at the outside surface R_o be represented by Q, in Btu/hr/sq ft. Assuming radial flow only, a heat balance for the element may be obtained from:

$$\text{Heat into element} = QR_o d\theta \tag{60}$$

$$\text{Heat flowing through element} = \frac{CRd\theta dT}{dR} \tag{61}$$

Equating expressions (60) and (61) and solving for dT:

$$dT = \frac{QR_o}{C} \cdot \frac{dR}{R} \tag{62}$$

For relatively small changes in temperature, C may be considered constant. Equation (62) may then be integrated between R and R_o, corresponding to temperatures of T and T_o, respectively:

$$T_o - T = \frac{QR_o}{C} \log \frac{R_o}{R} \tag{63}$$

where the log term as used here and subsequently is to the base e.

For any given angle θ (see Fig. 3), an equation similar to Equation 12 may be written for the outside of the tube under weight stresses, as:

$$\frac{\dot{\epsilon}_o}{\dot{\epsilon}} = \frac{R_o}{R} \tag{64}$$

Substituting Equation (64) into (63) and solving for T:

$$T = \left(T_o - \frac{QR_o}{C} \log \dot{\epsilon}_o\right) + \frac{QR_o}{C} \log \dot{\epsilon} \tag{65}$$

This is seen to be a straight line relationship between temperature and log of creep rate with a slope of QR_o/C. It may be plotted, as shown in Fig. 6, on the same graph with curves for log σ'_s versus log $\dot{\epsilon}$.

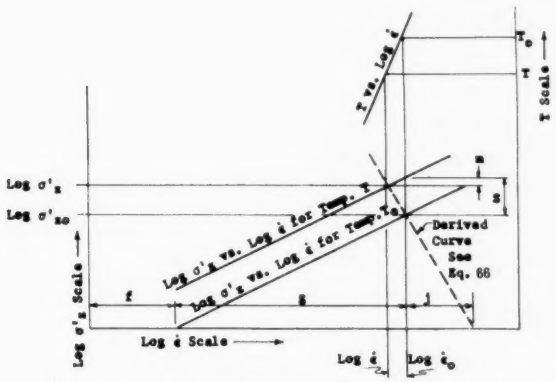

Fig. 6 Log σ'_s and T versus log $\dot{\epsilon}$

The dashed curve, found by intersections as shown, now represents the variation of stress with respect to creep rate for a given angle through the tube wall as the temperature changes due to heat flow. For practical purposes, considering creep data used in normal design use, this new curve may be assumed to be a straight line through the temperature variation. Lines for log σ'_s versus log $\dot{\epsilon}$ for temperature T and T_o may, likewise, be considered parallel.

The equation for the new dashed curve may be represented by the expression:

$$\log \sigma'_s = b'_w \log \dot{\epsilon} - b'_w \log B'$$

which may be rewritten:

$$\log \dot{\epsilon} = \log B' + n' \log \sigma'_s$$

or

$$\dot{\epsilon} = B'(\sigma'_s)^{n'} \tag{66}$$

where B' is the intercept on the log $\dot{\epsilon}$ axis, b'_w is the slope, and $n' = 1/b'_w$ = the change in log $\dot{\epsilon}$ with respect to log σ'_s. Study of the geometry of this curve permits us to write the following:

$$b'_w = \frac{1}{n'} = \frac{-(s-m)}{\log \dot{\epsilon}_o - \log \dot{\epsilon}} \tag{67}$$

$$b'_w = \frac{m}{\log \dot{\epsilon}_o - \log \dot{\epsilon}} - \frac{s}{\log \dot{\epsilon}_o - \log \dot{\epsilon}}$$

Let a = the average increase in stress interval between constant temperature lines of log σ'_s versus log $\dot{\epsilon}$ per decrease in temperature, or:

$$a = \frac{s}{T_o - T} \tag{68}$$

Substituting

$$b'_w = b - \frac{(T_o - T)}{\log \dot{\epsilon}_o - \log \dot{\epsilon}}$$

where $b = 1/n$ = slope of log σ'_s versus log $\dot{\epsilon}$ curves for constant temperature. Inserting the value of $T_o - T$ found from combining Equations (63) and (64):

$$b'_w = b - \frac{\frac{aQR_o}{C}(\log \dot{\epsilon}_o - \log \dot{\epsilon})}{(\log \dot{\epsilon}_o - \log \dot{\epsilon})}$$

or

$$b'_w = b - \frac{Qad_o}{2C} \tag{25}$$

Values of term a may be found and tabulated for different materials at various service temperatures, thus permitting solutions for b'_w.

APPENDIX 4

Creep Stress and Deflection With Heat Transfer Case of Low Pressure Stress

From Equations (64) and (66), the relationship between stresses through the wall for a given angle θ is:

$$\sigma'_s = \sigma'_{so}\left(\frac{R}{R_o}\right)^{1/n'} \tag{69}$$

or

$$\sigma'_s = \sigma'_{si}\left(\frac{R}{R_i}\right)^{1/n'} \tag{70}$$

where σ'_{so} and σ'_{si} are the stresses at the inner and outer walls, respectively, at angle θ. For different angles, but at the same

radius, the relationship no longer depends on n' but on n because of constant temperature. From Equation (47), substituting R_i for R and σ'_{z1} for σ'_{z1} we get:

$$\sigma'_{zi} = \sigma'_{z1}\left(\frac{R_i \sin\theta}{R_i}\right)^{1/n} \tag{71}$$

Therefore:

$$\sigma'_z = \sigma'_{z1}(\sin\theta)^{1/n}\left(\frac{R}{R_i}\right)^{1/n'} \tag{72}$$

instead of as given in Equation (47), which was for no heat transfer. Substituting Equation (72) into the basic moment Equation (45) gives:

$$M = \frac{\sigma'_{z1}}{(R_i)^{1/n'}}\int_{R_i}^{R_o}\int_0^{2\pi}(R)^{\frac{2n'+1}{n'}}(\sin\theta)^{\frac{n+1}{n}}\,d\theta\,dR \tag{73}$$

which yields, after solution similar to the development of Equation (13):

$$\sigma'_{z1} = \frac{3n'+1}{4n'}\cdot\frac{M(R_i)^{1/n'}}{(R_o)^{\frac{3n'+1}{n'}} - (R_i)^{\frac{3n'+1}{n'}}} \tag{26}$$

When the value of σ'_z found in Equation (72) is inserted in Equation (66), we get:

$$\dot\epsilon = B'(\sigma'_{z1})^{n'}(\sin\theta)^{n'/n}\left(\frac{R}{R_i}\right) \tag{74}$$

B' may be expressed in terms of the material constants for the outside or inside temperatures, B_o or B_i, by considering Fig. 6. Log B', being the intercept on the log $\dot\epsilon$ axis, equals the sum of f, g, and j, or:

$$\log B' = \log B_o + n\log\sigma'_{zo} + (-n')\log\sigma'_{zo}$$

or

$$B' = B_o(\sigma'_{zo})^{n-n'} \tag{75}$$

B' may similarly be expressed in terms of B_i as:

$$B' = B_i(\sigma'_{z1})^{n-n'} \tag{76}$$

Equation (74) now becomes:

$$\dot\epsilon = B_i(\sigma'_{z1})^{n-n'}\cdot(\sigma'_{z1})^{n'}\cdot(\sin\theta)^{n'/n}\left(\frac{R}{R_i}\right) \tag{77}$$

which is a form of the creep rate equation for any point considering inside fiber stresses and material constants. When upper or lower inside fibers are considered, $\theta = \pi/2$, $R = R_i$, σ'_{zi} becomes equal to σ'_{z1} and $\dot\epsilon$ is now $\dot\epsilon_1$. Equation (77) reduces to the simple expression:

$$\dot\epsilon_1 = B_i(\sigma'_{z1})^n \tag{78}$$

As in the development of the deflection equations for the case of no heat flow, the following set of equations may similarly be written:

$$\frac{d^2y}{dz^2} = \frac{B_i(\sigma'_{z1})^n\cdot t}{R_i} \tag{79}$$

$$\frac{d^2y}{dz^2} = B_i\left[\frac{3n'+1}{4n'}\cdot\frac{M(R_i)^{1/n'}}{(R_o)^{\frac{3n'+1}{n'}} - (R_i)^{\frac{3n'+1}{n'}}}\right]^n\frac{t}{R_i} \tag{80}$$

$$\frac{d^2y}{dz^2} = \frac{B_i t}{R_i}\left(\frac{M}{(d_i)^2 h}\right)^n \tag{81}$$

which is similarly solved for y_{max}:

$$y_{max} = \frac{2B_i v(w)^n(L)^{2n+2}t(12)^{n+2}}{(10)^{n+1}(d_i)^{2n+1}(h)^n} \tag{29}$$

APPENDIX 5

Creep Stress-Strain Rate Derivations Case of High Pressure Stress

Creep Stress. Equation (31) leads to

$$\frac{\dot\epsilon}{\dot\epsilon_1} = \frac{\sigma'_z}{\sigma'_{z1}}\left(\frac{\sigma_\theta - \sigma_r}{\sigma_{\theta 1} - \sigma_{r1}}\right)^{n-1} \tag{82}$$

From other pressure stress investigations [1, 7]

$$(\sigma_\theta - \sigma_r) = \frac{2bp\left(\frac{R_i}{R}\right)^{2/n}}{1 - \left(\frac{R_i}{R_o}\right)^{2/n}} \tag{83}$$

so that

$$\left(\frac{\sigma_\theta - \sigma_r}{\sigma_{\theta 1} - \sigma_{r1}}\right)^{n-1} = \left(\frac{R_1}{R}\right)^{\frac{2n-2}{2}} \tag{84}$$

Substituting Equation (12) and Equation (84) in Equation (82), gives

$$\sigma'_z = \sigma'_{z1}\sin\theta\left(\frac{R}{R_i}\right)^{\frac{3n-2}{n}} \tag{85}$$

The differential equation for bending moment now becomes

$$M = \frac{\sigma'_{z1}}{(R_i)^{\frac{3n-2}{n}}}\int_{R_i}^{R_o}\int_0^{2\pi}(R)^{\frac{5n-2}{n}}\sin^2\theta\,d\theta\,dR \tag{86}$$

Integrating Equation (86) yields

$$\sigma'_{z1} = \frac{6n-2}{\pi n}\cdot\frac{M(R_i)^{\frac{3n-2}{n}}}{(R_o)^{\frac{6n-2}{n}} - (R_i)^{\frac{6n-2}{n}}} \tag{33}$$

Deflection Under Creep Conditions. Combining Equation (35) with elementary beam expressions (18) and (19), we obtain

$$\frac{d^2y}{dz^2} = \frac{B\sigma'_{z1}(\sigma_{\theta 1} - \sigma_{r1})^{n-1}t}{R_i} \tag{87}$$

$$\frac{d^2y}{dz^2} = \frac{Mt(\sigma_{\theta 1} - \sigma_{r1})^{n-1}}{D} \tag{88}$$

where

$$D = \frac{1}{B}\cdot\frac{\pi n}{6n-2}\cdot\frac{(R_o)^{\frac{6n-2}{n}} - (R_i)^{\frac{6n-2}{n}}}{(R_i)^{\frac{2n-2}{n}}} \tag{89}$$

When Equation (52) is substituted for M, integration of Equation (88) gives an expression similar to Equation (55). The value of B given by Expression (58) may then be inserted, giving an equation for maximum deflection

$$y_{max} = \frac{0.99wL^4t(12)^3(\sigma_{\theta 1} - \sigma_{r1})^{n-1}}{10^8(2\tau_a)^n}\cdot\frac{6n-2}{\pi n}\cdot\frac{(R_i)^{\frac{2n-2}{n}}}{(R_o)^{\frac{6n-2}{n}} - (R_i)^{\frac{6n-2}{n}}} \tag{36}$$

Heat-Transfer Effects. For this condition (high pressure stress), a log-log plot of Equation (31) is similar to Fig. 6 except that the

slope is equal to unity, with the intercept being dependent on pressure stresses as well as material constant, B. The dashed line, again, represents the creep stress-strain rate relationship for any angle θ through the wall as affected not only by temperature but pressure stress changes as well. By a process similar to the development of Equation (25), the slope, b'_w may be shown to be

$$b'_w = 1 - \frac{Qa'd_o}{2C} \tag{90}$$

where a' corresponds to stress interval factor, a, as defined in Equation (68), or

$$a' = -\frac{d(\log \sigma'_z)}{dT} \tag{91}$$

$$a' = \frac{\log B_o - \log B}{T_o - T} + \frac{(n-1)d(\log \sigma_\theta - \sigma_r)}{dT} \tag{92}$$

Using Fig. 6 and Equation (62), this becomes

$$a' = \frac{a}{b} + \frac{CR(n-1)}{QR_o}\frac{d[\log(\sigma_\theta - \sigma_r)]}{dR}$$

Differentiating Equation (83) and substituting we get

$$a' = \frac{a}{b} - \frac{C(n-1)}{QR_o}\frac{2}{n} \tag{93}$$

Equation (90) then becomes

$$b'_w = \frac{1}{n'} = 3 - 2b - \frac{Qad_o}{2Cb} \tag{39}$$

The relationship between stresses through the wall for a given angle θ is given by Equation (70). For different angles, but at the same radius, from Equations (12) and (81), the relationship is

$$\sigma'_{z\theta} = \sigma'_{z1}\sin\theta \tag{94}$$

Combining Equations (94) and (70) gives

$$\sigma'_z = \sigma'_{z1}\sin\theta\left(\frac{R}{R_i}\right)^{1/n'} \tag{95}$$

Substituting Equation (95) into basic moment Equation (45) gives

$$M = \frac{\sigma'_{z1}}{(R_i)^{1/n'}}\int_{R_i}^{R_o}\int_0^{2\pi}(R)^{\frac{2n'+1}{n'}}\sin^2\theta\, d\theta dR \tag{96}$$

which yields, after integration

$$\sigma'_{z1} = \frac{3n'+1}{\pi n'}\cdot\frac{M(R_i)^{1/n'}}{(R_o)^{\frac{3n'+1}{n'}} - (R_i)^{\frac{3n'+1}{n'}}} \tag{40}$$

When this equation is substituted in Equation (87) and the resultant expression integrated and simplified, using $n' = -0.25$, we get

$$y_{\max} = \frac{0.99wL^4(12)^3 \times 8B_i}{10^2\pi d_i^3 h}\cdot\frac{d_o}{d_i}\cdot(\sigma_{\theta 1} - \sigma_{r1})^{n-1} \tag{43}$$

KURT HAIN
GERHARD MARX

Research Scientists, Institut für Landtechnische Grundlagenforschung der Forschungsanstalt für Landwirtschaft, Braunschweig, Germany

How to Replace Gears by Mechanisms (Linkages)

A practical method is shown for designing four-bar mechanisms having a prescribed transmission ratio held within prescribed tolerances, for a limited range of motion. Such mechanisms may economically replace gears in many applications. Charts enable the designer to choose the mechanism having the best transmission angle possible.

Preface

IN MOST ENGINEERING BRANCHES oscillating transmissions with uniform ratio of transmission are demanded. Gears and cams can be used for this problem and are able to fulfill the exact uniform ratio. Mechanisms have a varying ratio of input angular velocity ω_a to output angular velocity ω_c, but they can be manufactured much cheaper and easier. Therefore, if small deviations from the constant transmission are admissible, mechanisms should be used.

In special cases exact transmissions are available [1, 2, 3],[1] for instance when $i = \frac{\omega_a}{\omega_c} = 1$ or $i = \frac{\omega_a}{\omega_c} = 2$ or 0.5, that is when a parallel-crank linkage or a slider crank is considered. The latter should have a crank which is equal to the base. Other linkages, especially the four-bar linkage, have a varying ratio of transmission, and, in the sense mentioned, it has to be ordered that the ratio of transmission be as constant as possible. Thus the best linkage will be the one which has the smallest deviations from constant transmission. Papers [4, 5, 6] have been published referring to the mechanism synthesis. By this four-bar linkages can be designed when certain positions of input and output link are prescribed. Hall [7] used the curvature of the instant center, referring to input and output link, and replaced gears by four-bar linkages.

The method shown in this paper treats four-bar linkages for oscillating motions and approximately constant transmission. The deviations from this constant amount are prescribed within certain tolerances. It is possible to graph diagrams by which the deviations and the quality of transmission can be obtained. The coefficients of these diagrams make possible the simple design of the corresponding linkage.

Definitions

The ratio of transmission i is the quotient of the angular velocity ω_a of input link to the angular velocity ω_c of output link

$$i = \frac{\omega_a}{\omega_c} \tag{1}$$

Ratio i is changing when the linkage is moved. Fig. 1 shows a four-bar linkage having a as input link and c as output link. The instant center Q referring to a and c is determined by the intersection point of coupler b and base d. The distance of Q from the bearings A_0 and B_0 can be used to determine the ratio of transmission

$$i = \frac{q_b}{q_a} = \frac{\omega_a}{\omega_c} \tag{2}$$

The extreme values of i can be determined by the method of Freudenstein [8, 9], by which the angle λ, formed by the coupler b and the collineation axis PQ, should be $\lambda = 90$ deg.

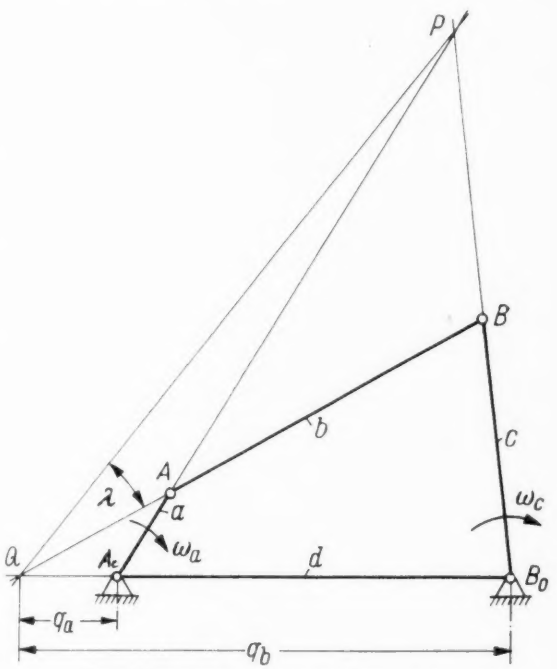

Fig. 1 The definition of the ratio of transmission i

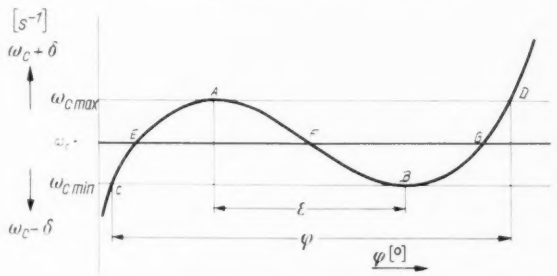

Fig. 2 Deviation δ within the limits of the angular velocity of output link

[1] Numbers in brackets designate References at end of paper.

Contributed by the Machine Design Division and presented at the Semi-Annual Meeting, Detroit, Mich., June 15–19, 1958, of THE AMERICAN SOCIETY OF MECHANICAL ENGINEERS.

NOTE: Statements and opinions advanced in papers are to be understood as individual expressions of their authors and not those of the Society. Manuscript received at ASME Headquarters, March 24, 1958. Paper No. 58—SA-33.

In the following the best four-bar linkages have been determined in accordance with Fig. 2. The angular velocity ω_a of the input link is constant and the angular velocity ω_c of the output link c should have the prescribed extreme values $\omega_{c\,max}$ and $\omega_{c\,min}$, represented by the diagram points A and B. From the maximum position $\omega_{c\,max}$ to the minimum position $\omega_{c\,min}$ the crank a runs through the angle ϵ. But both $\omega_{c\,max}$ and $\omega_{c\,min}$ exist once more in the diagram points C and D, by which the crank angle φ is represented. Thus all the motion of the linkage is limited through the angle φ between $\omega_{c\,max}$ and $\omega_{c\,min}$. It is important that the exact value ω_c is realized three times at the points E, F, and G. The linkage having a transmission in accordance with Fig. 2, seems to be the best one for a constant ratio of transmission.

Calculations

The deviation δ should be related to the angular velocity ω_c of the output link c, when the angular velocity ω_a of the input link a is constant. According to Fig. 1 the instant center Q is determined by its distance q_a from A_0 or q_b from B_0. If $\omega_{c\,max}$ and $\omega_{c\,min}$ are given the distances $q_{a\,max}$ and $q_{a\,min}$ can be found

$$q_{a\,max} = \frac{\omega_{c\,max} \cdot d}{\omega_a - \omega_{c\,max}} \tag{3}$$

$$q_{a\,min} = \frac{\omega_{c\,min} \cdot d}{\omega_a - \omega_{c\,min}} \tag{4}$$

Assuming the deviation

$$\delta = \frac{\omega_{c\,max} - \omega_c}{\omega_c} \tag{5}$$

or

$$\delta = \frac{\omega_c - \omega_{c\,min}}{\omega_c} \tag{6}$$

and using the ratio of transmission $i = \frac{\omega_a}{\omega_c}$, it can be found

$$i_{max} = \frac{i}{1 + \delta} \tag{7}$$

$$i_{min} = \frac{i}{1 - \delta} \tag{8}$$

In order to design a four-bar linkage for given positions of the instant center Q the distances $q_{a\,max}$ and $q_{a\,min}$ are used. It is suitable to have these values related to the base d. By this the design of the four-bar linkage becomes independent of the scale to which the drawing is made

$$\frac{q_{a\,max}}{d} = \frac{1}{\frac{i}{1 + \delta} - 1} \tag{9}$$

$$\frac{q_{a\,min}}{d} = \frac{1}{\frac{i}{1 - \delta} - 1} \tag{10}$$

Fig. 1 shows a position of the linkage in which the ratio of transmission is greater than 1. If it is smaller than 1 the instant center Q is situated on the other side of the base d next B_0. The distance q_a is greater than q_b. It follows

$$q_{a\,max} = \frac{\omega_{c\,max} \cdot d}{\omega_{c\,max} - \omega_a} \tag{11}$$

$$q_{a\,min} = \frac{\omega_{c\,min} \cdot d}{\omega_{c\,min} - \omega_a} \tag{12}$$

and

$$\frac{q_{a\,max}}{d} = \frac{1}{1 - \frac{i}{1 + \delta}} \tag{13}$$

$$\frac{q_{a\,min}}{d} = \frac{1}{1 - \frac{i}{1 - \delta}} \tag{14}$$

When input link a and output link c move in a different direction the ratio of transmission i may have the negative sign. Then the instant center Q is situated between A_0 and B_0. The equations are as follows

$$q_{a\,max} = \frac{\omega_{c\,max} \cdot d}{\omega_a + \omega_{c\,max}} \tag{15}$$

$$q_{a\,min} = \frac{\omega_{c\,min} \cdot d}{\omega_a + \omega_{c\,min}} \tag{16}$$

$$\frac{q_{a\,max}}{d} = \frac{1}{\frac{i}{1 + \delta} + 1} \tag{17}$$

$$\frac{q_{a\,min}}{d} = \frac{1}{\frac{i}{1 - \delta} + 1} \tag{18}$$

Mechanism Design

After calculating the distances $q_{a\,max}$ and $q_{a\,min}$ with regard to the equations already mentioned, the points Q_1 and Q_2 are drawn, Fig. 3. After this any angle φ' is plotted to A_0Q_1 and a crank length A_0A is chosen as follows: The crank A_0A has to be smaller than A_0Q_2, when i is prescribed greater than 2, or between 0.5 and 1, or i is negative. The crank A_0A has to be greater than A_0Q_1 when i is prescribed greater than 1 to 2, or greater than 0 to 0.5. In all cases Q_1 represents $q_{a\,min}$, and Q_2 represents $q_{a\,max}$. The design has to be started using Q_1 or Q_2. Having A_0A smaller than A_0Q_2 the instant center Q_1 should be used and A_0A greater than A_0Q_1 the instant center Q_2 should be used.

According to Fig. 3, point A is connected to Q_1. The perpendicular in Q_1 intersects A_0A in the second instant center P. Join B_0 with P and find B as intersection point of this line with AQ_1. Now the dimensions of the corresponding four-bar linkage are given. After this the other extreme position of this linkage should be drawn by trial in such a manner that the collineation axis $P'Q'$ is perpendicular to $A'B'$. Generally point Q' does not coincide with Q_2. Therefore another A_0A has to be chosen until this coincidence is fulfilled. This is true in Fig. 4. The crank positions A_0A and A_0A' of the extreme positions of the linkage include the angle ϵ according to Fig. 2. Now the linkage should be moved beyond these extreme positions until the instant centers Q_1 and Q_2 are intersection points of A_1B_1 with A_0B_0 and of A_2B_2 with A_0B_0. By the crank positions A_0A_1 and A_0A_2 the greatest angle φ is given (see Fig. 2).

The quality of transmission is represented by the so-called angle of transmission μ [10], which is the angle between output link B_0B and the connecting rod AB.[2] In order to be able to compare different linkages the smallest angle μ_{min} should be taken. The value of μ_{min} is dependent on the initial angle φ'; the greater φ' the smaller becomes μ_{min} and φ increases. But there is a best angle μ_{min} depending on φ'. This can be seen in the following diagrams.

[2] Best transmission is obtained when $\mu = 90$. The difference from 90 deg marks the quality of transmission. For instance the angle $\mu = 70$ deg has the same significance as $\mu = 110$ deg. Any transmission becomes impossible when $\mu = 0$ deg or $\mu = 180$.

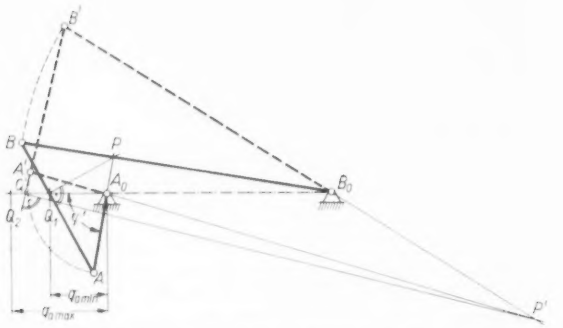

Fig. 3 Four-bar linkage having two extreme positions when any A_0A and φ' are given

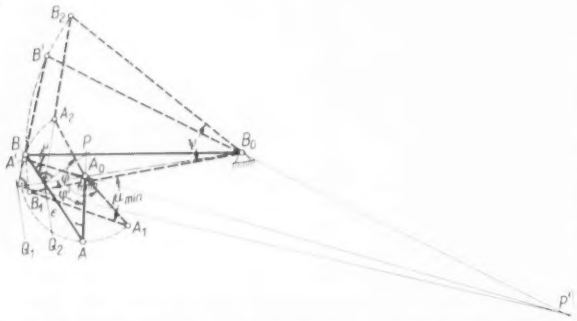

Fig. 4 Four-bar linkage having two extreme positions when instant centers Q_1 and Q_2 are prescribed

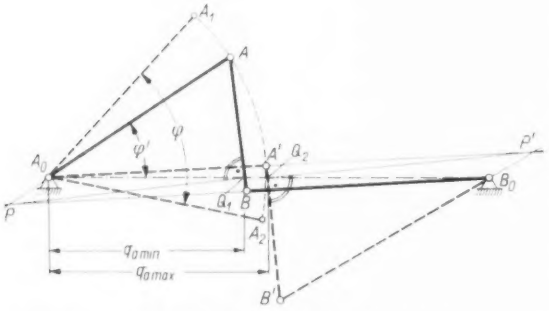

Fig. 5 Four-bar linkage like Fig. 4, when negative ratio of transmission i is prescribed

Fig. 5 shows a four-bar linkage having an opposite turning of the output link to the input link. The design is similar to that of Fig. 4. As just mentioned, the instant centers Q_1 and Q_2 are situated between A_0 and B_0.

In Fig. 6 the ratio of transmission i is greater than 0 and smaller than 0.5. The design has to be started at point Q_2. For the rest the same manipulations should be made as in Figs. 3 and 4.

The deviation δ must always be smaller than 100 per cent, otherwise the sign would change from positive to negative and vice versa. If $\delta = 100$ per cent the extreme value $i_{min} = 0$ and the instant center Q_1 coincides with A_0. In this position of the mechanism a dead-center position would appear. If $i = 1$ the instant center is infinitely situated and the deviation δ becomes 0, i.e., the parallel-crank linkage should be used and has an exact constant transmission.

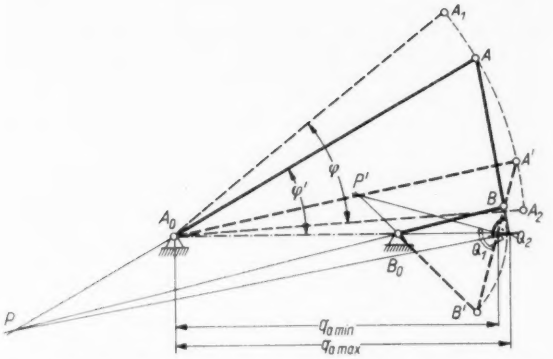

Fig. 6 Four-bar linkage like Fig. 4, when ratio of transmission i is smaller than 1

All mechanisms according to the diagram Fig. 2 do not fulfill the Grashof rule, i.e., there are no full rotating motions.

The Use of Diagrams

The diagrams, Figs. 7 and 11, allow a survey of the favorable four-bar linkages with regard to the deviation δ and the angle of transmission μ_{min}. These coefficients are dependent on the crank angle φ. The motion of the mechanism is similar to that of Fig. 2. Fig. 7 has value for the same direction of the movement of input and output link and for $i = +4$, Fig. 11 relates to the opposite direction of input and output link for $i = -4$.

Assuming the range of motion is given and is represented by the crank angle φ the most suitable linkage can be chosen with regard to δ and μ_{min}. For instance, if $\varphi = 150$ deg (Fig. 7) and $i = +4$ are prescribed and a certain deviation δ is admissible, that linkage with the best μ_{min} can be determined. If $\delta = \pm 10$ per cent is admissible, a best $\mu_{min} = 41$ deg is available.

The extreme value μ_{min} appears in an end position of the mechanism like Fig. 4, when the right-hand parts of the diagrams, Figs. 7 and 11, are used. Using the left-hand parts of these diagrams the angle μ_{min} appears in a similar position as the mechanism in Fig. 8, i.e. when the crank position A_0A_1 covers with the base A_0B_0. The maximum points of the diagrams represent a linkage in which the minimum value μ_{min} appears twice, namely in the "covering" and in an end position of the mechanism.

Generally it has to be mentioned that dimensions of the linkages become larger when δ approaches smaller values. The diagrams also show curves having $\delta \sim 0$, that means the accuracy is limited by drawing methods and the curve, corresponding to Fig. 2, becomes an approximately straight line. In Fig. 9 two linkages represented by the intersection point of two curves $\delta = \pm 10$ per cent and ± 20 per cent (Fig. 7) have been drawn. Having the same angle φ and the same quality of transmission μ_{min} the lengths AB and B_0B of the 20 per cent linkage are smaller than the lengths $A'B'$ and B_0B' of the 10 per cent linkage.

In most cases only the right-hand parts of the curves should be used, because the left-hand parts are less satisfactory.

With regard to angle φ', which is most important for mechanism design, it should be mentioned that it can be taken up to 180 deg. For this value μ_{min} becomes zero and AB and B_0B become infinitely long. If $\varphi' = 0$ the angle of transmission becomes zero too, AB becomes zero, A_0A will be equal to A_0Q_1 and $B_0B = B_0Q_1$.

Figs. 10 and 12 show the coefficients which are necessary for designing the linkages in accordance with Figs. 7 and 11.

Example. The best four-bar linkage for a constant transmission $i = +4$ is to be designed, when the crank angle $\varphi = 100$ deg and the deviation $\delta = \pm 5$ per cent are demanded.

Fig. 7 shows the angle of transmission $\mu_{min} = 60$ deg, which is very advantageous. Taking $i = +4$ and $\delta = 0.05$ it yields

$$\frac{a_{max}}{d} = \frac{1}{\frac{4}{1 + 0.05} - 1} = \frac{1}{3.81 - 1} = 0.356$$

$$\frac{a_{min}}{d} = \frac{1}{\frac{4}{1 - 0.05} - 1} = \frac{1}{4.21 - 1} = 0.312$$

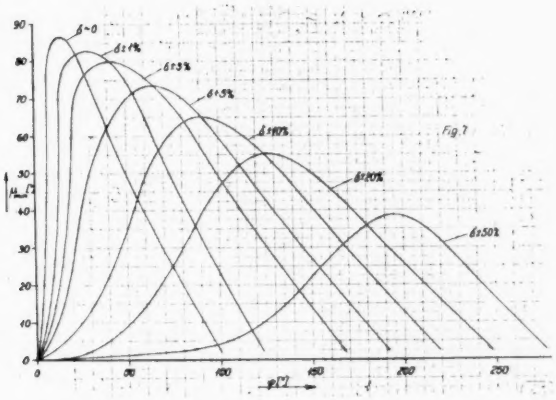

Fig. 7 Diagrams for the best four-bar linkages. $i = +4$.

Now the positions of Q_1 and Q_2 are given (see Fig. 4). From Fig. 10 the values $\varphi' = 40$ deg and $a/d = 0.3495$ are available. If any base d is prescribed the true value $a = A_0A$ can be calculated. Now the design is possible in accordance with Fig. 4. The similar method has value for negative ratios of transmission (see Figs. 11 and 12).

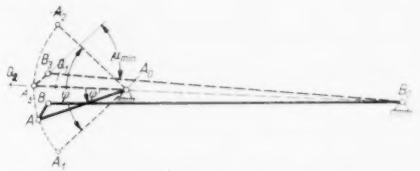

Fig. 8 Extreme value of μ_{min} in "covering" position

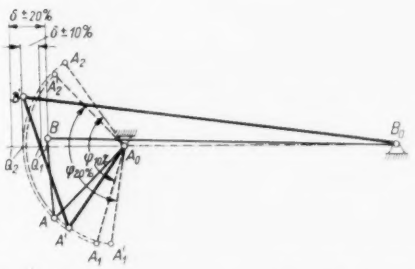

Fig. 9 The four-bar linkages representing an intersection point of Fig. 7

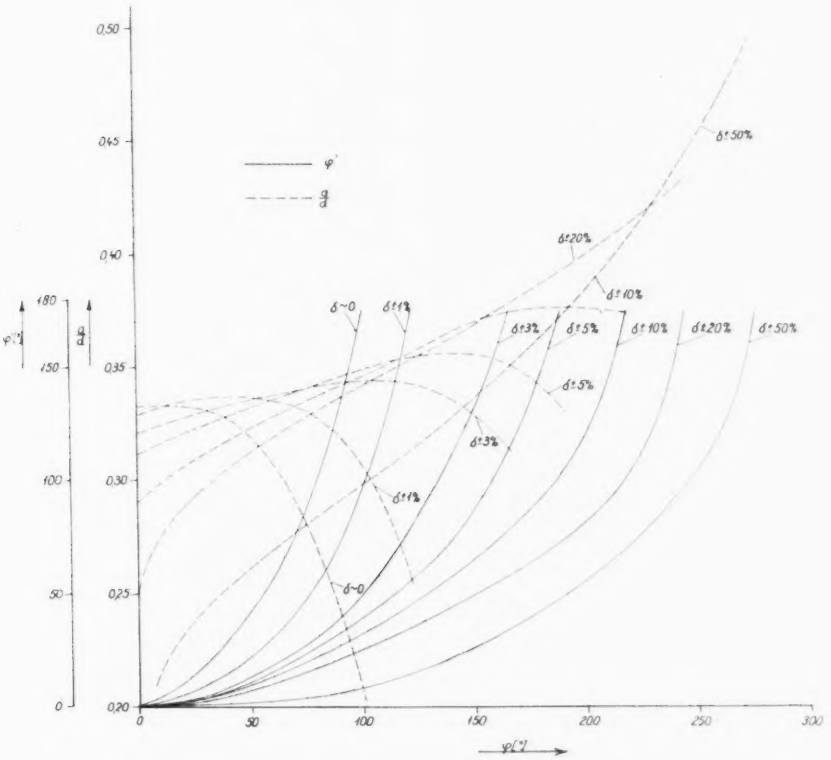

Fig. 10 Coefficients for mechanism design according to Fig. 7

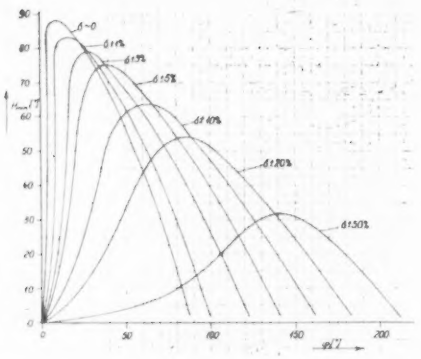

Fig. 11 Diagrams for the best four-bar linkages. $i = -4$.

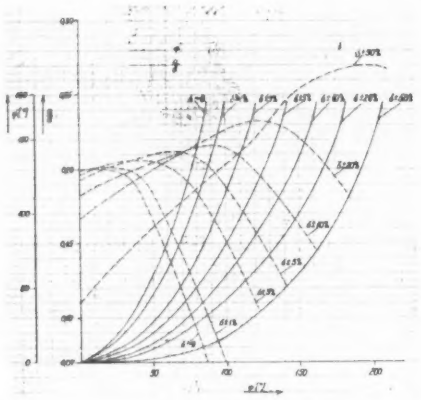

Fig. 12 Coefficients for mechanism design according to Fig. 11

Summary

In general mechanisms are essentially cheaper than gears. Therefore gears should be replaced by mechanisms where the accuracy is sufficient and the range of motion is large enough. The diagrams shown in this paper give an adequate survey of the possibilities of mechanisms. It should be mentioned that mechanisms are able to transmit greater forces. If mechanisms are arranged in series the usable angles φ increase taking the same values μ_{min} and δ.

Diagrams for other ratios of transmission are intended. Having all the important diagrams the designer has excellent means for his work. He will save much time and he will be sure that he has the best mechanism for his purpose.

The diagrams have been determined by graphical methods only, which seem precise enough. The accuracy represented by δ can seldom be expressed mathematically. Moreover it is not necessary that the angle μ_{min} be very exact, since it is only used to make comparisons.

References

1 F. G. Altmann, "Koppelgetriebe für gleichförmige Übersetzung," *Zeitschrift des Vereines Deutscher Ingenieure*, vol. 92, 1950, pp. 909–916.

2 R. Beyer, "Kinematische Getriebesynthese," Julius Springer Verlag, Berlin, Germany, 1953.

3 K. Rauh, "Praktische Getriebelehre," vol. 1, Julius Springer Verlag, Berlin-Göttingen-Heidelberg, Germany, 1951.

4 K. Hain, "Angewandte Getriebelehre," Hermann Schroedel Verlag, Hannover-Darmstadt, Germany, 1952.

5 K. Hain, "Periodische Winkelgeschwindigkeits- und Drehmomentenwandler," *Zeitschrift des Vereines Deutscher Ingenieure*, vol. 93, 1951, pp. 239–244.

6 K. Hain, "Volle Ausnützung des Gelenkvierecks als Funktionsgetriebe," *Reglungstechnik*, 1956, pp. 40–45.

7 A. S. Hall and A. C. Dunk, "Designing Four-Bar Linkages to Substitute for Gears," *Machine Design*, vol. 25, 1953, pp. 233–236.

8 F. Freudenstein, "On the Maximum and Minimum Velocities and Acceleration in Four-Link Mechanisms," TRANS. ASME, vol. 78, 1956, pp. 779–787.

9 W. Meyer zur Capellen, "Die Extrema der Geschwindigkeiten an Kurbeltrieben," *Ingenieur-Archiv*, vol. 25, 1957, pp. 140–154.

10 H. Alt, "Der Übertragungswinkel und seine Bedeutung für das Konstruieren periodischer Getriebe," *Werkstattstechnik*, vol. 26, 1932, pp. 61–64.

DISCUSSION

A. E. Richard de Jonge[3]

To replace gears and cams by linkages has been an old dream of kinematicians the world over. Unfortunately, it cannot be done accurately, thus it still remains a dream. The question then is, under which circumstances can it be done approximately and how good is the approximation?

The authors have given a practical answer to this question, namely, where large forces are concerned and where the total angle of oscillation is relatively small, that is, smaller than 180 deg. The greater the angle, the greater is the deviation from the derived true transmission ratio which has to be achieved. The angle of transmission μ (or its complement), which was introduced in cam applications over half a century ago by Hartmann of Germany, was later used for cam design by Furman in the United States, was revived and applied more generally by H. Alt of Germany, also must not decrease below a certain value. As far as making use of this angle is concerned, the diagrams presented by the authors should prove valuable.

The equations and constructions are correct, but the latter suffer from the fact that a trial-and-error process is involved in arriving at the limits.

The writer agrees with the authors in that, when large forces are concerned and one has to choose between gears or a linkage, it is often advantageous to choose a linkage rather than gears, for large gears also would have to be designed specially. However, where any degree of accuracy and not too large forces are involved, the logical choice would be either gears or band drives which, in such cases, are far cheaper than specially designed and manufactured linkages, because gears for none too large forces may now be obtained from stock for a few dollars to various degrees of accuracies, and bands can be applied so as to eliminate any backlash.

It must be left to the good judgment of the designer to choose the best of these devices for any particular case of application. It would be quite imprudent, however, to advise, for example, in precision devices, indiscriminate use of linkages which, in addition to their inherent inaccuracy, also have a certain amount of backlash even when ball or roller bearings are used.

How far the deviation in such linkages from the true mathematical relationship extends has been investigated carefully by F. Freudenstein, who has reported on his results in a companion paper.

[3] The Reeves Instrument Corporation; Adjunct Professor, The Polytechnic Institute of Brooklyn; Lecturer, The City College of New York, New York, N. Y. Mem. ASME.

NORMAN ZLATIN

Vice-President, Metcut Research Associates, Inc., Cincinnati, Ohio. Mem. ASME

JOHN V. GOULD

Project Engineer, Metcut Research Associates, Inc. Assoc. Mem. ASME

The Effect of a Lead Additive on the Machinability of Alloy Steels

Introduction

For many years free-machining additives such as sulfur, selenium, or lead have been used in low-carbon steels to improve tool life and surface finish. During the past ten years free-machining additives have also been used in the medium-carbon alloy steels. However, the principal use of these free-machining grades of alloy steels has been at hardness levels under 300 Bhn. With the trend toward higher strength steels (400 Bhn and higher), the machining problems have become more difficult. Considerable thought has been given to the use of a lead additive as a means of alleviating the machining problems at the higher hardnesses.

The data presented in this paper are the results of turning tests, using carbide tools, on two medium-carbon steels at several different hardness levels. These data demonstrate at what hardness levels the lead additives are most effective.

Definition of Machinability

An improvement in the machinability of a metal usually infers that:

(*a*) Tool life has been extended, and/or (*b*) coefficient of friction between the sliding chip and tool has been reduced, thereby resulting in an improvement in surface finish, and/or (*c*) tool forces and power consumption have been reduced.

In most machining operations tool life is the most important factor; however, in some cases surface finish may be the factor which determines whether or not the machinability of the metal is satisfactory.

Test Procedure

Test Bars. The alloy steels under test in this program were: (1) AISI 4147H plain and leaded, and (2) AISI 4340H plain and leaded. Both the leaded and plain steels of each grade were from the same heat. All of the steel was in the form of forged bars 4 in. diam × 36 in. long.

The steels were machined in each of the following heat-treated conditions:

AISI 4147H	Normalized R_c 22
AISI 4147H	Quenched and tempered R_c 26
AISI 4147H	Quenched and tempered R_c 31
AISI 4147H	Quenched and tempered R_c 40
AISI 4340H	Normalized R_c 34.5
AISI 4340H	Quenched and tempered R_c 26
AISI 4340H	Quenched and tempered R_c 33
AISI 4340H	Quenched and tempered R_c 41

Contributed by the Production Engineering Division and presented at the Semi-Annual Meeting, Detroit, Mich., June 15–19, 1958, of The American Society of Mechanical Engineers.

Note: Statements and opinions advanced in papers are to be understood as individual expressions of their authors and not those of the Society. Manuscript received at ASME Headquarters, March 13, 1958. Paper No. 58—SA-53.

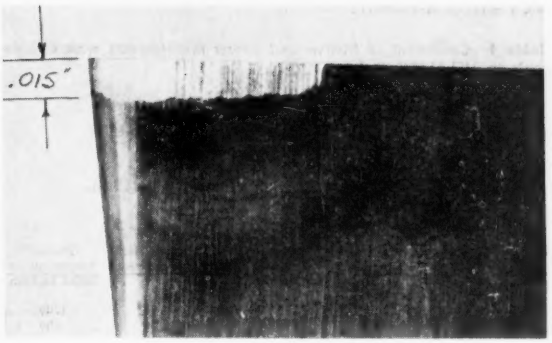

Fig. 1 Example of flank wear on carbide tool

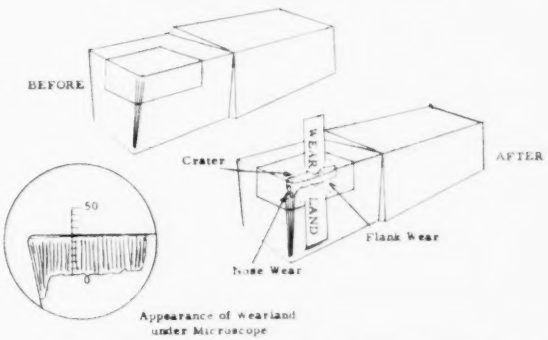

Fig. 2 Wear land measurement in tool-life testing: Test stopped at 0.015 in. wear land on carbide tool

Cutting Tools. A general purpose grade of carbide was used for tool life tests. The tool angles were as follows:

Back rake: 0 deg	Side rake: 6 deg
Side-cutting edge angle: 6 deg	End-cutting edge angle: 6 deg
Relief: 6 deg	Nose radius: 0.040 in.

Tool-Life End Point. A wear land of 0.015 in. or tool failure (whichever occurred first) constituted the test end point. Examples of the wear land formed on a carbide tool are shown in Figs. 1 and 2.

Coefficient of Friction and Power Requirements

The addition of lead to the low-carbon steels results in a low coefficient of friction, thereby improving the surface finish and prolonging tool life. However, very few data are available for leaded steels in the hardened condition.

The coefficient of friction between the sliding chip and the tool can be calculated from force measurements made with a tool dynamometer. If a turning tool having a zero side-cutting edge

angle (lead angle) and zero back rake is used, the coefficient of friction can be computed from the equation developed by Merchant.[1]

$$\text{Coefficient of friction} = \frac{F_t + F_c \tan a}{F_c - F_t \tan a}$$

where

F_t = thrust force, lb
F_c = cutting force, lb
a = rake angle of the tool

Tables 1 and 2 show the results obtained from machining tests when using a tool dynamometer. These data show that the addition of lead in steel will produce a marked reduction in coefficient of friction, even in the harder steels (R_c 40 and R_c 41). Three feeds, 0.005, 0.009, and 0.019 in. per revolution, were used in the turning tests on the AISI 4147H steel and, in every case, the coefficient of friction was lower for the leaded steel. Note also that a substantial reduction in power requirements was obtained by the addition of lead in the steel.

[1] M. Eugene Merchant, "Basic Mechanics of the Metal Cutting Process," *Journal of Applied Mechanics*, vol. 12, TRANS. ASME, vol. 66, 1944, pp. A-168–175.

Table 1 Coefficient of friction and power requirements with carbide tools on AISI 4147H steel

Material: AISI 4147H (plain and leaded)
Tool: Carbide grade 78B
Back rake: 0 deg; side rake: 6 deg
Side cutting-edge angle: 0 deg
End cutting-edge angle: 6 deg
Relief: 6 deg; nose radius: 0.040 in.
Depth of cut: 0.100 in.
Cutting fluid: None

Plain & Leaded	Heat Treatment	Cutting Speed ft./min.	Feed in./rev.	Coefficient of Friction	Power Requirements HP/cu. in./min.
Plain	Normalized R_c 22	150-250	.005	.98	1.00
Plain	Normalized R_c 22	150-250	.009	.88	.88
Plain	Normalized R_c 22	150-250	.019	.72	.78
Leaded	Normalized R_c 22	150-250	.005	.72	.91
Leaded	Normalized R_c 22	150-250	.009	.84	.85
Leaded	Normalized R_c 22	150-250	.019	.64	.72
Plain	Quenched & Tempered R_c 26	125-200	.005	1.02	1.08
Plain	Quenched & Tempered R_c 26	125-200	.009	.95	.95
Plain	Quenched & Tempered R_c 26	125-200	.019	.79	.78
Leaded	Quenched & Tempered R_c 26	125-200	.005	.81	.87
Leaded	Quenched & Tempered R_c 26	125-200	.009	.80	.76
Leaded	Quenched & Tempered R_c 26	125-200	.019	.68	.63
Plain	Quenched & Tempered R_c 31	125-200	.005	1.00	1.12
Plain	Quenched & Tempered R_c 31	125-200	.009	.95	.93
Plain	Quenched & Tempered R_c 31	125-200	.019	.80	.76
Leaded	Quenched & Tempered R_c 31	125-200	.005	.75	.83
Leaded	Quenched & Tempered R_c 31	125-200	.009	.72	.79
Leaded	Quenched & Tempered R_c 31	125-200	.019	.63	.69
Plain	Quenched & Tempered R_c 40	50-75	.005	.97	1.18
Plain	Quenched & Tempered R_c 40	50-75	.009	.85	1.01
Plain	Quenched & Tempered R_c 40	50-75	.019	.75	.86
Leaded	Quenched & Tempered R_c 40	50-75	.005	.67	.96
Leaded	Quenched & Tempered R_c 40	50-75	.009	.65	.84
Leaded	Quenched & Tempered R_c 40	50-75	.019	.61	.75

Table 2 Coefficient of friction and power requirements with carbide tools on AISI 4340H steel

Material: AISI 4340H (plain and leaded)
Tool: Carbide grade 78B
Back rake: 0 deg; side rake: 6 deg
Side cutting-edge angle: 0 deg
End cutting-edge angle: 6 deg
Relief: 6 deg; nose radius: 0.040 in.
Speed: 75 to 125 fpm
Feed: 0.009 in. per rev
Depth of cut: 0.100 in.
Cutting fluid: None

Plain & Leaded	Heat Treatment	Coefficient of Friction	Power Requirements HP/cu. in./min.
Plain	Normalized R_c 34.5	.80	1.20
Leaded	Normalized R_c 34.5	.58	.90
Plain	Quenched & Tempered R_c 26	.78	1.10
Leaded	Quenched & Tempered R_c 26	.57	.82
Plain	Quenched & Tempered R_c 33	.79	1.06
Leaded	Quenched & Tempered R_c 33	.63	.80
Plain	Quenched & Tempered R_c 41	.85	1.04
Leaded	Quenched & Tempered R_c 41	.58	.86

Surface Finish

One of the difficulties encountered in comparing surface finishes is the resulting feed lines on the machined surface. These feed lines tend to mask out differences in surface finish. In order to overcome this difficulty, the surface finish was measured on the shoulder of the workpiece. The rotational speed of the workpiece was low enough so that the feed could be disengaged and the tool moved away fast enough to prevent the tool from passing over the surface while the feed was disengaged. The surface-finish measurements thus obtained are listed in Tables 3 and 4. In every case there was a definite improvement in the quality of surface finish on the leaded grade.

Table 3 Surface finishes obtained on AISI 4147H steel with carbide tools

Material: AISI 4147H (plain and leaded)
Tool: Carbide grade 78B
Back rake: 0 deg; side rake: 6 deg
Side cutting-edge angle: 0 deg
End cutting-edge angle: 6 deg
Relief: 6 deg; nose radius: 0.040 in.

Plain or Leaded	Heat Treatment	Feed in./rev.	Cutting Speed ft./min.	Surface Finish micro-inches
Plain	Normalized R_c 22	.005	150	100
Leaded	Normalized R_c 22	.005	150	60
Plain	Normalized R_c 22	.009	150	120
Leaded	Normalized R_c 22	.009	150	90
Plain	Quenched & Tempered R_c 26	.005	125	90
Leaded	Quenched & Tempered R_c 26	.005	125	65
Plain	Quenched & Tempered R_c 26	.009	125	100
Leaded	Quenched & Tempered R_c 26	.009	125	70
Plain	Quenched & Tempered R_c 31	.005	125	75
Leaded	Quenched & Tempered R_c 31	.005	125	50
Plain	Quenched & Tempered R_c 31	.009	125	90
Leaded	Quenched & Tempered R_c 31	.009	125	60
Plain	Quenched & Tempered R_c 40	.005	60	50
Leaded	Quenched & Tempered R_c 40	.005	60	40
Plain	Quenched & Tempered R_c 40	.009	60	60
Leaded	Quenched & Tempered R_c 40	.009	60	50

Table 4 Surface finishes obtained on AISI 4340H steel with carbide tools

Material: AISI 4340H (plain and leaded)
Tool: Carbide grade 78B
Back rake: 0 deg; side rake: 6 deg
Side cutting-edge angle: 0 deg
End cutting-edge angle: 6 deg
Relief: 6 deg; nose radius: 0.040 in.

Plain or Leaded	Heat Treatment	Feed in./rev.	Cutting Speed ft./min.	Surface Finish micro-inches
Plain	Normalized R_c 34.5	.005	100	85
Leaded	Normalized R_c 34.5	.005	100	60
Plain	Normalized R_c 34.5	.009	100	125
Leaded	Normalized R_c 34.5	.009	100	65
Plain	Quenched & Tempered R_c 26	.005	100	50
Leaded	Quenched & Tempered R_c 26	.005	100	40
Plain	Quenched & Tempered R_c 26	.009	100	50
Leaded	Quenched & Tempered R_c 26	.009	100	40
Plain	Quenched & Tempered R_c 33	.005	100	50
Leaded	Quenched & Tempered R_c 33	.005	100	40
Plain	Quenched & Tempered R_c 33	.009	100	60
Leaded	Quenched & Tempered R_c 33	.009	100	40
Plain	Quenched & Tempered R_c 41	.005	100	40
Leaded	Quenched & Tempered R_c 41	.005	100	30
Plain	Quenched & Tempered R_c 41	.009	100	50
Leaded	Quenched & Tempered R_c 41	.009	100	35

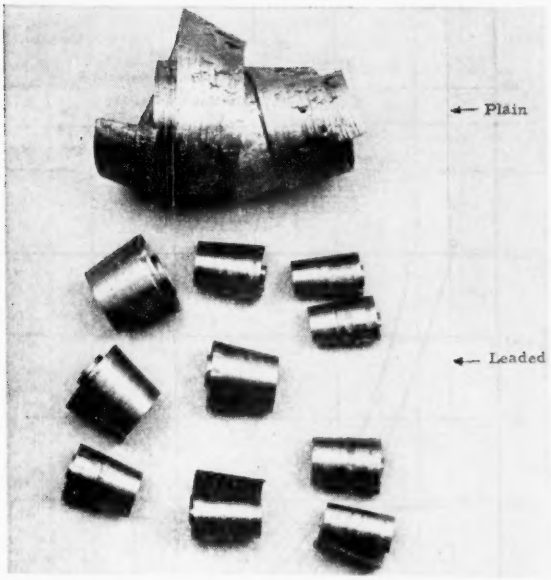

Fig. 3 Chips cut from normalized AISI 4147H steel—R_c 22: Tool, 78B carbide; cutting speed, 100 fpm; feed, 0.009 in. per revolution; cutting fluid, soluble oil. The upper large single chip is plain, the group of smaller ones leaded.

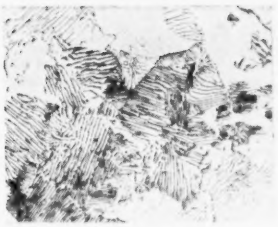

Fig. 4 AISI 4147 plain steel, normalized to R_c 22, etched in Nital, enlarged 2000X

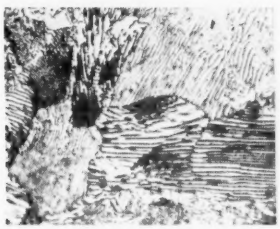

Fig. 5 AISI 4147 leaded steel, normalized to R_c 22, etched in Nital, enlarged 2000X

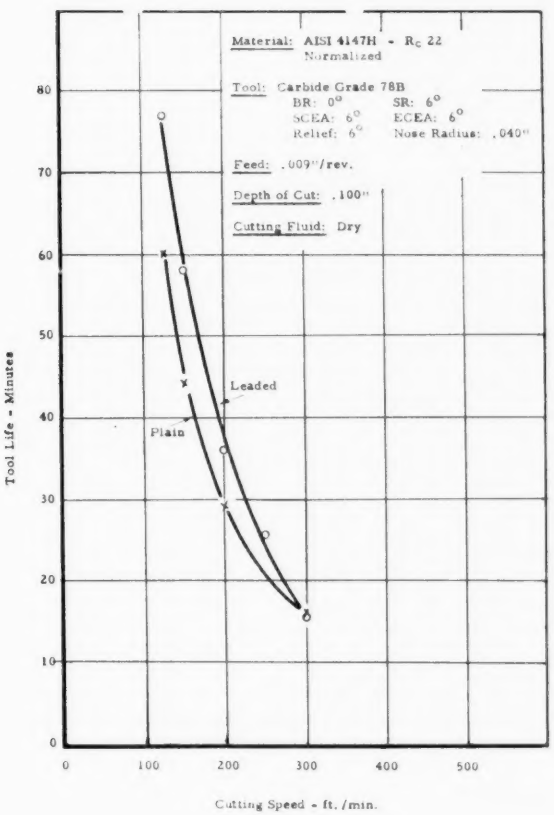

Fig. 6

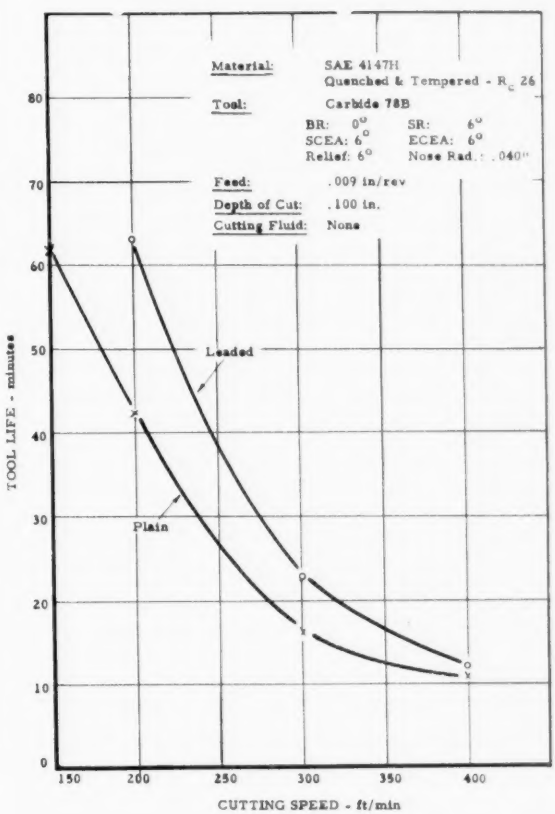

Fig. 7

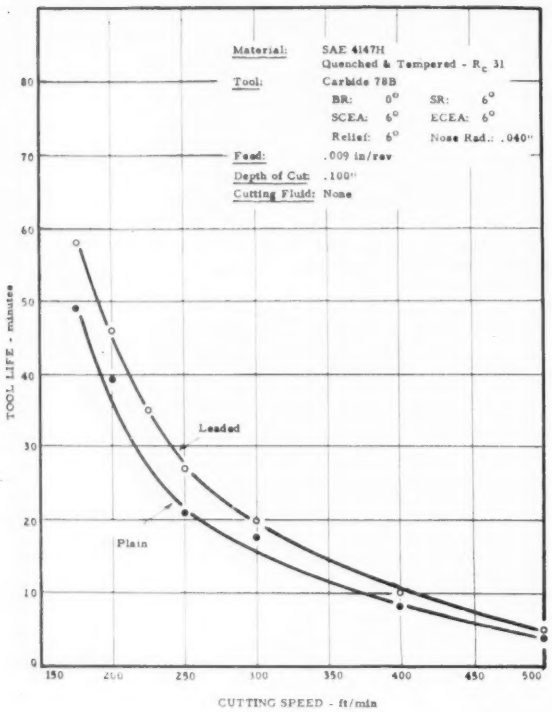

Fig. 8

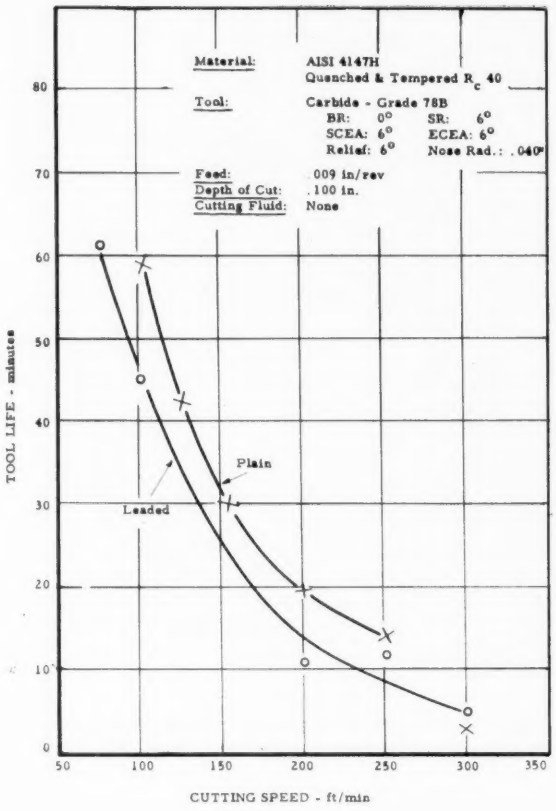

Fig. 9

Further evidence of the improvement in surface finish as a result of the lead additive was revealed by a comparison of the chips cut from the normalized and leaded 4147 steels with carbide tools. Chips from the two steels are shown in Fig. 3. Compare the shiny smooth surfaces of the short, tightly curled chips machined from the leaded bar with the rough surface of the chip cut from the plain bar.

Tool Life

Comparisons of tool-life results can be made on either relative cutting speeds for a given tool life or relative tool-life values for a given cutting speed. Comparing the relative cutting speeds for a given tool life has an advantage, in that one can easily determine whether or not the increase in cutting speed (production rate) justifies the additional cost of the free-machining additive in the steel. In cases where the material is very difficult to machine, the interest will then be principally one of improving the tool life. Under these conditions, a comparison of the relative tool-life results at a given cutting speed is most important.

AISI 4147H Steels. Typical microstructures of the AISI 4147H plain and leaded steels in the normalized condition are shown in Figs. 4 and 5. Tool life curves obtained with carbide tools on both the plain and leaded 4147H steels in four heat-treated conditions are presented in Figs. 6 through 9. The improvement in tool life on the normalized steel R_c 22 was about 35 per cent, and over 40 per cent on the quenched and tempered steel having a hardness of R_c 26. The beneficial effect of the lead additive decreased at the higher hardness levels. At a hardness of R_c 40 the tool life for the leaded steel was even less than that of the plain steel.

An examination of the type of tool wear obtained on the plain and leaded steels revealed that the cratering on the face of the tool was greater when the leaded steel was machined. This condition is not unusual, since the use of a free machining additive results in a more tightly curled chip (see Fig. 3) which has more of a tendency to cause a cratering type of tool wear. Normally, this cratering effect is of no serious consequence; however, it is detrimental when very hard metals are being cut. The net effect of cratering on the face of the tool is to increase the rake angle and thereby reduce the strength of the cutting edge. When the work material is very hard, there is a tendency for the cutting edge to chip off as the cratering becomes pronounced. Under these circumstances, tool life on the hard leaded steels will be less than on the hard plain steels.

AISI 4340H Steels. The tool-life curves obtained on the AISI 4340H steels in the various heat-treated forms are shown in Figs. 10 through 13. An examination of these curves reveals that, at the hardness level of R_c 26, an improvement in tool life of over 40 per cent resulted from the lead additive. However, on the remaining three heat-treated forms, covering a hardness range of 33 to 41 R_c, the tool life curves of the leaded steels almost coincided with that of the plain steels. In most of the tests at the higher cutting speeds, the tool life on the leaded steel was even less than that on the plain steel. Only at the low cutting speeds (100 fpm and less) did the leaded steel produce a longer tool life. The recommended cutting-speed range for these steels would be 100 to 200 fpm. In this cutting speed range, the lead additive would not be beneficial to tool life.

Conclusions

1 The use of a lead additive in medium-carbon alloy steels will

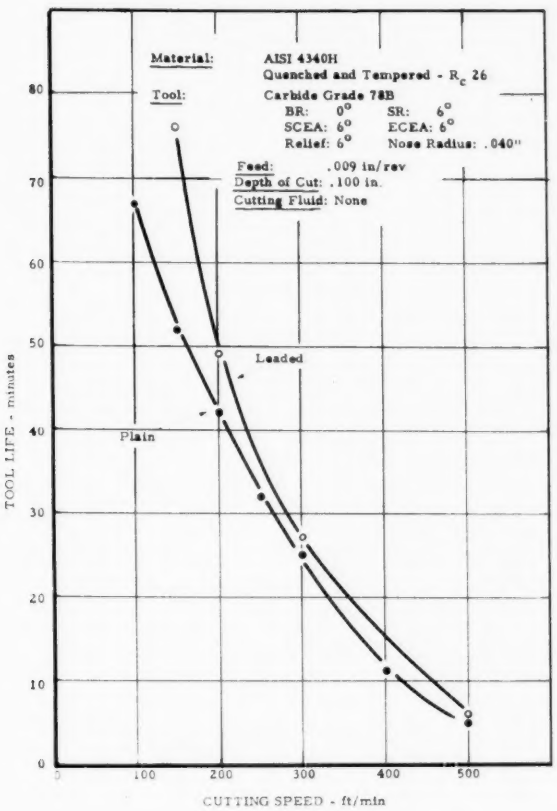

Fig. 10

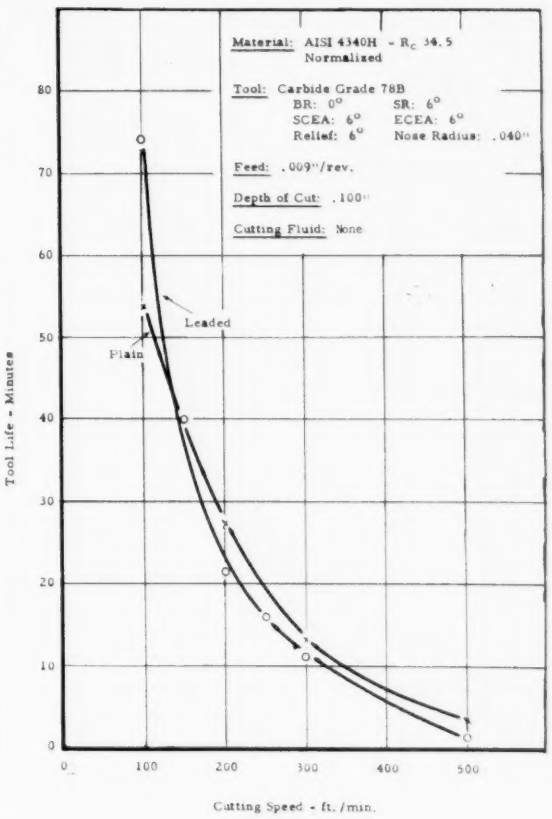

Fig. 11

result in appreciable increases in tool life for those steels having a hardness of R_c 30 or less. The advantage of the lead additive will decrease as the hardness of the steel increases beyond R_c 30. At some point in the hardness range of R_c 35 to R_c 40 or higher, the presence of the lead additive may be detrimental to tool life.

2 Appreciable improvement in surface finish is obtainable on medium-carbon alloy steels, regardless of the hardness of the steel.

3 The addition of lead to medium-carbon steels at various hardness levels will result in a reduction of 15 to 25 per cent in power required in machining.

Acknowledgment

The data reported herein were taken from a series of tests in a program sponsored by the Ordnance Tank—Automotive Command, Detroit Arsenal, U.S. Army, under Contract No. DA-33-008-ORD-1172. The authors hereby express their sincere appreciation to that Command for the support of the program.

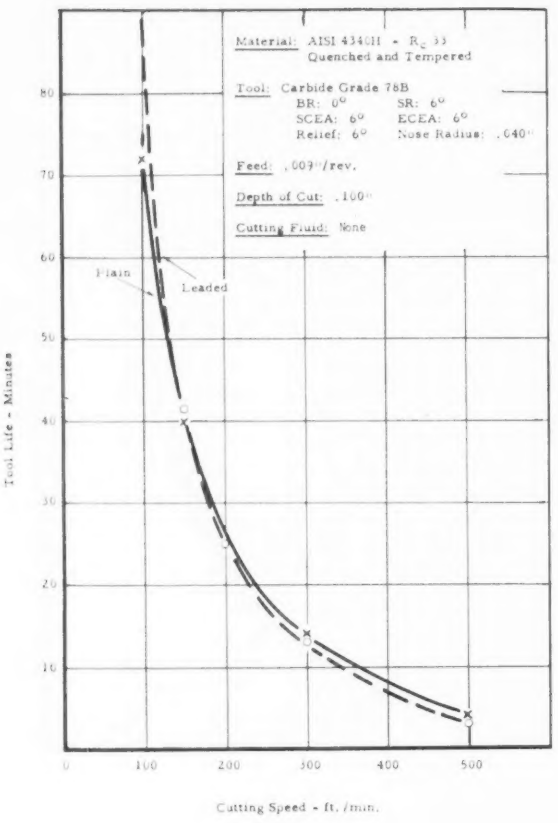

Fig. 21

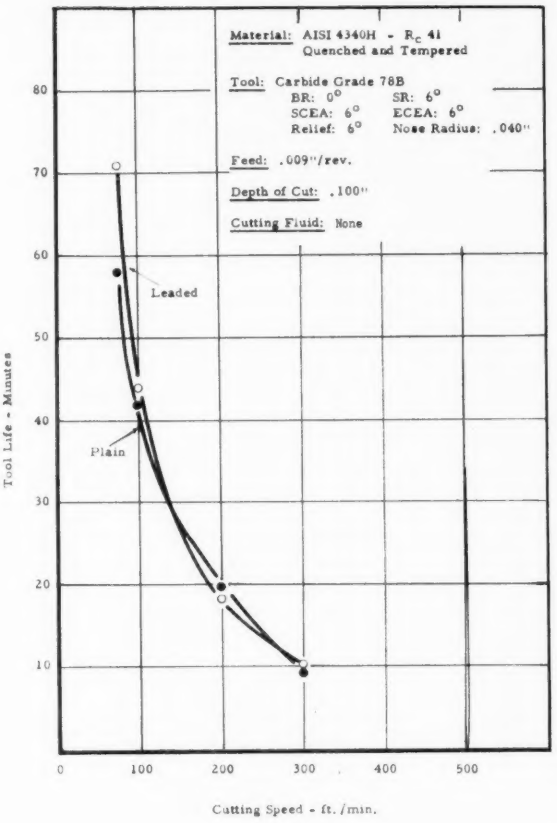

Fig. 13

DISCUSSION

F. W. Boulger[2]

The authors are to be congratulated on an interesting contribution to knowledge in an important area of metal cutting. There are a few points which should be clarified, however, lest some of the readers draw more sweeping conclusions than those considered justified by the authors.

In the first place, are the actual compositions of the steels known? In many cases, samples from the same heat differ significantly in composition and appreciably in machining properties. We have tested bars from the same heat of free-cutting steel which differed 20 per cent in tool life at the same cutting speed. It would be especially helpful to know the lead contents of the leaded steels. Finally, were the leaded and lead-free comparison samples given the same heat-treatments? Sometimes, steels tempered to the same hardness by using different time-temperature schedules do not perform alike in machining tests even though they have the same chemical composition.

The authors point out that cratering was greater for the leaded than for the standard 4147H steel. Did the tools fail by cratering or by flank wear and was the same end-point criterion used for both steels? Japanese investigators have shown that tools sometimes develop exaggerated wear rates after flank wear exceeds 0.017 in. Therefore, it would be of interest to know whether or not any data were obtained for larger amounts of flank wear than 0.015 in. It may be that the width of the wear land at which accelerated wear starts varies between workpiece materials.

[2] Chief, Division of Ferrous Metallurgy, Battelle Memorial Institute, Columbus, Ohio. Mem. ASME.

The authors' observation that cratering was more severe with one of the leaded steels is probably quite important. Did they investigate the possibility that the benefits of lead might persist at higher hardness levels if a more crater-resistant tool material or tool shape is used?

Statistical examination of tool-life data published by various authors indicates that the coefficient of variation in tool-life values is ordinarily about 18 per cent. When this is true, differences in average tool-life values based on triplicate determinations should exceed 30 per cent in order to be judged significant. If this rigorous criterion is used for drawing conclusions, it appears that no real differences in tool life between leaded and lead-free steels were detected except on bars tempered to 26 Rockwell C. Even at that hardness level, the 4340 steels differed only in tests below 200 fpm. Nevertheless, the data obviously justify the authors' conclusion that at higher strength levels lead may not exert the benefits expected from experience on steels machined at lower hardnesses.

G. Dementis[3]

This paper is of a great deal of interest because of the long-standing proprietory position of the writer's company in the production of leaded steels.

The reported results on the tool-life phase of the investigations, which indicated lower tool life for leaded steels for the higher hardness levels, appear to be somewhat perplexing. In view of the fact that the measured coefficient of friction is appreciably

[3] Metallurgist, Research and Development Department, Inland Steel Company, East Chicago, Ind.

smaller for all the corresponding pair leaded steels, it might be predicted that tool-life results also would be favorably affected by lead additions.

Recent work done by Chao and Trigger[4] would seem to offer a possible explanation for this behavior. In the cited study, these authors seem to indicate that there is an optimum tool-chip contact distance. Contact distances both longer and shorter than this optimum lead to higher tool temperatures (and presumably lower tool life).

If this is true, it would seem possible that with given tool design and coolant conditions, the formation of the "tighter" curl leaded chips could lead to a shorter tool life than the longer curl nonleaded types.

Therefore it would be expected that an action of changing the cutting-tool design and introducing a water-base coolant would reverse the tool-life results reported for the leaded and nonleaded hardened AISI 4147H steels. Some indication that this would be true is the result reported for the testing of the hardened (R_c 41) AISI 4340H steels where a soluble-oil cutting fluid was used. This introduction of a coolant appears to be responsible for the hardened-leaded steel showing a tool life about equal to the nonleaded sample.

V. V. Donaldson[5]

The authors deserve the sincerest thanks for the work presented in this paper. There are too few people engaged in the sometimes thankless and always tedious work of this sort which is so necessary before the machining art can approach the status of a science. The following remarks are not to be taken as derogatory to the authors in any sense whatever and critical only to the extent that there is still much more work to be done before theory and practice can be reconciled.

It must be understood that only one or two aspects of machining can possibly be dealt with in a paper of this kind. To cover adequately all of the variables with which one has to contend in practical or production machining would require more space than could be permitted here. Cuts of $^1/_2$ to $^3/_4$ in. at feeds of $^3/_{32}$ in., for example, intensify the effect of variables not included in this presentation. Conditions under which a tool with positive rake actually cuts at an effective negative rake angle are also beyond the scope of this work. However, since "leaded steels" as a class exhibit more variation in machinability from one supplier's product to another's than do regular grades, we must include some "out-of-scope" remarks.

The nonlinear relationship of coefficient of friction and power requirements which can be seen in Tables 1 and 2 should be noted as arising from the use of a formula derived from strictly orthogonal cutting conditions in which there is no edge build-up. For most purposes the use of the formula under more practical cutting conditions gives a usable semiquantitative measure of the coefficient of friction. However, in certain instances, in which a fundamental difference in material is involved, it may be misleading.

Fig. 3 illustrates the difference in chip formation using the same tool geometry and nominal cutting conditions for two essentially different materials. It is obvious that the two types of chip result from fundamentally different cutting conditions. Unless the difference in effective shear angle is considered as one of the major parameters, the cutting conditions are not comparable either in practice or for test comparison.

Our experience with Hi-Qua-Led[6] forgings, ranging from mild, plain-carbon steels to relatively high-carbon alloy steels, indicates that there is a fundamental difference in the shear angle ϕ between the leaded and nonleaded materials. Thus the use of the same tool geometry and cutting conditions, speed, feed, and depth of cut, does not practically compare the two materials.

In the last section of the paper, Tool Life, the cratering effect is apparently taken by the authors to be a function of the material rather than of tool geometry and cutting conditions. Our experience coincides with that of the practical machinist whose attitude may be taken as "the tool knows more about how the metal should be cut than you do." If the tool cannot be ground to suit the cutting conditions, the conditions should be changed.

Every day in commercial machine shops, cratering is avoided or alleviated by one or a combination of the following procedures: (*a*) increase speed, (*b*) increase feed, (*c*) regrind or change tool geometry. In single-point turning it is generally true that both the tool and speed must be changed for optimum results. (The word "increase" in *a* and *b* is not a misprint, and applies to properly leaded steel forgings.)

Although certain steels, notably 4100's and 4300's, exhibit a hiatus at a little over 300 Bhn, whether leaded or plain, Hi-Qua-Led forgings have shown distinct machining advantages in both rough and finish cutting to Brinell hardnesses above 535.

Improvement in machinability has ranged for such forgings from 40 to 50 per cent to over 100 per cent in production runs involving single and multipoint turning, boring, drilling, gear hobbing, gear shaping, and milling operations. A few cases have been encountered in which the improvement was only 25-30 per cent because of the condition and power or speed limitations of the equipment being used. In these instances, tool life was improved by a factor of 50 per cent or better—in one case, 1600 per cent.

E. S. Nachtman[7]

This paper properly presents three basic laboratory test methods for evaluating machinability. These comparative data are most valuable and are, we feel, the proper method for presenting any laboratory evaluation of machinability.

The three tests which evaluated tool life, tool forces, and surface finish indicate the fallacy involved in using any one method to relate the machinability of steel to a specific production situation. On the high-strength levels, it is apparent that two criteria, namely, tool forces and surface finish, clearly indicate a superiority for lead. The third criterion, tool life, indicates that there is no improvement.

We have found in our work in attempting to relate laboratory tests to production situations that one must be very careful in assessing the relative value of any one laboratory test, particularly when, depending upon the test used, the result may indicate good or bad machining characteristics.

It is this situation precisely dealing with the attempt to translate laboratory results into production guidance that remains in question. Any conclusions based upon such laboratory tests must be evaluated carefully before attempting to apply these conclusions to the production machining situation.

We have found in the machining of steels at hardness levels up to 30 R_c using high-speed steel tools similar phenomena as reported here using carbide tooling on higher strength steels containing lead. It is interesting, however, to note that in those situations where tool life has fallen off with the hardness of leaded steels that this factor can be changed completely by appropriate changes in the geometry of the tool. Whether these changes which are effective in maintaining the value of lead using tool-steel tools can also be applied to this higher hardness level using carbide tools has not been investigated.

---

[4] B. T. Chao and K. J. Trigger, "Controlled Contact Cutting Tools," published in this issue, pp. 139–151.

[5] Project Engineer, Alco Products, Inc., Latrobe, Pa.

[6] Alco Products Inc., patented process of lead addition for high-quality steel forgings.

[7] LaSalle Steel Company, Chicago, Ill. Assoc. Mem. ASME.

W. B. Wragge[8]

As one who has been associated with engineering and machining problems for many years, the writer offers the following comments:

The "tool-life end point" which is used as the criterion of wear life is based on the flank wear of the tool. The abrasive nature of steel has far more effect on flank wear than has orthodox wear on the chip sliding surface which is related to machinability. For example, steel with abrasive inclusions rapidly creates flank wear, although the chip sliding surface may not show anything like the same degree of wear.

Putting it another way, front flank wear of a tool is in the main caused by rubbing effect of abrasive inclusions, usually at relatively low specific pressures, whereas chip sliding-surface wear is the result of the surface softening of the tool by tempering caused by frictional heat generated resulting from chip pressure on the tool surface and the chip sliding velocity.

Therefore, tool-life end point measured by a degree of flank wear can only be considered correlatable with conventional Taylor type tool-wear tests if the various materials tested have precisely similar quantities of abrasive inclusions present.

The cutting speed-tool life curves presented in the paper are interesting, but in certain cases require credulity on the part of the reader. For example, one graph, Fig. 13, showing the results for leaded and nonleaded steel at the relatively high hardness level of 380 to 400 Brinell indicated very little difference, yet elsewhere (Table 2) in the paper the authors record that, under the machining conditions, the coefficient of friction for the leaded steel is only 0.58 as compared with 0.85 for the nonleaded, while the horsepower requirements for machining were 0.86 for leaded and 1.04 for the nonleaded. In other words, the total work done on leaded steel was appreciably less for the same volume of metal removed. One would have expected the heat generated to be less, and as from the nature of the curves, tool life appears work-dependent and therefore temperature-dependent, one would have expected tool life increase in favor of the leaded steel. Certain explanations are needed regarding this anomaly.

Authors' Closure

The authors wish to thank the discussers for their comments in that a number of important thoughts have been brought forth for further discussion.

In answer to Mr. Boulger's comments, a certified copy of the chemical analysis of each group of bars was furnished by the mill supplying the steel. The mill analysis was further verified by an independent chemistry laboratory. The lead content was 0.15 to 0.35 in both the leaded 4147H and 4340H grades. As noted in the paper, both the leaded and nonleaded steel in each grade were from the same heat. Also, in every case the leaded and nonleaded bars were heat-treated at one time. In addition, the microstructures of both were examined and their hardnesses measured.

In the original work from which the paper was abstracted, both high speed steel and carbide tools were used. As with the carbide tools, the tool life with the high speed steel tools was also less with the leaded 4147H steel at R_c 40, and only slightly better on the leaded 4340H steel at R_c 41.

Throughout the entire series of turning tests, the cratering type of wear on the tool was more pronounced on the leaded steels with both the high speed steel and carbide tools. However, as pointed out in the paper, at the lower hardness levels the cratering did not adversely influence tool life. It should also be noted that, in general, for all of the steels tested, after a given time of cutting the flank wear on the tool machining the leaded steels was less than on the tool cutting the nonleaded steels. However, the excessive cratering on the harder grades of leaded steels caused the tool to fail, even though the wear land on the flank of the tool was less than 0.015 in. The tool life end point on the carbide tools was a 0.015-in. flank wear land or tool failure, whichever occurred first.

It should also be noted that in a number of the tests, many more test points were obtained than were plotted on the charts presented. This was particularly true where the differences in tool life values were small or where the results were the reverse of what one might expect.

The authors regret to state that an error was made in the information given for the tool life curves on the 4340H steel; no cutting fluid was used with the carbide tools. However, as mentioned earlier, the results were similar with the high speed steel tools and, of course, a cutting fluid was used with these tools.

Mr. Donaldson's remarks regarding considerable improvement in tool life values in leaded forgings in the Brinell hardness range above 500 are very interesting. The authors' experience with free machining grades of steels has been with steels having a maximum hardness of R_c 41 or 380 Brinell.

The authors wish to point out that in all of the tests, the cutting speed was increased until the tool life obtained was 10 minutes or less. Also, although not reported in the paper, three feeds, namely, 0.005, 0.009, and 0.019 in/rev, were used on the 4340H grade of steel. The results did not change the conclusions stated. It is the opinion of the authors that the cratering effect was a function of the material, since all other variables were held constant in each comparison. As a matter of fact, similar cratering wear on high speed steel tools has been observed by the authors when highly active cutting fluids were used.

In answer to both Messrs. Nachtman and Wragge, the results of the tool life tests prove once again that the machinability factors such as coefficient of friction, tool forces, or surface finish cannot be used alone as reliable guides for measuring tool life. There are too many other important factors. The fact that, under carefully controlled conditions as regards grade of carbide, geometry of tool, speeds, feeds, and depth of cut, the tool life results led to certain conclusions cannot be ignored. One can only speculate as to whether or not, under other cutting conditions, the relative tool life results would have been different.

[8] Exors of James Mills Limited, Bredbury Steel Works, Woodley near Stockport, Cheshire, England.

B. T. CHAO
Professor of Mechanical Engineering, University of Illinois

K. J. TRIGGER
Professor of Mechanical Engineering, University of Illinois, Urbana, Ill.
Mem. ASME

Controlled Contact Cutting Tools[1]

A substantial reduction in power consumption, an increase in tool life, more effective utilization of cutting fluids, and improved surface finish on the machined workpiece have been achieved by suitably controlling the length of tool-chip contact. Reasons for these findings are discussed in terms of basic variables in chip formation mechanics.

Artificially restricted contact tools open new avenues for metal cutting research. Machining data obtained with such tools provide further evidence of the invariant behavior of the dynamic shear stress of metals under high-speed cutting conditions, and unfold interesting information on the intricate nature of tool-chip contact.

Introduction

WHILE THE BASIC MECHANICS of metal machining was not properly understood until Piispanen in 1937 and Merchant [1][2] in 1944 independently expounded and analyzed the shear theory of chip formation, the desirability of reducing tool-chip friction and hence improving tool performance had long before been recognized. DeLeeuw [2] in 1922 suggested the use of lathe tools with limited rake surface in order to facilitate chip flow. Such tools had actually been used by Klopstock [3]. Fig. 1 is an artist's sketch of the latter's tool. In a paper presented at a meeting of THE AMERICAN SOCIETY OF MECHANICAL ENGINEERS, Klopstock reported that the use of such tools resulted in a minimum of compression and deformation of the chip, with the consequent reduction in tool forces, saving on power consumption, and a more favorable manner of wear. Klopstock's tool was made in dies by forging to produce the characteristic cup-shaped top surface. Visualizing the difficulty of preparing a tool of such intricate form, Herbert [4] suggested a truncated or compound tool which combined the advantages of both the obtuse and acute angle tools. The performance of double rake tools has been reported by Almdale [5] in turning, and by Armitage and Schmidt [6] in milling. After experimenting on several different combinations of primary and secondary rake tools, the last two investigators concluded that a milling cutter, provided with a 15 or 30-deg positive secondary radial rake and a negative primary radial rake surface extending, in width, one to two times the feed per tooth, was the most effective cutter. They attributed the superior performance of the double rake cutter to (i) increased mechanical strength of the cutting edge afforded by the negative primary rake and (ii) lower power consumption with positive secondary rake angle tools. A somewhat different but more basic explanation is presented in this paper. By using a double rake cutting tool, the tool-chip interface temperature may either be higher or lower than that of a conventional tool without the secondary rake, depending on the extent of the tool-chip contact. Other important effects like reduction of tool-chip frictional force, increasing effectiveness of cutting fluid action, improved surface finish, etc., by *properly* restricting the length of tool-chip contact are discussed.

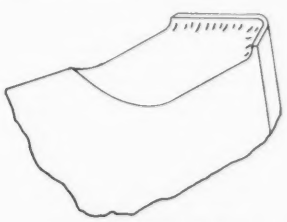

Fig. 1 The Klopstock tool

The Influence of the Extent of Tool-Chip Contact on Interface Temperature, Shearing Strain, and Apparent Contact Stress

The role which tool-chip contact plays in affecting tool-chip friction and cutting temperature was pointed out by the authors in 1951 [7]. Since then, further research has led to the development of procedures for computing temperature distribution over the tool-chip contact [8] and to the clarification of the mechanism of crater wear [9]. Recognizing that the tool-chip contact length is one of the fundamental quantities in chip-formation mechanics, the authors decided early in 1957 to investigate (*a*) the effect of artificially controlling the length of contact on interface temperatures, tool forces, and tool life; and (*b*) the feasibility of utilizing such control in improving the over-all economy of the machining process. From a theoretical point of view, artificially restricting tool-chip contact also provides a useful means of studying the basic variables in chip-formation mechanics.

Experimental evidence has established that, by reducing the contact length below the "natural" value, the tool-chip interface temperature first decreases, passes through a minimum, and eventually rises again upon further reduction of contact. Fig. 2(*a*) illustrates the variation of tool-chip interface temperature, as measured by the tool-work thermocouple technique, for the machining of an annealed pearlitic alloy steel at three different cutting speeds with a suitable grade of carbide as the contact length is successively reduced. The reduction in temperature amounts to about 100 F. Such reduction may oftentimes be significant in view of the findings of Schallbroch, Schaumann, and Wallichs [10] and those of the authors [9, 11]. The former investigators reported that, in dry cutting with high-speed steel tools, the tool life varied inversely as approximately the 20th power of the tool-chip interface temperature. While it is known that the foregoing rule must be applied with caution, the results of Schallbroch, et al., do demonstrate the profound influence of interface temperature on tool life when the cutting conditions are such that the wear is essentially temperature sensitive.

Fig. 2(*b*) illustrates a similar variation of the measured interface temperature with tool-chip contact length for the machining of electrolytic copper with high-speed steel tools. Due to lack of

[1] This work evolved from a project sponsored by the Office of Ordnance Research, U. S. Army, under contract No. DA-11-022-ORD-1980.

[2] Numbers in brackets designate References at end of paper.

Contributed by the Production Engineering Division and presented at the Semi-Annual Meeting, Detroit, Mich., June 15–19, 1958, of THE AMERICAN SOCIETY OF MECHANICAL ENGINEERS.

NOTE: Statements and opinions advanced in papers are to be understood as individual expressions of their authors and not those of the Society. Manuscript received at ASME Headquarters, March 31, 1958. Paper No. 58—SA-42.

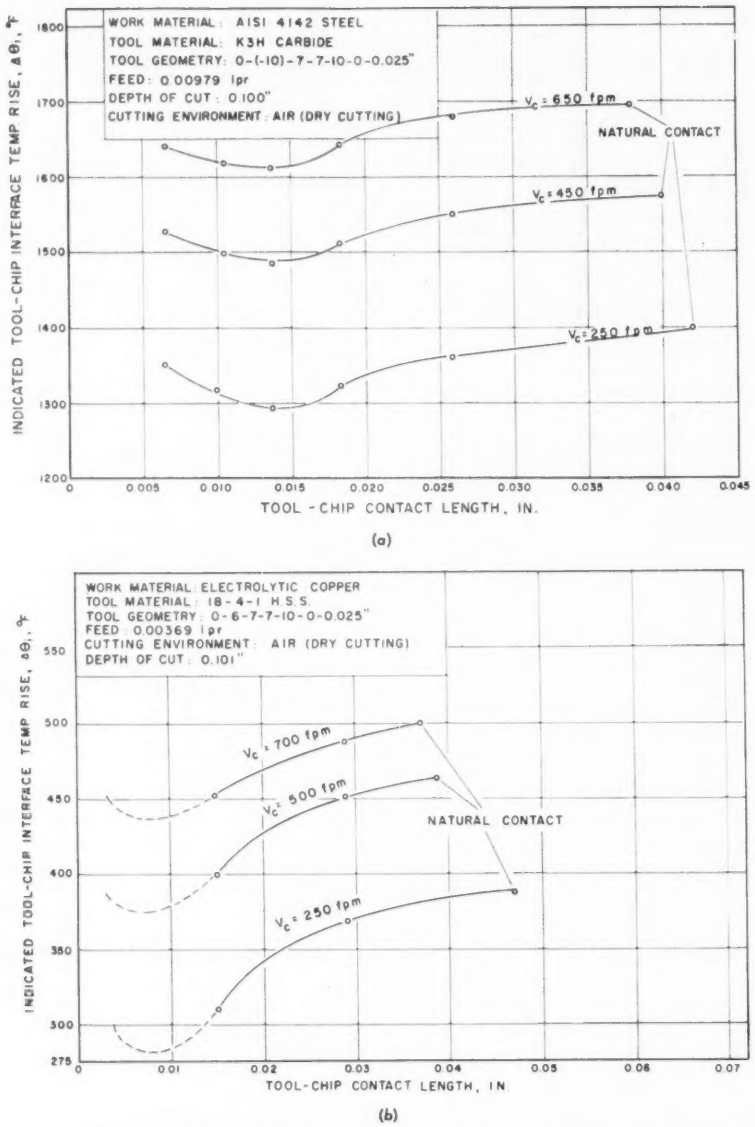

Fig. 2 Effect of tool-chip contact length on average tool-chip interface temperature at different cutting speeds

work material, data for contact lengths less than those indicated are not available. It is anticipated, however, that upon further reduction of the tool-chip contact, the interface temperature will eventually swing upward in a manner similar to that shown in Fig. 2(*a*).

As has been pointed out in the literature [12], tool-chip interface temperature consists of two major components, namely, (i) that due to main chip shear and (ii) that due to frictional sliding of the already heated chip on the tool top surface. It is instructive to find how the two components may vary with changes in contact length. The results of calculation are shown in Fig. 3(*a* and *b*). Curve ② in both figures was obtained from tool-force dynamometer readings and chip thickness ratio measurements, employing equations given in reference [8]. In Fig. 3(*a*), some scatter of data for the shear zone temperature rise was noted for low values of contact length. This is attributed to the rather abnormal behavior in chip formation and the variation of chip thickness as is illustrated in Fig. 4. Chip formation appeared to be going through some sort of "transition." The observed decrease in tool-chip interface temperature with decreasing length of contact is due partly to the reduction in main chip shear and partly to the reduction in frictional energy dissipation at the top surface. Further decrease in contact length will eventually reverse the latter's trend and bring forth an over-all increase in interface temperature. In the case of machining copper, the observed decrease in interface temperature is due basically to the reduction in main chip shear as the length of contact is decreased. On the other hand, the temperature rise due to tool-chip sliding first stays more or less constant and then increases at an accelerated pace, with decrease in contact length. While no data

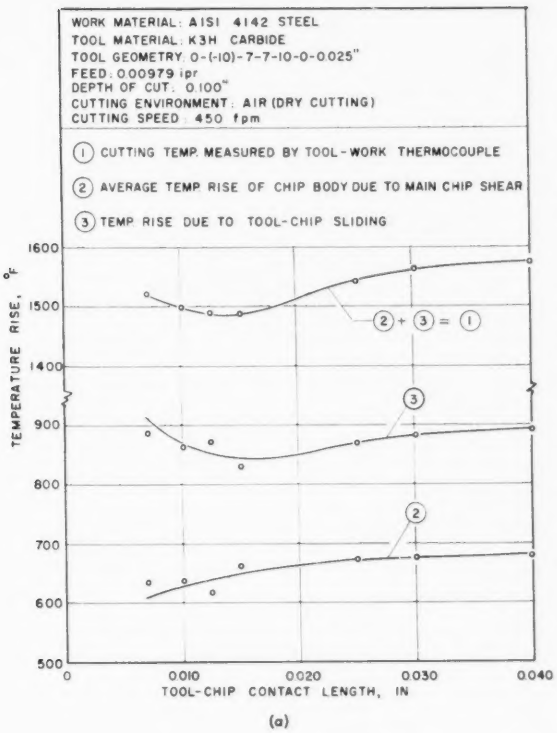
WORK MATERIAL: AISI 4142 STEEL
TOOL MATERIAL: K3H CARBIDE
TOOL GEOMETRY: 0-(-10)-7-7-10-0-0.025"
FEED: 0.00979 ipr
DEPTH OF CUT: 0.100"
CUTTING ENVIRONMENT: AIR (DRY CUTTING)
CUTTING SPEED: 450 fpm
(1) CUTTING TEMP. MEASURED BY TOOL-WORK THERMOCOUPLE
(2) AVERAGE TEMP. RISE OF CHIP BODY DUE TO MAIN CHIP SHEAR
(3) TEMP. RISE DUE TO TOOL-CHIP SLIDING
(2) + (3) = (1)
TEMPERATURE RISE, °F
TOOL-CHIP CONTACT LENGTH, IN
(a)

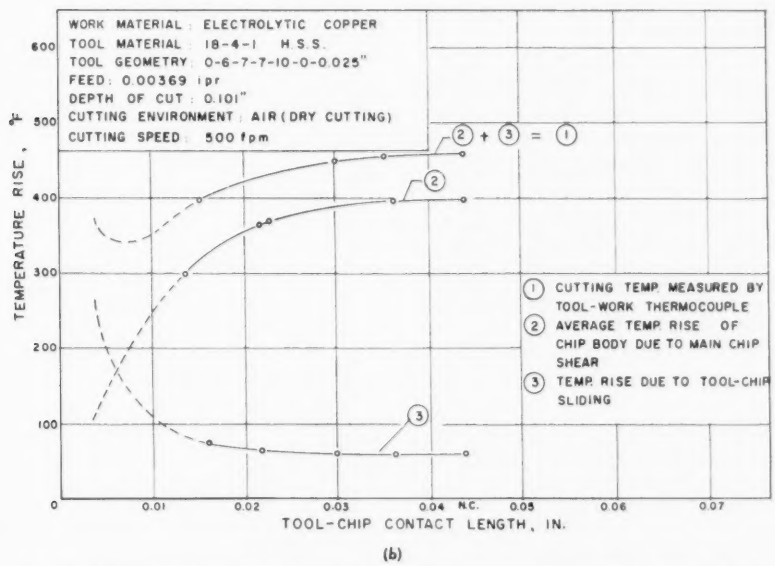
WORK MATERIAL: ELECTROLYTIC COPPER
TOOL MATERIAL: 18-4-1 H.S.S.
TOOL GEOMETRY: 0-6-7-7-10-0-0.025"
FEED: 0.00369 ipr
DEPTH OF CUT: 0.101"
CUTTING ENVIRONMENT: AIR (DRY CUTTING)
CUTTING SPEED: 500 fpm
(2) + (3) = (1)
(1) CUTTING TEMP. MEASURED BY TOOL-WORK THERMOCOUPLE
(2) AVERAGE TEMP. RISE OF CHIP BODY DUE TO MAIN CHIP SHEAR
(3) TEMP. RISE DUE TO TOOL-CHIP SLIDING
N.C.
TEMPERATURE RISE, °F
TOOL-CHIP CONTACT LENGTH, IN.
(b)

Fig. 3 Influence of varying contact length on the two components of tool-chip interface temperature

are available for contact length less than 0.015 in., it may be expected that the variation will follow a course shown dotted in Fig. 3(*b*). The nadir of the cutting temperature occurs where curves ② and ③ intersect.

The relative importance of main-chip shear and tool-chip sliding in contributing to the over-all interface temperature rise for the machining of copper and steel is of interest. Due to the unusually high strain experienced in copper chips, the shear zone temperature rise is by far the predominating component. On the other hand, the relatively small temperature rise due to tool-chip rubbing is a consequence of the low sliding stress and the high thermal conductivity of copper which dissipates the frictional energy more readily than a steel chip.

While the chip strain is higher in machining copper, decreasing the tool-chip contact brings forth a substantial reduction in such strain. This is illustrated in Fig. 5. When the length of contact is reduced from 0.04 in. to 0.014 in., the shear strain decreases from 7.7 to 4.4, representing a decrease of approximately 43 per cent. In the case of steel chips, the corresponding values are 3.0 and 2.8, representing a decrease of only 7 per cent. It is recognized that the foregoing comparison may not be completely justified since different tool material and tool geometry are involved. Nevertheless, the trend is considered to be a representative one.

One of the major, and stubborn, problems in the mechanics of chip formation concerns the frictional behavior of the tool-chip contact. It is illuminating to examine the changes taking place in the *apparent* frictional sliding stress (S_a) and *apparent* contact stresses (H_a) as the contact length decreases. The results as calculated from tool force and chip thickness data are shown in Figs. 6(*a* and *b*). It is seen that, in machining either steel or copper, the apparent sliding and contact stresses both increase with diminishing contact, with the contact stress changing more rapidly.

Several years ago, the authors attempted to elucidate the frictional behavior at the interface by studying the influence on both S_a and H_a of changes in cutting speed, feed, and tool rake, but were not able to reach any definite conclusion [13]. While the importance of the extent of tool-chip contact was recognized, its influence could not be independently evaluated at that time. On the other hand, when the variation of interface friction was examined in terms of temperature changes, independent effects due to feed, speed, and tool rake were definitely found to exist. Results obtained in this investigation have shed considerable light on the subject.

The contact and sliding stresses, H_a and S_a, respectively, in Figs. 6(*a* and *b*) are apparent values. The true stresses depend

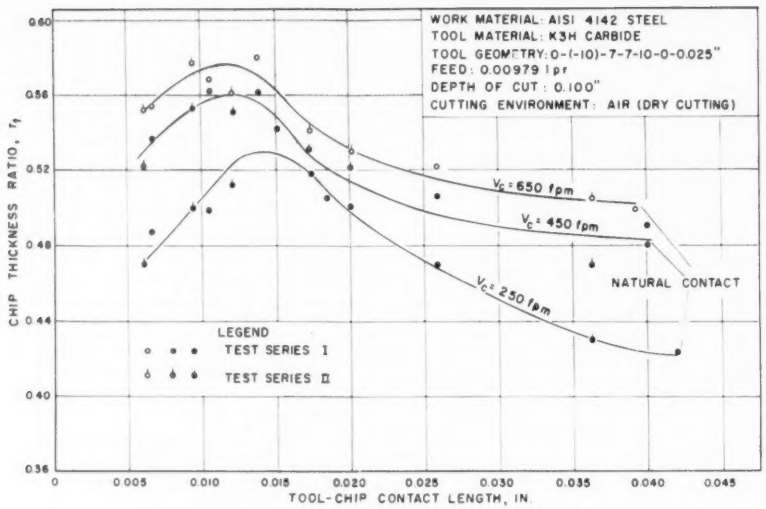

Fig. 4 Variation of chip thickness ratio with contact length

on the *real* area of contact. If these true stresses are represented by σ and τ they are related to H_a and S_a by the following expressions:

$$H_a = \sigma A_r/A_a \quad \text{and} \quad S_a = \tau A_r/A_a$$

where subscripts "r" and "a" refer to real and apparent values, respectively. τ is construed to include the "plowing" component.

To investigate the manner by which the true stresses may vary with respect to changes in contact length (and interface temperature) reference is made to Figs. 2(*a*) and 6(*a*).

(A) Effect of Reduced Contact at Fixed Speed (450 fpm)

Reducing the contact length from 0.040 in. (natural) to 0.010 in. decreases the interface temperature by 90 deg or about 4½ per cent on the absolute scale. This may be expected to have some influence on τ but is not considered to be of primary importance. Reduction in contact length also results in a slight decrease in chip-strain and chip-bulk temperature. In so far as the conditions at the tool-chip contact asperities are concerned, the latter two exert only minor influence and tend to counteract each other. Consequently, for the case under study, and as a first approximation, τ may be regarded as a constant. With the equations relating H_a and S_a to σ and τ one can write

$$\frac{\tau}{\tau_{\text{n.c.}}} = \frac{S_a}{(S_a)_{\text{n.c.}}} \frac{(H_a)_{\text{n.c.}}}{H_a} \frac{\sigma}{\sigma_{\text{n.c.}}}$$

where the subscript n.c. refers to natural contact. For constant τ the left-hand side of the equation reduces to unity.

From the tool force and chip thickness data, the ratio τ/σ (which is customarily referred to as the coefficient of friction) may be readily obtained and is shown in Table 1.

It is seen that a significant reduction in the τ/σ ratio occurs when the contact length is reduced from 0.040 to 0.010 in. On the assumption that the real area for σ and τ is the same and that an arbitrary value of 85,000 psi is selected for τ, the contact stress σ and real contact area may be calculated, and are included in Table 1. Since the dynamic shear stress of the 4142 steel has been found to be 98,000 psi, it is unlikely that the average frictional sliding stress could exceed that value. 85,000 psi is believed to be a reasonable estimate under existing conditions.

The pronounced increase in σ and consequently the reduction in τ/σ is attributed to a restraining effect imposed by adjoining asperities as the population density, which may be measured by

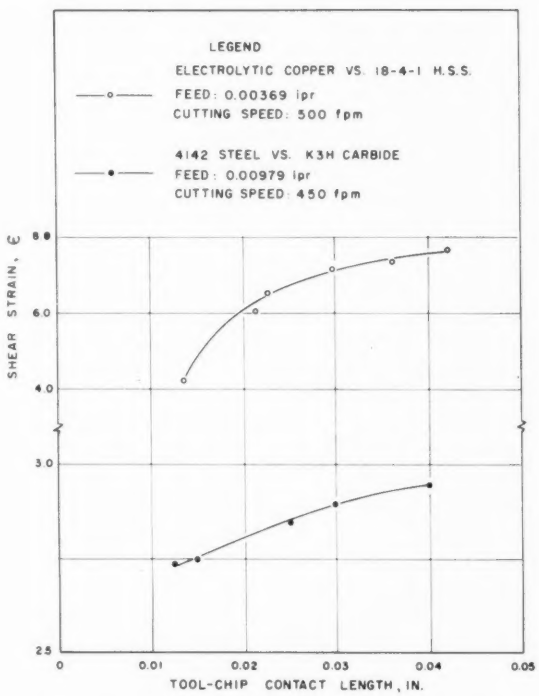

Fig. 5 Variation of shear strain with reducing length of contact

the ratio of real to apparent area, increases due to reduction of the contact length. While there is a decrease in real area of contact due to increase in σ, the ratio of A_r/A_a actually increases as tabulated in Table 1. Though the absolute magnitude of the real contact area depends on the assumptions used, the relative values are believed to be quite representative.

The restraint or interference on the propagation of plastic deformation, due to the proximity of individual asperities, increases with population density, and, in the ultimate, the asperity hardness becomes the bulk hardness of the strain hardened chip.

Table 1

Contact length, in.	Normal force, N-lbs	Friction force, F-lbs	$\frac{\tau}{\sigma}$	τ, psi	σ, psi	A_r, in^2 × 10^3	A_r/A_a, pct
0.040	402	167	0.415	85000	205000	1.965	48.5
0.030	390	146	0.374	85000	227000	1.72	56.8
0.020	370	120	0.324	85000	262000	1.41	69.8
0.015	350	100	0.286	85000	297000	1.18	77.8
0.010	330	78	0.237	85000	358000	0.92	91.0

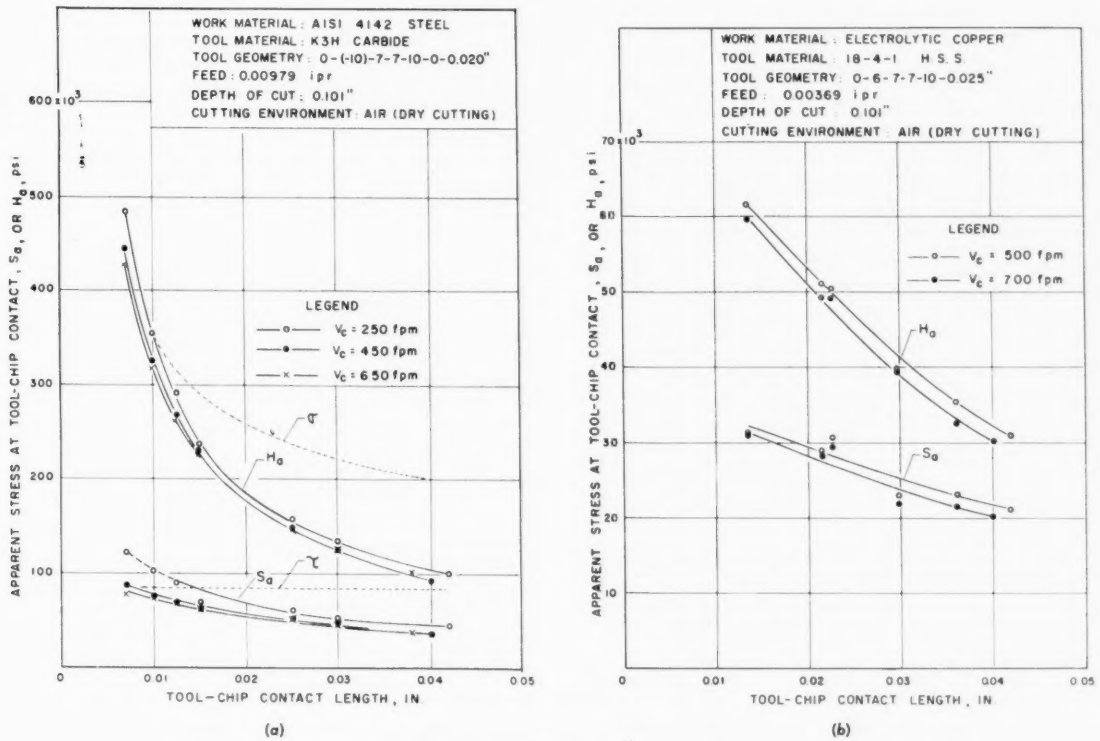
WORK MATERIAL : AISI 4142 STEEL
TOOL MATERIAL : K3H CARBIDE
TOOL GEOMETRY : 0-(-10)-7-7-10-0-0.020"
FEED : 0.00979 ipr
DEPTH OF CUT : 0.101"
CUTTING ENVIRONMENT : AIR (DRY CUTTING)
LEGEND
Vc = 250 fpm
Vc = 450 fpm
Vc = 650 fpm
σ
Ha
τ
Sa
APPARENT STRESS AT TOOL-CHIP CONTACT , Sa , OR Ha , psi
TOOL-CHIP CONTACT LENGTH , IN.
(a)
WORK MATERIAL : ELECTROLYTIC COPPER
TOOL MATERIAL : 18-4-1 H.S.S.
TOOL GEOMETRY : 0-6-7-7-10-0.025"
FEED : 0.00369 ipr
DEPTH OF CUT : 0.101"
CUTTING ENVIRONMENT : AIR (DRY CUTTING)
LEGEND
Vc = 500 fpm
Vc = 700 fpm
Ha
Sa
APPARENT STRESS AT TOOL-CHIP CONTACT , Sa , OR Ha , psi
TOOL-CHIP CONTACT LENGTH , IN.
(b)

Fig. 6 Influence of varying contact length on the apparent contact and sliding stress at tool top surface

In the foregoing discussion, a uniform population density of the contact asperities was assumed. It is quite likely that the distribution is nonuniform, being less dense toward the region where the chip leaves the tool at natural contact length. A change in population density or a shift of contact asperities toward the cutting edge would also contribute to the sharp upward bend of the σ curve, Fig. 6(a). If a temperature effect on τ is considered or if the plowing component is appreciable, σ will be even higher than indicated in Table 1.

As a consequence of asperity restraint, and its effect on σ, the kinetic coefficient of friction decreases as the contact length is reduced. A similar effect is believed to be associated with changes observed in cutting hardened steels, or by changes in speeds, feeds, rake angles, etc. During the cutting tests, discontinuities in force components, scatter in chip thickness data, and a reversal in trend of the latter, change in chip to a wavy form (suggesting instability of the shear "plane") occurred at contact lengths less than $\sim^1/_3$ of natural. There appeared to be a change in the mechanics of chip formation.

(B) Effect of Cutting Speed at Fixed Reduced Contact

The experimental data reveal an increase in interface temperature and chip thickness ratio, and a decrease in both force components and natural contact length as the cutting speed is increased.

Table 2 summarizes the restraining effect and interface temperatures for several contact lengths at three cutting speeds.

Table 2

Contact length, in.	V_c = 250 fpm $\sigma/\sigma_{n.c.}$	250 fpm $\Delta\theta_i$*	V_c = 450 fpm $\sigma/\sigma_{n.c.}$	450 fpm $\Delta\theta_i$	V_c = 650 fpm $\sigma/\sigma_{n.c.}$	650 fpm $\Delta\theta_i$
natural	1.0	1400	1.0	1575	1.0	1700
0.030	1.10	1370	1.11	1555	1.09	1690
0.020	1.26	1335	1.28	1525	1.26	1650
0.010	1.59	1310	1.75	1495	1.73	1620

* Temperature rise above the initial workpiece temperature which varied from 75 to 93 F.

An inspection of Table 2 reveals that the change in interface temperature has but a secondary role on the restraining effect and that the major factor is reduction of the contact length as noted by the general agreement of the $\sigma/\sigma_{n.c.}$ ratios.

The numerical values of σ and τ do decrease with increasing temperature as expected, but the principal effect on interface fric-

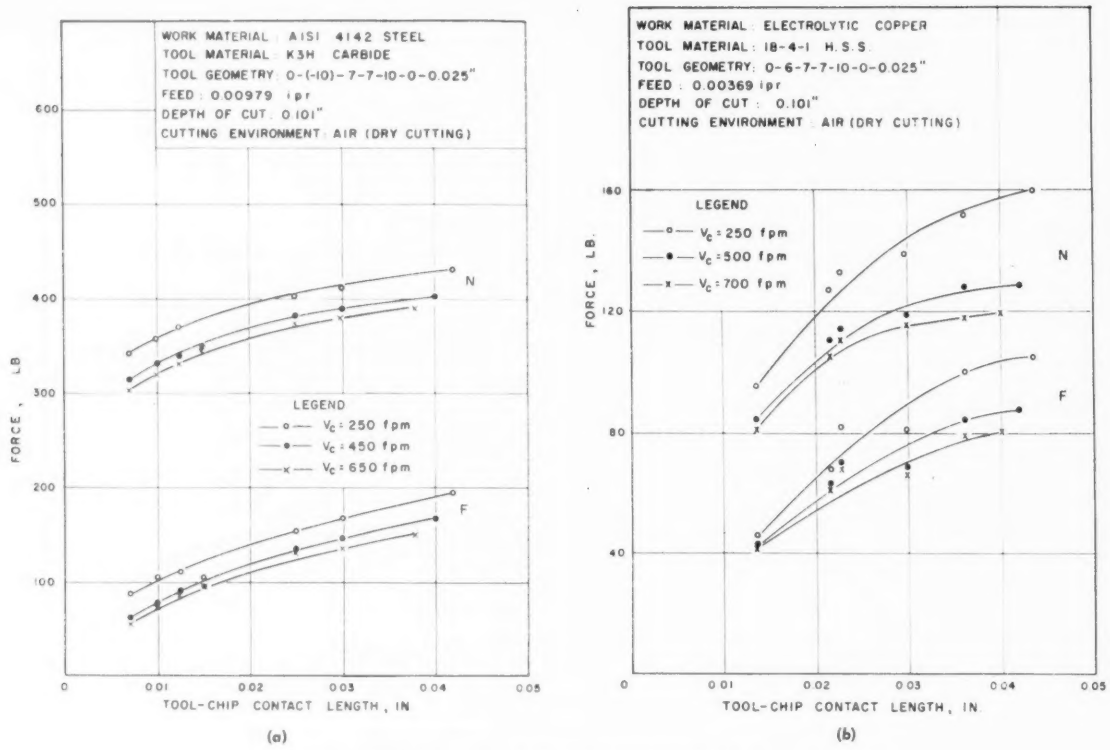

Fig. 7 Variation of normal and tangential forces on rake face with tool-chip contact length

tion is through the restraint imposed at high asperity population density.

A similar analysis for the data in the cutting of copper with high-speed steel tools at speeds of 250 to 700 fpm reveals the same kind of trends though the relative changes are smaller.

Very recently, a method has been introduced to determine the distribution of normal stress (H_a) at the tool-chip contact [14]. In the cutting of brass, Takeyama and Usui reported a linear decrease of the tangential and normal forces on the rake face with a reducing contact. This observation, however, is at variance with results obtained in the current investigations. Figs. 7(*a* and *b*) illustrate the typical variation of the two force components with changing contact lengths. The deviation from linearity is pronounced in the case of machining copper with HSS tools. While the authors have no data for cutting brass, it is clear that Takeyama and Usui's results cannot, in general, be regarded as representative.

Constancy of Dynamic Shear Stress—A True Property of Work Materials

It has long been the contention of the authors that the average dynamic shear stress exhibited by metals in present-day high-speed machining operations is essentially a constant [15. 13]. The heating effect due to plastic deformation occurs only after shear has taken place. Machining with reduced contact cutting tools offers a novel means to test further the general validity of such dynamic stress-strain relationship. It is one of the basic physical laws without which a rational analysis of chip-formation mechanics cannot be made. Results of calculation for cutting both steel and copper are summarized in Fig. 8 which illustrates,

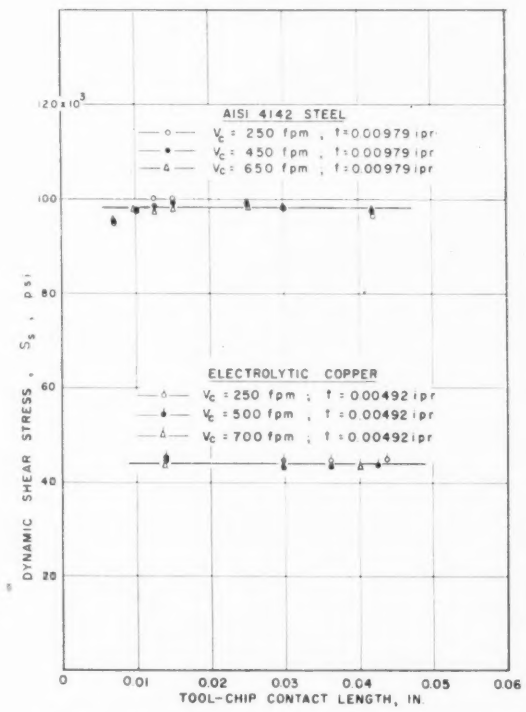
AISI 4142 STEEL
Vc = 250 fpm , f=0.00979 ipr
Vc = 450 fpm , f=0.00979 ipr
Vc = 650 fpm , f=0.00979 ipr
ELECTROLYTIC COPPER
Vc = 250 fpm , f = 0.00492 ipr
Vc = 500 fpm , f = 0.00492 ipr
Vc = 700 fpm , f = 0.00492 ipr
DYNAMIC SHEAR STRESS , Ss , psi
TOOL-CHIP CONTACT LENGTH, IN.

Fig. 8 Constancy of dynamic shear stress of work material

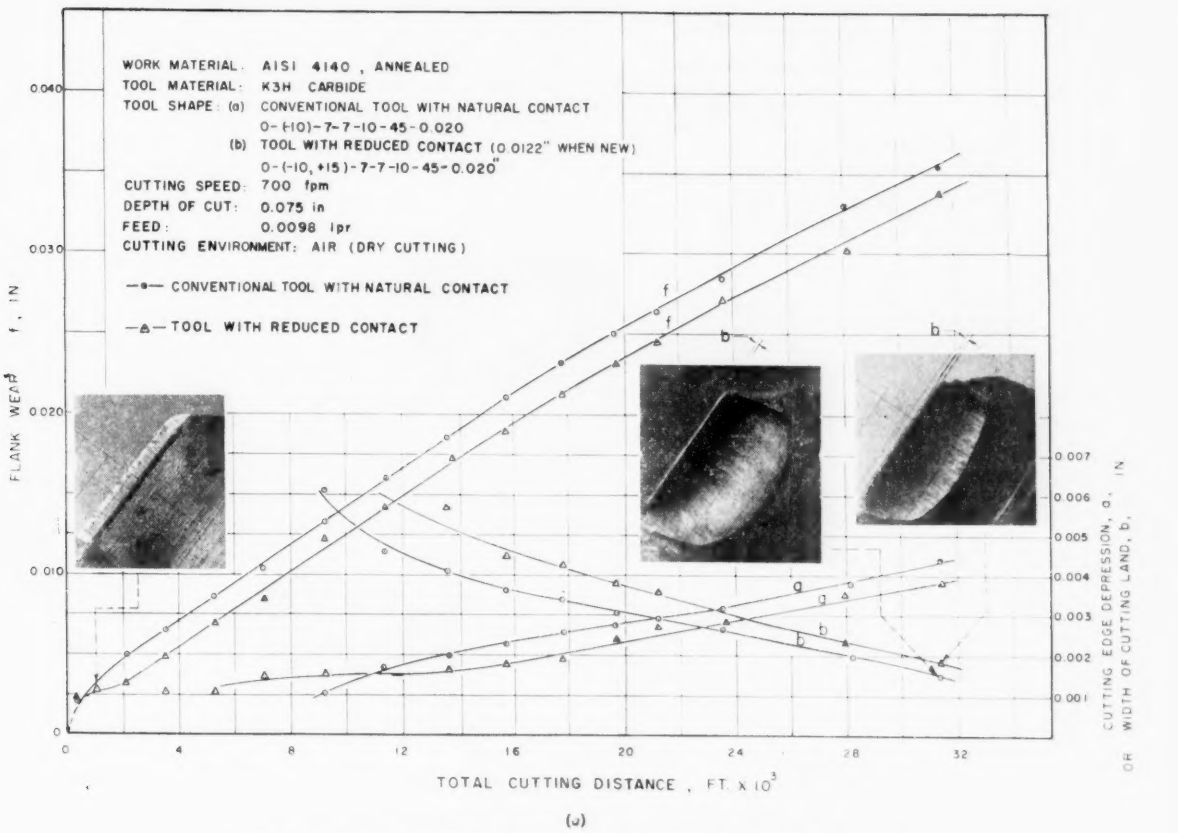

(a)

Fig. 9 Comparative tool life: Conventional tool versus tool with controlled contact

once again, the invariant behavior of this dynamic property. It appears, beyond doubt, that under such high strain rates as those experienced in the shear zone of the work material during high speed machining operations, the dynamic shear stress remains unaltered irrespective of variations in cutting conditions. In other words, it is a true property of the work material.

Tool Life, Surface Finish, Power Consumption as Influenced by Proper Control of Tool-Chip Contact

The fact that there is a minimum in the interface temperature as contact length is reduced suggests the possibility of lengthening the usable life of a cutting tool by properly controlling tool-chip contact. This is indeed borne out by comparative tool-life tests for (*a*) dry machining of annealed AISI 4140 steel with a suitable carbide, and (*b*) machining of a high-temperature alloy (Timken 16-25-6) with high-speed steel tools, using a commercial cutting oil with additives containing sulfur and chlorine. In the first case, the development of tool wear, both at the flank and on the top surface of the tool, is shown plotted in Fig. 9(*a*). Shown also are photographs of the conventional and controlled contact tool at several identical cutting times. It is significant that the cutting edge depression "*a*" is consistently smaller and the width of cutting land "*b*" is consistently greater for the *controlled contact tool*. It is the eventual break-through of the cutting land to the adjoining flank which ultimately causes tool failure.

Fig. 9(*b*) shows the rather spectacular increase in tool life using the controlled contact tool in the presence of a cutting fluid. The increase in usable life is over 150 per cent. Profilometer readings were 170–190 microinches for the work surface machined with a conventional tool as compared to 120–130 microinches obtained with a controlled contact tool.

The greater effectiveness of a cutting fluid with the controlled contact tool (believed to be due to more favorable conditions for its entry) is not necessarily beneficial. If the fluid is chemically active to the cutting tool, reduced contact may be expected to accentuate the effects. This is illustrated by machining tests on AISI 4340, heat treated to 48 R_c, using suitable carbide tools and a chlorine-additive emulsifiable oil. In three tests tools with natural contact outlasted reduced contact tools over 2 to 1 (20 min to 9 min). On the other hand, the controlled contact tool was definitely superior when used with a commercial cutting oil.

The effect of reduced contact is strikingly demonstrated by cutting at the temperature sensitive range of high-speed steel tools. In a test on 4150 steel at 142 fpm and 0.011 ipr, the tool life to failure was increased $2^1/_2$ times by reducing the contact length from natural to $^1/_4$ of that value.

The cutting forces are lower with reduced contact tools. This is, of course, to be expected since the frictional force on the tool top face is smaller and the chips are thinner with reduced length of contact. For example, consider the machining of electrolytic copper with high-speed steel tools. At a cutting speed of 500 fpm, the power component of the cutting force for the tool with positive 6-deg rake angle drops from 166 lb to 96 lb when the contact is reduced from the natural length to 0.0136 in. This represents a decrease of over 40 per cent. For a positive 20-deg rake tool, the corresponding values are 152 lb for the tool with natural contact and 106 lb with contact reduced to 0.0132 in.—

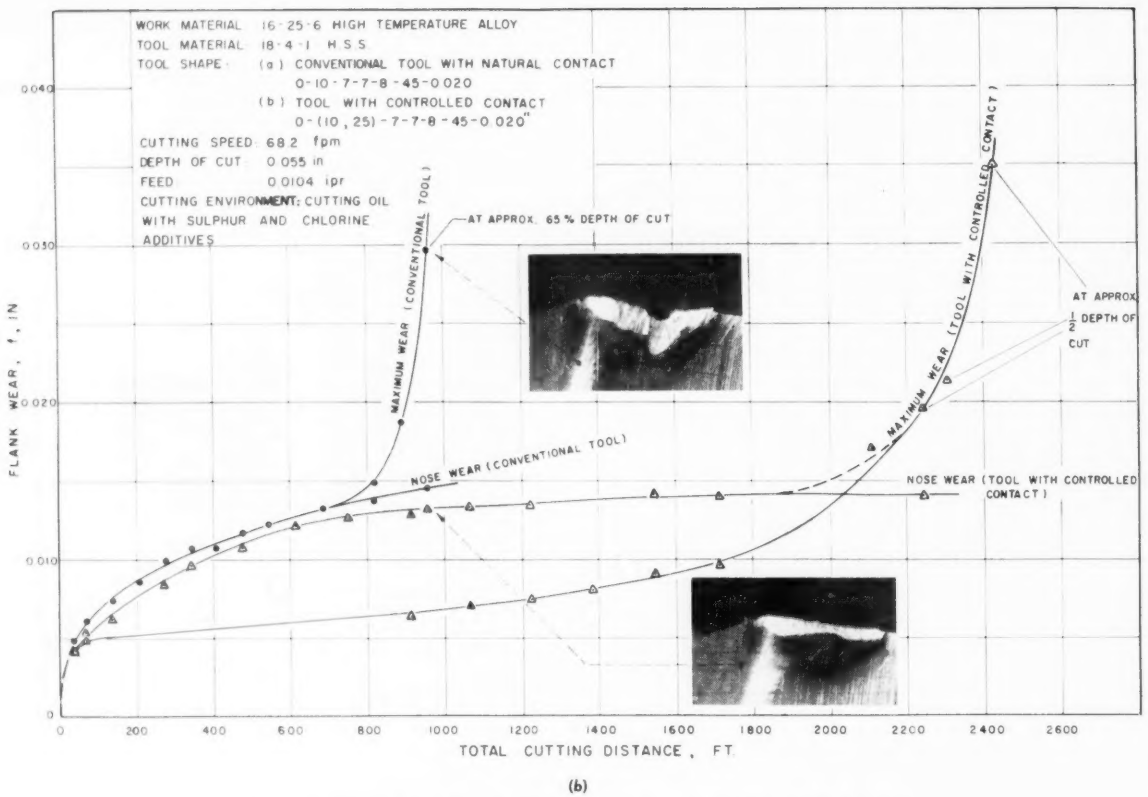

(b)

Fig. 9 Comparative tool life: Conventional tool versus tool with controlled contact

this represents a decrease of about 30 per cent. Similar reductions but of less extent have been noted in the machining of steel.

After the tool has been in use for some time, wear develops both at the top surface and at the flank. The development of the crater wear will cause contact to spread to the secondary rake surface. In order to ascertain the saving in power consumption for actual machining operations, tool-force data have been continuously monitored during prolonged cutting. The results are shown plotted in Fig. 10. In the 30-minute cutting period, the saving in power consumption amounts to over 17 per cent.

Conclusions

(A) Of Theoretical Interest

1 The dynamic shear stress of a metal may be regarded as a constant in commercial high-speed machining operations.

2 Tool-chip contact length, through its influence on chip asperity flow stress, is a major factor influencing interface friction. Temperature variations, both chip bulk temperature and interface temperature, play a secondary role.

3 The restraining effect, as asperity population density increases, has a pronounced influence on asperity flow stress.

4 Reduced contact cutting tools provide a valuable means for study of the basic problems in the mechanics of chip formation.

(B) Of Practical Utility

5 The measured tool-chip interface temperature decreases to a minimum as the length of tool-chip contact is reduced to about $^1/_3$ of the natural value.

6 Machining with tools of properly controlled contact results in longer tool life, greater effectiveness (good or bad) of cutting fluids, improvement in surface finish, and reduction in power consumption.

Acknowledgments

The authors express their appreciation to the Office of Ordnance Research, U. S. Army, for support of the program; to Kennametal, Inc., Latrobe, Pennsylvania, for the carbide tools used in the investigation; to Mr. Y. J. Hu, Department of Mechanical Engineering, University of Illinois, for his valuable work in the research; and to Mrs. Betty Turcott for her patience and skill in preparing the manuscript.

References

1 M. E. Merchant, "Basic Mechanics of the Metal-Cutting Process," *Journal of Applied Mechanics*, vol. 11, TRANS. ASME, vol. 66, 1944, pp. A-168–175.

An earlier Finnish paper by V. Piispanen in 1937 was cited by Merchant. Piispanen's approach is very similar to that of Merchant.

2 A. L. DeLeeuw, "Metal Cutting Tools," McGraw-Hill Book Company, New York, N. Y., 1922, p. 18.

3 H. Klopstock, "Recent Investigations in Turning and Planing and a New Form of Cutting Tool," paper presented at the Spring Meeting of THE AMERICAN SOCIETY OF MECHANICAL ENGINEERS, 1925.

4 E. G. Herbert, "Cutting Tools Research Committee, Report on Machinability," The Institution of Mechanical Engineers, London, England, part V, 1928, pp. 19–21.

5 E. Almdale, "Chip Control When Machining Steel With Carbide," *Tool and Die Journal*, vol. IX, 1943, pp. 105–109.

6 J. B. Armitage and A. O. Schmidt, "An Investigation of

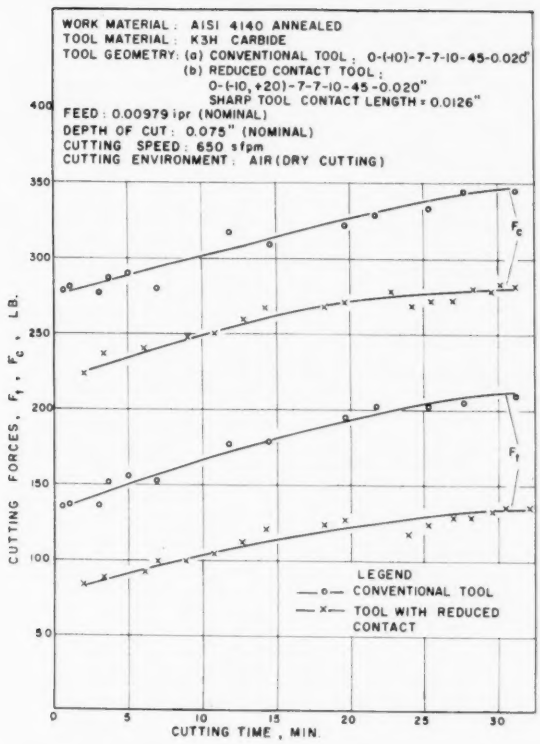
WORK MATERIAL : AISI 4140 ANNEALED
TOOL MATERIAL : K3H CARBIDE
TOOL GEOMETRY: (a) CONVENTIONAL TOOL : 0-(-10)-7-7-10-45-0.020"
(b) REDUCED CONTACT TOOL :
0-(-10, +20)-7-7-10-45-0.020"
SHARP TOOL CONTACT LENGTH = 0.0126"
FEED : 0.00979 ipr (NOMINAL)
DEPTH OF CUT : 0.075" (NOMINAL)
CUTTING SPEED : 650 sfpm
CUTTING ENVIRONMENT : AIR (DRY CUTTING)
CUTTING FORCES, F_f, F_c, LB.
CUTTING TIME, MIN.
F_c
F_f
LEGEND
—o— CONVENTIONAL TOOL
—x— TOOL WITH REDUCED CONTACT

Fig. 10 Tool forces during prolonged cutting: Conventional tool versus reduced contact tool

Radial Rake Angles in Face Milling," TRANS. ASME, vol. 66, 1944, pp. 633–643.

7 B. T. Chao and K. J. Trigger, "Cutting Temperatures and Metal-Cutting Phenomena," TRANS. ASME, vol. 73, 1951, pp. 777–793.

8 B. T. Chao and K. J. Trigger, "Temperature Distribution at the Tool-Chip Interface in Metal Cutting," TRANS. ASME, vol. 77, 1955, pp. 1107–1121.

9 K. J. Trigger and B. T. Chao, "The Mechanism of Crater Wear of Cemented Carbide Tools," TRANS. ASME, vol. 78, 1956, pp. 1119–1126.

10 H. Schallbroch, H. Schaumann, and R. Wallichs, "Testing for Machinability by Measuring Cutting Temperatures and Tool Wear," *Vortrage den Hauptversammlung der Deutsche Gesellschaft für Metallkunde*, VDI Verlag, 1938.

11 B. T. Chao and K. J. Trigger, "Temperature Distribution at Tool-Chip and Tool-Work Interface in Metal Cutting," TRANS. ASME, vol. 80, 1958, pp. 311–320.

12 K. J. Trigger and B. T. Chao, "An Analytical Evaluation of Metal-Cutting Temperatures," TRANS. ASME, vol. 73, 1951, pp. 57–68.

13 B. T. Chao, K. J. Trigger, and L. B. Zylstra, "Thermophysical Aspects of Metal Cutting," TRANS. ASME, vol. 74, 1952, pp. 1039–1054.

14 H. Takeyama and E. Usui, "The Effect of Tool-Chip Contact Area in Metal Machining," TRANS. ASME, vol. 80, 1958, p. 1089.

15 B. T. Chao and G. H. Bisacre," The Effect of Speed and Feed on the Mechanics of Metal Cutting," *Proceedings of The Institution of Mechanical Engineers*, vol. 165, 1951, W.E.P. no. 63, pp. 1–13.

DISCUSSION

P. Albrecht[3]

The chip-tool contact length in metal cutting is usually allowed to assume a "natural length" which depends on a number of cutting conditions. Restricting artificially this contact length or "controlling" it, as the title of the paper says, one obtains a new variable in tool geometry.

The study of effects of this variable upon the cutting process is at present being given far more attention than in the past, and this paper is a significant contribution to the study of the role which the chip-tool contact length plays in metal cutting.

There is, however, another new variable which will be introduced into the cutting process as soon as the chip-tool contact length is restricted. To show the meaning of this second variable let us first look at a conventional situation—unrestricted chip-tool contact and tool-flank clearance angle, Fig. 11(*a*). The tool-flank clearance angle is a well-known and indispensable feature of every cutting tool in metal cutting, the purpose of this angle being to prevent excessive rubbing between the tool and workpiece surface.

Now considering generally the restriction of chip-tool contact one can see that probably the most practical way of achieving such restriction would be the introduction of a "tool-face clearance angle," Fig. 11(*b*). The tool-face clearance angle then is the second variable we introduce in the cutting-tool geometry together with restricted chip-tool contact length. The tool-face clearance angle provides a clearance between the chip and tool face in a direct analogy to the tool-flank clearance angle which provides a clearance between the workpiece and tool. We can even say that the tool-face clearance reduces excessive rubbing between the chip and tool in exactly the same manner. The results presented in Fig. 7(*a*, *b*) show friction force being reduced when clearance between the chip and tool face is provided.

As we have seen there is a similarity in the meaning and effect of both clearances angles, the first on the tool flank and the

[3] Senior Research Engineer, Physical Research Department, The Cincinnati Milling Machine Company, Cincinnati, Ohio.

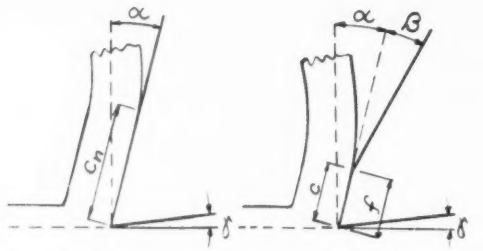

c_n = natural chip-tool contact length
α = rake angle
γ = tool flank clearance

f = restricted tool face width
c = chip-tool contact length
α = rake angle
β = tool face clearance angle
γ = tool flank clearance angle

Fig. 11(a) Conventional tool geometry: Unrestricted tool face width

Fig. 11(b) Relieved tool face geometry

other on the tool face. It would also be interesting to follow the differences between these two clearances. The main difference would lie in the fact that the tool-flank clearance can start from the cutting edge leaving only the cutting edge to rub against the workpiece surface, whereas tool-face clearance cannot start from the cutting edge if a clearance effect is to be obtained. A certain "width of tool face" (or restricted chip-tool contact length) should be left. Otherwise, starting to clear on the tool face directly from the extreme cutting edge, we obtain just a tool with increased rake angle and a natural chip-tool contact length. On the other hand, if the tool-face width is greater than the natural chip-tool contact length, the clearance of the tool face, naturally, would have no effect upon performance of the tool. Between these limits clearance of the tool face has an effect upon the performance of the tool.

Now let us consider the possible effects of the magnitude of tool-face clearance angle. We can expect in advance that the variation of the tool-face clearance angle may have a more pronounced effect upon the cutting process than the variation of the clearance angle on the tool flank. This may be expected because the flank-clearance angle provides a clearance between the tool and workpiece both of which are very rigid, and do not change shape appreciably during cutting. Contrary to that, the tool-face clearance angle provides a relief between the tool which is rigid and the chip which is comparatively flexible. Even at the point where the face clearance starts, the chip undergoes a change of shape from being straight, as it runs along the tool face, to being curled at the point when it leaves the tool face. Here a situation may arise when the chip is only partially cleared by the tool-face clearance angle.

As Fig. 12(c) illustrates, in such a case the chip is in contact not only with the tool face but also at some length beyond where clearance starts. Such a situation of partial clearance occurs when the tool-face clearance angle is very small or the remaining tool-face width is small, of the order of uncut chip thickness t_1 or less. For instance, if only the width of the tool face is altered, Fig. 12, in an experiment, and tool-face clearance angle is kept constant and large enough to clear the chip at the beginning of reduction of the chip-tool contact, Fig. 12(b), then for a certain reduced tool-face width the tool-face clearance angle ceases to clear the chip completely, Fig. 12(c).

Further reduction of the tool-face width increases the chip contact over the relieved area until the tool-face width is zero, Fig. 12(d). Here we have again a conventional tool shape with a rake angle increased by the magnitude of tool-face clearance angle β. Fig. 12(c) shows actually that the chip-tool contact does not necessarily decrease when the width of the tool face is reduced beyond a certain minimum. The chip simply starts to be supported by the relieved portion of the tool face and the contact area increases with decreased tool-face width.

These considerations lead to the conclusion that the chip-tool contact area is not always identical with the restricted width of the tool face. Fig. 13 shows qualitative relation between the actual chip-tool contact length c and the width of the restricted tool face f, the letters indicating the portions of the curve correspond to the conditions illustrated in Fig. 12.

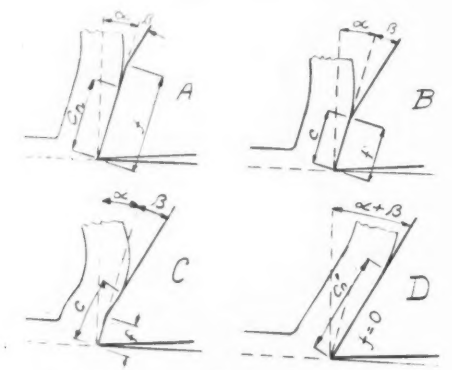

Fig. 12

A Relieved tool face does not reduce the chip-tool contact length when the tool face width is larger than the natural chip-tool contact length $f > c_n$.

B Reduction of chip-tool contact c is obtained when the tool face width f is smaller than the natural chip-tool contact length c, $f < c_n$. Chip-tool contact is equal to the reduced tool face width, $c = f$.

C Further reduction of f results in a partial clearance of the chip and the chip-tool contact is greater than the tool face width, $c > f$.

D Original tool face reduced to zero, $f = 0$, and because of that a cutting tool of a higher rake angle $\alpha + \beta$ is obtained. A different natural chip-tool contact length c_n' would correspond to this new rake angle of the tool.

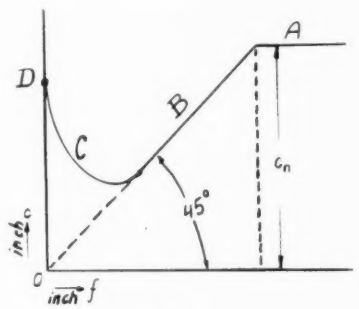

Fig. 13

Qualitative relation between the actual chip-tool contact length c and the width of the restricted tool face f. Portions of the curve A, B, C, and point D correspond to the conditions illustrated in Fig. 12.

Portion A of the curve in Fig. 13 corresponds to a condition where the tool-face width is greater than the length of the natural tool-chip contact as shown in Fig. 12(a). Here relief of the tool face does not restrict the chip-tool contact. Reducing the width of the tool face f we come to the point where the tool-face width and the chip-tool contact length are equal, at the beginning of the section B of the curve. From here on a 45-deg line, B passing through zero shows that the tool-face width is smaller than the natural chip-tool contact length and that the chip-tool contact c is reduced and equal to the width f, Fig. 12(b).

Reducing further the width of the tool face f we would naturally never reach a "zero contact length" between the chip and the

tool simply because the stress on the contact area reaches the plastic-flow limit of the chip material and the chip will yield, thus increasing the contact area again as Fig. 12(*c*) shows. Further reduction of f would be accompanied by the increase of contact length on the relieved portion of the tool face, and when $f = 0$ the chip-tool contact length will reach a natural value OD, Fig. 13, for a tool with an increased rake angle as shown in Fig. 12(*d*).

Now let us look at the Fig. 6(*a*) where the variation of the apparent stress at the chip-tool contact is presented. In the light of the foregoing considerations we can see that the curve shown for H_a would not increase still further in the vicinity of zero but will reach a certain maximum because the chip-tool contact area reaches a certain minimum (according to Fig. 13). Then, of course, the H_a curve will turn down as the tool-face width decreases and at zero will reach a value corresponding to that of the increased rake-angle tool as shown in Fig. 12(*d*). The shape of such a curve is given in Fig. 14. A similar trend would hold for curve S_a.

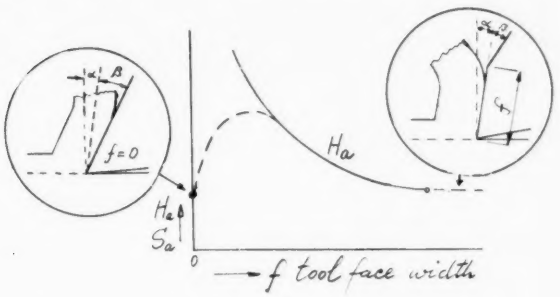

Fig. 14

Effect of partial clearance would bring the curve H_a down again in the region of small values of f.

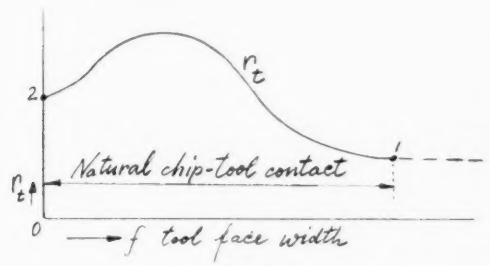

Fig. 15

Variation of chip thickness ratio, Fig. 4 of the paper. On the right side the curve levels to a horizontal line after point 1. At the zero width or original tool face the curve reaches point 2 which would lie higher than the horizontal line on the left side, because the chip thickness ratio is usually higher for a higher rake angle.

Fig. 4, showing variation of chip-thickness ratio, can be made more complete by extending the curve to point 2 as shown in Fig. 15. Point 2 should lie higher than point 1 because the chip-thickness ratio usually increases with rake angle.

Similar alterations of the curve trend for the small tool-face width are appropriate also for Figs. 7(*a* and *b*). Here the forces N and F at the point where the tool-face width is zero will reach values corresponding to the conventional tool geometry with an increased rake angle shown in Fig. 12(*d*).

Furthermore, curves for the shear strain and extrapolated portions of the temperature curves can be partly altered and made more complete in accordance with the foregoing considerations showing that the restriction of chip-tool contact is possible only up to a certain limit where the chip materials start to yield plastically and a transition to the tool with a higher rake angle will begin.

M. C. Shaw[4]

The authors have presented interesting data concerning the performance of cutting tools with artificially limited contact lengths. One of the most interesting observations that have been made concerns the influence that a reduction in contact length has upon the apparent shear and normal stresses on the tool face, Fig. 6. Here it is evident that the shear stress increases more slowly than does the normal stress when the contact length between chip and tool is reduced, which in turn causes a reduction in the so-called coefficient of tool-face friction with contact length. This behavior was predicted in a discussion of the friction process in cutting previously published in this journal.[5] Here it was reasoned that for ordinary friction sliders the real area of contact, A_R, is a very small percentage of the apparent area of contact, A, and under such conditions the plastic flow associated with sliding is predominantly confined to surface asperities. It is under such conditions ($A_R/A << 1$) that Amonton's law of friction holds, which states that the shearing frictional stress for a slider is proportional to the normal stress. Amonton's law holds in region A of Fig. 16.

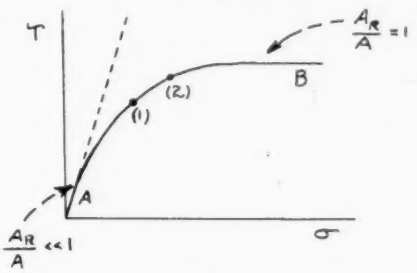

Fig. 16

At the other end of the friction spectrum we have the case where all of the plastic flow associated with sliding occurs within the bulk of the metal. In this case $A_R = A$ and we encounter a shear plane within a solid metal. Here, as is well known, the shear stress is independent of normal stress, and this condition is illustrated by B in Fig. 16. Intermediate values of A_R/A will be found along the connecting curve. Under normal metal-cutting conditions the ratio (A_R/A) is intermediate between that at A and B (such as point 1 in Fig. 16), since the normal stress on the tool face is a very high but finite value. When the contact length is artificially reduced, the operating point will shift from 1 to 2 in Fig. 16, and it is evident that the normal stress will increase a greater amount than does the shear stress, a result which is in agreement with the authors' findings in Fig. 6.

One of the important quantities the authors have not discussed in connection with limited tool-face contact length is *chip curvature* or *curl*. In this paper the authors have studied but one method of varying contact length, namely, the geometrical one of grinding material away from the tool face, so that it is not possible to have extensive contact. Chip curl is the natural way in which a variation of contact length is effected under ordinary machining conditions. When an effective low-speed cutting fluid is used (such as CCl_4) the primary influence this material has is not in the lubrication of the tool face, as is commonly thought,

[4] Professor of Mechanical Engineering, Massachusetts Institute of Technology, Cambridge, Mass. Mem. ASME.

[5] I. Finnie and M. C. Shaw, "The Friction Process in Metal Cutting," TRANS. ASME, vol. 78, 1956, p. 1649.

but is rather associated with a change in chip curvature. This, in turn, causes a reduction in the chip-tool contact length which has just as dramatic an effect upon cutting forces and tool performance as the geometrically produced reductions in area that are here discussed by the authors. A detailed discussion of this new view of the action of cutting fluids was given in a paper presented at the 1958 Annual Meeting of the American Chemical Society in Chicago.

The authors infer that a cutting fluid which functions by chemical action (i.e., a fluid containing sulfur or chlorine) will be more effective when used in conjunction with a limited-contact tool than when used with a tool of conventional design. The reasoning behind this statement is clear and lies in the reduction in contact length, making it easier for the fluid to penetrate the shorter distance to the tool tip. However, there are two additional actions which are overruling and which result in there being a smaller rather than a larger percentage improvement in performance when a good cutting fluid (such as CCl_4) is used at low speed with a tool of reduced contact length:

1 The major improvement to be derived from the fluid which lies in a reduction in contact length is anticipated by the geometrical reduction in contact length and hence cannot be realized.

2 The geometrical limitation of contact length causes an appreciable increase in the normal stress on the tool face (and hence causes an increase in A_R/A) which in turn makes it more difficult for the fluid vapor to find its way to the tool point so that it can act chemically.

The increased improvement found with a cutting fluid by the authors resulted from cooling and not from chemical action. It was found by the authors that a reduction in contact length improved tool life in all cases except one; i.e., when a hardened steel was cut (48 R_c). In this case the intensification of normal stress associated with the reduction in contact length gave a tool temperature that was too high. A similar result was found by Zlatin and Gould.[6] In this case it was found that lead was beneficial to tool life in all cases except when the workpiece was hard (R_c 40). One of the major effects of lead in steel is to increase chip curvature and thus reduce contact length. As in the case of the authors' results a reduction in contact length was beneficial except when the steel was very hard. It is possible still to achieve a gain due to reduction in contact length in such cases if the chip and tool are strongly cooled (no cutting fluid was used in the Zlatin-Gould tests). This was apparently the case in the authors' test. From the improved effect of the cutting fluid observed with reduced contact length in this case it should not be concluded that such an effect will always be associated with a fluid; as for instance, at lower speeds where the major function of the fluid ceases to be of a cooling nature and shifts to one of chemical origin. In cases where chemical action is predominant the reduction in contact length should hinder, not aid, the penetration of fluid between chip and tool.

In addition to the cutting fluid there are several other methods of naturally increasing chip curl and thus in reducing chip-tool contact length.

Authors' Closure

The authors wish to thank both discussers for their interesting comments. Dr. Albrecht's remarks concerning the influence of secondary tool-face contact are very pertinent. The reverse in the trend of variation of r_t with decreasing length of tool chip contact, as shown in Fig. 4 of the paper, has been found to coincide with the occurrence of secondary tool-face contact. Recent data indicate that the extent to which the primary contact length may be restricted without causing secondary contact depends, among other things, on the secondary rake angle β.[7] Let this limiting, or critical, length of primary contact be designated by f_{cr}. For the machining of electrolytic copper with HSS tools, it has been found that $f_{cr}/t_1 \simeq 2$ for $\alpha = 6$ deg, $\beta = 24$ deg, and $t_1 = 0.00492$ ipr. Changing the cutting speed from 250 fpm to 500 fpm produces no noticeable effect on this ratio. On the other hand, when β is increased to 64 deg, f_{cr}/t_1 becomes less than 0.75 under otherwise identical conditions. Fig. 17 illustrates the variation of measured chip-thickness ratio with the reduction of primary cutting-edge width. The precise value of f_{cr} for the second case was not obtained due to the poor mechanical strength of the tool edge. Interpretation of H_a and S_a, as shown by the dotted portion of the curve in Fig. 14, becomes difficult since even the averaged stresses at the primary and secondary contact surface will be very different. Dr. Albrecht stated: "There is, however, another new variable which will be introduced into the cutting process *as soon as* the chip-tool contact length is restricted."

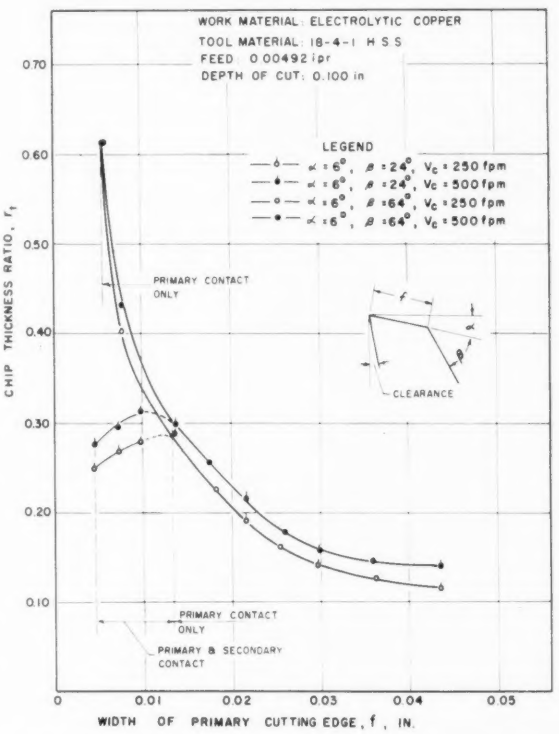

Fig. 17 Influence of primary cutting-edge width on chip-thickness ratio

With this, the authors cannot concur since a two to threefold increase in H_a may be readily experienced without the occurrence of secondary contact. The primary purpose of the paper was to evaluate the theoretical as well as practical implications of machining with a controlled contact tool in which the contact between the chip and tool was essentially on the primary rake surface. The regime of investigation corresponds to portion B in Fig. 13, which may extend to nearly $^3/_4$ of the length of the 45-deg line shown.

Professor Shaw's comments regarding the influence of the ratio of apparent-to-real areas of contact on tool-chip friction behavior are in harmony with the view expounded in the paper. In fact,

[6] N. Zlatin and J. V. Gould, "The Effect of a Lead Additive on the Machinability of Alloy Steels," published in this issue, pp. 131–138.

[7] β was referred to as tool-face clearance angle by Dr. Albrecht.

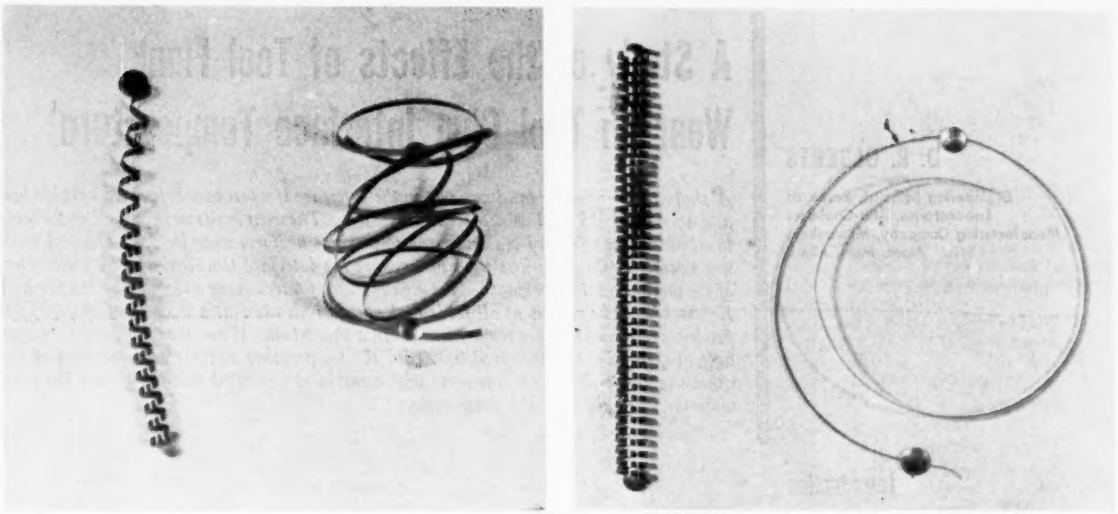

Tool: K3H carbide
Work: AISI 4140 annealed
Tool shape: per Fig. 9(*a*)
Sfpm: 700

Feed: 0.0098 ipr
Dry cut
Left: Reduced contact
Right: Natural contact

Tool: TI HSS
Work: 16-25-6 alloy
Tool shape: per Fig. 9(*b*)
Sfpm: $68\frac{1}{2}$

Feed: 0.0104 ipr
Fluid: Cutting oil with additives
Left: Reduced contact
Right: Natural contact

Fig. 18 Chip curl as influenced by contact length

the results shown in Fig. 6 are, perhaps, the best supporting evidence of the empirical relationship depicted in Fig. 16 when A_R/A is close to unity.

The authors have only recently had the opportunity to study the *new* view proposed by Professor Shaw in the paper, "On the Action of Metal-Cutting Fluids at Low Speeds," referred to in his discussion.

Representative data presented in his paper for the cutting of B1213 steel and lead with HSS tools in the presence of various cutting fluids were obtained at a cutting speed of 1 in/min. Contact asperity conditions, strain rate, strain gradient, adiabaticity, reaction time, etc., in a process under such conditions are vastly different from those which obtain under the conditions cited in the authors' paper (68. + fpm with HSS tools and up to 700 fpm with carbides).

Since the preparation of the paper numerous tests on Timken 16-25-6 alloy, CF4 and CF8 austenitic stainless-steel castings with HSS tools under dry cutting conditions have demonstrated the improvement possible with controlled contact tools. The tool life expressed in flank wear is 20 to 30 per cent longer with tools having the contact restricted to about $\frac{1}{2}$ of the natural value. The surface finish improvement was particularly noticeable in the soft CF4 and CF8 alloys.

Restriction of contact area has the effect of "hardening" a soft material in so far as surface finish and tool-chip friction are concerned.

If a cutting fluid is more active to the tool than to the work, flank wear is accelerated (compared to dry cutting) and the effect is more pronounced with reduced contact tools.

During the course of the investigation it was observed that artificially restricting the tool-chip contact had a significant influence on chip curl. Reduction in contact length (except to below the limiting value) was accompanied by an increase in chip curvature. Fig. 18 illustrates the effect. Zlatin and Gould[8] report a lower coefficient of friction for leaded steels in several conditions and refer to the "more tightly curled chip." It has often been stated that the chip is born curled. Professor Shaw contends that chip curl is the fundamental variable which controls tool-chip contact (and influences the friction there). The authors contend that tool-chip interface friction (whether altered by contact length, lead, and so forth) is more basic and that chip curl is the result rather than the cause. They cannot agree that observations made at cutting speeds of 1 in/min (where the cutting-fluid action is of a chemical nature) are representative of conditions at speeds many hundredfold higher (where the cutting-fluid function is principally cooling).

A Study of the Effects of Tool Flank Wear on Tool Chip Interface Temperature[1]

D. R. OLBERTS

Engineering Scientist, Research Laboratories, Allis-Chalmers Manufacturing Company, Milwaukee, Wis. Assoc. Mem. ASME

A study of the effect of land wear upon the interface temperature between a carbide tool and an AISI 1015 steel workpiece is presented. The wear lands were ground on the tools to eliminate the effects of cratering and to produce uniform wear lands. The tool-work thermocouple technique was used to measure the interface temperature. A calibration of the thermocouple was obtained through the use of a technique suggested by Backer and Krabacher. The results at all feeds and speeds indicate that a wear land of 0.010 in. produces a lower interface temperature than a sharp tool. When the wear land increases beyond 0.010 in. to 0.020 and 0.030 in. the temperature again rises. Studies of the variation of the chip thickness ratio with wear land indicated that the greater the land wear the lower the chip thickness ratio.

Introduction

THE TEMPERATURES of the cutting tool and its role in determining tool life were first emphasized by Taylor [1][2] in his book "On the Art of Cutting Metals." Since then many articles have appeared on the measurement of tool temperatures and the correlation of tool temperature with tool life.

One approach to the problem has been to study the effect of land wear on tool-work and tool-chip interface temperature. Chao and Trigger [2] have presented an analytical means that will allow calculation of temperatures throughout the interface and the effect of land wear upon the interface temperature.

A different approach was used in the present study in that an experimental determination of the effect of ground-on-wear land on interface temperature was made. Wear lands were ground on the tools to eliminate crater wear as a variable and to provide uniform and accurate wear lands. The experimental variables were land wear, cutting speed, and cutting feed. The tool-work thermocouple technique was used to determine interface temperatures.

Experimental Setup

The experimental setup is illustrated in Fig. 1. The thermoelectric circuit used is similar to that described by Trigger [3]. The machining experiments were conducted on a 14-in. Reed-Prentice Corp. lathe. The workpiece was an annealed AISI 1015 seamless steel tube of 0.250-in. wall thickness and $6^{3}/_{4}$ in. outside diameter which was machined down to a wall thickness of 0.156 in. and an outside diameter of $6^{21}/_{32}$ in. The tube was held firmly in a four jaw chuck and tube distortion caused by chuck pressure was minimized with a heavy plug which was pressed in the chuck end of the tube (see Fig. 2). All cutting experiments were conducted dry.

The tip shape and the design of the tool holder are shown in Fig. 3. The carbide inserts were Grade NS-6, "Newcomer" blank No. 1490. Five tools were made so that five different wear lands could be ground at the same time and thus produce

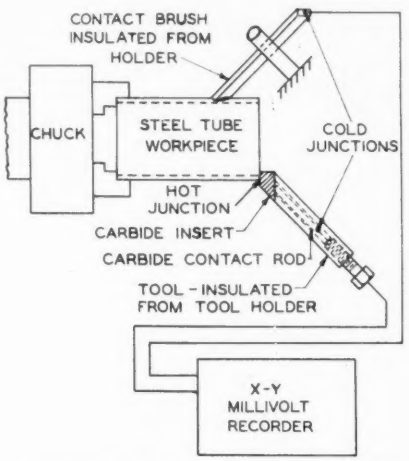

Fig. 1 Experimental setup used to determine cutting temperatures

wear land and tool geometries as similar as possible. The clearance faces, rake angles, and wear lands were ground with a Norton tool grinder using a 6-in. diam, 120-grit diamond wheel. The width of the wear lands were checked with a Bell & Howell Co., optical "Pocket Comparator."

The y co-ordinate of the x-y millivolt recorder was supplied with a voltage that increased uniformly with respect to time, thereby providing cutting time as one co-ordinate and the tool-work thermocouple output as the other. Iron-constantan thermocouples were brazed to the reference end of the carbide rod and workpiece brush to monitor the reference junction temperatures during experimentation.

Calibration Procedure

Several different ways of calibrating the tool-work thermocouple were studied. Most of the calibration methods required a fairly long cycle time to insure that the tool-work thermocouple and reference thermocouple remained at equal temperatures. It was found that a long calibration cycle was not convenient with the short carbide rod used in this investigation because the cold junction of the rod heated up thereby causing an inaccurate calibration.

The simplest and by far the quickest method found to calibrate the thermocouple was similar to the technique suggested by

[1] This paper is based on a thesis submitted in partial fulfillment of the requirements for the degree of Master of Science (Mechanical Engineering) at the University of Wisconsin, 1958.

[2] Numbers in brackets designate References at end of paper.

Contributed by the Production Engineering Division and presented at the Semi-Annual Meeting, Detroit, Mich., June 15–19, 1958, of THE AMERICAN SOCIETY OF MECHANICAL ENGINEERS.

NOTE: Statements and opinions advanced in papers are to be understood as individual expressions of their authors and not those of the Society. Manuscript received at ASME Headquarters, March 31, 1958. Paper No. 58—SA-41.

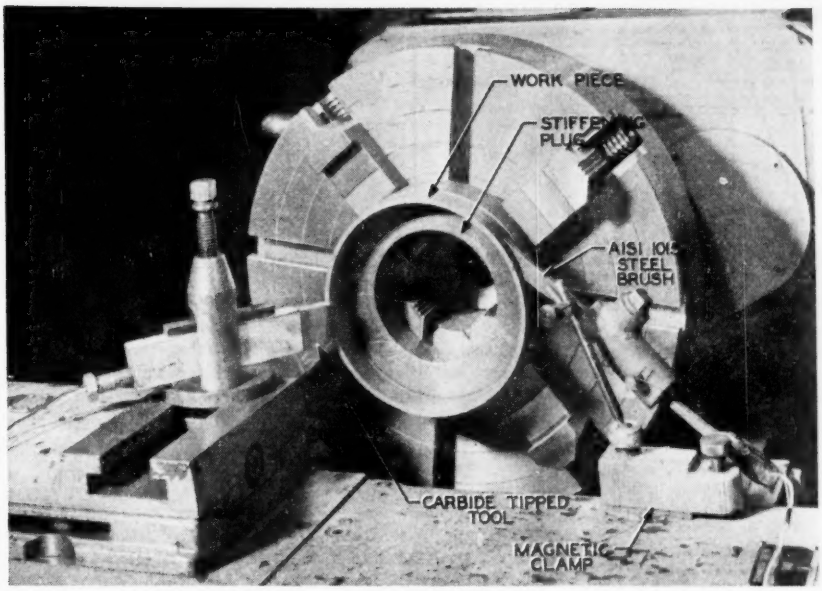

Fig. 2 The workpiece, tool, and brush in cutting position for determination of interface temperature

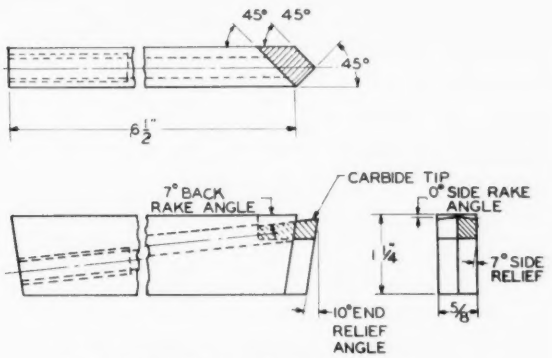

Fig. 3 Tool used for determination of interface temperature

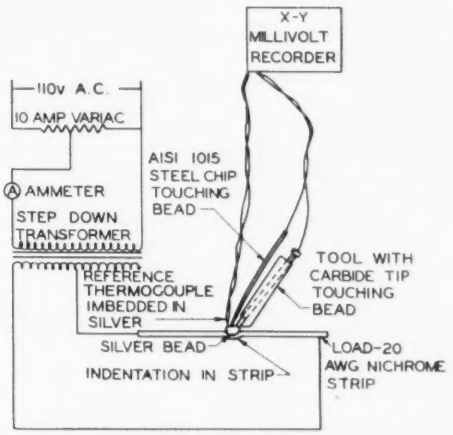

Fig. 4 Experimental setup used to calibrate tool-work thermocouple

Backer and Krabacher [4]. The setup is shown in Fig. 4. In this technique a reference thermocouple and the tool-work thermocouple were heated simultaneously in a manner that maintained the temperature of the two thermocouples essentially equal at all times. The output of each thermocouple was recorded on an x-y millivolt recorder. Since the output of the reference thermocouple with respect to temperature was known, the record provided a simple calibration chart for the tool-work thermocouple.

The two thermocouples were maintained at equal temperatures by placing the reference thermocouple in a $^1/_4$-in. diam bead of silver. The carbide rod and a chip from the workpiece were then touched on the surface of the bead. The bead was placed against a nichrome strip which was heated by passing a large electrical current through it. The good thermoconductivity of the silver insured that temperature gradients in the bead were small. The bead was heated rapidly, but at a rate below the response rate of the recorder. After about 15 seconds the temperature approached the melting point of the silver and the electric current was shut off. The temperature in the bead dropped to near room temperature in about three minutes and provided a check on the amount of variation in temperature between the two thermocouples. The more the temperature variation, the greater was the spread between the increasing and decreasing curve.

Each of the five tools used in this study was calibrated. A comparison of the calibration curves revealed that three of the five tools had calibration curves that were the same, but which differed substantially from the other two which were also the same. Fig. 5(a) shows the calibration curve obtained with the three tools, and Fig. 5(b) the curve obtained with the other two tools. A calibration curve was also obtained with the carbide rod and the chip. This curve coincided with curve (b).

Each of the calibration curves was reproducible within ±25 F. Room temperature, which was 80 F, was used as a reference junction temperature. As may be seen in Fig. 5, the calibration curve was not linear but appeared to be formed of two linear parts joined by a gradual bend. The upper part of the calibration curve was found to be linear up to about 1600 F (the melting point of the silver bead). For higher temperatures, the upper part of the calibration curve was assumed to continue on linearly.

Trigger [3] has pointed out that slight differences between the

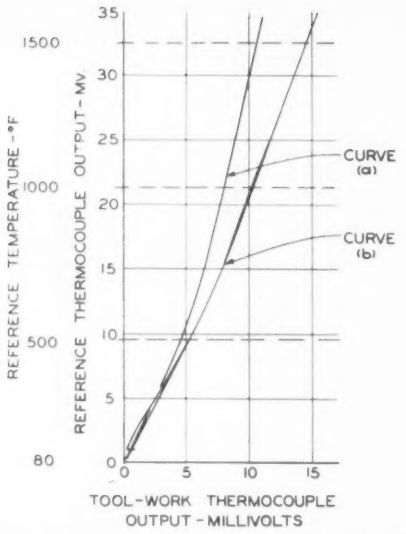

Fig. 5 Typical calibration curves for grade NS-6 carbide-AISI 1015 steel, tool-work thermocouple, (a) curve obtained with three carbide tips, (b) curve obtained with two tips that had same composition as the carbide rod

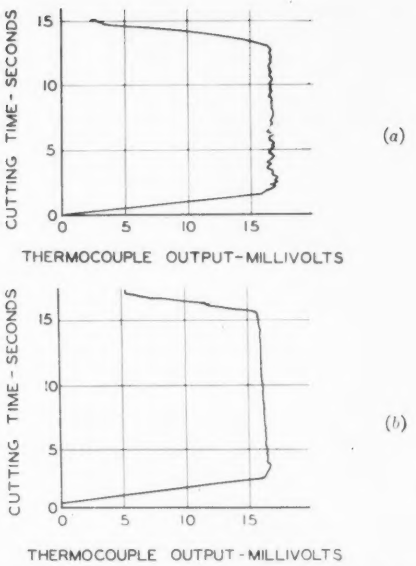

Fig. 6 Recording of tool-work thermocouple output for NS-6 carbide tool and AISI 1015 steel workpiece

(a) Feed: 0.075 ipr Land wear: 0.030 in.

(b) Feed: 0.015 ipr Land wear: 0.010 in.

chemical composition of a carbide tip and carbide rod can cause a considerable change in the emf output of a tool-work thermocouple. Apparently, two of the tips and the carbide rod were of the same exact chemical composition, while three of the tips were of a slightly different composition. The existence of this difference between the three tips and the rod might be significant because as the carbide tip heats up during a cutting operation a parasitic emf would be generated between the carbide rod and the dissimilar tip material. This emf could obscure the main emf generated at the cutting interface.

An experiment was conducted to see whether or not a parasitic emf would be generated between one of the three like carbide tips and the carbide rod. The normal calibration procedure was followed except that when a silver bead temperature of 1400 F was reached, a torch flame was played upon the carbide tip in the vicinity of the tip-rod junction. This heated the tip to about 270 F and altered the calibration curve by up to 50 F. Because the temperature at the junction of the tool tip and the carbide rod seldom rose above 145 F and never above 165 F during the machining experiments, any errors in temperature measurements that may have been caused by a parasitic emf did not appear to be significant enough to alter the temperature trends found in this investigation.

Several machining experiments confirmed these conclusions. In these experiments the same wear land was ground on both of the two types of tips and cuts were made with each tool under the same cutting conditions. The temperatures obtained were either the same or the differences were within the possible experimental error.

Experimental Procedure

The tube was first turned and bored to size. The tool to be experimented with was then placed in the tool post and the wear land aligned with the end of the tube so that an end cut could be made. This gave a two-dimensional or orthogonal cut. The proper speed and feed were set up on the lathe, the millivolt recorder zeroed, and readings taken of the temperatures at the reference junctions. The lathe was then started and the feed mechanism placed in gear. Just before the tool touched the workpiece, the time-proportional-voltage generator of the x-y recorder was started. After 10 to 20 seconds of cutting, the lathe was stopped and final readings of the reference junction temperature were taken. This procedure was repeated for all of the cutting conditions.

In this manner the emf output of the tool-work thermocouple was determined with tools having ground on wear lands of 0.000, 0.010, 0.020, 0.030, and 0.040 in.; with lathe speeds of 145, 283, 457, and 532 sfm; and feeds of 0.0075 and 0.015 ipr. The depth of cut was constant at $^5/_{32}$ in. and corresponded to the tube wall thickness.

Chip specimens were also obtained at the start and near the finish of each cut. Several 10-in. lengths of tube were used to complete the experiments. Each 10-in. tube was cut from the same 20-ft length of commercial tube to insure that the chemical composition and physical properties of the tubes were as uniform as possible. Several reruns of all data were conducted in this manner. The tools were reground for the reruns.

Two typical records of the tool-work thermocouple output versus cutting time are shown in Fig. 6. In general, the record smoothness varied between that of the two examples. The reproducibility for a given run without regrinding was within plus or minus 0.2 millivolt (plus or minus 20 F). With regrinding, 66 per cent of the millivolt readings fell within 0.2 millivolt of the original reading, and in 85 per cent of the cases the spread was 0.3 millivolt or less.

Effect of Land Wear on Temperature

The variation in the interface temperature with land wear for each speed and feed is given in Fig. 7. It is seen that each plot follows a similar pattern. When the wear land was increased from zero to 0.010 in., the interface temperature decreased by up to 110 F. When the wear land increased from 0.010 in. to 0.020 and 0.030 in., the temperature increased, and finally at a 0.040 in. wear land the temperature again decreased.

The initial drop in interface temperature is predicted by the interface-temperature calculations of Trigger and Chao [2].

Table 1 Temperature differences that occur at the tool-work interface when the feed and cutting speed are doubled

Wear land, in. $\times 10^{-3}$	Temperature difference, deg F: Double speed from 145 to 283 sfm at a constant feed of 0.0075 in/rev	Double feed from 0.0075 to 0.015 in/rev at a constant speed of 145 sfm	Double speed from 283 to 537 sfm at a constant feed of 0.0075 in/rev	Double feed from 0.0075 to 0.015 in/rev at a constant speed of 283 sfm	Double feed from 0.0075 to 0.015 in/rev at a constant speed of 532 sfm
0	480	280	200	40	100
10	460	320	245	100	70
20	310	150	265	80	40
30	480	175	180	−10	5
40	335	170	295	30	5

Their work indicates that a noticeable drop in tool-chip interface temperature (up to 100 F) occurs as the wear land increases from zero to about 0.005 in. When the wear land further increases to 0.010 in. the temperature increases slightly.

The tool-work interface temperature, however, is considerably lower than the tool-chip interface temperature as the wear land forms (less than half). The tool-work interface temperature then increases continuously as the wear land increases. The temperature shown on Fig. 7 is an average of these two interface temperatures (except when a sharp tool is used). The drop in the measured interface temperature at 0.010-in. wear land is apparently caused by a combination of the drop in tool-chip interface temperature and the averaging effect of the lower temperature tool-work interface. For greater wear lands the tool-work interface temperature increased substantially and, consequently, the measured temperature increased.

The calculations of Trigger and Chao were not carried out for wear lands larger than 0.010 in. Somewhere between 0.010 and 0.020-in. land wear, the measured interface temperature again equaled that obtained with a sharp tool. Apparently, the tool-work interface temperature became equal to or surpassed the tool-chip interface temperature at this point. The increase in temperature coincides with a rapid increase in the rate of land wear which has been observed experimentally [2].

It is interesting to note that at the highest studied speed of 532 sfm and a feed of 0.015 ipr the average interface temperature did not surpass the temperature obtained with a sharp tool. Crater wear might be expected to be as severe as land wear in this range of feeds and speeds.

Fig. 7 also reveals why, assuming the same cutting speed to start with, a given percentage increase in feed is sometimes more beneficial than a similar percentage increase in cutting speed as far as tool life is concerned. The volume of metal removed is the same, but the increased feed produced a lower interface temperature than did the increased speed.

For example, when the speed was approximately doubled from 145 to 283 sfm, a 480-F increase in temperature occurred with a sharp tool. When the speed was held constant at 145 sfm, and the feed was doubled from 0.0075 to 0.015 ipr, a 280-F temperature increase occurred. The 200-F difference in temperature might well produce a substantial decrease in tool life for the same amount of metal machined.

This comparison is made for higher speeds and other land wears in Table 1. When the speed is increased from 283 to 537 sfm, the temperature increase is smaller than it is when the speed is increased from 145 to 283 sfm; however, the temperature increase in this speed range is still greater when the speed is doubled than when the feed is doubled. Apparently, the advantage of a lower temperature increase for increased feed rather than increased speed holds even at high speeds. Unfortunately, the amount of feed increase obtainable for a given cutting operation is quite limited by lathe rigidity because the cutting force increases considerably with feed while it decreases with speed, other cutting conditions being constant.

Table 1 indicates that the temperature change caused by doubling the feed at a speed of 532 sfm is small and approaches zero with the larger wear lands. It appears that the increased wear land offers more heat-transfer surface which tends to decrease the average interface temperature.

Effect of Speed on Interface Temperature

A log-log plot of the variation in cutting temperature with speed is shown in Fig. 8. According to the general equation $T =$

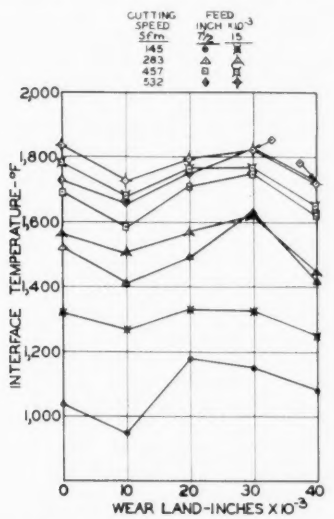

Fig. 7 Variation in interface temperature with ground-on-land wear at various feeds and speeds when end cutting on AISI 1015 steel tube with NS-6 carbide tool

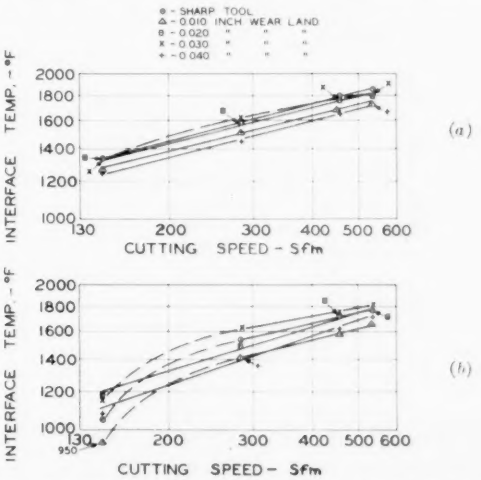

Fig. 8 Relationship between interface temperature and cutting speed for various wear lands and feeds when cutting AISI 1015 steel with NS-6 carbide tool, (a) 0.015 ipr feed, (b) 0.0075 ipr feed

CV^n (where T equals the interface temperature, C equals a constant, V equals the cutting speed, and n equals a constant), the plots should appear as straight lines. This is generally the case with a feed of 0.015 ipr, Fig. 8(*a*). With a feed of 0.0075 in., Fig. 8(*b*), the straight-line relationship holds at the higher cutting speeds, but at the lowest speed studied (145 sfm) the temperature tends to fall away from a straight line.

An inspection of the chips obtained at 145 sfm and feed of 0.0075 ipr revealed that a continuous chip with a built-up edge was formed. The real cutting interface, therefore, existed between steel and steel. As a result, the steel-carbide interface most likely would have been at a somewhat lower temperature than the steel-steel interface where the cutting actually took place. The built-up edge may not have covered the tool-work interface where the wear land occurs. The resultant temperature as indicated by the tool-work thermocouple would then be somewhere between the tool-work interface temperature and the lowered tool-chip interface temperature.

The reason no built-up edge occurred at a speed of 145 sfm and a feed of 0.015 ipr may be explained as follows. It is known that an increase in feed at constant speed will raise the cutting temperature. As the cutting temperature increases the friction coefficient between the tool and chip decreases, tending to lower the amount of adhesion of the chip to the tool. At a certain critical temperature, adhesion will not occur [2]; the result is that the built-up edge is eliminated.

The Effect of Wear Land on Chip-Thickness Ratio

The variation in the chip-thickness ratio with wear land is shown in Figs. 9 and 10. The chip-thickness ratio was determined by the weight-measurement technique wherein a chip of a measured length and width is weighed. Since the chip density, weight, length, and width are known, the thickness can be calculated.

It is seen from Figs. 9 and 10 that the chip-thickness ratio is largest with a sharp tool. As tool wear land was increased the chip-thickness ratio decreased and finally leveled off at 0.040-in. land wear. The results also show that the use of 0.015-ipr feed produced a higher chip-thickness ratio than did the 0.0075-ipr feed. Metal cutting literature in general indicates that the higher the chip-thickness ratio, the better the surface finish of the machined part, the lower the power consumed, the lower the chip temperature as it leaves the tool, the lower the friction coefficient between the chip and the tool, and the longer the wear life. Thus the chip-thickness ratio gives an indication of tool life.

Conclusions

The study of the effects of land wear upon the tool-work interface temperature has indicated that:

1 The average interface temperature decreased slightly as wear land increased from zero to 0.010 in. Such a decrease was observed at 0.010-in. land wear with all of the speeds and feeds studied.

2 When land wear was increased from 0.010 to 0.020 and 0.030 in., the interface temperature increased.

3 A considerably larger increase in interface temperature occurs when the feed was doubled at a cutting speed of 145 sfm than when the feed was doubled at a cutting speed of 532 sfm.

4 The interface temperature at the lowest feed and speed studied (0.0075 ipr and 145 sfm) was lower than a log-log plot of speed versus temperature indicated that it should be. The low temperature was believed to have been caused by a built-up edge that formed at the tool tip.

5 The chip-thickness ratio appeared to give an indication of the degree of tool land wear for wear lands up to 0.020 in. the more the land wear, the lower the chip-thickness ratio.

Acknowledgment

Grateful acknowledgment is made to Mr. R. T. Baugh of the Research Laboratories, Allis-Chalmers Manufacturing Company, for his valuable help in conducting many of the experiments in this investigation.

References

1 F. W. Taylor, "On the Art of Cutting Metals," TRANS. ASME, vol. 28, 1907, p. 31.

2 B. T. Chao and K. J. Trigger, "Temperature Distribution at Tool-Chip and Tool-Work Interface in Metal Cutting," TRANS. ASME, vol. 80, 1958, pp. 311–320.

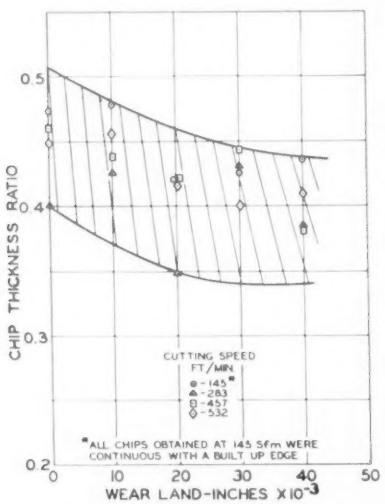

Fig. 9 Variation in chip-thickness ratio with land wear for various cutting speeds when cutting AISI 1015 steel with NS-6 carbide tool. Feed: 0.0075 ipr.

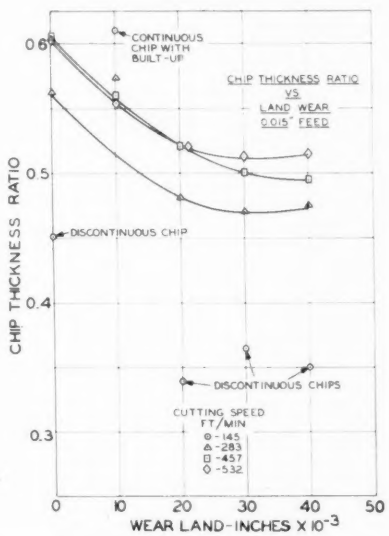

Fig. 10 Variation in chip-thickness ratio with land wear for various cutting speeds when cutting AISI 1015 steel with NS-6 carbide tool. Feed: 0.015 ipr.

3 K. J. Trigger, "Progress Report No. 1 on Tool-Chip Interface Temperatures," TRANS. ASME, vol. 70, 1948, p. 91.

4 W. R. Backer and E. J. Krabacher, "New Techniques in Metal-Cutting Research," TRANS. ASME, vol. 78, 1956, p. 1497.

DISCUSSION

R. E. McKee[3]

The author is to be congratulated on his contribution to the metal-cutting literature in providing further evidence of the effects of flank land on the performance of carbide cutting tools in the machining of a low-carbon steel at specified feeds and depths of cut.

The position of the tool relative to the workpiece represents an ideal condition for forces, wherein the cutting-edge angle is placed perpendicular to the center of rotation, in order that there is only axial thrust load to be considered and the limitations provided by the nose radius eliminated. However, this entering angle gives the shortest tool life for carbide tools when used in production operations.

The 7-deg back-rake angle as shown in Fig. 3, in combination with the position shown in Fig. 2, would provide an excess amount of positive rake as compared to the method in which such tools are usually applied. In the opinion of the writer further research investigations should more closely simulate the actual conditions that are used in most of our shops; that is, negative back and side rakes or 0-deg back rake combined with positive side rake.

Materials such as AISI 1015 steel often present the problem of excessive built-up edge on the cutting tool, which is conducive to chipping of carbides because of tension forces in the area adjacent to the cutting edge.

The honing of carbide tools provides a severe negative rake at the cutting edge, which in itself, allows definite improvements in the cutting speed for a given tool life or extended tool life for a given cutting speed. It would seem reasonable that the definition of a wear flank of 0.010 in. would assist in providing compressive loads on the carbide tool, thus enhancing its tool life.

The author indicates an increase of 480 deg F in temperature with a cutting-speed increase of approximately 100 per cent, whereas the same percentage increase in feed rate provided only an increase of only 280 deg F. The difference in the temperature obtained by doubling the feed, as compared to speed, might not necessarily preclude that the temperature differential allows for a substantial decrease in tool life with increase in cutting speed as compared to feed rate. It would appear that improved tool life as a function of increase in feed rate might be due to compressive loading on the face of the tool as compared to the tension loading that often occurs at the cutting edge when using light feed rates.

The assumption that the cutting force increases considerably with feed and decreases with speed, other conditions being constant, is subject to comment. Positive-rake tools used in a tool dynamometer usually indicate an exponential value of feed in the order of 0.8, when cutting forces are plotted as ordinate and feed as abscissa. If cutting force is plotted versus velocity, the exponential value of velocity is likely to be zero over a given range of speeds. It has been found in numerous tests that for given conditions of cut, in varying the velocity from maximum for a given tool material through the entire range to zero (normal speed ranges) cutting force remains constant within the experimental deviation. There have been indications of reductions in cutting force as a function of speed increase from a few investigators, but others have observed that force is not reduced with increase in cutting speed except over extended ranges. It seems to depend somewhat on geometry of the cutting-tool application and the particular combination of conditions of cut. Data compiled by the writer on high-speed-steel, positive-rake and negative-rake carbides, all indicate that cutting force and cutting speed are independent of each other, within the expected experimental deviation.

It is interesting to note that the author shows some variation in the interface temperatures, Fig. 8 as plotted versus cutting speed for the different feed rates. He notes points obtained at the light feed rates indicate some variation from that of a straight line, and this same type of erratic performance has been indicated in compiling data wherein cutting force is used as ordinate and feed rate as abscissa.

It might be of interest in subsequent work, if the author would study the influence of honing various widths and angles of land on carbide cutting tools that are used in standard tool holders, to provide industry with information relative to recommended values based upon temperature effects for this important part of the carbide-tool geometry.

[3] The R. K. LeBlond Machine Tool Company, Cincinnati, Ohio.

J. R. Roubik[4]

The behavior of tools as influenced by various types of wear is a subject of practical importance. An effort, such as this paper constitutes, to evaluate the influence of increasing flank wear is therefore commendable.

To isolate the effect of flank wear the author has resorted to simulating several conditions with artificial or ground-on wear lands. The degree of similarity between these lands and actual wear is open to some question. Actual wear is, more often than not, nonuniform in width, as well as being different from a ground surface with regard to surface-finish characteristics. Within what limits was the ground wear land parallel to the finished surface freshly produced by the cutting edge?

H. J. Siekmann[5]

Tool wear and its effect on the interface temperatures of the tool are of great interest to the carbide-tool manufacturer. We feel that accurate measurements of cutting-edge temperatures may be one of our best clues to the development of improved tool materials. The author's technique of artificially creating the wear land without introducing the side effects of cratering should improve our ability to study the effect of tool failures on interface temperatures.

It is felt that the problem of slight differences in chemical composition of carbide tips mentioned by Trigger [3] and confirmed by the author may have been minimized by recent improvements in tool chip-interface measurement techniques. The problem of manufacturing a long carbide rod with identical thermal-electric properties as small cutting tips presents some difficulty.

Not only would chemical-composition variations between the rod and the tips be troublesome, but grain size, cobalt and carbon distribution, and other variables not as easily controlled as chemistry are possible sources of difficulty in getting accurate interface-temperature measurements.

By combining work done at Massachusetts Institute of Technology and at University of Illinois, we evolved the following simplified calibration and hot-junction lead techniques which enables the use of $^1/_2$-in. square disposable inserts and two relatively short carbide rods. It has been found that these carbide sections can be made up with rather uniform thermal-electric properties. This method also eliminates the necessity of special tool holders which accommodate the long carbide rod.

In order to obtain a direct contact to the cutting tip without introducing intermediate hot-junction potentials, the contact was made with a copper-constantan thermocouple. A 100-ohm

[4] Research Engineer, Kearney and Trecker Corporation, Milwaukee, Wis. Assoc. Mem. ASME.

[5] Metallurgical Products Department, General Electric Company, Detroit, Mich. Assoc. Mem. ASME.

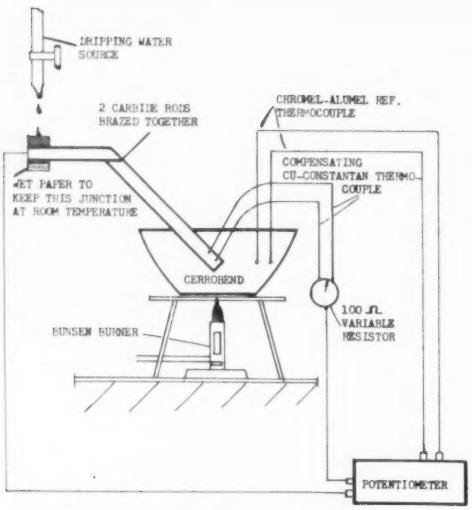

Fig. 11 1045-carbide thermocouple calibration setup

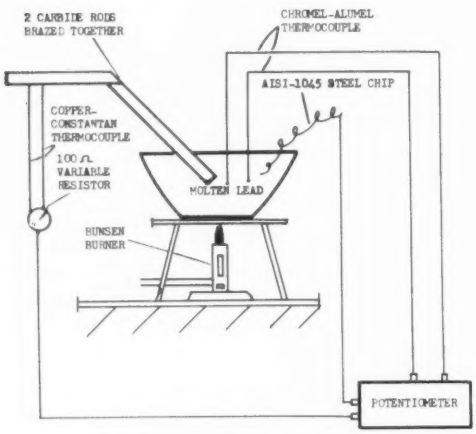

Fig. 12 1045-carbide calibration setup

variable resistor was placed in series with the thermocouple leads and, using the calibration setup shown in Fig. 11, the resistor is adjusted so that the emf, generated by the carbide-copper-constantan thermocouple junction not being at room temperature, will be balanced out to approximately zero at all temperatures up to 600 F. Over this range, variations from zero run approximately ±0.5 millivolt.

The two short carbide bars brazed together form the carbide side of the calibration circuit. Since the temperature drop across the braze is very small this presents no problelm. Water dripped on wet paper keeps the potentiometer lead end at room temperature. The carbide-copper-constantan thermocouple junction was kept at the same temperature by immersing it in a low-melting-point material called "Cerrobend." The junction temperature was monitored by a chromel-alumel thermocouple also immersed in the low-melting-point material. Having determined the best setting of the variable resistor, the thermocouple was then used as the lead to the cutting tip by clamping it down on top of the tip which was held in a standard mechanical tool holder.

To calibrate the tool-work thermocouple, the same carbide rods, using the copper-constantan thermocouple as one lead, were immersed in molten lead along with a long steel chip with the other potentiometer lead attached, Fig. 12. Using a chromel-alumel thermocouple as a reference, the calibration curve was determined. This curve was found to be linear up to 1300 F, the maximum temperature used for calibration.

Authors' Closure

The comments offered by Messrs. McKee, Roubik, and Siekmann are greatly appreciated by the author. Studies of the chip-workpiece zone with a tool tripping mechanism were made along with the tool-work thermocouple studies. The chip studies were inconclusive and have not been presented. They did, however, dictate some of the experimental conditions used during the work presented, such as the position of the tool relative to the workpiece and honing of the cutting edge. Honed edges were used to reduce cutting edge breakage during tool tripping studies.

Mr. McKee's remarks on the effect of cutting velocity on cutting force were enlightening. The author's statement that cutting force decreases with a velocity increase was based on an incomplete literature survey and should be corrected considering Mr. McKee's comments.

The use of negative rakes was planned but has not been carried out to date.

The author agrees with Mr. Roubik that the ground land surface finish does not usually simulate the actual finish on a tool land. Based upon a submicroscopic asperity concept of friction, however, the surfaces could well be similar. Alignment of the wear lands was first attempted by an elaborate procedure which made use of a telescope with a vertical cross-hair. In the final procedure, a bright white light was placed in back of the tool and workpiece. The tool was then adjusted until no light passed through the interface. Only the slightest amount of misalignment allowed light to pass through. The reproducibility of the data seemed to further verify that the lands were adequately aligned.

Mr. Siekmann's calibration method and hot-junction lead technique are excellent suggestions particularly with the use of carbide rods having uniform thermoelectric properties. The lead pot technique of heating the tool and chip was tried in the present study, but the heating rate had to be quite rapid to keep the carbide rod from heating. This rapid heating of the lead apparently caused some variation in temperature throughout the lead and gave a poor calibration. The use of a variable resistor may have solved the problem.

FERDINAND FREUDENSTEIN

Associate Professor of Mechanical Engineering, Columbia University, New York, N. Y. Mem. ASME

GEORGE N. SANDOR

Chief Engineer, Time, Inc., Springdale Laboratories Division, Springdale, Conn. Mem. ASME

Synthesis of Path-Generating Mechanisms by Means of a Programmed Digital Computer[1]

A general method is presented for synthesizing plane, linked mechanisms obtainable from a single, closed kinematic chain. Using complex numbers and the matrix theory of linear systems, these methods have been applied to 4-link mechanisms for generating a path through up to five arbitrary points with prescribed corresponding crank rotations. The five-point synthesis is programmed for automatic computation on the IBM 650 digital computer, which determines all existing solutions (a maximum of 12 linkages), selects one on the basis of a quality index, and computes the generated path.

THE advent of high-speed digital computers and the increasing complexity of mechanisms used in industry render desirable the development of design techniques for advanced forms of mechanism such as have been but little considered heretofore. Accordingly, a program of research was initiated in this department with the aim of setting up general methods of synthesis adaptable to computer programming. As a first step, the general single-loop chain has been investigated and the results applied to 4-bar mechanisms. In this approach, complex-number representation of coplanar vectors is particularly well suited. Complex numbers have been used for obtaining *prescribed velocities and accelerations* [1, 2, 3, 4, 5, 6, 7][2]; Hackmueller [8] has used complex numbers to derive expressions for two of the fundamental *curves of synthesis*. *Function generation* with complex numbers has been dealt with by Blokh [9], Sieker [10, 11, 12], and Freudenstein [13]. The application of complex numbers to *path generation* is due to Blokh [9] and, independently, to Sieker [12]. The methods of neither have been reduced to engineering practice, however. Blokh's treatment is quite general and is utilized in the present development with the following noteworthy features and additions:

1 Generality of treatment—methods not limited to one particular form of mechanism.

2 The graphical trial-and-error methods used in the intermediate steps of Blokh have been eliminated, thereby obtaining all solutions in a systematic manner.

3 The path-increment technique to be described later is novel. Thereby the maximum number of conditions may be imposed with the least amount of algebra.

4 The prescribed conditions of path versus crank rotation in the 4-bar mechanism illustrated are similar to those used in the design of many cams, and this mechanism thus warrants consideration in applications for which cams have been used,[3] particularly in high-speed, high-load applications.

5 The methods are comparatively simple, are adapted for desk-calculator or automatic-digital-computer techniques, and thus become readily usable design tools. Applications exist in the machine-design field whenever a controlled motion is needed —for power transmission as well as for motion-conversion purposes.

6 The detailed computational procedure is given fully in reference [15], which, together with prepunched IBM card-decks, may be used without further acquaintance with the theory.

Generalization of Complex-Number Techniques

As shown by Blokh [9], any plane single-loop kinematic chain with lower-pair connections, i.e., with pivots and slides, can be represented by a general chain consisting of pivotally connected bar-slider pairs, Fig. 1. The position of the pivot on the kth slider relative to the pivot of the kth bar, Fig. 2, can be defined in the starting position by the vector or complex number

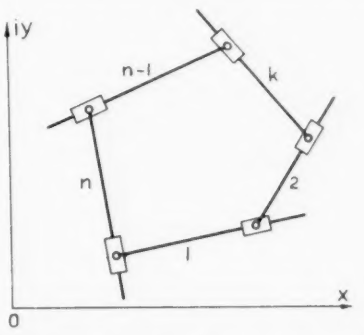

Fig. 1 General, plane, single-loop kinematic chain with lower-pair connections

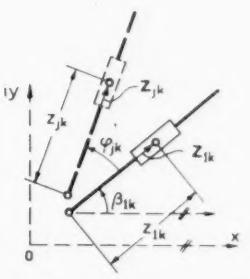

Fig. 2 Vector notation: The complex number z_{1k} represents the kth bar-slider pair of the general chain in the starting position, z_{jk} in the jth position

[1] Based on part of a dissertation in preparation by the second author toward partial fulfillment of the requirements for the degree of Doctor of Engineering Science, Department of Mechanical Engineering, Columbia University.

[2] Numbers in brackets designate References at end of paper.

[3] "Linkages Gain on Cams," Staff Report, *Product Engineering*, vol. 28, December 23, 1957, p. 75.

Contributed by the Machine Design Division and presented at the Annual Meeting, New York, N. Y., November 30–December 5, 1958, of THE AMERICAN SOCIETY OF MECHANICAL ENGINEERS.

NOTE: Statements and opinions advanced in papers are to be understood as individual expressions of their authors and not those of the Society. Manuscript received at ASME Headquarters, July 1, 1958. Paper No. 58—A-85.

$$\mathbf{z}_{1k} = z_{1k}e^{i\beta_{1k}} \tag{1}$$

and in the jth position by

$$\mathbf{z}_{jk} = z_{jk}e^{i(\beta_{1k}+\varphi_{jk})} = (z_{jk}/z_{1k})e^{i\varphi_{jk}}\mathbf{z}_{1k} = \lambda^{(1)}{}_{jk}\mathbf{z}_{1k}, \tag{2}$$

where the symbols z_{1k}, z_{jk}, β_{1k}, and φ_{jk}, are defined in Fig. 2.

$$\lambda^{(1)}{}_{jk} = (z_{jk}/z_{1k})e^{i\varphi_{jk}} \tag{3}$$

is called the *displacement coefficient* of the kth bar-slider pair for the jth position of the chain.

The *equation of closure* for the n-bar general chain of Fig. 1 expresses the closure of the loop in the starting position

$$\sum_{k=1}^{n} \mathbf{z}_{1k} = 0, \tag{4}$$

and the jth *displacement equation* expresses closure in the jth position

$$\sum_{k=1}^{n} \mathbf{z}_{jk} = \sum_{k=1}^{n} \lambda^{(1)}{}_{jk}\mathbf{z}_{1k} = 0. \tag{5}$$

Differentiation of equation (5) with respect to time leads to the *velocity equation* for the jth position

$$\sum_{k=1}^{n} \mathbf{v}_{jk} = \sum_{k=1}^{n} \lambda^{(2)}{}_{jk}\lambda^{(1)}{}_{jk}\mathbf{z}_{1k} = 0 \tag{6}$$

which expresses the closure of the polygon formed by the relative velocity vectors $\mathbf{v}_{jk}$, where

$$\lambda^{(2)}{}_{jk} = (v_{jk}/z_{jk}) + i\omega_{jk} \tag{7}$$

is called the *velocity coefficient*, v_{jk} is the sliding velocity of the slider on the kth bar, and ω_{jk} is the angular velocity of the kth bar with respect to the fixed plane of reference, i.e., the absolute angular velocity. Successive further differentiations yield the equations of acceleration, shock, or second acceleration, and so forth.

From the viewpoint of synthesis, each equation can be regarded as a type of constraint on the unknowns $\mathbf{z}_{1k}$. If only displacement equations are used, the synthesis will be a "point approximation;" if equation (4) and several of its derivatives are employed, one obtains an "order approximation," and combined "point-order approximations" will utilize several displacement and derivative equations. Among the types of synthesis obtainable in this uniform fashion are: Path, function, velocity, acceleration, pressure angle, and force synthesis.

Compatibility Conditions. If s constraints in the form of s equations in the complex plane are imposed on an n-bar chain, we have a system of s homogeneous linear equations in the n unknowns $\mathbf{z}_{1k}$ with complex coefficients λ_{jk}. If $s \leq (n-1)$, all coefficients λ_{jk} can be chosen arbitrarily, provided the resulting equations are linearly independent.

If $s > (n-1)$, nonzero solutions for the $\mathbf{z}_{1k}$ will exist if and only if the $(s \times n)$ matrix M of the coefficients is of rank $(n-1)$

$$M = [\lambda_{jk}], \quad j = 1, 2, \ldots, s, \quad k = 1, 2, \ldots, n, \text{ rank} = (n-1). \tag{8}$$

This requirement of rank yields the *compatibility conditions* that every nth order determinant of M must vanish

$$|\lambda_{jk}| = 0, \quad (s - n + 1) \text{ equations.} \tag{9}$$

The Equivalent General Chain, EGC, of a Mechanism. The parameters contained in the coefficients λ_{jk}, such as (z_{jk}/z_{1k}), φ_{jk}, and so on, are subject to constraints which render the general chain of Fig. 1 equivalent to a mechanism of a given type. This is illustrated by the example in Fig. 3. The structure of, and the constraints imposed upon, the equivalent general chain of Fig. 3(*b*) are expressed in full by the symbolic notation

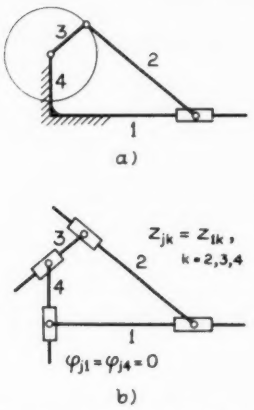

Fig. 3 (a) Slider-crank mechanism and (b) its equivalent general chain

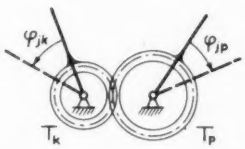

Fig. 4 Gear-pair which can be represented by imposing constraint (11) on a general chain

$$\text{EGC } (1, 2, 3, 4) \; [z_{jk} = z_{1k} \; (k = 2, 3, 4), \; \varphi_{j1} = \varphi_{j4} = 0], \tag{10}$$

where (1, 2, 3, 4) identifies the link indexes; the constraints are stated inside the brackets.

Certain higher-pair connections can also be represented in the general chain by appropriate constraints. The gear pair of Fig. 4, for instance, would be represented by the constraint

$$\varphi_{jk} = -(T_p/T_k)\varphi_{jp}, \tag{11}$$

where T_k and T_p are the number of teeth in the gears attached to the kth and pth links, respectively, and j is the position index.

Degrees of Freedom. The number of the degrees of freedom of the general chain must be equal to the number of degrees of freedom of the mechanism represented by it. An adaptation of Artobolevskii's structural analysis [14] will serve to verify this criterion of equivalence, although other analyses, such as Grueb-ler's, could also have been used. In the following adaptation of Artobolevskii's approach, the number of degrees of freedom of motion f of any plane mechanism is expressed by the formula

$$f = 3m - 2l - h, \tag{12}$$

where

m = number of movable links (bars, sliders, and the like)
l = number of lower-pair connections (pivots and slides)
h = number of higher-pair connections (gear mesh, cam contact, and so forth).

Since all $2n$ links of the n-bar general chain of Fig. 1 are movable, the application of equation (12) yields

$$f' = 3(2n) - 2(2n) - 0 = 2n.$$

Fixing one pivot removes two translational degrees of freedom. Therefore if r denotes the number of constraints of equivalence imposed upon bar rotations and sliding movements, the number

of degrees of freedom of motion f of an equivalent general chain is expressed by

$$f = 2n - r - 2. \tag{13}$$

For example, in Fig. 3, we have

$m = 3$ (2 bars and 1 slider), $l = 4$ (3 pivots and 1 slide),
$h = 0$ (no higher-pairs), $n = 4$ (4 bars in the general chain),

and $r = 5$ ($\varphi_{jk} = 0, k = 1, 4$ and $z_{jk} = z_{1k}, k = 2, 3, 4$).

Substituting these in equations (12) and (13) we obtain one degree of freedom for both the mechanism and its equivalent general chain.

Permissible Number of Imposed Constraints. Thus in applying the general system of equations of synthesis to a particular problem, a number of the quantities contained in the coefficients λ_{jk} are "a priori" determined by our preconception of the type of mechanism to be synthesized; some quantities are to be prescribed in accordance with the desired performance, and others must be left unspecified, to be determined from the compatibility equations (9). Detailed consideration of these conditions has led to the determination of the greatest permissible number of imposed constraints under various conditions.

For example, when only displacement equations are used (point approximations), the allowable maximum number of equations s is given by the formula

$$s \leq (2n - 3). \tag{14}$$

The derivation of relation (14) is outlined in Appendix 5. When $n = 4$, as in the case of pivoted 4-link mechanisms, relation (14) yields $s \leq 5$, i.e., 5-point approximations can be obtained.

In the following application to path generation by means of pivoted 4-link mechanisms, the notation has been simplified to eliminate double subscripts.

Application to the Coupler Motion of a 4-Bar-Linkage

In general, the task of kinematic synthesis is to find the principal dimensions and the starting position of a mechanism of a given type which will perform in a prescribed manner.

The plane pivoted 4-link mechanism dealt with here is shown in Fig. 5. The performance under consideration is path generation. The path lies in the plane of the fixed link and is prescribed by means of the co-ordinates of distinct points on the path, the so-called precision points, Fig. 6. The precision points must lie on the path of a point on the coupler, called the "tracer point" in Fig. 5. As the tracer point passes through the numbered precision points, the driving crank must rotate through the correspondingly numbered angles $\varphi_2, \varphi_3, \ldots$, (measured from the starting position) which are likewise prescribed, Fig. 7.

Notation. The radius vector to the jth precision point of the prescribed path is denoted by the complex number, Fig. 6

$$\mathbf{r}_j = r_j e^{i\theta_j} = r_{jx} + i r_{jy} = r_j(\cos\theta_j + i \sin\theta_j) \tag{15}$$

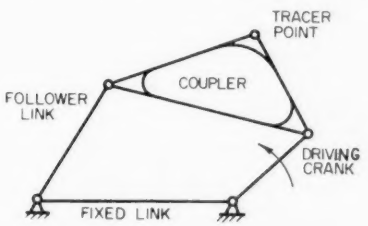

Fig. 5 Plane four-link mechanism

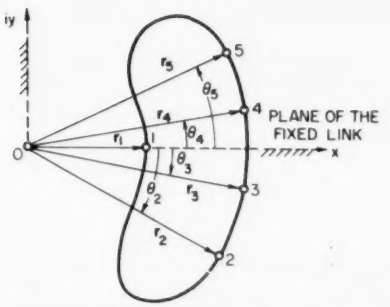

Fig. 6 Path to be generated by the tracer point of Fig. 5, prescribed by five precision points

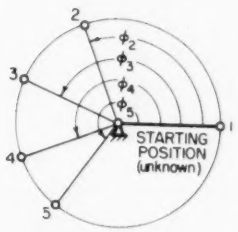

Fig. 7 Prescribed crank rotations: for instance, position 3 in Fig. 7 corresponds to point 3 in Fig. 6

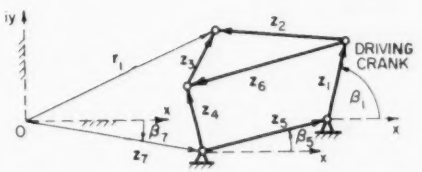

Fig. 8 Plane vectors, $\mathbf{z}_1$ to $\mathbf{z}_7$, defining the mechanism in its starting position

referred to an arbitrary $(x - y)$ co-ordinate system in the plane of the fixed link.

The links, referred to the same fixed co-ordinate system, are designated in the starting position by the complex numbers

$$\mathbf{z}_k = z_k e^{i\beta_k} = z_{kx} + i z_{ky} \tag{16}$$

Fig. 8, where $z_k (k = 1, 2, \ldots, 6)$ is the distance between the centers of pivots of the kth link, and $\mathbf{z}_7$ is the radius vector to the fixed pivot of the follower link.

The Displacement Equations. At the jth precision point, the driving crank has rotated from the starting position through the angle φ_j, the coupler through angle γ_j, and the follower link through the angle ψ_j, Fig. 9. The displacement of the tracer point is represented by the vector chord of the path $\tilde{\mathbf{o}}_j = \mathbf{r}_j - \mathbf{r}_1$.

We define the *displacement coefficients* for the three movable links as follows

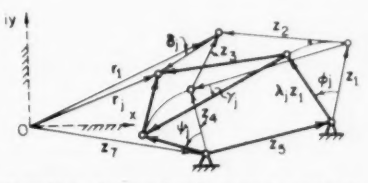

Fig. 9 The jth position, showing that the original and the jth positions of the crank $\mathbf{z}_1$ and coupler side $\mathbf{z}_2$ form a closed polygon with $\tilde{\mathbf{o}}_j$, chord of the generated path, equation (19)

$$\lambda_j = e^{i\varphi_j}, \quad \mathbf{v}_j = e^{i\gamma_j}, \quad \text{and} \quad \underline{\mathbf{u}}_j = e^{i\psi_j}. \tag{17}$$

With these we can write the *displacement equations* for links 1 and 2, Fig. 9 in accordance with the *path increment technique*

$$\lambda_j \mathbf{z}_1 + \mathbf{v}_j \mathbf{z}_2 - \mathbf{z}_1 - \mathbf{z}_2 = \tilde{\boldsymbol{\delta}}_j, \tag{18}$$

or

$$(\mathbf{v}_j - 1)\mathbf{z}_2 + (\lambda_j - 1)\mathbf{z}_1 = \tilde{\boldsymbol{\delta}}_j, \tag{19}$$

and for links 3 and 4

$$(\underline{\mathbf{u}}_j - 1)\mathbf{z}_4 + (\mathbf{v}_j - 1)\mathbf{z}_3 = \tilde{\boldsymbol{\delta}}_j. \tag{20}$$

Four-Point Approximation. Application of the method to four points leads to two systems of three equations—equations (19) and (20) — with $j = 2, 3,$ and 4. Each system is a set of three simultaneous nonhomogeneous linear equations with complex coefficients in two unknowns. In the first system, solutions will exist for the two unknowns $\mathbf{z}_1$ and $\mathbf{z}_2$ only if the augmented matrix of the system is of rank two, that is, if the following determinant vanishes:

$$\begin{vmatrix} (\mathbf{v}_2 - 1) & (\lambda_2 - 1) & \tilde{\boldsymbol{\delta}}_2 \\ (\mathbf{v}_3 - 1) & (\lambda_3 - 1) & \tilde{\boldsymbol{\delta}}_3 \\ (\mathbf{v}_4 - 1) & (\lambda_4 - 1) & \tilde{\boldsymbol{\delta}}_4 \end{vmatrix} = 0. \tag{21}$$

For short, we will represent such determinants by their diagonal elements. Thus we rewrite equation (21)

$$|(\mathbf{v}_2 - 1), \quad (\lambda_3 - 1), \quad \tilde{\boldsymbol{\delta}}_4| = 0 \tag{22}$$

Denoting the minors as follows

$$|(\lambda_3 - 1), \quad \tilde{\boldsymbol{\delta}}_4| = \boldsymbol{\Delta}_2, \qquad |(\lambda_4 - 1), \quad \tilde{\boldsymbol{\delta}}_2| = \boldsymbol{\Delta}_3,$$
$$|(\lambda_2 - 1), \quad \tilde{\boldsymbol{\delta}}_3| = \boldsymbol{\Delta}_4 \tag{23}$$

and

$$\sum_2^4 \boldsymbol{\Delta}_j = -\boldsymbol{\Delta}_1, \tag{24}$$

and expanding the determinant (22) in terms of its first column yields equation (1-4) in Table 1, the *1st Compatibility Equation*, to be satisfied by the coupler rotation coefficients $\mathbf{v}_j$.

The Compatibility "Linkage." Equations (24) and (1-4) may be regarded as the equations of closure of a 4-bar linkage in its starting and displaced positions as shown in Fig. 10. γ_2 can be assumed in accordance with the rules in lines (1-6) to (1-11) of Table 1, and equation (1-4) solved trigonometrically for γ_3 and γ_4 according to lines (1-12) to (1-19).

Table 1 Mathematical procedure for path generation through four points with prescribed crank rotations

Note: All angles are positive counterclockwise.

Given: $\mathbf{r}_j$ of equation (15) and Fig. 6, $j = 1, 2, 3, 4,$ and φ_j of equation (17) and Fig. 7, $j = 2, 3, 4.$

Wanted: $\mathbf{z}_k$ of equation (16) and Fig. 8, $k = 1, 2, \ldots, 7.$

Procedure:

$$\tilde{\boldsymbol{\delta}}_j = \delta_{jx} + i\delta_{jy} = \mathbf{r}_j - \mathbf{r}_1, \qquad j = 2, 3, 4. \tag{1-1}$$

$$\lambda_j = \lambda_{jx} + i\lambda_{jy} = e^{i\varphi_j}, \qquad j = 2, 3, 4. \tag{1-2}$$

See equations (23) and (24) for

$$\boldsymbol{\Delta}_j = \Delta_{jx} + i\Delta_{jy}, \qquad j = 1, 2, 3, 4. \tag{1-3}$$

The *1st Compatibility Equation*

$$\boldsymbol{\Delta}_1 + \sum_2^4 \boldsymbol{\Delta}_j \mathbf{v}_j = 0, \tag{1-4}$$

where

$$\mathbf{v}_j = e^{i\gamma_j}. \tag{1-5}$$

If

$$|\boldsymbol{\Delta}_1| + |\boldsymbol{\Delta}_2| \leq |\boldsymbol{\Delta}_3| + |\boldsymbol{\Delta}_4|, \tag{1-6}$$

and

$$\big||\boldsymbol{\Delta}_1| - |\boldsymbol{\Delta}_2|\big| \geq \big||\boldsymbol{\Delta}_3| - |\boldsymbol{\Delta}_4|\big|, \tag{1-7}$$

assume γ_2 arbitrarily. (1-8)

If neither (1-6) nor (1-7) holds, assume γ_2 such that $\boldsymbol{\Delta}_2\mathbf{v}_2 = \boldsymbol{\Delta}_2 e^{i\gamma_2}$ falls in the shaded sectors in Fig. 11, i.e.,

$$\gamma_2^{\mathrm{I}} < \gamma_2 < \gamma_2^{\mathrm{II}} \quad \text{or} \quad \gamma_2^{\mathrm{IV}} < \gamma_2 < \gamma_2^{\mathrm{III}}. \tag{1-9}$$

If (1-6) holds but (1-7) does not hold, assume γ_2 in the range, Fig. 11

$$\gamma_2^{\mathrm{IV}} < \gamma_2 < \gamma_2^{\mathrm{II}}. \tag{1-10}$$

If (1-6) does not hold but (1-7) holds, the allowable limits for γ_2 are, Fig. 11

$$\gamma_2^{\mathrm{I}} < \gamma_2 < \gamma_2^{\mathrm{V}}. \tag{1-11}$$

$$\mathbf{D} = \boldsymbol{\Delta}_1 + \boldsymbol{\Delta}_2\mathbf{v}_2, \qquad \text{where } \mathbf{v}_2 = e^{i\gamma_2} \tag{1-12}$$

$$\cos\alpha_3 = \cos\tilde{\alpha}_3 = \frac{|\boldsymbol{\Delta}_4|^2 - |\boldsymbol{\Delta}_3|^2 - |\mathbf{D}|^2}{2|\boldsymbol{\Delta}_3\mathbf{D}|} \quad \text{(see Fig. 10)} \tag{1-13}$$

$$\sin\alpha_3 = +|(1 - \cos^2\alpha_3)^{1/2}|, \sin\tilde{\alpha}_3 = -|(1 - \cos^2\alpha_3)^{1/2}| \tag{1-14}$$

$$\gamma_3 = \arg\mathbf{D} + \alpha_3 - \arg\boldsymbol{\Delta}_3, \quad \tilde{\gamma}_3 = \arg\mathbf{D} + \tilde{\alpha}_3 - \arg\boldsymbol{\Delta}_3 \tag{1-15}$$

$$\cos\alpha_4 = \cos\tilde{\alpha}_4 = \frac{|\boldsymbol{\Delta}_3|^2 - |\boldsymbol{\Delta}_4|^2 - |\mathbf{D}|^2}{2|\boldsymbol{\Delta}_4\mathbf{D}|} \tag{1-16}$$

$$\sin\alpha_4 = +|(1 - \cos^2\alpha_4)^{1/2}|, \sin\tilde{\alpha}_4 = -|1 - \cos^2\alpha_4)^{1/2}| \tag{1-17}$$

$$\gamma_4 = \arg\mathbf{D} - \alpha_4 - \arg\boldsymbol{\Delta}_4, \quad \tilde{\gamma} = \arg\mathbf{D} - \tilde{\alpha}_4 - \arg\boldsymbol{\Delta}_4 \tag{1-18}$$

Use γ_3 and γ_4 or $\tilde{\gamma}_3$ and $\tilde{\gamma}_4$ to obtain $\mathbf{v}_3$ and $\mathbf{v}_4$, where

$$\mathbf{v}_j = e^{i\gamma_j} \quad \text{or} \quad \mathbf{v}_j = e^{i\tilde{\gamma}_j}, \quad j = 3, 4. \tag{1-19}$$

$$\boldsymbol{\Delta}_{p2} = |(\mathbf{v}_3 - 1), \tilde{\boldsymbol{\delta}}_4|, \qquad \boldsymbol{\Delta}_{p3} = |(\mathbf{v}_4 - 1), \tilde{\boldsymbol{\delta}}_2|,$$
$$\boldsymbol{\Delta}_{p4} = |(\mathbf{v}_2 - 1), \tilde{\boldsymbol{\delta}}_3|, \qquad \boldsymbol{\Delta}_{p1} = -\sum_{j=2}^{4} \boldsymbol{\Delta}_{pj} \tag{1-20}$$

The *2nd Compatibility Equation*

$$\boldsymbol{\Delta}_{p1} + \sum_{j=2}^{4} \boldsymbol{\Delta}_{pj}\underline{\mathbf{u}}_j = 0, \tag{1-21}$$

where

$$\underline{\mathbf{u}}_j = e^{i\psi_j}. \tag{1-22}$$

To solve equation (1-21), proceed according to lines (1-6) to (1-15), but use $\boldsymbol{\Delta}_{pj}$ instead of $\boldsymbol{\Delta}_j$, $\underline{\mathbf{u}}_j$ instead of $\mathbf{v}_j$, (1-23)
and ψ_j instead of γ_j. (1-24)

$$\mathbf{D}_5 = |\tilde{\boldsymbol{\delta}}_2, (\underline{\mathbf{u}}_3 - 1)|, \mathbf{D}_6 = |(\mathbf{v}_2 - 1), (\lambda_3 - 1)|,$$
$$\mathbf{D}_7 = |(\mathbf{v}_2 - 1), (\underline{\mathbf{u}}_3 - 1)| \tag{1-25}$$

$$\mathbf{z}_1 = \frac{\boldsymbol{\Delta}_{p4}}{\mathbf{D}_5}, \quad \mathbf{z}_2 = -\frac{\boldsymbol{\Delta}_4}{\mathbf{D}_5}, \quad \mathbf{z}_3 = \frac{\mathbf{D}_6}{\mathbf{D}_5}, \quad \mathbf{z}_4 = \frac{\boldsymbol{\Delta}_{p4}}{\mathbf{D}_6},$$
$$\mathbf{z}_5 = \mathbf{z}_2 - \mathbf{z}_3 \tag{1-26}$$

$$\mathbf{z}_6 = \mathbf{z}_4 - \mathbf{z}_5 - \mathbf{z}_1, \qquad \mathbf{z}_7 = \mathbf{r}_1 - \mathbf{z}_3 - \mathbf{z}_4 \tag{1-27}$$

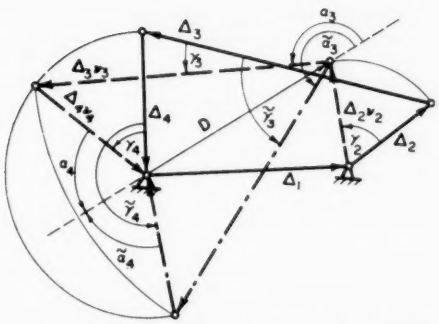

Fig. 10 The compatibility "linkage" in its starting position (full lines) represents the relationship (24) of the coefficients Δ_j of the compatibility equation (1-4). The displaced positions of the linkage illustrate the two alternate solutions of equation (1-4).

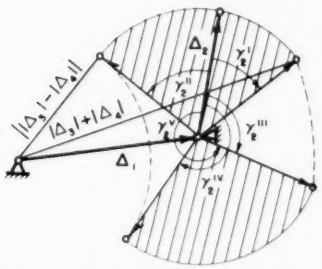

Fig. 11 Permissible ranges for the assumed value of γ_2 in the 4-point approximation, Table 1

The *2nd Compatibility Equation* (1-21) arises in a similar manner from the system of three displacement equations of type (20). The unknowns in this equation are the follower link rotations ψ_j. The method of solution, analogous to that of Equation (1-4), is indicated in lines (1-23) and (1-24).

Thus having obtained a set of compatible coefficients for the two systems of three displacement equations, one system based on equation (19) the other on equation (20), we solve these systems for the linkage dimensions in accordance with lines (1-25) to (1-27) of Table 1.

Five-Point Approximation. The procedure for the four-point approximation presented in Table 1 is readily manageable with the aid of a desk calculator. The five-point method, presented hereafter, serves as the basis for an automatic digital-computer program developed in Reference [15].

The five-point problem involves two systems of four displacement equations each based on equations (19) and (20)

$$(\mathbf{v}_j - 1)\mathbf{z}_2 + (\boldsymbol{\lambda}_j - 1)\mathbf{z}_1 = \tilde{\boldsymbol{\delta}}_j, \quad j = 2, 3, 4, 5, \tag{25}$$

$$(\boldsymbol{\mu}_j - 1)\mathbf{z}_4 + (\mathbf{v}_j - 1)\mathbf{z}_3 = \tilde{\boldsymbol{\delta}}_j, \quad j = 2, 3, 4, 5. \tag{26}$$

To assure the existence of solutions for the $\mathbf{z}_j$, the augmented matrix M of both systems must be of rank two. Thus for system (25)

$$M = \begin{bmatrix} (\mathbf{v}_2 - 1) & (\boldsymbol{\lambda}_2 - 1) & \tilde{\boldsymbol{\delta}}_2 \\ (\mathbf{v}_3 - 1) & (\boldsymbol{\lambda}_3 - 1) & \tilde{\boldsymbol{\delta}}_3 \\ (\mathbf{v}_4 - 1) & (\boldsymbol{\lambda}_4 - 1) & \tilde{\boldsymbol{\delta}}_4 \\ (\mathbf{v}_5 - 1) & (\boldsymbol{\lambda}_5 - 1) & \tilde{\boldsymbol{\delta}}_5 \end{bmatrix}, \tag{27}$$

and all 3rd-order determinants of the matrix M (27) must vanish. This is guaranteed by the singularity of any two such determinants, say (22) and (28)

$$|(\mathbf{v}_2 - 1), \quad (\boldsymbol{\lambda}_3 - 1), \quad \tilde{\boldsymbol{\delta}}_5| = 0. \tag{28}$$

The notation of equations (23) and (24) is extended as follows

$$|(\boldsymbol{\lambda}_3 - 1), \quad \tilde{\boldsymbol{\delta}}_5| = \boldsymbol{\Delta}_2', \qquad |(\boldsymbol{\lambda}_5 - 1), \quad \tilde{\boldsymbol{\delta}}_2| = \boldsymbol{\Delta}_3',$$

$$-\boldsymbol{\Delta}_2' - \boldsymbol{\Delta}_3' - \boldsymbol{\Delta}_4 = \boldsymbol{\Delta}_1'. \tag{29}$$

Expanding the determinants (22) and (28) with the aid of this notation, we obtain the *1st Pair of Compatibility Equations*

$$\boldsymbol{\Delta}_1 + \boldsymbol{\Delta}_2\mathbf{v}_2 + \boldsymbol{\Delta}_3\mathbf{v}_3 + \boldsymbol{\Delta}_4\mathbf{v}_4 = 0, \tag{30}$$

$$\boldsymbol{\Delta}_1' + \boldsymbol{\Delta}_2'\mathbf{v}_2 + \boldsymbol{\Delta}_3'\mathbf{v}_3 + \boldsymbol{\Delta}_4\mathbf{v}_5 = 0. \tag{31}$$

Recalling that $\mathbf{v}_j = e^{i\gamma_j}$, it is seen that these are nonlinear equations in the four unknowns γ_j.

Solution of the Compatibility System. To adapt the five-point method for automatic machine computation, the nonlinear system of equations (30) and (31) with the four unknowns γ_j was solved analytically, i.e., without resorting to geometric procedures. This was achieved by eliminating from the system all unknowns but γ_2, which left a 4th-degree equation, (45) of Appendix 1, with the tangent of ($\gamma_2/2$) as the unknown. An outline of the derivation of this equation is given in Appendix 1. Any real root of equation (45) will yield a value for γ_2 which will satisfy the system (30)-(31). We substitute such values of γ_2 in equations (30) and (31) and solve these equations for γ_3, γ_4, and γ_5 as outlined in Appendix 2.

The Second Pair of Compatibility Equations. With the values of γ_j thus determined from the first pair of compatibility equations (30) and (31), we can calculate the values of $\mathbf{v}_j$, and so obtain a set of compatible coefficients for system (25). Compatible values for the coefficients $\boldsymbol{\mu}_j$ for system (26) remain to be found. The augmented matrix (32) of this system gives rise to the *Second Pair of Compatibility Equations* (33) and (34)

$$\begin{bmatrix} (\boldsymbol{\mu}_2 - 1) & (\mathbf{v}_2 - 1) & \tilde{\boldsymbol{\delta}}_2 \\ (\boldsymbol{\mu}_3 - 1) & (\mathbf{v}_3 - 1) & \tilde{\boldsymbol{\delta}}_3 \\ (\boldsymbol{\mu}_4 - 1) & (\mathbf{v}_4 - 1) & \tilde{\boldsymbol{\delta}}_4 \\ (\boldsymbol{\mu}_5 - 1) & (\mathbf{v}_5 - 1) & \tilde{\boldsymbol{\delta}}_5 \end{bmatrix}, \tag{32}$$

$$|(\boldsymbol{\mu}_2 - 1), \quad (\mathbf{v}_3 - 1), \quad \tilde{\boldsymbol{\delta}}_4| = 0, \tag{33}$$

$$|(\boldsymbol{\mu}_2 - 1), \quad (\mathbf{v}_3 - 1), \quad \tilde{\boldsymbol{\delta}}_5| = 0. \tag{34}$$

From here on the procedure is analogous to the expansion and solution of equations (22) and (28)—the determinant forms of the 1st pair of compatibility equations—with the modifications stated in Appendix 3.

With the set of compatible displacement coefficients $\mathbf{v}_j$ and $\boldsymbol{\mu}_j$ thus obtained, we proceed to solve the first two displacement equations of system (25) for $\mathbf{z}_1$ and $\mathbf{z}_2$ and solve the first two of system (26) for $\mathbf{z}_3$ and $\mathbf{z}_4$.

This completes the outline of the derivations and the mathematical procedure for the five-point synthesis.

Nature and Existence of Solutions. If any two columns of matrix (27) or (32) are proportional, the solution may fail due to the linear dependence of the displacement equations. The second and third columns of matrix (27) are proportional when the figure formed by the precision points is geometrically similar to the circular figure made by a point on the driving crank in the corresponding positions. Such configurations are to be avoided.

An indication whether or not solutions to the 5-point synthesis exist is obtained from the roots of the quartic equation (45): If there are no real roots, there are no solutions. The automatic computer program of reference [15] reaches this stage in less than two minutes. However, the presence of real roots for equation (45) does not guarantee that the synthesized linkages will be workable solutions, for the following reason:

If the path points and driving-crank rotations are prescribed

arbitrarily, it may happen that not all of the generated precision points fall on the same branch of the generated path, i.e., that one or more prescribed points can be reached only by temporarily disconnecting one joint of the mechanism. Ways to avoid this, outlined in reference [15], include the use of an atlas, reference [16], or of a quick geometric method, reference [17], to obtain an approximate idea of the mechanism proportions, and thus to arrive at a reasonable set of prescribed driving-crank rotations. Examples 1 and 2 of Table 2 were set up with the first of these preliminary methods, Example 5 with the second.

Related Solutions. The nature of dual solutions can be summarized in the following theorem and its corollary (see Appendix 4 for the proof).

Theorem 1. If, in the systems of displacement equations, equations (19) and (20) or (25) and (26), each displacement coefficient of the coupler is interchanged with the corresponding displacement coefficient of the follower link, Fig. 5, then the two synthesized linkages will generate the same path with the same driving-crank rotations, Fig. 13, and will be related to one another by Roberts' Theorem, reference [3], pp. 147–151.

Corollary 1. Upon the noncommon fixed pivots of the two linkages of Theorem 1, using appropriate vectors taken from these two linkages, it is possible to construct the third Roberts related linkage (dot-dash lines in Fig. 13), which will also generate the prescribed path with the same accuracy as the first two linkages.

It is to be observed that, in the mechanism of Corollary 1, the *coupler* performs the rotations prescribed for the *crank*, so that this third linkage is only a partial solution to the problem of synthesis.

Automatic Computation. The computer program given in reference [15] begins with computing the coefficients of and solving the quartic equation (45) of Appendix 1. If there are no real solutions, the computer stops. If there are two real roots, say τ_1 and τ_2, τ_1 is first used to obtain a value for γ_2, τ_2 for ψ_2, and the dimensions of the linkage identified by the symbol L_{12}, Fig. 13, are determined. Next τ_1 and τ_2 are automatically interchanged in storage, and L_{21}, related to L_{12} (Theorem 1), is synthesized.

If all four roots of equation (45) are real, then τ_j are cyclically rotated in storage after the synthesis of each linkage until all L_{jk} have been calculated. This yields six related pairs: The 12 complete solutions of the problem of synthesis. If the third linkage related to each pair (Corollary 1) is also counted as a solution to the problem of path generation without prescribed crank rotations, then the number of solutions is raised to 18.

The dimensions of all the two or 12 complete solutions are punched out, and the synthetic quality index

$$Q = \frac{z_{\min}}{z_{\max}} \Delta\varphi \qquad (35)$$

is automatically attached to each linkage, where $\Delta\varphi$, the range of driving-crank rotation, is less than 2π for incomplete crank rotation. Because of the practical importance of complete crank rotation, $\Delta\varphi$ is set equal to 4π when φ is not limited, thus weighting the index two-to-one in favor of this desirable characteristic. Other possible factors for use in a quality index are, for example, pressure angles or proximity of dead-center positions between coupler and follower links, and the ratio of maximum link length to maximum chordal path length.

Finally, the linkage with the highest quality index is automatically selected, its essential dimensions punched out, and coordinates of points on its generated path are computed and punched out for every degree of crank rotation. If the designer feels that a nonselected linkage may better suit his requirements, he can use the auxiliary program of reference [15] to compute the path of any hand-picked mechanism.

Examples. Table 2 lists five examples illustrated in Figs. 12 to 15. Example 1 is a 4-point approximation, with three of the prescribed points located on a circular arc. Example 2 has a path similar to that of Example 1 but prescribed with five points, four of which are on the circular segment, spaced arbitrarily. Example 3 is a rerun of Example 2 after these four points were relocated in accordance with Freudenstein's Respacing Formula

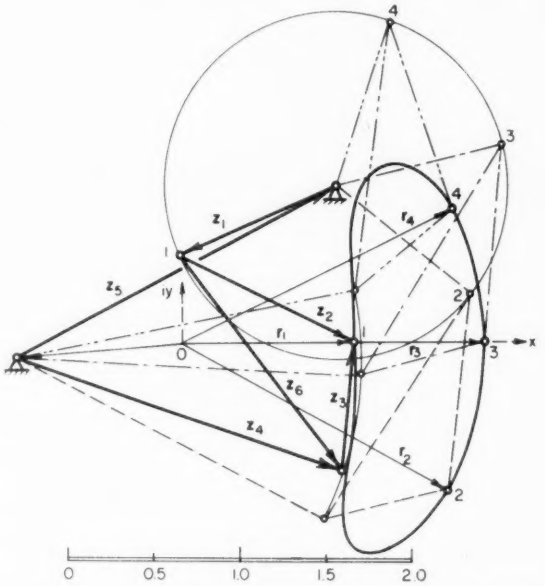

Fig. 12 The synthesized linkage of Example 1: Path generation through four points with prescribed crank rotations

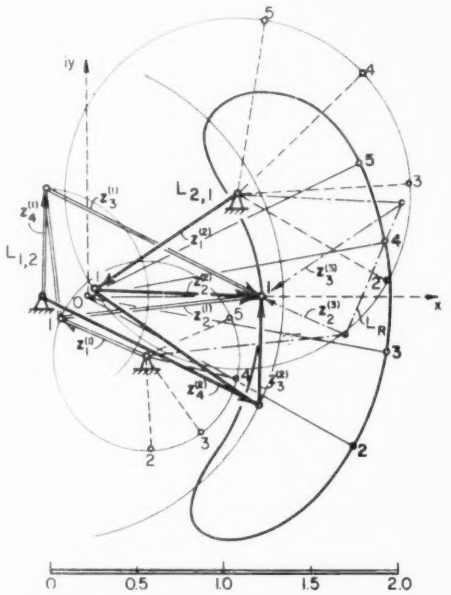

Fig. 13 Path generation through 5 points with prescribed crank rotations, Example 3. Linkages L_{12} and L_{21}, related by Theorem 1, are two of the twelve solutions obtained by automatic digital computation. The third related linkage L_R also generates the prescribed path, but without fulfilling the prescribed crank rotations. L_{21} was automatically selected as having the highest quality index Q, equation (35).

Table 2 Numerical examples of 4 and 5-point approximations. Example 1 was solved by desk calculation following the procedure of Table 1.

Example number			1	2	3	4	5
Number of precision points			4	5	5	5	5
Method of calculation			Desk calc.	Automatic digital computer, Reference [15]			
Drawing number			Fig. 12	None	Fig. 13	Fig. 14	Fig. 15
Prescribed performance (see Fig. 6, 7)	Precision point 1	r_1	1.0000000	1.0000000	1.0000000	1.3250130	1.7600000
		θ_1 deg	0.0000000	0.0000000	0.0000000	−41.000000	131.00000
	2	r_2	1.7400000	1.7400000	1.7400000	1.0863604	1.3400000
		θ_2 deg	−29.200000	−29.200000	−29.500000	−23.000000	120.00000
		φ_2 deg	117.50000	117.50000	117.00000	−24.000000	−57.000000
	3	r_3	1.7400000	1.7400000	1.7400000	1.0000000	1.3400000
		θ_3 deg	0.0000000	−12.200000	−10.700000	0.0000000	87.000000
		φ_3 deg	170.00000	147.50000	150.00000	−42.000000	−135.00000
	4	r_4	1.7400000	1.7400000	1.7400000	1.0863604	1.6000000
		θ_4 deg	25.900000	5.4000000	10.300000	23.000000	68.000000
		φ_4 deg	228.00000	180.50000	191.00000	−60.000000	−169.00000
	5	r_5		1.7400000	1.7400000	1.3250130	1.7600000
		θ_5 deg		25.900000	25.900000	41.000000	54.000000
		φ_5 deg		228.00000	228.00000	−84.000000	−194.00000
Synthesized linkage (see Fig. 8)	Location (see Fig. 8)	z_{7x}	−0.9661828	−0.5373553	−0.2616303	−0.0610645	−0.0153447
		z_{7y}	−0.0872788	0.0017581	0.0004545	−1.0714912	−0.0441123
	Fixed link	z_{5x}	1.8534637	1.3962042	1.1260167	1.2739279	0.7114933
		z_{5y}	0.9805387	0.6603938	0.5825329	1.0715018	0.3969146
	Driving crank	z_{1x}	−0.9040305	−0.8481371	−0.8293872	−0.5263664	−0.3201976
		z_{1y}	−0.3963926	−0.4967889	−0.5362726	−0.4739537	0.4708757
	Coupler	z_{2x}	1.0167496	0.9892881	0.9650008	0.3135030	−1.5306150
		z_{2y}	−0.4968674	−0.1653630	−0.0467148	−0.3953437	0.5046108
		z_{6x}	0.9381487	0.9690021	0.9381027	−0.0990651	−0.6166645
	Foll. link	z_{4y}	−0.6456966	−0.6356831	−0.6173462	1.1683265	0.8449927
Generated path (see Fig. 6)	Precision point 1	r_1		1.0000000	1.0000000	1.3250130	1.7599999
		θ_1 deg		0.0000119	−0.0000134	−41.000001	131.00000
	2	r_2		1.7399947	1.7400001	1.0863603	1.3400000
		θ_2 deg		−29.199842	−29.499998	−22.999999	120.00000
	3	r_3		1.7400002	1.7400001	1.0090361	1.3399999
		θ_3 deg		−12.200131	−10.700002	0.7388921	87.000006
	4	r_4		1.7400018	1.7400024	1.0863579	1.6000032
		θ_4 deg		5.3996484	10.299987	22.999911	67.999884
	5	r_5		1.7400002	1.7400002	1.3250131	1.7599998
		θ_5 deg		25.899992	25.900002	40.999998	53.999963
Structural error: Extreme normal deviation from ideal path between precision points	1 and 2					−0.0166039	
	2 and 3			0.0023910	0.0040784	0.0096191	
	3 and 4			−0.0021263	−0.0042712	−0.0017289	
	4 and 5			0.0072560	0.0055978	0.0000671	
Approximate straightline, Example 4, generated abscissa		r_{1x}	1.0000000				
		r_{2x}	1.0000000				
		r_{3x}	1.0089522				
		r_{4x}	0.9999984				
		r_{5x}	1.0000001				

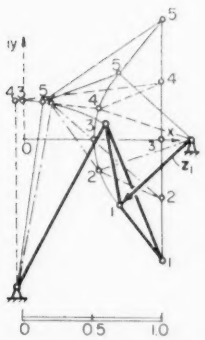

Fig. 14 Approximate straightline generation through 5 points with prescribed crank rotations: Example 4

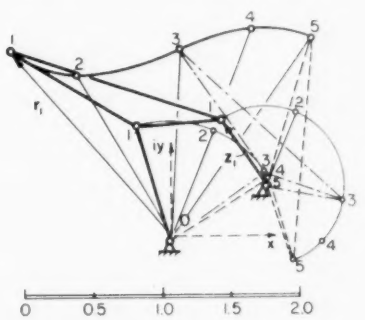

Fig. 15 Generating an arbitrary path through five points with prescribed crank rotations: Example 5

(3-8), reference [13], resulting in a reduction of the extreme structural error. The linkage of Example 4 generates an approximate straight line extending somewhat beyond the five prescribed points with notable accuracy.

Acknowledgments

The authors take pleasure in expressing their appreciation to the Electronic Research Laboratories and the Watson Laboratory—both of Columbia University—for the time generously allowed on the IBM 650 computer. The second author owes deep gratitude to his wife, Eugenia Nancy, who made it possible for him to engage in doctoral research work.

APPENDIX 1

Outline of the Derivation of the Quartic, Equation (45)

Since $\overline{\mathbf{v}_j} = \mathbf{v}_j^{-1}$, equations (30) and (31) can be combined with their complex conjugates to eliminate $\mathbf{v}_4$ and $\mathbf{v}_5$ respectively; this leads to the two equations

$$\mathbf{c}_m\mathbf{v}_2 + d_m + \mathbf{c}_m\mathbf{v}_2^{-1} = 0, \qquad (m = 1, 2), \tag{36}$$

where

$$\mathbf{c}_1 = \boldsymbol{\Delta}_3(\overline{\boldsymbol{\Delta}_1} + \overline{\boldsymbol{\Delta}_2}\mathbf{v}_2^{-1}), \qquad \mathbf{c}_2 = \boldsymbol{\Delta}_3'(\overline{\boldsymbol{\Delta}_1}' + \overline{\boldsymbol{\Delta}_2}'\mathbf{v}_2^{-1}), \tag{37}$$

$$d_1 = \boldsymbol{\Delta}_2\overline{\boldsymbol{\Delta}_1}\mathbf{v}_2 + \sum_1^3 \boldsymbol{\Delta}_j\overline{\boldsymbol{\Delta}_j} - \boldsymbol{\Delta}_1\overline{\boldsymbol{\Delta}_4} + \boldsymbol{\Delta}_4\overline{\boldsymbol{\Delta}_2}\mathbf{v}_2^{-1}, \tag{38}$$

and the expression for d_2 is obtained from that of d_1 when the $\boldsymbol{\Delta}_j$ and $\overline{\boldsymbol{\Delta}_j}$, for $j = 1, 2, 3$, are replaced by the $\boldsymbol{\Delta}_j'$ and $\overline{\boldsymbol{\Delta}_j}'$. If we multiply equations (36) by $\mathbf{v}_2$, we obtain

$$\mathbf{c}_m\mathbf{v}_2^2 + d_m\mathbf{v}_2 + \bar{\mathbf{c}}_m = 0, \qquad (m = 1, 2). \tag{39}$$

We now eliminate $\mathbf{v}_2$ from the system of four equations, two in (36) and two in (39), by writing the eliminant

$$\begin{vmatrix} 0 & \mathbf{c}_1 & d_1 & \bar{\mathbf{c}}_1 \\ 0 & \mathbf{c}_2 & d_2 & \bar{\mathbf{c}}_2 \\ \mathbf{c}_1 & d_1 & \bar{\mathbf{c}}_1 & 0 \\ \mathbf{c}_2 & d_2 & \bar{\mathbf{c}}_2 & 0 \end{vmatrix} = 0. \tag{40}$$

Expanding and collecting terms we obtain

$$\Re(\mathbf{p}\mathbf{v}_2^3 + \mathbf{q}\mathbf{v}_2^2 + \mathbf{s}\mathbf{v}_2) + t = 0, \tag{41}$$

where $\mathbf{p}$, $\mathbf{q}$, and $\mathbf{s}$ are complex numbers ($\mathbf{p} = p_x + ip_y$, and so forth) t is real, and all four are functions of the $\boldsymbol{\Delta}_j$ and $\boldsymbol{\Delta}_j'$, given in full in reference [15]. In trigonometric form equation (41) becomes

$$p_x \cos(3\gamma_2) - p_y \sin(3\gamma_2) + q_x \cos(2\gamma_2) - q_y \sin(2\gamma_2) + s_x \cos\gamma_2 - s_y \sin\gamma_2 + t = 0. \tag{42}$$

By means of trigonometric identities equation (42) is transformed to contain, as unknowns, powers of the sines and cosines of γ_2 only, all expressed in terms of a single variable

$$\tau = \tan(\gamma_2/2). \tag{43}$$

Thus we obtain the equation

$$\tau^5 + a_4\tau^4 + a_3\tau^3 + a_2\tau^2 + a_1\tau + a_0 = 0, \tag{44}$$

the coefficients of which are real and are functions of the $\boldsymbol{\Delta}_j$ and $\boldsymbol{\Delta}_j'$.

Referring to equations (21) and (28) we see that $\mathbf{v}_j = \boldsymbol{\lambda}_j$ will satisfy equations (30) and (31). Therefore $\tau_0 = \tan(\varphi_2/2)$ is a known root of equation (44). Eliminating τ_0 by synthetic division reduces equation (44) to a quartic with real coefficients

$$\tau^4 + b_3\tau^3 + b_2\tau^2 + b_1\tau + b_0 = 0. \tag{45}$$

Complete procedure for the computation of the coefficients b_0, b_1, b_2, and b_3 is given in reference [15].

APPENDIX 2

Simultaneous Solution of the Compatibility Equations (30) and (31) for γ_3, γ_4, and γ_5

A value of γ_2, determined from a real root of equation (45), is first substituted in equation (30), which is then solved for γ_3 and $\tilde{\gamma}_3$ following the procedure in lines (1-12) to (1-15) in Table 1. The same value of γ_2 is substituted in equation (31), which is then solved for the same variable, calling the solutions γ_3' and $\tilde{\gamma}_3'$. Equality of γ_3 or $\tilde{\gamma}_3$ with γ_3' or $\tilde{\gamma}_3'$ reveals the common root: If, for instance, $\gamma_3 = \gamma_3'$, then γ_3 and not $\tilde{\gamma}_3$ is the common solution. In that case, for instance, it follows that after completing the solution of equation (30) for γ_4 in accordance with lines (1-16) to (1-18) in Table 1, and similarly solving equation (31) for γ_5, that γ_4 and γ_5 will be the right solutions rather than $\tilde{\gamma}_4$ and $\tilde{\gamma}_5$, see Fig. 10. It is advisable to compute the residues of equations (30) and (31) for verification.

APPENDIX 3

Solution of the 2nd Compatibility System (33)-(34) for ψ_2, ψ_3, ψ_4, and ψ_5

The expansion and solution of equations (33) and (34) are analogous to those of equations (22) and (28) with these modifications:

(*a*) $\mathbf{v}_j$ replaces $\boldsymbol{\lambda}_j$, γ_j replaces φ_j, $\underline{\mathbf{u}}_j$ replaces $\mathbf{v}_j$, ψ_j replaces γ_j and the second-order minors are written as $\boldsymbol{\Delta}_{\nu j}$ and $\boldsymbol{\Delta}_{\nu j}'$ instead of $\boldsymbol{\Delta}_j$ and $\boldsymbol{\Delta}_j'$.

(*b*) The two or four possible values for γ_2, obtained from the real roots of equation (45), are also possible values for ψ_2. However, the value already used for γ_2 cannot be reused for ψ_2, because this would lead to $\underline{\mathbf{u}}_j = \mathbf{v}_j$, which is trivial. It is important to note that the computations of the coefficients of the quartic equation (45) and the solution of that equation need not be repeated.

(*c*) ψ_4 and ψ_5 need not be computed, except for verification of the solutions, if desired.

APPENDIX 4

Proof of Theorem 1

(*a*) Denote the links of the first synthesized linkage by the superscript(1) (see the linkage in double lines in Fig. 13) and the second by(2) (heavy lines in Fig. 13). In the system (20) or (26), interchanging the coefficients of the unknowns interchanges the solutions

$$\mathbf{z}_4^{(1)} = \mathbf{z}_4^{(2)}, \qquad \mathbf{z}_4^{(1)} = \mathbf{z}_3^{(2)}. \tag{46}$$

Furthermore, in accordance with the structure of the given type of mechanism, Fig. 8, the tips of the vectors $\mathbf{z}_4^{(1)}$ and $\mathbf{z}_4^{(2)}$ are pivoted to the tails of vectors $\mathbf{z}_3^{(1)}$ and $\mathbf{z}_3^{(2)}$, respectively. Since the tips of $\mathbf{z}_3^{(1)}$ and $\mathbf{z}_3^{(2)}$ meet at each prescribed path point, Fig. 13, the four vectors form a parallelogram in each prescribed position, and so the tails of $\mathbf{z}_4^{(1)}$ and $\mathbf{z}_4^{(2)}$ also meet in these positions of the mechanisms. But the tails of $\mathbf{z}_4^{(1)}$ and $\mathbf{z}_4^{(2)}$ are connected to fixed pivots and these pivots coincide at each prescribed position, hence, they coincide always. This establishes one of the three typical Roberts' parallelograms [3].

(*b*) By writing out the solutions in determinant form, it is easy to show that, for instance,

$$\mathbf{z}_3^{(1)}/\mathbf{z}_2^{(1)} = (\mathbf{z}_2^{(2)} - \mathbf{z}_3^{(2)})/\mathbf{z}_2^{(2)}, \tag{47}$$

which proves the similarity of the coupler triangles.

(*c*) The angles of rotation of the driving cranks $\mathbf{z}_1^{(1)}$ and $\mathbf{z}_1^{(2)}$ are correspondingly equal at each prescribed position, so that a bellcrank $\mathbf{z}_2^{(3)}$, $\mathbf{z}_3^{(3)}$, Fig. 13, pivoted at the tracer point, can be parallelogram-connected to both cranks. Thus the second and third Roberts' parallelograms are established.

(*d*) With the method of section (*b*) we can show that

$$\mathbf{z}_1^{(1)}/\mathbf{z}_1^{(2)} = (\mathbf{z}_2^{(1)} - \mathbf{z}_2^{(1)})/\mathbf{z}_2^{(1)} \tag{48}$$

which, by way of the parallelograms of section (*c*), establishes the third similar coupler triangle.

APPENDIX 5

Derivation of Relation (14)

Very briefly, relation (14) is derived as follows. In a displacement equation at most one motion characteristic, such as a stretch ratio (z_{jk}/z_{1k}) or a rotation φ_{jk} may be left unprescribed, otherwise the equation is meaningless from the viewpoint of synthesis.

Since the first equation of any set of s equations must be equation (4), which contains no motion characteristics, the number of unprescribed motion characteristics cannot exceed $(s - 1)$. Also, each motion characteristic is a real quantity, and each of the $(s - n + 1)$ compatibility equations (9) represents two real equations. The number of unprescribed reals must equal or exceed the number of (real) compatibility equations to be satisfied by them. Therefore

$$s - 1 \geq 2(s - n + 1) \tag{49}$$

which is readily simplified to relation (14).

References

1 S. Sh. Blokh, "On the Synthesis of Four-link Mechanisms," *Izvestia Akademii Nauk*, USSR, 1940, *Otdelniye Tekhnischeskich Nauk*, no. 1, pp. 47–54 (Russian).

2 R. Beyer, "Gelenkviereecke mit vorgeschriebenen Geschwindigkeits und Beschleunigungs-verhältnissen," *Getriebetechnik*, vol. 11, July, 1943, pp. 293–295.

3 R. Beyer, "Kinematische Getriebesynthese," Springer Verlag, Berlin-Göttingen-Heidelberg, Germany, 1953, pp. 189–191.

4 N. Rosenauer, "Gelenkviereeke mit vorgeschriebenen Groesst- und Kleinstwerten der Abtriebs-Winkelgeschwindigkeit," *Getriebetechnik*, vol. 12, January-February, 1944, pp. 25–27.

5 N. Rosenauer, "Anwendung von komplexen Veränderlichen zur Synthese einer Kurbelschwinge mit vorgeschriebenen Grenzen der Abtriebs-Winkel-Geschwindigkeit," *Ingenieur-Archiv*, vol. 24, 1956, pp. 43–46.

6 N. Rosenauer, "Complex Variable Method for Synthesis of Four-Bar Linkages," *Australian Journal of Applied Science*, vol. 5, 1954, pp. 305–308.

7 N. Rosenauer, "Synthesis of Four-Bar Linkages With Prescribed Reduction Ratio Limits: Application of Complex Variables," *Australian Journal of Applied Science*, Sydney, N.S.W., Australia, vol. 7, 1956, pp. 1–9.

8 E. Hackmueller, "Eine analytisch durchgeführte Ableitung der Kreispunkts und Mittelpunktskurve," *Zeitschrift für Angewandte Mathematik und Mechanik*, vol. 18, 1938, pp. 252–254.

9 I. I. Artobolevskii, S. Sh. Blokh, and V. V. Dobrovolskii, "Synthesis of Mechanisms," State Publishing House, Moscow and Leningrad, USSR, 1944, pp. 253–374 (Russian).

10 K. H. Sieker, "Analytische Betrachtung des Gelenkviereckes, insbesondere der Burmesterschen Punkte," *VDI Berichte*, vol. 5, 1955, pp. 55–60.

11 K. H. Sieker, "Winkel-Längen-Zuordnung an der Schubkurbel, Darstellung mittels komplexer Zahlen," *Konstruktion*, vol. 6, September, 1954, pp. 351–353.

12 K. H. Sieker, "Zur algebraischen Mass-Synthese ebener Kurbelgetriebe," *Ingenieur-Archiv*, vol. 24, Part 1, 1956, pp. 188–215; Part 2, 1956, pp. 233–257.

13 F. Freudenstein, "Structural Error Analysis in Plane Kinematic Synthesis," TRANS. ASME, series B, JOURNAL OF ENGINEERING FOR INDUSTRY, vol. 81, 1959, pp. 15–22.

14 I. I. Artobolevskii, "Theory of Mechanisms and Machines," third edition, Ministry of Culture, Moscow, USSR, 1953, pp. 88–90.

15 G. N. Sandor and F. Freudenstein, "Kinematic Synthesis of Path-Generating Mechanisms by Means of the IBM 650 Computer," IBM 650 Program Library File No. 9.5.003, obtainable from: Applied Programming Publications, IBM Corporation, 590 Madison Avenue, New York 22, N. Y.

16 J. A. Hrones and G. L. Nelson, "Analysis of the Four-Bar Linkage," John Wiley & Sons, New York, N. Y., 1951.

17 K. Hain, "Angewandte Getriebelehre," Hermann Schroedel Verlag, Hannover, Germany, 1952, pp. 326–341.

DISCUSSION

T. P. Goodman[4]

This paper, like Freudenstein's previous papers, makes a major contribution to kinematic synthesis. Its value lies not only in its presentation of a solution to one important kinematic-synthesis problem, but in its general approach which can be applied in the solution of many other problems.

For those interested in applying the authors' solution, it would be of interest to know approximately the amount of computing time which the IBM 650 computer requires to produce a column of Table 2.

N. Rosenauer[5]

The paper is a valuable contribution to the synthesis of mechanisms in which the most rational methods of solution are applied.

The modern method of complex numbers is combined with the advanced convenience of a digital computer.

The list of references is impressive, but, unfortunately, while mentioning under [1] the publication by S. Sh. Blokh, "On the Synthesis of Four-Link Mechanisms," which deals with synthesis satisfying velocity limits, the authors have missed another publication by the same S. Sh. Blokh: "Applications of Coupler Curves to the Synthesis of Plane Mechanisms," *Izvestia Akademii Nauk*, USSR, 1940; *Otdelenie Teknischeskich Nauk*, N. 7, pages 31–37, which is more related to the author's work. Furthermore, a whole book of 179 pages by N. I. Levitsky, "Design of Plane Mechanisms With Lower Pairs," edition of the Academy of Science, USSR, 1950, is left out of consideration. Chapters III and V of this book, pages 93–140 and 160–175, deal with the analytical "Synthesis of Path-Generating Four-Link Mechanisms."

In the German literature, the authors refer in [8] to E. Hackmüller, "Eine analytisch durchgeführte Ableitung der Kreispunkts und Mittelpunktskurve," which deals with the derivation of two fundamental curves in synthesis, but have missed another of his publications, E. Hackmüller, "Die Ermittlung von Koppeltrieben aus zwei Kurbel-Schub-Kurventrieben," *Ingenieur-Archiv*, 1943, vol. 14, no. 3, pages 141–154, in which the synthesis of path-generating mechanisms is developed, using complex numbers.

Further, in the German literature may be found some remarkable publications on the graphical synthesis of multilink mechanisms by J. Muller:

1 "Zur Analyse und Synthese achtgliedriger Gelenkgetriebe ohne Gelenkviereecke," *Wissenschaftliche Zeitschrift der Technischen Hochschule*, Dresden, Germany, vol. 3, no. 3, 1953–54, pp. 427–432.

2 "Zur Konstruktion achtgliedriger Gelenkgetriebe ohne

[4] Kinematics Engineer, General Engineering Laboratory, General Electric Company, Schenectady, N. Y. Assoc. Mem. ASME.

[5] New South Wales University of Technology, Sydney, New South Wales, Australia.

Gelenkvierecke," *Maschinenbautechnik*, vol. 3, no. 4, 1954, pp. 213–217.

3 "Konstruktionsverfahren zur Ermittlung der Abmessungen von acht-und zehngliedrigen Gelenckgetrieben," *Maschinenbautechnik*, vol. 3, no. 5, 1954, pp. 229–247.

Additional references by K. Hain follow:

1 "Volle Ausnutzung des Gelenkvierecks als Funktionsgetriebe," *Regelungstechnik*, vol. 4, no. 2, 1956, pp. 40–45.

2 "Die Verwendung der Gelenkvierecks zur Erzeugung gegebener ebener Kurven," *Messtechnik*, vol. 20, 1944, pp. 33–37 and 59–61.

3 "Die Analyse und Synthese der achtgliedrigen Gelenkgetriebe," *Verein Deutscher Ingenieure*, Berichte, vol. 5, 1955, pp. 81–93.

It would be worth while to attempt the solution of similar problems by the use of complex numbers and digital computers.

Authors' Closure

The authors are grateful to Drs. Goodman and Rosenauer for their kind and valuable discussions.

The amount of computing time required on the IBM 650 for one column of Table 2 is:

Solve Eq. (45)	1–2 minutes
Compute linkage dimensions (6 minutes for 2 linkages)	6–36 minutes (36 minutes for 12 linkages)
Compute path of selected mechanism (7 seconds per degree of crank rotation)	7–42 minutes
Total:	14–80 minutes

The authors appreciate the critical examination of references by Dr. N. Rosenauer; they have been aware of all the references cited by our distinguished colleague. In citing literature the authors have been guided by the philosophy to list all directly related investigations, but not to list remotely related material because of space limitations. Dr. Rosenauer's added references fall in this latter category in our estimation. Thus, regarding Russian literature, our reference [9] contains the results of all the earlier works of Professor Blokh cited by Dr. Rosenauer; concerning the book by Levitskii, far from being unaware of its contents, the first author referred to this work in one of his previous papers ("Structural Error Analysis in Plane Kinematic Synthesis, TRANS. ASME, series B, JOURNAL of ENGINEERING FOR INDUSTRY, vol. 81, 1959, pp. 15–21) and in fact, suggested a refinement of Levitskii's method therein (page 19, Table 4). Levitskii's book was not cited this time because the least square methods on which it is based have little connection with complex-number methods and because Levitskii's results are limited to points on the coupler *in line* with the coupler pivots and even then no crank rotations are co-ordinated to the path displacements. Similar remarks apply to the German literature. Reference [1], listed by Dr. Rosenauer, in connection with the works of K. Hain, for instance, is mentioned in the first author's "Five-Line Construction for a Computing Linkage," (*Journal of Applied Mechanics*, vol. 24, TRANS. ASME, vol. 79, 1957, pp. 621–622). This and the other German references were deemed too unrelated in methods and results to warrant inclusion in the present references.

The authors appreciate Dr. Rosenauer's scholarship and agree with him that the results of some of the German investigations mentioned by him could well have been derived by the complex-number approach and that it would be very much worth while to attempt the solution of similar problems by the digital-computer setup. As part of their future plans, the authors intend to develop the complex-number methods further and to construct tables of useful synthesized mechanisms with the aid of the IBM 650 computer. It is hoped that in the long run such design tables will become an integral part of mechanial design procedure.

PHILIP BARKAN

General Electric Company, Switchgear and Control Division, Philadelphia, Pa. Mem. ASME

E. J. TUOHY

General Electric Company, Switchgear and Control Division, Philadelphia, Pa.

Synthesis of the Four-Bar Linkage to Match Prescribed Velocity Ratios

A method is described for synthesizing a four-bar linkage in terms of its velocity ratio at two or three positions of the input crank. The two-point synthesis problem is readily solved by either graphical or longhand mathematical techniques. The method also lends itself to computer solution for the three-point synthesis problem and also for determining the best match of a desired function over a specified range of input crank motion.

THE four-bar linkage is frequently employed as a force or energy-transmitting device. In such applications, the velocity ratio of the four-bar linkage, as a function of its motion, is an important design criterion. For example, the dynamic behavior of circuit breakers [1][1] on both opening and closing operations is significantly influenced by the velocity-ratio characteristics of the four-bar linkages employed. Consider the four-bar linkage in Fig. 1; the differential element of energy introduced into the linkage at the driving crank is $T_\theta d\theta$ and the corresponding element of energy at the output crank is $T_\psi d\psi$. Neglecting friction and inertia effects in the linkage, conservation of energy requires that

$$T_\theta d\theta = T_\psi d\psi$$

or

$$\frac{T_\theta}{T_\psi} = \frac{d\psi}{d\theta} = \psi'$$

where ψ' is the velocity ratio. If an energy source with a known torque-displacement relationship is coupled to the input crank, the output torque will be a function of the velocity-ratio characteristics of the four-bar linkage. The design of a coupling between a prime mover and some machine entails detailed consideration of the velocity ratio of the four-bar linkage.

This paper considers the synthesis of a four-bar linkage in terms of specified values of velocity ratio (ψ') at either two or three positions of the input crank.

It also outlines a least-squares method for two positions. In this the fit of the linkage ψ' at a number of points over the desired range is optimized.

The paper describes the methods and their application. Derivations are given in the Appendix.

Description of Methods

All of the methods to be described are based on the following theorem of the four-bar linkage, which is proved by Brand [2], and described more recently by Freudenstein [3] and Carter [4].

Referring to Fig. 1; in any four-bar linkage, the coupler, A, extended if necessary, divides the fixed link, C, into two segments whose lengths are inversely proportional to the angular velocities of the adjacent links.

In Fig. 1

$$\psi_i' = \left(\frac{d\psi}{d\theta}\right)_i = \frac{e_i}{e_i + C}$$

or

$$e_i = \frac{C\psi'_i}{1 - \psi_i'} \tag{1}$$

The remainder of this text concerns itself with application of this relationship to the synthesis problem.

Graphical Solution: Two-Point Synthesis Problem.

Given:

At $\theta = \theta_1$ $\quad \psi' = \psi_1'$ $\quad$ link C
At $\theta = \theta_2$ $\quad \psi' = \psi_2'$

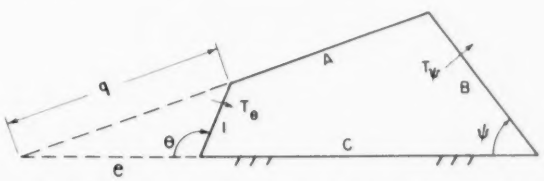

Fig. 1 Typical four-bar linkage showing nomenclature used

[1] Numbers in brackets designate References at end of paper.

Contributed by the Machine Design Division and presented at the Annual Meeting, November 30–December 5, 1958, New York, N. Y., of THE AMERICAN SOCIETY OF MECHANICAL ENGINEERS.

NOTE: Statements and opinions advanced in papers are to be understood as individual expressions of their authors and not those of the Society. Manuscript received at ASME Headquarters, July 15, 1958. Paper No. 58—A-115.

Nomenclature

The nomenclature is illustrated in Figs. 1 and 2.

A = coupler-link length relative to input-crank length
B = output-link length relative to input-crank length
C = fixed-link length relative to input-crank length
e_i = distance from center of rotation of input crank to intercept of A on C, each extended if necessary, Fig. 1
k = spring gradient
T_θ = torque applied to input crank (1)
T_ψ = torque applied to output crank (B)
θ = input-crank angle
ψ = output-crank angle

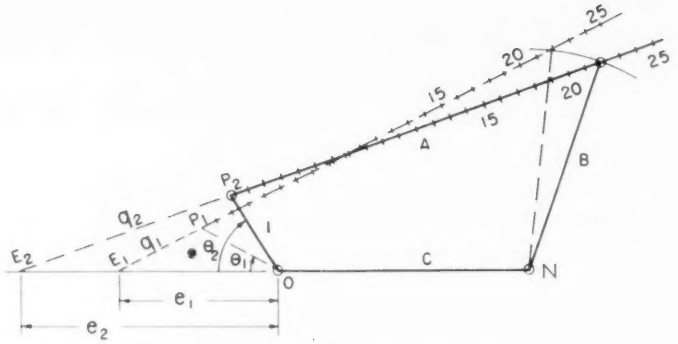

Fig. 2 Illustration of graphical two-point synthesis

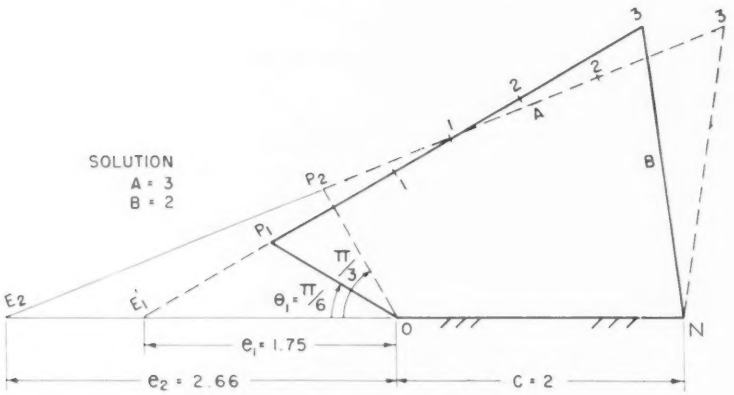

Fig. 3 Graphical two-point synthesis—Example I

Find: A, B, the remaining links of the desired four-bar linkage.

Solution (see Fig. 2):

1 From equation (1), compute lengths e_1 and e_2, retaining their algebraic sign. An infinite value of e implies that A is parallel to C.

2 To any convenient scale for which the input crank is of unit length, draw the fixed link, C, and the input crank (1) at its two specified positions.

3 Starting from point O lay out lengths e_1 and e_2 along C. If the sign of e is positive, plot on the extension of C; if negative, plot along C.

4 Draw lines $E_2 P_2$ and $E_1 P_1$, extended in both directions.

5 With points P_1 and P_2 as the origins, lay off equal divisions in both directions along $E_2 P_2$ and $E_1 P_1$.

6 With point N as an origin, lay off a series of arcs of different radii, intersecting both $E_1 P_1$ and $E_2 P_2$. By trial determine the length of radius whose arc intersects both lines at the same length A. This constitutes the required linkage.

Example I. Find the four-bar linkage which satisfies the following conditions:

$$\theta = 30 \text{ deg} \qquad \psi' = 0.466$$

$$\theta = 60 \text{ deg} \qquad \psi' = 0.571$$

$$C = 2$$

Solution (see Fig. 3):

1 From equation (1) calculate lengths e_1 and e_2

$$e_1 = \frac{2 \times 0.466}{0.534} = 1.75$$

$$e_2 = \frac{2 \times 0.571}{0.429} = 2.66$$

2 Draw the fixed link $C = 2$ to a convenient scale and the input crank with unit length in position $\theta_1 = 30$ deg and $\theta_2 = 60$ deg.

3 Starting from point O lay out length $e_1 = 1.75$ and $e_2 = 2.66$ along C extended (both e_1 and e_2 are positive).

4 Draw lines $E_1 P_1$ and $E_2 P_2$ extending beyond these points in both directions.

5 With points P_1 and P_2 as origins lay off equal divisions in both directions along $E_2 P_2$ and $E_1 P_1$.

6 With point N as origin lay off a series of arcs of different radii intersecting both $E_1 P_1$ and $E_2 P_2$. The arc which intersects both lines at the same length A is the required link $B = 2$. The link $A = 3$ is then measured. This constitutes the required linkage.

Mathematical Solution, Two-Point Synthesis. Because in equation (1)

$$\lim_{\psi' \to 1} e_i = \infty$$

it is necessary to divide the mathematical approach into three cases depending upon whether the velocity ratio at one or more points is exactly equal to unity.

Case I

$$\psi_i' \neq 1$$

Given: Relative length C and the following conditions:

$$\theta = \theta_1; \qquad \psi' = \psi_1'$$
$$\theta = \theta_2; \qquad \psi' = \psi_2'$$

Find: Link lengths A and B of four-bar linkage satisfying these conditions

Solution. As derived in the Appendix, for these conditions the length of coupler link, A, is

$$A = \frac{C\,[\cos\theta_2 - \cos\theta_1]}{\frac{1}{q_1}[1 - (e_1 - C)\cos\theta_1 - Ce_1] - \frac{1}{q_2}\,[1 - (e_2 - C)\cos\theta_2 - Ce_2]} \tag{2}$$

where

$$q = \frac{e + C}{|e + C|}\,(e^2 + 1 - 2e\cos\theta)^{1/2} \tag{3}$$

The length of the remaining crank link B is also shown in the Appendix I to be

$$B = \left\{C^2 + A^2 + 2C\cos\theta_1 + \frac{2A}{q_1}\,[1 - (e_1 - C)\cos\theta - Ce_1] + 1\right\}^{1/2} \tag{4}$$

Here A retains the sign dictated by equation (2). Adherence to the indicated sign convention is essential. In constructing the linkage after solution for A and B, it will frequently be found that two possible configurations of four-bar linkages will satisfy the specified link lengths; only one of which will satisfy the specified velocity ratios. This problem is readily overcome by introducing the value of e_1 in the construction. Thus, in graphically constructing the linkage at a position where $\theta = \theta_1$, the orientation of link A is dictated by the sign and magnitude of e_1.

Case II. Analytical solution, two-point synthesis, $\psi' = 1$ at one point:

Given: Relative length C and the following conditions:

$$\theta = \theta_1 \qquad \psi' = 1$$
$$\theta = \theta_2 \qquad \psi' \neq 1$$

Find: Link lengths A and B.

Solution. As derived in the Appendix the length of link A under these conditions is given by

$$A = \frac{C[\cos\theta_1 - \cos\theta_2]}{\frac{1}{q_2}\,[1 + (C - e_2)\cos\theta_2 - Ce_2] + C + \cos\theta_1} \tag{5}$$

With A and its sign known, B is then obtained from equation (4), with data at the point where $\psi' \neq 1$. If data at the point where $\psi' = 1$ are used, the following equation should be used to evaluate link B:

$$B = [1 + A^2 - 2A(c + \cos\theta_1) + c^2 + 2c\cos\theta_1]^{1/2} \tag{6}$$

Case III. $\psi_1' = \psi_2' = 1$ is a trivial problem which is satisfied by any parallelogram. For this condition $A = C$, and $B = 1$.

Example II. Find mathematically the four-bar linkage which satisfies the following conditions:

$$\theta = 30 \text{ deg} \qquad \psi' = 0.466$$
$$C = 2, \qquad \theta = 60 \text{ deg} \qquad \psi' = 0.571$$

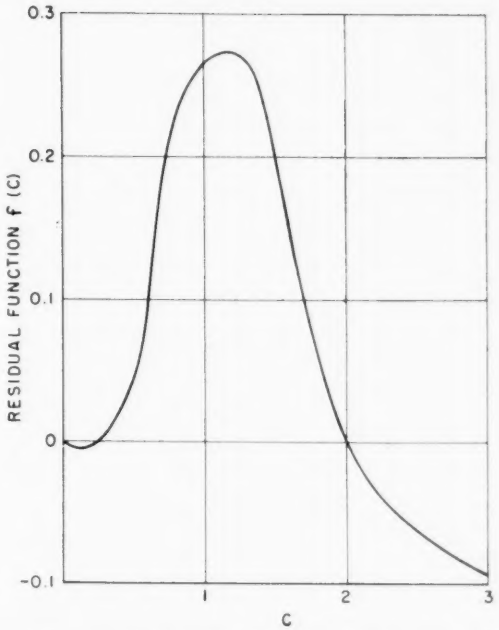

Fig. 4 Residual function of equation (7)—Example III

Solution. From equation (2), $A = 3.00$; from equation (4), $B = 2.00$.

Synthesis of a Four-Bar Linkage in Terms of the Velocity Ratio at Three Positions of the Input Crank

Given: $\psi_1', \psi_2', \psi_3'$ at $\theta_1, \theta_2, \theta_3$

Find: Link lengths A, B, C of the four-bar linkage satisfying this requirement, or a recommended best fit if no exact solution is possible.

Solution. As derived in the Appendix an equation relating C and the three given data is:

$$f(C) = (\cos\theta_1 - \cos\theta_2)q_1q_2\left\{C\left(\left[1 - \frac{e_3}{C}\right]\cos\theta_3 - e_3\right) + 1\right\}$$
$$+ (\cos\theta_2 - \cos\theta_3)q_2q_3\left\{C\left(\left[1 - \frac{e_1}{C}\right]\cos\theta_1 - e_1\right) + 1\right\}$$
$$+ (\cos\theta_3 - \cos\theta_1)q_3q_1\left\{C\left(\left[1 - \frac{e_2}{C}\right]\cos\theta_2 - e_2\right) + 1\right\} = 0 \tag{7}$$

where e_i and q_i are defined by equations (1) and (3) with the same restriction that $\psi' \neq 1$. A trivial solution of equation (7) is $C = 0$. Equation (7) does not lend itself to convenient reduction to an explicit expression for C. However, where a high-speed digital computer is available it is possible to evaluate and plot the residual function $f(C)$ defined by equation (7) at fixed increments of C. The intercepts of the plot represent the desired solution; e.g., see Fig. 4. An advantage of the plot is that it shows not only if exact solutions exist for the specified conditions, as evidenced by zero values for the residual function, but also values of C which, while not exact solutions, are probably good approximations as evidenced by a relatively small value for the residual function. Thus a satisfactory fit might be found in a desirable range of C, even though no exact solution exists. This is best demonstrated by the example in Fig. 6. The range of values of C to be explored can be limited to those which will produce practical proportions of four-bar linkages. Usually, $C < 10$. In our ex-

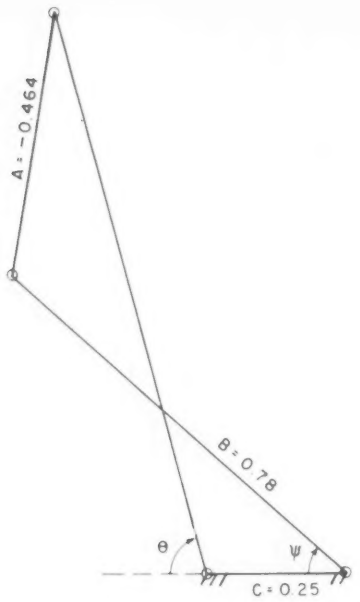

Fig. 5 One of two linkages matching specified ψ' points of Example III

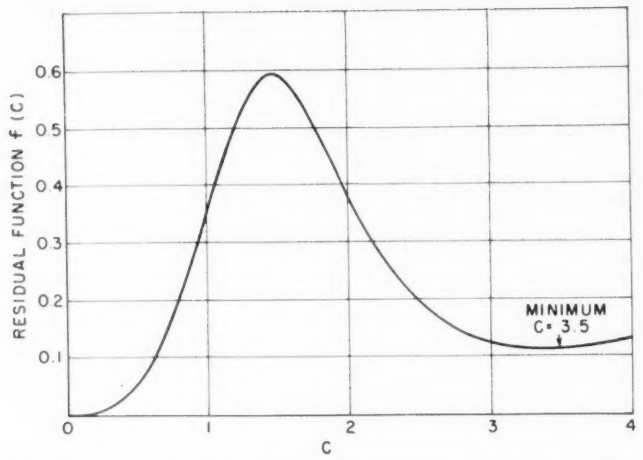

Fig. 6 Residual function of equation (7) for constant-torque linkage of Example IV

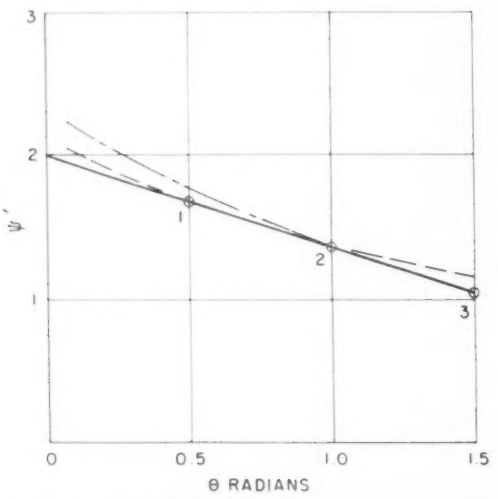

Fig. 7 Velocity ratio required to produce constant output torque with linear spring gradient on input crank—Example IV

————— Function to be synthesized
— — — — — Linkage satisfies points 1 and 2
— - — - Linkage satisfies points 2 and 3

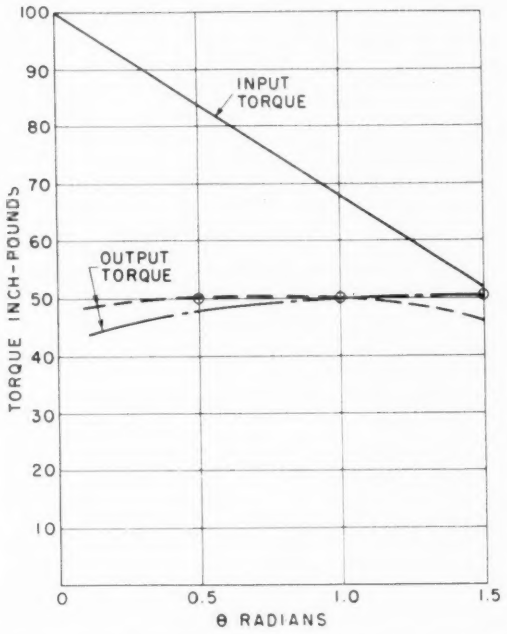

Fig. 8 Torque output of two linkages with a linear spring input—results of solution to Example IV. Same key as Fig. 7.

perience with this method a rather coarse increment, say $\Delta C = 0.5$ is adequate to evaluate the function.

Example III. Find the four-bar linkage which satisfies the following conditions:

$$\theta = \pi/6 \qquad \psi' = 0.466$$

$$\theta = \pi/4 \qquad \psi' = 0.522$$

$$\theta = \pi/3 \qquad \psi' = 0.571$$

The foregoing specifications are fed to the digital computer which is programmed to solve equation (7) for a range of values of C. The result is plotted in Fig. 4. Intercepts of this curve represent the desired solution. Two solutions are revealed. Corresponding to $C = 2$ the remaining links are $B = 2, A = 3$. Corresponding to $C = 0.25$ the remaining links are $A = -0.464, B = 0.78$, Fig 5.

Example IV—Constant Torque From a Spring. A four-bar linkage can be used as a means of approximately converting a linearly decaying spring torque to a nearly constant-output torque over a moderate range of output angle. The input spring torque can be expressed as

$$T_\theta = T_0 - k\theta \qquad (8)$$

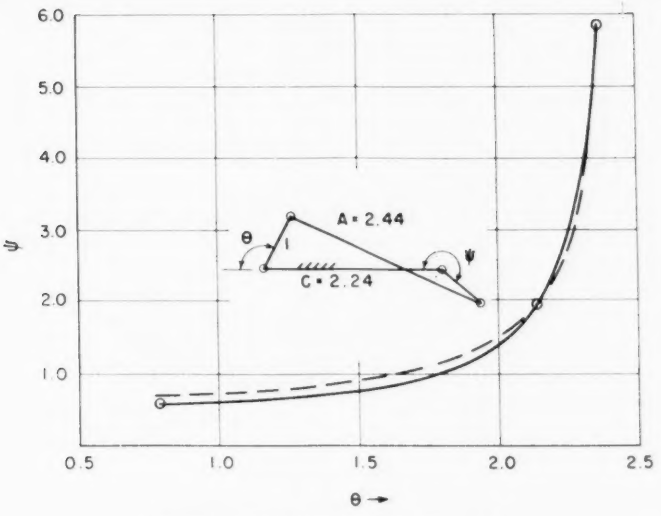

Fig. 9 Synthesis of log function—Example V

If T_ψ is to be a constant torque we must have

$$\frac{d\psi}{d\theta} = \frac{T_\theta}{T_\psi} = \frac{T_0}{T_\psi} - \frac{k\theta}{T_\psi} \tag{9}$$

With $T_0 = 100$, $T_\psi = 50$, $k = 100/\pi$, it is desired to design a four-bar linkage which will yield an output torque of approximately 50 over the range $\theta = 0.5$ to 1.5 radians. Use equation (7) for the three-point solution. Design values are given in Table 1:

Table 1

	θ	ψ'
θ_1	0.5	1.682
θ_2	1.0	1.364
θ_3	1.5	1.046

For the condition cited, Fig. 6 shows that no exact solution was found; but that $C = 3.5$ provides a minimum residual which we interpret as a good match. The following two slightly different solutions then arise depending on which pair of points is used to compute A and B:

$$A_{12} = 3.276 \qquad A_{23} = 3.438$$

Two possible velocity-ratio curves are shown in Fig. 7. The calculated torque output from these two linkages is shown in Fig. 8. It is seen that each is relatively constant over different ranges of θ.

Example V—Log Function Using Three-Point Synthesis. Given the three points of Table 2 from the equation

$$\frac{\psi'}{0.682} = \frac{d}{d\theta}\,[\ln(2.47 - \theta)]$$

No exact solution was found, but a value $C = 2.24$ left the smallest residual, Fig. 11. With this C the remaining links were calculated so that the first two points would be exactly satisfied, giving $A = 2.44$, $B = 0.77$. The linkage and its velocity-ratio curve, along with the desired ψ'-curve, are shown in Fig. 9.

Table 2

	θ	ψ'
θ_1	2.36	−5.85
θ_2	2.12	−1.95
θ_3	−0.786	−0.585

Influence of Initial Input Angle

In many problems the *range* of the input angle θ is of importance rather than the absolute value of θ. Thus, if we let $\theta_i = \theta_1 + \Delta\theta_i$ it is possible to extend the study by systematically varying θ_1 over a range of values. The influence of θ_1 in the previous problem is shown in Figs. 10 and 11. It is seen in Fig. 11 that two exact solutions satisfying the three precision points are found if $\theta_1 = 2.66$ rather than $\theta_1 = 2.36$ as in Example V. Fig. 13 shows the two linkages. By varying θ_1 over a range $0 \leqslant \theta_1 \leqslant \pi$ all possible solutions can be found. Again, a rather coarse increment in θ_0 can be used with interpolation to obtain all solutions to a particular problem.

Least-Squares Match for a Velocity-Ratio Curve

It can be seen from Fig. 10 that the solution which matches all three specified points of the function is not necessarily the best match over the complete range of the curve. Thus it frequently is desirable to use a minimum root-mean-error as a criterion of optimum design. Two points are matched exactly as values of link C are systematically varied. Since the linkage is defined for each value of C the velocity ratio can be calculated at a number of test points. These results are compared with the desired velocity-ratio curve. The criterion of the best C (or best linkage) is that for which the sum of the squares of the error is a minimum. It is evident that this technique requires use of a digital computer.

References

1 P. Barkan, "Dynamics of High Capacity Outdoor Oil Breakers," *AIEE Trans.*, vol. 74, Part III, 1955, pp. 671–676.

2 L. Brand, "Vectorial Mechanics," John Wiley & Sons, New York, N. Y., 1930.

3 F. Freudenstein, "On the Maximum and Minimum Velocities and the Accelerations in Four-Bar Link Mechanisms," TRANS. ASME, vol. 78, 1956, pp. 779–787.

4 W. J. Carter, "Kinematic Analysis and Synthesis Using Collineation-Axis Equations," TRANS. ASME, vol. 79, 1957, pp. 1305–1312.

5 J. A. Hrones and G. L. Nelson, "Analysis of the Four-Bar

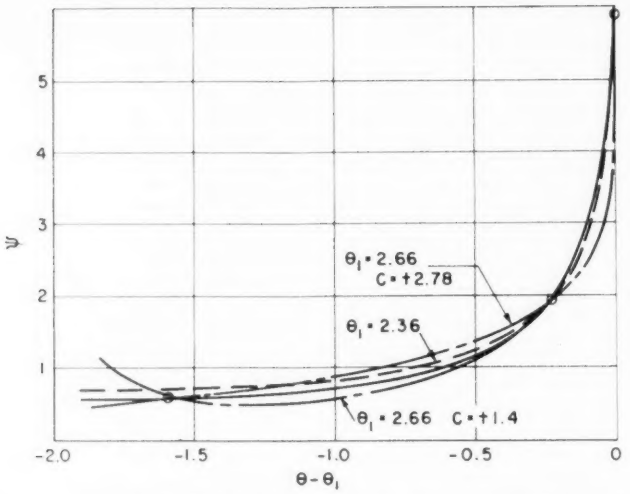

Fig. 10 Comparison of log function synthesis with different input initial angles

——— Function to be synthesized
— — — — Linkage characteristics for best match with $\theta_1 = 2.36$
— — — Best match with $\theta_1 = 2.66$

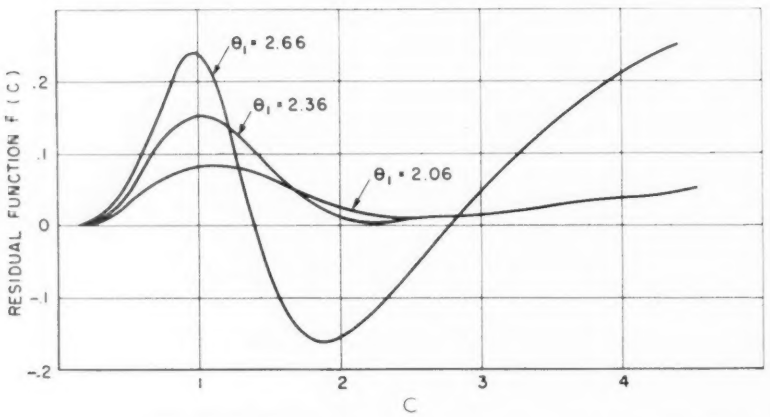

Fig. 11 Residual function of equation (7) for different initial angles. Solution for log function.

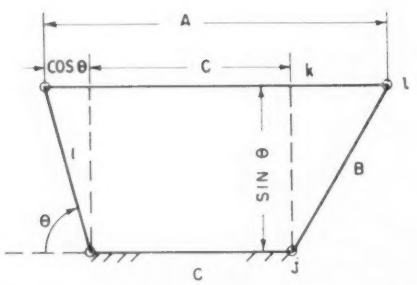

Fig. 12 Four-bar linkage showing conditions when $\psi' = 1$

Linkage," M.I.T. Technology Press and John Wiley & Sons, New York, N. Y., 1951.

APPENDIX

Derivation of Equation for Synthesizing a Four-Bar Linkage to Match Two Specified Velocity Ratios. In any position of the linkage (designated by the subscript i) the law of cosines requires that

$$B^2 = (e_i + C)^2 + (A + q_i)^2 - 2(A + q_i)(e_i + C)\cos\phi_i \quad (10)$$

where e is considered positive if it extends beyond rather than overlaps C. In Fig. 1, by dropping the perpendicular from the apex of triangle ($q_i \sim 1 \sim e_i$), we obtain

$$\cos\phi_i = \frac{e_i - \cos\theta_i}{q_i} \quad (11)$$

Also, by applying the law of cosines in the triangle $q \sim 1 \sim e_1$

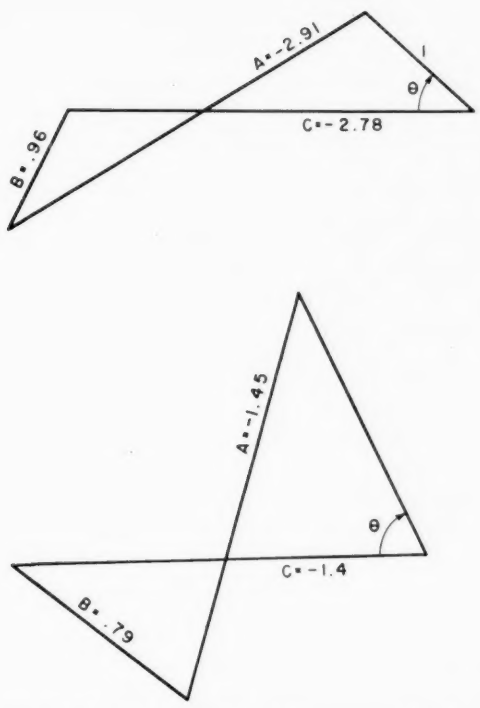

Fig. 13 Two linkages which match three precision points of log function of Example V

$$q_i = \frac{e_i + C}{|e_i + C|} \{e_i^2 + 1 - 2e_i \cos \theta\}^{1/2} \qquad (12)$$

From geometric considerations it can be shown that q_i must follow the sign of $(e + C)$. Expanding equation (10) and substituting for $\cos \phi_i$ and q_i^2 from equations (11) and (12) yields

$$B^2 = 1 + C^2 + A^2 + 2C \cos \theta_i + \frac{2A}{q_i} [1 - (e_i - C) \cos \theta_i - Ce_i] \qquad (13)$$

Taking the square root of (13) gives equation (4). Since B is a constant we can equate equation (13) at two arbitrary values of θ_i. Designating these two arbitrary positions by subscripts 1 and 2 and simplifying the resulting equation, gives

$$A = \frac{C[\cos \theta_2 - \cos \theta_1]}{\frac{1}{q_1}[1 - (e_1 - C) \cos \theta_1 - Ce_1] - \frac{1}{q_2}[1 - (e_2 - C) \cos \theta_2 - Ce_2]} \qquad (14)$$

These equations are valid provided e is finite. Since $\lim_{\psi' \to 1} e = \infty$ it is necessary to consider the following cases.

Case II. $\psi' = 1$ at one of two specified points. Given that $\psi' = 1$ at θ_1; $\psi' \neq 1$ at θ_2. Then from equation (1), $e_1 = \infty$, which implies that coupler link A must be parallel to C as shown in Fig. 12. Since A is parallel to C

$$kj = \sin \theta; \quad kl = A - (C + \cos \theta)$$

$$B^2 = \sin^2 \theta + [A - (C + \cos \theta_1)]^2$$

$$B^2 = 1 + A^2 - 2A(C + \cos \theta_1) + C^2 + 2C \cos \theta_1 \qquad (15)$$

when $\psi_1' = 1$.

For the second point θ_2 where $\psi_2' \neq 1$, equation (13) applies. Equating equations (13) and (15) and solving for A gives

$$A = \frac{C[\cos \theta_1 - \cos \theta_2]}{\frac{1}{q_2}[1 + (C - e_2) \cos \theta_2 - Ce_2] + C + \cos \theta_1} \qquad (5)$$

Equation (5) is subject to the restriction $\psi_1' = 1$; $\psi_2' \neq 1$.

Derivation of Equation for Three-Point Synthesis. Equation (2) defines link A of a linkage which satisfies required velocity ratios at two positions θ_1 and θ_2. We designate this as link A_{12}. A second expression for A, designated A_{13}, can be obtained for positions θ_1 and θ_3 and their corresponding values ψ_1' and ψ_3'. The derivation is restricted to the case $\psi' \neq 1$. If a value of C can be found for which $A_{12} = A_{13}$, a li kage can be defined which satisfies the three designated values of velocity ratio. Thus

$$f(c) = A_{12} - A_{13} = 0 \qquad (16)$$

This equation in C, when satisfied, defines the desired linkage. However, the equation in this form is not conducive to convenient numerical solution by either of the methods described in the text. This arises because for certain values of C the denominator of equation (2) goes to zero, resulting in an extremely erratic function which is thus difficult to solve numerically.

A more suitable function in C is obtained as follows: Substitute (2) in (16) and multiply through by the following factor:

$$q_1 q_2 q_3 \left[q_2 - q_1 + \frac{(e_1 + C)(e_1 - \cos \theta_1)}{q_1} + \frac{(e_2 + C)(e_2 - \cos \theta_2)}{q_2}\right] \left[q_3 - q_1 + \frac{(e_1 + C)(e_1 - \cos \theta_1)}{q_1} + \frac{(e_3 + C)(e_3 - \cos \theta_3)}{q_3}\right]$$

Expanding the resulting function and recombining terms yield equation (7) after some tedious algebra. Equation (7) is a much better behaved function than equation (16).

DISCUSSION

C. W. Allen[2]

The problem considered by the authors is a variation of the function generation problem covered by Freudenstein[3] and others. There exist possible further applications as a function generation procedure as shown by Example V.

The use of energy-torque-velocity relations in approaching the problem clearly illustrates a relation between the kinematics and dynamics often overlooked by others.

In the authors' "Graphical Solution: Two-Point Synthesis," the final steps involve a trial-and-error solution that can be replaced by a direct construction. The solution is carried through step number 4 and completed by the following procedure. The design at this point is considered to consist of two separate bodies. Each body will be allowed to move relative to the other, but no relative motion of points will be allowed within either body. Thus points E_2, P_2, O, and N are considered a part of body two and can be moved with respect to points E_1, P_1, O, and N of body one. (Both O and N are considered to be points on both bodies one and two.) Body two is rotated about point O until point P_2 is coincident with point P_1. E_2 now is located at some new point

[2] Engineer, General Electric Company, Richland, Wash.

[3] F. Freudenstein, "Approximate Synthesis of Four-Bar Linkages," TRANS. ASME, vol. 77, 1955, pp. 853–861.

E_2' and point N of body two is located at a new point N'. Body two is next rotated about point P_1 until lines $E_2'P_1$ and E_1P_1 are coincident. During this rotation point N' is moved to some new position N''. The pin joint between links A and B can now be located by finding the intersection of the perpendicular bisector of NN'' and the line E_1P_1.

A. E. Richard de Jonge[4]

The authors distinguish between a "graphical" and a "mathematical solution." Both are, however, "mathematical" solutions, the first being a "geometrical" one and the second an "algebraic" or "analytical" solution.

The analytical relationship on which the geometrical solution is based is correct. As far as the authors' geometrical solution is concerned, they have solved the problem of finding the lengths of the coupler and of the lever (follower) by a trial-and-error process. This is not necessary, however, because an exact solution by means of kinematic geometry can be applied.

This solution is based on considering the two positions of the coupler as being obtained by a simple rotation about the rotopole[5] for the two coupler positions. The rotopole is found as the intersection of the mid-perpendiculars of the chords belonging to the arcs of rotation of any two points of the coupler. All the mid-points of such chords lie on a straight line called the "mid-line."[6]

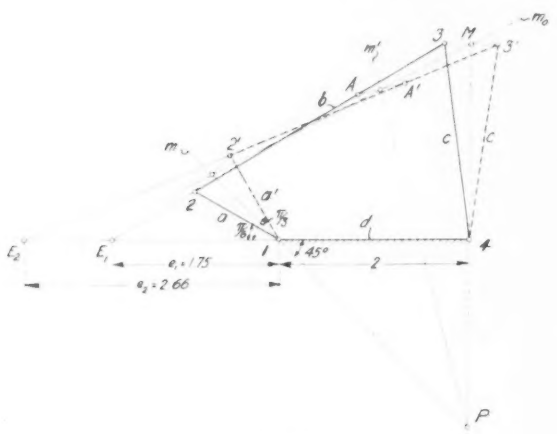

Fig. 14

In the accompanying Fig. 14, 1-2 and 1-2′ are the given positions a and a' of the crank, E_1-2 and E_2-2′ the two positions of the coupler centerline. m is the mid-perpendicular of chord 2-2′ and passes through 1, the fixed pivot of crank a. Assume any point A on the first position of the coupler E_1-2 and find its corresponding point A' on the second position of the coupler so that 2-A = 2′-A', thus yielding chord AA'. The mid-perpendicular m' of AA' meets m in the rotopole P for the rotation which brings 2A into the position 2′A'. All the mid-points of the chords lie on the mid-line m_0. Let 4 be the fixed pivot of lever 3-4 of the four-bar linkage 1234 or 12′3′4 to be determined. To find the position of point 3 at which the coupler b is to be hinged to the lever c = 3-4, join P with 4. P-4 meets m_0 in M, and a perpendicular at M to PM meets the two positions of the coupler centerline in the hinge points 3 and 3′, respectively, and thus yields the end points of the lever 3-4 and 3′-4′, respectively. 2-3 or 2′-3′ is the length of the coupler b, and 3-4 or 3′-4′ that of the lever c.

The remainder of the paper appears to be correct.

Ferdinand Freudenstein[7] and G. N. Sandor[8]

The authors deserve credit for having created an easy-to-visualize design tool, a welcome gift to the practicing designer, and also for the use of advanced computational techniques in the solution of a "velocity-ratio" synthesis. The following complex-number solution is based on the general method of reference [1][9] and is offered as an illustration of another approach.

Nomenclature. Same as that used by the authors, Fig. 1, with the following additions:

$$\left.\begin{array}{ll} \text{Driving crank vector,} & \mathbf{Z} = Ze^{i\theta} \\ \text{Coupler vector,} & \mathbf{A} = Ae^{i\gamma} \\ \text{Output link vector,} & \mathbf{B} = Be^{i(\psi+\pi)} \end{array}\right\} \qquad (17)$$

The angles in equation (17) are measured clockwise from the left-directed line-of-centers to the link in question, while the vector polygon formed by these links has a clockwise sense of rotation.

The *incremental equation of closure*, expressed in the manner of a vanishing *path vector chord*, takes the form

$$(1 - e^{i\theta_{12}})\mathbf{Z} + (1 - e^{i\gamma_{12}})\mathbf{A} + (1 - e^{i\psi_{12}})\mathbf{B} = 0 \qquad (18)$$

where the subscript "12" denotes the change in the angle in going from position "1" to position "2". Differentiation of the polygonal closure equation (18) yields the "velocity closure" equation:

$$(e^{i\theta_j}j)\mathbf{Z} + \gamma_j'(e^{i\gamma_j}j)\mathbf{A} + \psi_j'(e^{i\psi_j}j)\mathbf{B} = 0, \quad j = 1, 2 \qquad (19)$$

where the prime denotes differentiation with respect to θ, and j denotes the position at which the derivative is computed.

Equations (18) and (19) represent a set of three simultaneous equations, homogeneous and linear in the three unknowns $\mathbf{Z}$, $\mathbf{A}$, and $\mathbf{B}$. Solutions exist, provided the determinant of the coefficients vanishes:

$$\nabla = \begin{vmatrix} 1 - e^{i\theta_{12}} & 1 - e^{i\gamma_{12}} & 1 - e^{i\psi_{12}} \\ 1 & \gamma_1' & \psi_1' \\ e^{i\theta_{12}} & \gamma_2'e^{i\gamma_{12}} & \psi_2'e^{i\psi_{12}} \end{vmatrix} = 0 \qquad (20)$$

This equation implies free choice of any five of the seven quantities, say, θ_{12}, ψ_{12}, γ_{12}, ψ_1', and ψ_2', which then determine the remaining two; namely, γ_1' and γ_2'. Compatible coefficients for the three equations (18) and (19) thus having been determined, one of the vectors, say, $\mathbf{Z}$, can be assumed arbitrarily, and the other two found as the simultaneous solution of any two of the three equations.

In conclusion, it may be worth mentioning the previous work of K. Hain [2, 3, 4] who has given simple, albeit special, constructions for prescribed angular velocity ratios in two positions.

References

1 F. Freudenstein and G. N. Sandor, "Synthesis of Path-Generating Mechanisms by Means of a Programmed Digital Computer," published in this issue, pp. 159-168.

[4] Mechanical Engineer, The Reeves Instrument Corporation; Adjunct Professor, The Polytechnic Institute of Brooklyn; Lecturer, The City College of New York, New York, N. Y. Mem. ASME.

[5] For the origin of the new terminology introduced by the writer, see his paper, "A Brief Account of Modern Kinematics," TRANS. ASME, vol. 65, 1943, p. 663.

[6] Introduced by Arthur Schönfliess, 1886.

[7] Associate Professor, Department of Mechanical Engineering, Columbia University, New York, N. Y. Assoc. Mem. ASME.

[8] Chief Engineer, Springdale Laboratories, Division of Time, Inc., Springdale, Conn.

[9] Numbers in brackets designate References at end of this discussion.

2 K. Hain, "Periodische Winkelgeschwindigkeits- und Drehmomentwandler," *Zeitschrift des Vereins Deutscher Ingenieure*, vol. 93, 1951, pp. 239–244.

3 K. Hain, "Volle Ausnutzung des Gelenkvierecks als Funktionsgetriebe" *Regelungstechnik*, vol. 2, no. 2, 1956, pp. 40–45.

4 F. Freudenstein, "Five-Line Construction for a Computing Linkage Satisfying Five Precision Requirements," *Journal of Applied Mechanics*, vol. 24, TRANS. ASME vol. 79, 1957, pp. 621–622.

Bruce L. Harding[10]

This paper adds a sturdy block to the yet small structure of velocity synthesis in linkages. The simplicity of the concept should make it a popular technique. The equations presented will no doubt be of value in subsequent investigation of the four-bar linkage.

In their graphical solution, the authors use a somewhat trial-and-error technique to locate the missing pivot; this pivot can be located directly by application of inverted design. Having chosen a length for the stator C, calculated the dimensions e_1 and e_2, and shown the driving crank in the two desired positions with a chosen length, the two coupler lines can be drawn as shown in Fig. 2 of the paper. The known configurations of the linkage can then be inverted relative to the coupler A, making pivot N appear in two distinct positions. The perpendicular bisector of a line connecting these two inverted N-points will intersect the line of the coupler at the missing pivot.

Item 21a/S/1 of the *Kinematic Courier*, March, 1958, discusses the subject of velocity-position synthesis using inverted design techniques. Item 21a/T/3 lists the fifteen relationships defining all possible relative angular velocity ratios for one "mode" of the four-bar linkage; this item would be a convenient adjunct to the paper here under discussion.

While the paper discusses synthesis where the velocity of one crank is prescribed for positions of the other crank, the method is just as easily applied where velocity and position of the same crank are specified.

[10] Mechanical Design Engineer, The Heald Machine Company, Worcester Mass.

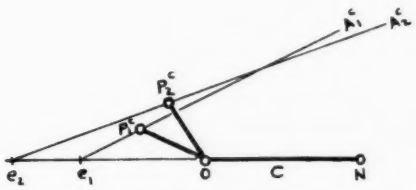

Initial layout

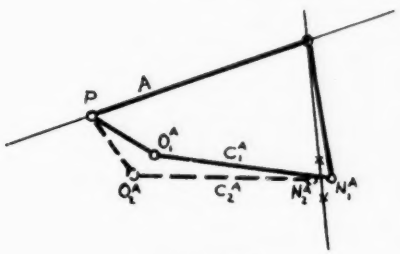

Inverted layout

Authors' Closure

We wish to thank all the discussers for the interest shown in our paper. The ideas and alternate methods they have contributed are a valuable supplement and pave the way for some future work.

Mr. Harding and Dr. Allen have described an alternate technique for determining the length of link A in the two-point graphical synthesis method. This inverted layout technique has the advantage of pointing directly to a solution with no trial and error. A transparent overlay can be effectively used to transform from the initial to the inverted layout.

Mr. de Jonge presents a different alternate two-point synthesis technique. His method also leads directly to a solution, but requires very accurate drafting.

A possible shortcoming of both of the alternate techniques is the difficulty of accurately erecting the perpendicular bisector of a short line segment.

Drs. Freudenstein and Sandor describe the application of their recently developed general vectorial approach to this problem. This further illustrates the generality and power of their method. They recognize, however, the appeal of the simplicity of our method to the practicing designer. We wish to thank them for calling attention to the work of K. Hain which also falls in this class.

All of these methods can be quickly learned and applied by the practicing engineer who should evaluate them on his own problems.

High-Range Plasticity of Metals Beyond Normal Work-Hardening

E. V. CRANE

Chief, Research and Development Engineering, E. W. Bliss Company, Canton, Ohio. Mem. ASME

W. S. WAGNER

Development Engineer, E. W. Bliss Company, Canton, Ohio

Metals, plastically worked for mass-production purposes are shown to have a little known and potentially valuable "high" working range, primarily compressive and substantially beyond commonplace practices and physicals. This "high range" lies beyond the point of normal tensile failure. It is distinguished by a steeper or more rapid rate of work-hardening. While some use has been made of it, to advantage, in wire-drawing, rolling, cold extrusion, and shell drawing, inadequate technical data concerning it may be attributed to unfamiliarity with the testing program. To provide pressed-metal engineering with the extended plastic-range data needed for planning operation sequences, a testing technique is outlined, which if not new, is at least unfamiliar and potentially useful until a better method is devised.

IN THE PLASTIC working of metals, for the purposes of maximum production, there is a rather elusive range beyond the point of normal tensile failure and in which the working of the metal must be essentially under compression. In order to visualize, evaluate, and utilize this high range, it is necessary first to obtain physical properties describing it. Rocket-motor bodies have been among the end items for which such maximum physical properties require consideration.

No single test procedure apparently has been developed which was suitable to give a complete picture of the plastic range. Therefore it has been necessary to correlate a number of tests in a composite curve.

The premise in doing this is that the progressive increase in true stress with strain is essentially the same whether the metal is worked by drawing, rolling, extrusion, testing-machine procedures, or other process.

This is obviously a faulty assumption, and yet, within certain broad limitations, it does prove revealing and useful.

The first restriction is that the working under consideration is all in the crystoplastic state, below the recrystallization temperature range. While this eliminates creep problems, there are still appreciable differences in the rate of work-hardening, depending upon the initial temperature, and heat generation in the working process. Further work is needed in the effect of work-generated heat upon the rate of work-hardening. In the research reported here, however, the slow movement of the testing machine does not raise the temperature of the samples appreciably.

A second problem in the composite grouping of a series of tests is possible variation of chemical composition and of mechanical preparation.

All of the material used in the several tests combined in Figs. 1 and 2, was taken from the same coil of steel for uniformity. All of it was processed together, up through hot-rolling to $^{41}/_{64}$ in. diam and spheroidize-annealing to a Brinell hardness of 160. As is shown in the tabulation, the tensile and compressive specimens for the No. 1 curves in both figures were taken from the coil in this state. The coil was then cold-drawn to $^{1}/_{2}$ in. diam, a reduction in area of 39 per cent. It was then Shuster straightened and showed a Brinell hardness of 242. Samples No. 3, for the tensile and the compressive tests in Figs. 1 and 2 were removed from this material.

The bar just described was then stress-relieved for 3 hr at 750 F, to retain the prior work-hardening while relieving the more severe stresses. It was then cold-drawn to $^{7}/_{16}$ in. diam. This is a total of 53 per cent reduction in area from the original $^{41}/_{64}$-in. diam. It was then Shuster straightened and again stress relief-annealed for 3 hr. At this point the Brinell hardness was 315. In this state, the specimens marked No. 7, for the tensile and the compressive tests of Figs. 1 and 2, were prepared.

The preparatory work of producing the material, spheroidize-annealing, cold-drawing, and stress relief-annealing was carried out by the Republic Steel Corporation, Union Drawn Division, Massillon, Ohio.[1]

After the compression test 7, the increase in area of the compressed slug was such that it was approaching possible tensile failure around the periphery. That is, at the end of compression test 7 it had reached a diameter of 0.695 in. and a thickness of 0.248 in. It was therefore placed in a lathe and turned down to a diameter of 0.252 in., retaining the thickness or height of 0.248 in. In doing this it is appreciated that the metal removed from the periphery had been less severely stressed and less severely work-hardened than the metal remaining which had formed the center portion of the previously worked slug. A study of such nonuniformity of working in a cylindrical compression specimen was presented during the panel discussion of the Plastic Working of Metals in December of 1954.[2]

Nevertheless, it is apparent from Fig. 2 that the difference was not enough to show a major discontinuity in the over-all plastic-range curve.

Fig. 1 gathers the three tensile tests. In any tensile test there is a general elongation up to the point at which some local weakness or grain-size difference permits the development of local necking. From that point on the change of stress and strain is localized at the neck. No equipment is available at present to record this change automatically. The true ultimate tensile strength (about 175,000 psi) is, of course, substantially higher then the nominal value (about 100,000 psi) which is obtained by taking a load value at about the point where generally elongation ceases and dividing it by the cross-section area back at the initial state, before any movement begins. Fig. 1 confirms general experi-

Contributed by the Metal Process Section of the Production Engineering Division and presented at the Annual Meeting, New York, N. Y., November 30–December 5, 1958, of THE AMERICAN SOCIETY OF MECHANICAL ENGINEERS.

NOTE: Statements and opinions advanced in papers are to be understood as individual expressions of their authors and not those of the Society. Manuscript received at ASME Headquarters, August 19, 1958. Paper No. 58—A-132.

[1] Through the courtesy of Mr. Eugene B. Files.

[2] E. V. Crane, "Plastic Metal Working," TRANS. ASME, vol. 78, 1956, p. 413.

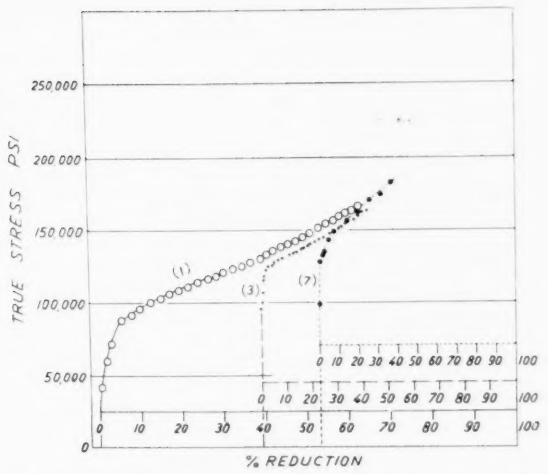

Fig. 1 True stress tensile tests of 4140 steel, from (1) spheroidize annealed state; (3) cold drawn, 39 per cent reduction; (7) stress-relieved and cold-drawn to a total of 53 per cent reduction and stress-relieved again

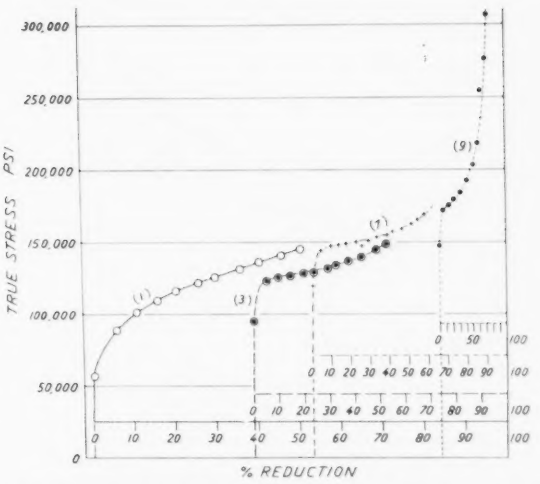

Fig. 2 Compression tests of 4140 steel from (1) spheroidize annealed state; (3) cold-drawn 39 per cent reduction; (7) stress-relieved, cold-drawn to a total of 53 per cent reduction from the initial rod, and stress-relieved again; (9) a continuation of test of specimen (7) except that it has been turned in its flattened state from 0.695 to 0.252 in. diam to obtain again a suitable ratio of diameter to height

ence that the true ultimate tensile strength varies comparatively little, regardless of the character of the annealing or the amount of prior working. An apparent exception to this rule will be shown in Fig. 3, where, however, the initiation of tensile fracture is inhibited by external pressure.

To show the change taking place at the neck, the tensile tests were carried out by a team of three men. The key man found the point at which necking began with a ball-point micrometer and continued to give a succession of readings of the diameter at this point. The second man read the pressure at the moment the diameter reading was given. The third man set down these simultaneous readings. The area at the time of each reading was computed from the diameter and the true unit stress was obtained from the comparison of this figure with the corresponding load. The percentage reduction in area from the original cross section also was computed for each point. In this way enough points are obtained to give a reasonably precise picture of the true stress-strain curve.

In co-ordinating the curves of the tensile tests from states 1, 3, and 7, curve 3 was started at 39 per cent reduction, as this was the amount which the metal had been worked by cold-drawing from state 1. Curve 7 was started at a point representing the 53 per cent reduction which had taken place from the original condition of state 1. It is shown that the differences in initial preparation are reasonably taken into account by this method and that the remaining plasticity after intermediate amounts of working is reduced as the prior working increases. The differences in point of failure may be attributed perhaps to small differences in grain size, impurities, or differences in alloy distribution. This point, however, limits further exploration of the plastic range by open tensile testing.

Compression testing is handicapped by the fact that it must start with a cylindrical slug which has a height of little more than the diameter because of the tendency to cock over to one side. The amount of compression in ordinary testing-machine practice is limited by the increasing area, the tendency to tensile fracture in the neighborhood of 100 per cent elongation of periphery, the influence of friction on the end surface, and the tendency to pyramiding of pressure toward the center of the slug when it becomes too thin. Nevertheless, it seems to be the only practical method of exploring the changes of physical properties which are

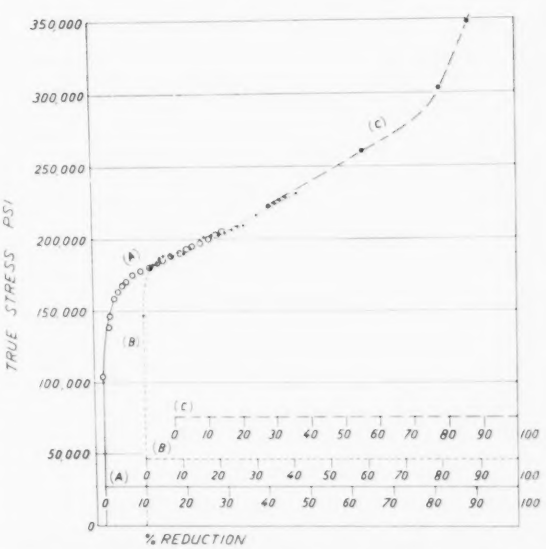

Fig. 3 Consolidation of tensile tests of heat-treated 4140 steel in which the first and second curves report tests performed in air and the third curve shows the results of a test performed in a hydraulic atmosphere at 365,000 psi

commercially obtainable when working primarily in compression. However, the grouping of a series of compression tests from different preparatory treatments of the same material does give a reasonably composite visualization of the change taking place.

In Fig. 2 are shown compression tests from each of the three initial states. In this case the pressure was brought up in a series of increments, and at each step the slug was removed and its height measured by micrometer and recorded against the corresponding pressure. It was then returned to the machine and the process repeated and each of the positions shown on the curves. The mean cross-sectional area was computed from the

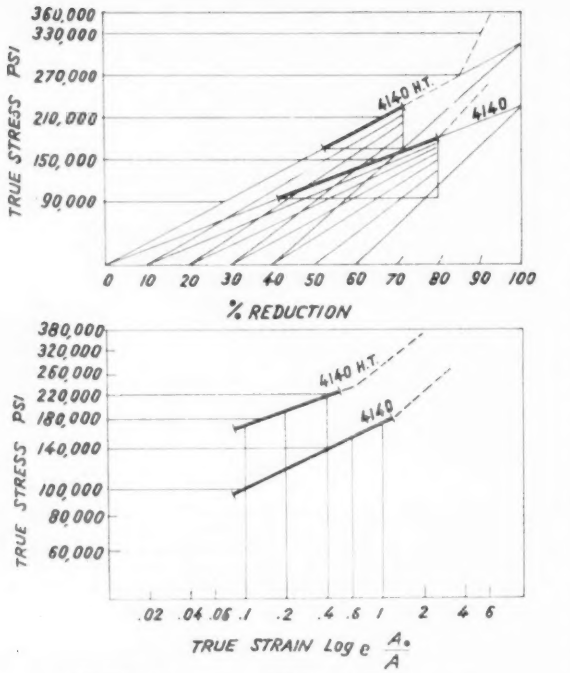

Fig. 4 Plastic-range, physical-property curves for 4140 steel, from annealed and heat-treated states in which dotted portions represent compressive working. Alternative choice of base curve is to suit mathematical preference.

original volume on the assumption that the volume remains constant which is nearly true. It is debatable whether one should use the mean cross-sectional area in computing the true unit stress for the slug bulges to some extent toward the center as the test progresses. This factor is probably one of the contributions to the irregularities shown in the comparative correlation of the related test curves, Figs. 1, 2 and 3. The grouping is again determined by starting the plot of each successive curve at the percentage reduction which that sample had undergone from the initial or prior state. Specimen 9 was obtained as has been described, by turning down specimen 7 to return the proportion to a shape which could be tested. Objections with regard to distribution of stresses and of working are valid, but the difference is not sufficiently great to interfere with the over-all objective.

The sharp rise in unit stress is that which is characteristic of what we have termed the high range or upper range of work-hardening.

Many years ago Templin[3] observed this phenomenon and described it as the point at which all slip planes which are favorably oriented to the direction of working have been used up. The characteristic has been observed many times since and the explanation still seems reasonably valid. Perhaps the ultimate plasticity curve, Fig. 4, should be plotted as a broad band which would recognize variations in composition and preparation as well as the weaknesses of testing technique. The use of the percentage-reduction curve in Fig. 4 is illustrated, for example, in the paper by Wagner[4] (his Fig. 3).

[3] R. L. Templin, "Effects of Cold Working on Physical Properties of Metals," *Trans. AIME*, vol. 89, 1930, pp. 466–480.

[4] W. S. Wagner, "Plastic Working of Metals," TRANS. ASME, vol. 78, 1956, pp. 401–405, Table 2, Fig. 6

Fig. 3 presents a still higher range in which the steel is heat-treated for dispersion-hardening, prior to being worked, with the resultant added work-hardening. This is obviously a tempting but difficult range in which tool loads will be extremely high. Some work has been done in the plastic working of heat-treated aluminum prior to aging but we know of comparatively little that has been done in the working of heat-treated steel. The offering of this curve is therefore academic for the present. It is revealing, however, that so much metal movement can take place and such high values can be achieved.

The AISI 4140 steel specimens used for the tests reported in Fig. 3 are unrelated to those reported in Figs. 1 and 2. The first specimen was normalized at 1650 F and air-cooled, giving hardness prior to testing of R_c 30. The second specimen was normalized at 1650 F, quenched from 1550 F, and drawn at 950 F, giving a hardness of R_c 34. Both of these specimens were turned from the same $1^1/_2$-in-diam cold-finished bar and were tested in the Bliss Metallurgical Laboratory at Canton, Ohio. The points were taken by the same procedure described in connection with Fig. 1.

The third specimen was one reported in a book by Prof. P. W. Bridgman.[5] It had been heat-treated to R_c 34.5 and then subjected to tensile test in a hydraulic atmosphere at 365,000 psi. Bridgman corrected the original test figures to show flow stress. He has attributed the extraordinary reduction to the high external pressure, preventing the initiation of tensile fracture. This seems like a logical explanation, but in any case, the procedure made possible the demonstration of the high-range properties for a heat-treated and work-hardened steel.

The relative positioning to show continuity and extent of the work-hardening curve had to be done arbitrarily in this case. It does demonstrate the differences resulting from different initial preparations. The difference in point of failure of the first two specimens which were tested at atmospheric pressure also may be attributed to the differences in preparatory heat-treatment.

Fig. 4 summarizes the plastic-range physical properties of AISI 4140 steel in the normal and the heat-treated states. In each case the normal range for which data were obtainable from tensile tests performed at atmospheric pressures is shown by a heavy line. The higher range, in which working had to be primarily or completely compressive, is shown by the dotted lines. In the upper group the true stress is plotted against strain represented as percentage reduction, which is convenient for algebraic proportioning. In the lower group true stress is plotted against true strain expressed as the natural logarithm of the change of area. This form is favored for the purposes of higher mathematics, but it should be noted that the straight-line relation does not hold beyond the point of normal tensile failure.

The correlation of different methods of expressing metal movement has been tabulated by Wagner.[4]

Rocket-Body Application

Fig. 5 shows the sequence of operations for the consideration of which the metallurgical research was performed. The designers of the part specified a minimum yield in the thin side wall of approximately 200,000 psi. Backward and forward extrusions were contemplated but in view of the relative metal thickness it was considered more economical and less troublesome to plan the drawing and ironing series shown. From the test data it was felt that the physical specification could be obtained without heat-treatment with a stress-relief anneal after the fourth or

[5] P. W. Bridgman, "Studies in Large Plastic Flow and Fracture," McGraw-Hill Book Company, Inc., New York, N. Y., 1952.

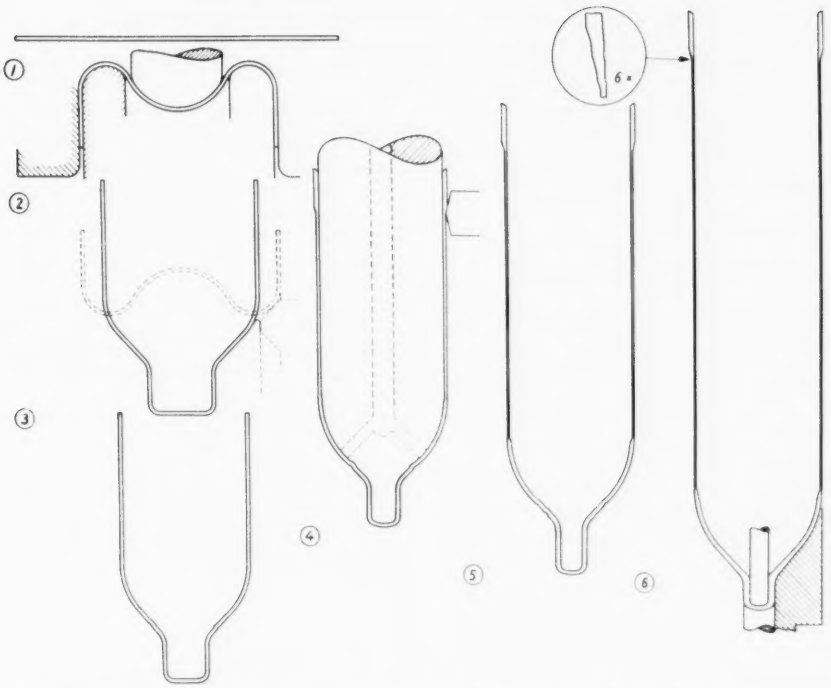

Fig. 5 Sequence of operations to produce the motor body (6), for which the physical-property tests were developed

fifth operation and probably a mouth or wall anneal early in the sequence.

On the other hand, an even higher value might be obtained by heat-treating and drawing, after the fourth or fifth operation, followed by ironing to correct the distortion in heat-treatment.

The sequence of operations is as follows:

1 Blank, draw, and indent, to gather the material for the neck.

2 Reverse and reduce the indent against the holding pad, and double-action redraw.

3 Single action, reduce the neck and redraw the wall.

4 Reduce the neck and perform the first ironing operation.

5 Reduce the neck and perform the second ironing operation.

6 Light finish ironing, bottom stamping, and neck upsetting.

In planning this sequence of operations, the tensile stresses are kept comparatively low. The resultant compressive stresses in the working area at the ironing ring are those which are to work the material up into the high stress range where a purely tensile stress would be likely to initiate fracture. Results are, therefore, reasonably predictable. Other operations which achieve the high range are primarily compressive metal movements in extrusion, rolling, and wire-drawing. The high stresses in the metal necessarily must result in even higher tool loads so that carbide rings in substantial prestressed holders are indicated. To prevent pressure welding or loading, with the resultant scratching, it is probable that a bonded-on zinc-phosphate protective coating, plus a bonded-on zinc-stearate coating, will be required. Some additional liquid lubricant may still be desirable.

DISCUSSION

Charles R. Bradlee[6]

The paper notes that an economic advantage may be found in working of metals in the high plastic range. This has certainly been substantiated by the experience of many manufacturers employing the techniques of cold extrusion in the manufacture of their products. Broad areas of application remain unexplored.

An adequate test of the behavior of various materials when worked in the "high plastic range" has long been needed. It has been needed for a multiplicity of reasons, but principle among them are:

1 The need for classification of various metals and their alloys as regards relative formability.

2 Better identification of the work-hardening properties of various alloying elements.

3 The test of raw materials which are purchased for forming operations in the high plastic range. (This test may ultimately be applied as a specification on the manufacturer where the nature of the forming operation is sufficiently critical as to allow the added cost of this control.)

The procedure outlined would appear to satisfy the need for a "plasticity test." The procedure is a cumbersome one, as would most likely be any other one. The principle deterrent to its use, however, would seem to be the use of cold drawing operations as the means of obtaining the initial reduction required.

[6] Senior Project Engineer, Process Development Staff, General Motors Corporation, Detroit, Mich. Assoc. Mem. ASME.

Acknowledging the basic soundness of the test as a means of obtaining a quantitative measurement of plasticity, a modification in procedure can be suggested which will obviate the need for the cold drawing operations. One further assumption is needed to permit this, namely, that the substitution of a rectangular prism having an initial height/width/length ratio of 1.2/1/1.5 would not affect the accuracy of the stress readings. The height/width ratio of 1.2/1 is selected as the maximum which can be upset uniformly.

The test procedure would be as follows:

1 The initial slug of material would be a right cylinder or simple prism of roughly cubic dimensions having a height of approximately 2 inches and parallel ends. Following the desired initial preparation, this blank would be upset to approximately 50 per cent its original height by any available means, such as a heavy press or testing machine. Because the low plastic range is of little interest, force and height readings need not be taken, initial and final height being the only information recorded.

2 The flattened blank of approximately one inch thickness obtained from step 1 would then be machined to a rectangular prism measuring 1.2 in. high, by 1 in. wide, by 1.5 in. long (with the 1-in. width dimension that established in the initial upset.)

3 The 1.2 in. $\times$ 1-in. $\times$ 1.5-in. prism would then be upset in a testing machine to a final height 56 per cent its original and readings of height and force taken at several points.

4 The resulting flattened shape would again be machined to a rectangular prism having as its width the final upset height of step 3 and a height and length in the ratio of 1.2 and 1.5 to the width.

5 Steps 3 and 4 would be repeated until the specimen became too small to use or until the necessary data have been assembled.

This procedure, if followed through the fifth upset, would result in a reduction in area of approximately 95 per cent (true strain $= -3$). Blank thickness following the fifth upset would be approximately 0.2 in., permitting further working if desired.

The design of this procedure takes into account and attempts to minimize the effects of end friction, heat of deformation, unsymmetrical upsetting, nonuniformity of working during upset, and pressure pyramiding. The result is a compromise. Quite probably a better one can be found. It is suggested primarily as a means of further defining the plasticity test proposed by the authors and implementing its use.

Regarding the presentation of results, the use of true strain would be a far better measure of plastic deformation than would be per cent reduction. This is especially true in the high plastic range where small increases of "per cent reduction" describe large amounts of plastic working.

The authors are to be congratulated on their studies to date and the steps taken to develop a useful test of plastic behavior in metals.

NATHAN H. COOK

Assistant Professor of Mechanical Engineering, Massachusetts Institute of Technology, Cambridge, Mass.

Self-Excited Vibrations in Metal Cutting[1]

The basic mechanisms which cause self-excited vibrations of a cutting tool relative to the work are discussed in a qualitative manner. Similarly, mechanisms inherent in the cutting process which can damp or limit vibrations are discussed. Experiments are presented which are in agreement with the theory.

In the usual metal-cutting operation, three processes occur simultaneously: Shear on the shear plane (A, Fig. 1); sliding between chip and tool (B, Fig. 1); and sliding between work and tool flank (C, Fig. 1). Each of these processes can be responsible for exciting vibrations between the tool and workpiece. In this paper we describe qualitatively the effect of each process upon tool-work vibrations.

When neither tool nor work is vibrating, the tool will assume some fixed position relative to the work. We consider vibrations to be departures from this fixed relationship. Although either tool or workpiece or both may be vibrating, we will consider the vibratory motion of the tool *relative* to the work, x and y, Fig. 1.

The Shear Process

The shear force exerted on the shear plane is equal to the shear stress τ_s times the shear-plane area. Shaw and Hölken [1][2] have shown that when vibrations exist, the shear angle of Fig. 1 may vary in such a way as to produce a net energy input to the system per cycle. The shear angle cannot vary at too great a rate relative to the cutting speed V or the shear plane will enter the chip. Hence this mechanism is restricted to relatively low-frequency vibrations. It is quite possible that this mechanism is present and may predominate in most low-frequency workpiece vibrations.

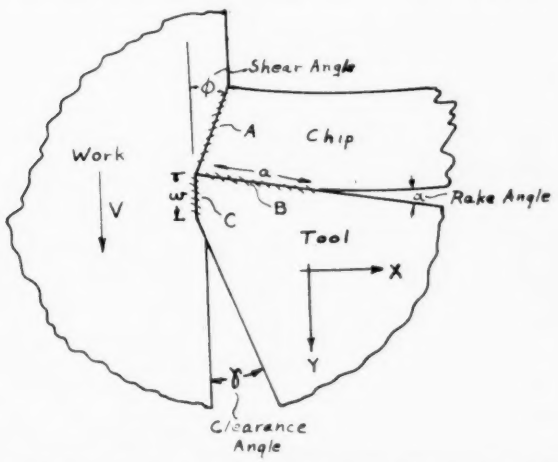

Fig. 1 A schematic view of cutting process showing three processes which occur simultaneously: A, shear; B, sliding; C, sliding

Vibration excitation due to varying shear stress on the shear plane has been shown very clearly for titanium machining [2]. Fig. 2 shows a typical titanium chip produced at high cutting speeds. The chip is seen to be composed of a series of "blocks" separated by zones of highly deformed metal. There are two primary reasons for this mechanism: At elevated temperatures the flow stress τ_s of titanium falls off rapidly; titanium has low thermal conductivity k and low volumetric specific heat ρc. A comparison of the values of $k\rho c$ for various metals is given in Table 1.

Table 1 Thermal property ($k\rho c$)

	$\frac{(\text{Btu/sq in. deg F})^2}{(\text{sec} \times 10^6)}$
1020 steel	27
18-8 stainless	7.5
Aluminum	34
Titanium	5.5

Owing to the low conductivity, heat generated by the shear process remains in the shear zone for a relatively long time;

Fig. 2 Photomicrograph of a titanium chip showing inhomogeneous strain distribution

[1] The major points of this paper are abstracted from the author's ScD thesis, Massachusetts Institute of Technology, 1955.

[2] Numbers in brackets designate References at end of paper.

Contributed by the Production Engineering Division and presented at a joint meeting with the Machine Design and Applied Mechanics Divisions at the Annual Meeting, New York, N. Y., November 30–December 5, 1958, of The American Society of Mechanical Engineers.

Note: Statements and opinions advanced in papers are to be understood as individual expressions of their authors and not those of the Society. Manuscript received at ASME Headquarters, August 28, 1958. Paper No. 58—A-189.

due to the low specific heat, it takes a relatively small amount of heat to raise a given volume of metal to a given temperature. Thus, as the metal is sheared, the shear zone becomes hot and softens. When this "thermal strain-softening" exceeds the conventional strain-hardening, the deformed metal becomes softer and more easily deformed than the parent metal, and deformation continues in one location. It is apparent from the chip, Fig. 2, that such a mechanism cannot exist without motion of the tool relative to the work. This vibration is unique in that its frequency increases with both speed and the natural frequency of the system. This mechanism usually can be spotted by the gross irregularities in the chip form. The mechanism is almost always seen when cutting high-strength, low-thermal-conductivity materials such as titanium and zirconium and is frequently present when machining some of the more common engineering materials.

Steel chips that have a "wavy" cross section or are almost discontinuous are probably formed by this thermal-softening mechanism. However, in the majority of cases, this mechanism is not present and we can expect that variations in the flow stress τ_s caused by vibration will tend to stabilize the vibration rather than excite it. The greater the value of $k\rho c$ and the more refractory the material, the greater the stabilizing tendency.

Sliding Between Chip and Tool

To understand the mechanism which occurs at B and C, let us look to the mechanism of sliding friction. The friction force which exists when one clean metal slides over another is generally considered to be the force required to shear the welds which are formed between the sliding members. The methods of Carslaw and Jaeger [3], can be used to estimate the interface temperature between the sliding surfaces in terms of the sliding speed, geometry, thermal properties, and the friction force. If we also know the way in which shear stress varies with temperature and strain rate, we can estimate the variation of friction force with velocity. When we do this, we find that the temperature increases with relative velocity and thus the friction force decreases at higher speeds. This analysis is in agreement with high-speed sliding tests where the friction force is found to decrease at high speeds. The analysis indicates that the mechanism will exist even when the velocity is changing rapidly as is the case in tool vibrations.

A straightforward analysis of a simple vibrational system shows that whenever the friction force decreases with increased velocity, self-excited vibrations can occur. The amount of damping present determines whether or not vibrations do occur.

This type of analysis can be applied to the tool-chip interface in cutting, using the analysis of Loewen and Shaw [4] to calculate the temperature, and the data of MacGregor and Fisher [5] to evaluate the effect of temperature and strain rate upon shear stress. Typical results are shown in Fig. 3. It is apparent that the shear stress and, hence, the friction force decrease with increased velocity of chip relative to tool. Thus, if the tool vibrates relative to the work in such a manner that the velocity of chip relative to tool varies, there will be a net energy input to the system which can sustain the vibration.

The normal force exerted by the chip on the tool will not directly excite vibration. However, if the velocity of the tool relative to the work in the y-direction exceeds the cutting speed, i.e.

$$V_y > V \tag{1}$$

the tool will not touch the chip during part of the cycle. This is a very strong "damping" mechanism and will limit the amplitude of vibration. Arnold [6], Chisholm [7], and Doi [8] found in their studies that the vibrational amplitude was limited in this

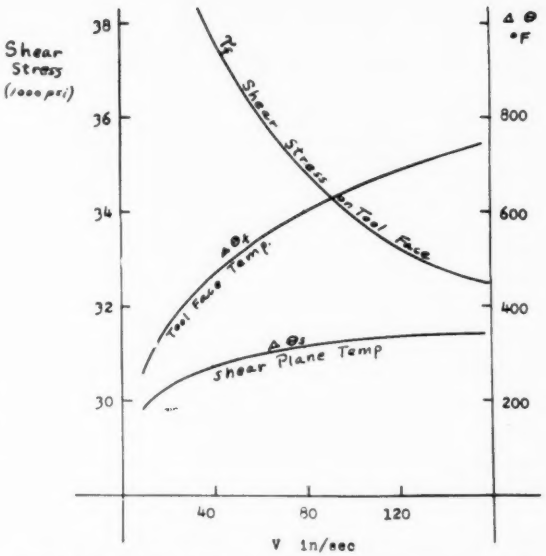

Fig. 3 Calculated variation of chip-tool interface temperature (θ_f) and chip-tool interface frictional stress (τ_f) with cutting speed V

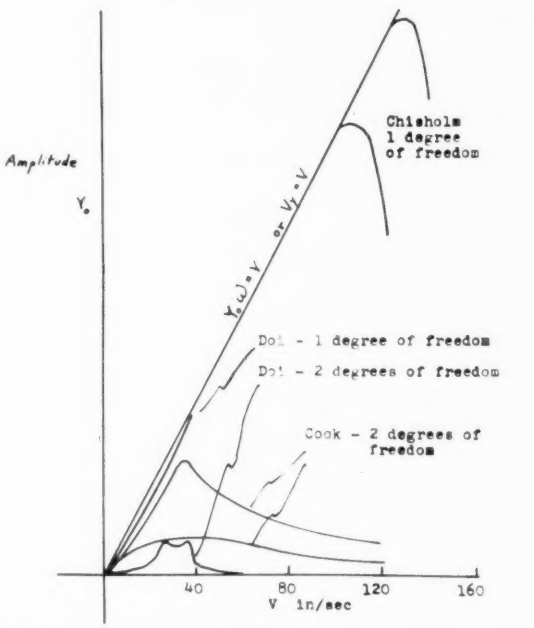

Fig. 4 Variation of vibration amplitude (y, Fig. 1) with cutting speed as determined by several investigators

manner, Fig. 4. Thus the contact between chip and tool face can have two effects:

1 Excitation of vibrations parallel to the tool face. Excitation of vertical vibrations (a variation in cutting speed V causes a variation in the speed of chip relative to the tool).

2 Limiting of vibrations perpendicular to the tool face.

Sliding Between Work and Tool Flank

When we cut, there is always some contact between the workpiece and the tool flank. On an ideally sharp tool, the contact

will be due to elastic rebound of the work material after it passes the cutting edge. As the tool wears, the wear land w, Fig. 1, also rubs against the work. It is clear that if the tool were free to vibrate in a vertical direction, our previous comments on the ability of sliding surfaces to excite vibrations apply. Thus, when there is vibration in the vertical (y) direction, the tool-flank friction force will feed energy into the system and sustain vibration. If, however, the tool vibrates in the horizontal direction, the force perpendicular to the wear land will remove energy from the system and, hence, reduce the vibrational tendency. In fact, if the horizontal velocity of the tool moving into the work exceeds the cutting speed times the tangent of the clearance angle, i.e.

$$-V_x > V \tan \gamma \qquad (2)$$

there will be a contact force exerted along the entire clearance face. This force will be certain to limit the amplitude of vibration in the x-direction. Thus we see that rubbing on the clearance face can have two effects:

1 Excitation in the vertical (y) direction.

2 Limiting and damping in the horizontal (x) direction.

To summarize, in the more usual case where "thermal-softening instability" does not occur on the shear plane:

(a) The shearing process damps vibrational motion which is parallel to the shear plane.

(b) The tool-chip interface friction force excites vibration along the tool face while the normal force may limit oscillation perpendicular to the tool face.

(c) The wear land and clearance-face friction force can excite vertical vibrations while the normal force can limit horizontal vibrations.

Which of these mechanisms predominates depends largely upon the cutting speed and the stiffness of tool relative to work in the x and y-directions (K_x and K_y). Generally, self-excited vibrations occur at either the natural frequency of the tool, or at the natural frequency of the workpiece as it is held in the machine. In general, tool natural frequencies are of the order of several thousand cycles per second, whereas workpiece natural frequencies are generally (though not necessarily) of the order of a few hundred cycles per second. We should not necessarily expect the same exciting mechanisms to obtain at these widely differing frequencies. Using this general observation, various lathe vibrations can be separated into two groups, namely, essentially single-degree-of-freedom systems when $K_x >>> K_y$ and two-degrees-of-freedom systems where $K_x \sim K_y$. Table 2 shows which lathe operation comes in which group and which types of excitation, damping, and limiting may occur.

Experimental Results

Several of the mechanisms discussed and summarized in Table 2 can be demonstrated clearly through experiment. Most previous investigators have not reckoned the important difference between one and two-degree-of-freedom systems and hence have produced much contradictory data.

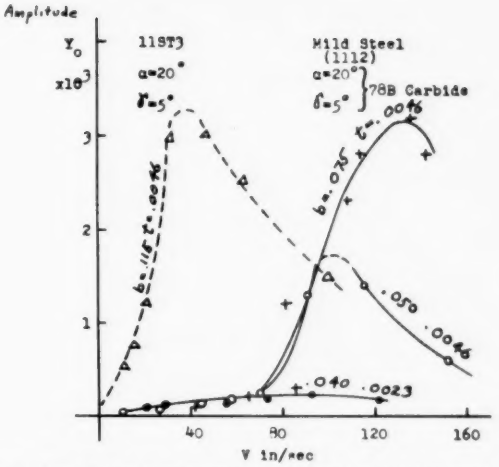

Fig. 5 Amplitude-velocity curve is seen to peak at a higher speed for steel than aluminum

Effect of Cutting Speed. From Fig. 3 we see that the negative slope of the τ_f-V curve is less severe at high speed; hence we might expect that at a sufficiently high speed, the system damping would overpower this exciting force. Indeed, this seems to be the case. Fig. 4 shows the type of data obtained by Chisholm, Dio, and the author; the limiting curve $V_{y\,max} = V$ is also shown. The speed at which the amplitude peaks depends upon many factors. The total energy involved in the cutting process is important because, if at a certain speed a certain portion of the total energy is left in the system, the greater the total energy, the greater the energy that must be absorbed in damping. Thus we generally find that the larger the area of cut bt (b = depth, t = feed) the higher the speed before the amplitude peaks. The work material is obviously important. If a material retains its strength to higher temperatures, we must go to higher speeds before the strength starts to diminish appreciably. When cutting aluminum, the author could always achieve a peak in the amplitude-velocity curve; however, it was difficult to do so with mild steel. Fig. 5 shows a comparison of amplitude versus velocity curves for these two materials.

Effect of Wear Land and Clearance. According to our theory, rubbing on the clearance or wear land can excite vibrations. Arnold[6] and Saljé[9] have both looked at this effect. Fig. 6 shows how the amplitude varied with wear land in a single-

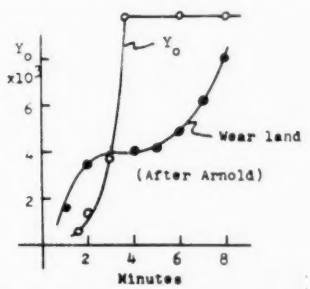

Fig. 6 Effect of wear land upon vibration amplitude for a single-degree-of-freedom system

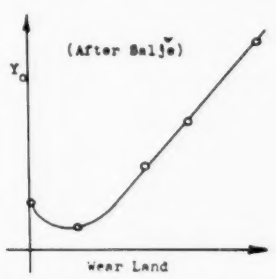

Fig. 7 Effect of wear land upon vibration amplitude for a two-degree-of-freedom system

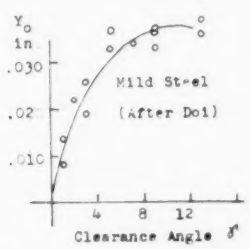

Fig. 8 In a two-degree-of-freedom system, the clearance angle can limit the amplitude of vibration

Table 2 Summary of vibrational predictions for lathe work

	Excitation			Damping		Limiting	
	Rubbing on tool face	Rubbing on clearance	Varying ϕ	Force perpendicular to clearance face	Shear stress on shear plane	Clearance angle, $\frac{V_{x\max}}{V} = \tan\gamma$	Separation of chip and tool $V_{y\max} = V$
Normal turning							
Low frequency $K_x >>> K_y$	√	√	√		√		√
High frequency $K_x \sim K_y$	√	√		√	√	√	√
Form cut							
Low frequency $K_x \sim K_y$	√	√	√	√	√	√ (Low speeds only)	√
High frequency $K_x >>> K_y$	√	√			√		√

degree-of-freedom system. Fig. 7 shows the results for a two-degree-of-freedom system. We note that in a two-degree-of freedom system, interference on the clearance face can limit oscillation. Thus, as the wear land grew, Fig. 7, it first limited, then excited oscillation. Doi investigated the effect of clearance angle upon his two-degrees-of-freedom system. Fig. 8 shows his results wherein amplitude increased with increased clearance. It is apparent that the clearance angle was limiting the oscillation. In fact, he stated that the effect is "more remarkable at low cutting speed."

Effect of Tool-Shank Geometry. Three tools having the same length and cross-sectional area were ground to have the following stiffness ratios:

Tool no. 1	$K_x = 4K_y$
2	$K_x = K_y$
3	$K_x = K_y/4$

Fig. 9 shows vertical amplitude y_0 versus speed and also the ratio y_0/x_0 versus speed. We see that the vertical stiffness k_y has much more effect upon the system than the horizontal stiffness k_x. This is probably due to the fact that when vertical oscillations are reduced, two exciting mechanisms are reduced; namely, the clearance and tool-face rubbing. When the horizontal oscillations are reduced, the clearance rubbing is unaffected while the tool-face rubbing is only affected to a small extent.

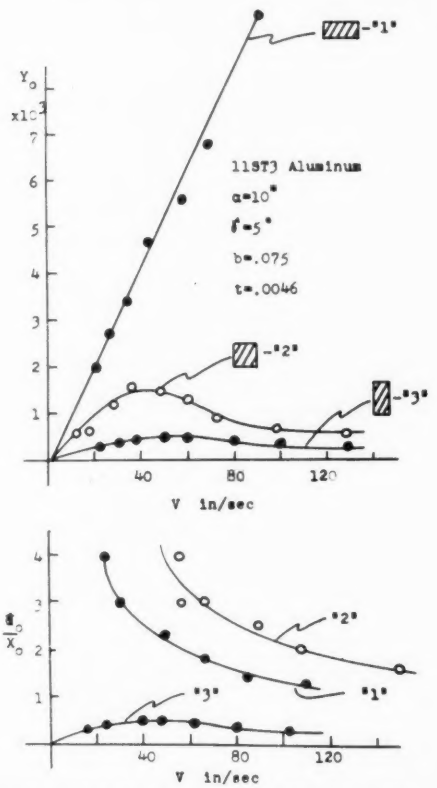

Fig. 9 Effect of tool-shank geometry upon vibration amplitude. Vertical stiffness is seen to be more influential than horizontal stiffness.

Summary

Metal-cutting vibrations can be excited by a variety of mechanisms. At high frequencies, the negative slope of the friction-velocity curve is apparently responsible. At low frequencies, the variation of shear angle may be the important factor. This mode of excitation requires more experimentation and verification. Damping can take place in the mechanical system and also in the shear plane. Amplitude limitation can occur by the chip leaving the tool face or by interference on the clearance face.

References

1 M. C. Shaw and W. Hölken, "Über Selbsterregte Schwingungen bei der Spanenden Bearbeitung," *Industrie-Anzieger*, no. 8, 1957.

2 N. H. Cook, "Visual Study of the Machining of Titanium," Report WAL 401/172-6, Watertown Arsenal, November, 1953.

3 H. S. Carslaw and J. C. Jaeger, "Conduction of Heat in Solids," Clarendon Press, Oxford, England, 1947.

4 E. G. Loewen and M. C. Shaw, "On the Analysis of Cutting-Tool Temperatures," TRANS. ASME, vol. 76, 1954, pp. 217–225.

5 C. W. MacGregor and J. C. Fisher, "Tension Tests at Constant True Strain Rates," *Journal of Applied Mechanics*, vol. 12, TRANS. ASME, vol. 67, 1945, pp. 217–227.

6 R. N. Arnold, "The Mechanism of Tool Vibration in the Cutting of Steel," *Proceedings of The Institution of Mechanical Engineers*, vol. 154, 1946, pp. 261–276.

7 J. Chisholm, "Metal Cutting and Machine Shop Productivity; The Cause of Chatter Vibrations," *Machinery*, vol. 75, 1949. pp. 51–53.

8 Shizuo Doi, "On the Chatter Vibrations of Lathe Tools," Memoirs of the Faculty of Engineering, Nagoya University, vol. 5, 1953.

9 E. Saljé, "Ursachen und Minderung von Werkzeugschwingungen," *Industrie-Anzeiger*, no. 80, October, 1955.

10 I. Tlusty and M. Polatschek, "The Theorie of Self-Excited Vibrations in Cutting and Machine Tool Stability Calculations," *Stanki i Instrument*, 1956 (Russian).

Journal of ENGINEERING FOR INDUSTRY

Information for Authors

• Manuscripts should be submitted in final form to the Editor. Each manuscript must be accompanied by a statement that it has not been published elsewhere nor has it been submitted for publication elsewhere. A paper which would occupy more than 8 pages of the Journal may be returned to the author for abridgment.

• The author should state his business connection, the title of his position, and his mailing address. A short abstract (50 to 100 words) should be included on the first page immediately preceding the introductory paragraph of the paper.

Three copies of the manuscript are required. One of these must be a carefully prepared printer's copy, typed in double spacing, on one side of the page only, with wide margins, on $8^1/_2$ by 11-in. opaque white paper. Mimeographed manuscripts, if prepared with exceptional care, can be accepted provided they are completely edited.

• As far as possible, all mathematical expressions should be typewritten. Greek letters and other symbols not available on the typewriter should be carefully inserted in ink. Care should be taken to distinguish between capital and lowercase letter, between zero (0) and the letter (*O*), between the numeral (1) and the letter (*l*), etc. A letter representing a vector cannot be printed with an arrow above or below it. The letter should be underscored with a single wavy line, wherever it appears in the text, to designate boldface type.

• A list of symbols carefully marked for the use of the editor (thus: κ, Greek l.c. kappa), if it has not been included in the body of the paper, should accompany the manuscript on a separate page.

• Before preparing a manuscript the author should study printed articles in the Journal, with special attention to the form and style of mathematical expressions, tables, footnotes, references, and abstract. Numbers that identify mathematical expressions should be enclosed in parentheses. Numbers that identify references at the end of the paper should be enclosed in brackets. Care should be taken to arrange all tables and mathematical expressions in such a way that they will fit into a single column when set in type. Equations that might extend beyond the width of one column (fractions that should not be broken or long expressions enclosed in parentheses) should be rephrased to go on two or more lines within column width. Fractional powers are preferred to root signs and should always be used in more elaborate formulas. The solidus should be used instead of the horizontal line for fractions wherever possible.

• A normal paper should not exceed 8 pages in the Journal. It is about 8000 words or 20 double-spaced typewritten pages exclusive of drawings. A Technical Brief should not exceed 750 words or about one page in the Journal inclusive of drawings.

• Originals and two copies of figures must accompany the manuscript. Line drawings should not be larger than $8^1/_2 \times 11$ in. and should be planned for reduction to column width. Lettering should be large enough to be clearly legible when the illustration is reduced. The originals of line drawings must be in India ink on white or pale blue tracing paper or tracing cloth. Photographs of equipment or test specimens must be glossy prints and should be used sparingly. Captions for figures should be typed double-spaced and included as the last page of the manuscript. The figure number and author's name should be written in the margin or on the back of each illustration.

• Titles of papers should be brief.

• Authors can obtain copies of the ASME Manual MS-4, "An ASME Paper," from the Editor and are urged to do so before drafting their papers in final form.

• Papers published in Journals of the Transactions of the ASME must be presented at a Meeting, either in person or by title. Scheduling of papers is in the hands of the Publications Committee.

• An author is entitled to 25 preprints free of charge (in the case of two authors, 15 each; three or more authors, 10 each). Larger quantities of preprints or reprints can be ordered from Editorial Department, The American Society of Mechanical Engineers, 29 West 39th Street, New York 18, N. Y. Quotations will be sent on request.

Please address all communications to:

Editor, ASME,

29 West 39th Street,

New York 18, N. Y.

ASME Publications Committee

Important ASME Publications

MATERIALS HANDLING HANDBOOK

Published 1958. $20.00. — With this Handbook you have the means for analyzing your own materials handling operations, planning for greater efficiency, installing and operating important systems, and measuring results. Illustrations, tables, cost, and work flow forms put best current practice at your finger tips. CONTENTS. Definition and Scope of Materials Handling • Analyzing Materials Handling Problems • Materials Handling Factors • Factory Planning • Materials Positioning in Production • Materials Handling Research • Materials Handling and Production Control • Communicating Systems • Training Personnel • Handling Bulk Materials • In-Process Handling of Bulk Materials • Unit Handling for Various Shapes • Unit Handling in Manufacturing • Scrap Classification and Handling • Uses of Containers in Industry • Industrial Packaging • Palletization • Warehousing and Yard Handling • Truck Terminal Handling • Railroad Terminal Handling • Marine Terminal Handling • Air Terminal Handling • Belt Conveyors • Elevating Conveyors • Chain Conveyors • Trolley Conveyors • Cable Conveyors • Haulage Conveyors • Vibrating and Oscillating Conveyors • Pneumatic Conveyors • Package Conveyors • Fixed Cranes, Derricks, and Cableways • Traveling Cranes and Towers • Portable Cranes • Elevators • Winches • Auxiliary Crane Equipment • Positioning Equipment • Powered Industrial Trucks • Industrial Hand Trucks • Industrial Tractors • Highway Trucks and Truck-Trailers • Railroad Freight Cars • Marine Carriers • Air Carriers • Containers.

ADVANCES IN MATERIALS HANDLING (*Being the Proceedings of the 1958 Conference of the ASME Materials Handling Division*)

Published 1958. $4.50.—The subject coverage ranges from materials handling on the management level to new developments in pneumatic materials handling and in industrial bulk handling, the application of advanced materials handling techniques to non-mass production plants, the design and development of special equipment such as used for high capacity bulk handling and handling nuclear materials, handling problems with radioactive materials, materials handling equipment in missile launching, and materials handling in logistics for missiles.

DIAPHRAGM CHARACTERISTICS, DESIGN AND TERMINOLOGY

Published 1958. $3.75.—This Manual defines a diaphragm and its performance characteristics, describes methods of measuring and representing them, shows how they are related and used, describes and illustrates the effects of design details and manufacturing methods on the characteristics. In the appendixes, the terms and notation used are defined, the equipment and methods of testing described, applications of the diaphragms classified and equations given.

PROCEEDINGS OF THE CONFERENCE ON LUBRICATION AND WEAR

Published 1958. $23.00—Here is the complete record of the 1957 Conference arranged by the Institution of Mechanical Engineers with the collaboration of the ASME for the purpose of evaluating current lubrication knowledge, bringing out the findings of important experiments conducted in the United States, Canada, United Kingdom, and Europe; and obtaining the views of those participating in the discussion. Subjects dealt with include hydrodynamic lubrication, boundary friction, boundary lubrication, bearing metals, novel bearing materials, glands and seals, solid lubricants, surface treatments, ball and roller bearings, gear lubrication, engine lubrication, miscellaneous lubricants and applications, additives, and wear. The 34 papers on the latter subject cover laws of wear rate; mechanism of wear; testing of materials for resistance to wear; surface films; effective temperature and environment; wear due to abrasion, fretting, scuffing, pitting; wear on cutting tools; wear in engines, gears, etc.; influence and nature of rubbing surfaces.

77-YEAR INDEX TO ASME TECHNICAL PAPERS

Published 1957. $20.00.—This is an index to the technical papers published in the ASME Transactions, the Journal of Applied Mechanics, and Mechanical Engineering for the past seventy-seven years. It is divided into two parts with the first covering the papers published between 1880 and 1939, and the second, indexing those published from 1940–1956. Each part has a subject and an author index. The former lists the titles of the papers chronologically under as many headings as are necessary and includes numerous cross-references to direct attention to related material. The alphabetically arranged authors' index gives the headings and the year under which each paper is listed in the subject index.

METALS ENGINEERING: PROCESSES

Published 1958. $13.50.—Presents detailed data on the various processes by which metals are converted into finished products. For each of the manufacturing methods, there is a compilation of the basic physical characteristics to be considered and the general advantages and limitations usually encountered. Concise, parallel data concerning the suitability of various metals for each process, and the tolerances on size and surface finish obtainable are included.

METALS ENGINEERING: DESIGN

Published 1953. $10.00.—This book discusses the essential properties which need to be evaluated by the design engineer in his selection of one material over another. Comprising 48 sections and written by 43 well-known authorities, it deals with the over-all problem of selection of material and takes up such specific items as high temperature considerations, plasticity, residual stresses, vibration, fatigue, shot peening, cold working, nitriding, flame strengthening, impact, corrosion, non-destructive testing, surface finish and mass production, and design theory and practice.

METALS PROPERTIES

Published 1954. $11.00.—Provides, in convenient charts and tables, data on a broad range of metals in common industrial use —AISI steels, ASTM steels, cast copper alloys, aluminum alloys, tin, magnesium, etc. Tabulated under each of the more than 500 metals listed is such information as the chemical composition of the metal; its brittleness, heat treatment and other characteristics; its industrial uses; treatment temperatures for forging, annealing, quenching, etc.; such technological properties as recrystallization temperature and hot working temperature, and a great deal of other pertinent information to help the designer choose the proper metal for each part or product.

ENGINEERING TABLES

Published 1956. $12.00.—A collection of tables often wanted by engineers but not commonly found in handbooks covering: Bar Stock and Shafting. Conversion Factors. Formulas for Stress and Strain. Properties of Sections and Cylinders. Bearings. Bearing Load Analysis. Spur Gears. Helical and Herringbone Gears. Bevel Gears. Worm Gears. Cylindrical Fits. Standard Tapers. Keys and Keyseating. Bolts. Counterbores. Screw Threads. Slots. Serrations and Splines. Nuts. Pins. Snaprings. Washers. Wrench Openings. Springs. Aircraft and Mechanical Tubing. Pressure Tubes. Pipe. Pipe Threads and Fittings. Electric Motors. Graphical Symbols. Welding. Gaskets. Hydraulic Standards and Symbols. O-Rings. Packings. Seals. Bibliography.

20% Discount to ASME members

THERMODYNAMIC AND TRANSPORT PROPERTIES OF GASES, LIQUIDS AND SOLIDS

Published 1959. $12.50.—Provides a wealth of information that can be profitably applied to the solution of many problems in various areas demanding a knowledge of thermal properties of materials. Specifically, the book surveys the present theoretical and experimental state of the science; reports a large amount of data on experimental and theoretical techniques; reviews and evaluates the present state of knowledge in the specific areas covered; and indicates the gaps of knowledge existing in both transport and thermodynamic properties, particularly at high temperatures and at high or even moderate pressures. The information was originally presented at a Symposium sponsored by the Standing Committee on Thermophysical Properties of the ASME Heat Transfer Division in February, 1959.

FLUID METERS, THEIR THEORY AND APPLICATION

Published 1959. $8.00.—This Fifth Edition includes information on a number of new types of fluid meters and metering procedures that have been developed in recent years. It is divided into three sections with the first giving the classification and nomenclature of fluid meters, together with definitions of special terms and other general information. The theory of fluid measurement and the steps taken to develop practical working equations from the theoretical relations are set forth in the second section. Figures and tables for use in solving practical fluid measurement problems, along with examples illustrating their proper use, are contained in the third section.

FLOW MEASUREMENTS (*Chapter 4, Part of 5 Instruments and Apparatus*)

Published 1959. $5.00.—These rules apply when the primary element is an orifice, a flow nozzle, or a Venturi tube. The fluid may be compressible or incompressible. The primary element may be installed within a continuous section of pipe flowing full, or at the inlet or exit of a plenum chamber. Specifically this Chapter includes information on the construction of these three primary elements, the recommended techniques governing tests, the necessary equations for computing rate of flow, examples to illustrate the application of typical data, a discussion of tolerances applicable to certain of the factors involved in the measurements, and an outline of the major advantages and disadvantages of various types of primary elements.

MANUAL ON THE CUTTING OF METALS WITH SINGLE POINT TOOLS

Published 1953. $10.00.—This book contains shop-tested data on the machining of high nickel alloys, stainless steels, copper and brass alloys, magnesium, cast irons and plastics. It offers valuable information on the structure of the metals to be machined, the correct tool material, size and shape of cut, and the proper cutting fluid. It shows how to predetermine the power requirements and best operating speed for all jobs. It helps time study men to set standards of practice and cost of production, and it provides 322 tables of cutting speeds and horsepower for various feeds and depths of cut when turning commonly used steels and cast iron.

RESISTANCE OF VARIOUS MATERIALS TO CAVITATION DAMAGE

Published 1957. $3.00.—This report contains information regarding the relative resistance of various materials to cavitation damage and is based on years of field experience under operating conditions and laboratory tests with accelerated cavitation machines. It also shows the correlation between these tests and experience and discusses the merits of several new materials and new methods which have been developed to give better cavitation resistance. Tables, photographs and charts supplement the text.

THE AMERICAN SOCIETY OF MECHANICAL ENGINEERS **29 W. 39th St., New York 18, N. Y.**